Laboratoire de Constructions Hydrauliques
Ecole Polytechnique Fédérale de Lausanne

Communication 20

High velocity aerated flows on stepped chutes with macro-roughness elements

Stéphanie André

Editeur : Prof. Dr A. Schleiss

Lausanne, 2004

Communications du Laboratoire de constructions hydrauliques ISSN 1661-1179
Ecole Polytechnique Fédérale de Lausanne
Editeur: Prof. Dr A. Schleiss

Preface

Since the development of RCC techniques for the construction of concrete dams, the behaviour of aerated flow on conventional stepped chutes was investigated by a large number of researchers. In parallel, several lining systems consisting of macro-roughness concrete elements for protecting the downstream face of embankment dams have been developed.

Dr. Stéphanie André carried out for the first time a systematic experimental study on stepped chutes equipped with additional macro-roughness elements with the purpose of increasing energy dissipation along the slope. The effect of endsills and blocks fixed on the steps was analyzed for alternate arrangements and different spacings. The numerous tests with various configurations of macro-roughness elements allowed a better understanding of the physical mechanism involved in the energy dissipation process. The influence of macro-turbulence phenomena such as circulation cell and transversal jet could be clearly shown. Several methods for the estimation of the residual energy at the toe of the chute i.e. dam, were analyzed in detail. This allowed a better understanding of the importance of the assumptions and their consequences on the flow characteristics.

Several concepts for the definition of the free surface of the highly aerated flow were compared. Based on flow smooth chutes, an efficient homogeneous flow depth was defined for the first time. Compared to previous works, not only skimming but also nappe and transition flow were studied. Their influence on air concentration, flow velocity and pressure distribution could be shown. For the first time, the variation of dynamic pressures acting on steps and macro-roughness elements (endsills and blocks) were directly measured with sensors for the three flow regimes and arrangements of macro-roughness elements. Spectral analysis of the dynamic pressures allowed detecting the change of the flow regime and the frequency of the macro-turbulence involved. Based on the experimental results, an original semi-empirical approach for the implementation of the Navier-Stokes equation could be proposed, which lead to a promising quasi -2D numerical model.

Dr. Stephanie André determined a head loss law, which considers the energy head, the number of steps, the critical flow depth and the non-dimensional parameter of the macro-roughness elements. Characteristics of an optimum system of macro-roughness elements were proposed which opens the door for further developments. Helpful empirical relationships were given for the determination of air concentration, flow velocity and residual energy for the different types of macro-roughness overlays. Finally, recommendations were given for the design of the macro-roughness elements.

We would like to thank Prof. Dr. Michel Pirotton and Benjamin Dewals from the University of Liège for their contributions in the field of numerical modelling. Furthermore we thank Dr. Henry T. Falvey, Colorado and Prof. Jorge Matos, University of Lisbon for their significant support and guidance. Finally we are grateful the Swiss Federal Office for Water and Geology for their financial support.

Prof. Dr. Anton J. Schleiss

Traduction: Il était une fois au bord de l'eau - Soline, 15/12/2003

...A SOLINE ET PHILIPPE...

Abstract

Uncontrolled overtopping during flood events can endanger embankment dams. Erosion of the downstream slope and scouring of its base caused by the high velocity and energy of the overflow can indeed lead to breach formation until complete failure.

In this context and faced with the important number of overtopped embankment dams to be rehabilitated, since the early eighties, researchers have investigated surface protection solutions for downstream slope. Overlays against erosion such as seeded goetextile or cable-tied cellular concrete blocks, are not sufficient. In fact, they can resist only short events with low discharge and velocity. Solution to overcome more severe overflow lies in overlays which dissipate flow energy along the downstream embankment slope. Conventional steps resulting from Roller Compacted Concrete (RCC) techniques fulfill efficiently this challenge.

However, flows over steep stepped chutes are quite complex, characterizing by great aeration, high turbulence and confused wavy free surface. Then, most of hydraulic studies of such flows are performed on physical model. Yet, understanding and definition of flow behaviour and accurate approach to estimate energy dissipation are still lacking. General guidelines of hydraulics of aerated flows over stepped macro-roughness chutes and for optimal design of protection overlay remain confusing.

To contribute to reduce these uncertainties, experimental study of flow over stepped chutes equipped with macro-roughness elements is performed in a laboratory gated flume for mild ($\simeq 1.7H : 1V$) and weak ($\simeq 3H : 1V$) chutes. Thus, they are representative of the range of embankment dams and spillways slopes.

Three types of stepped macro-roughness overlays are assessed, namely rectangular conventional steps, steps equipped with endsills fixed on their nose over all the flume width and steps equipped with rectangular spaced blocks. Endsills overlays were characterized with different longitudinal distributions whereas blocks overlays consisted in different transverse patterns. Tests were conducted for the three nappe, transition and skimming flow regimes. Results can be extrapolated to 1/5 to 1/15 scaled prototypes using the Froude similarity with negligible scale effects.

Flow depth, local air concentration and longitudinal velocities are measured with a double fiber-optical probe. Pressures at macro-roughness faces are taken with piezo-resistive sensors. Sequent depths of the hydraulic jump forced in the stilling basin at the flume base are measured with ultrasound sensors. Thus, this experimental phase of the thesis has allowed:

- to define flow parameters (regimes, depths, velocity and air concentration distributions, hydrodynamic forces) for tested overlays,
- to highlight that air-water flow depth is divided into:

  - a rough boundary layer influenced by shear stress and by drag form (macro-turbulence) caused by macro-roughness,
  - a homogeneous aerated layer which represents the main portion of flow involved in energy dissipation mechanism,
  - a free surface layer which must be considered in the side walls design,
- to stress that energy dissipation is mainly a question of drag losses,
- to validate indirect method of hydraulic jump for energy dissipation estimation,
- to estimate relative energy loss for several stepped macro-roughness overlays.

Tests finally show that an optimal alternative to dissipate the overflow energy during an overtopping event consists in spaced blocks, with transverse space larger than the width of block and fixed alternately on conventional steps.

However, experimental results remain related and limited to their tested domains. Then, in order to provide more general governing equations of aerated flows over macro-roughness stepped chutes, a numerical modeling of two phase flows over conventional stepped flume was performed in collaboration with the Laboratory of Applied Hydrodynamics and Hydraulic Constructions at University of Liège. A quasi-2D numerical model based on the finite volume method was developed. It consists in applying the classical depth-averaged simplified Navier-Stokes equations (viscosity and Coriolis terms neglected) to a 1D incompressible air-water mixture flow over mild and steep slopes with a stepped topography.

Self-aeration process is modeled by a transport equation of depth-averaged air concentration whereas turbulent structures are indirectly implemented through the Boussinesq coefficient.

This first 1D-approach of semi-theoretical description of aerated flow over steps is tested for a 30^o gated stepped flume and a 52^o crested spillway laboratory model. This numerical model leads to realistic results regarding mixture depth, mean flow velocity, air concentration and wave amplitudes of the flow free surface.

Finally, on the basis of existing protections of embankment dams and previous studies, the present experimental and numerical results contribute to extend the knowledge of high velocity aerated flows over macro-roughness and to provide elements of guidelines to optimize stepped macro-roughness overlays for embankment dams safety.

Résumé

Pendant une crue, le déversement incontrôlé sur un barrage en remblai peut mettre en danger sa stabilité. En effet, l'érosion du parement aval et l'affouillement de sa base causés par les hautes vitesses et l'énergie propre de l'écoulement peuvent ouvrir des brèches jusqu'à la rupture de l'ouvrage.

Dans ce contexte et face au nombre important de barrages en remblai nécessitant une réhabilitation, des recherches sont menées depuis le début des années quatre-vingt, sur des solutions de protection du coursier aval. Des couches protectrices superficielles, telles que du geotextile ensemencé ou des treillis de cellules de béton ne sont pas adéquates car elles ne résistent qu'à des petits déversements à faibles débit et vitesse. Par contre, un revêtement en marches d'escalier construit en béton compacté au rouleau (BCR) répond efficacement à ce défi de protection.

Les écoulements sur marches d'escalier sont très complexes car ils sont fortement aérés et turbulents avec de surcroît une surface libre ondulée mal définie. Par conséquent, la plupart des études concernant ces écoulements particuliers sont menées sur modèles physiques. Toutefois, la compréhension et la définition de l'écoulement ainsi que l'estimation correcte de l'énergie dissipée manquent toujours de clarté. L'hydraulique des écoulements aérés sur macro-rugosités et les outils de dimensionnement de systèmes de protection optimals restent confus.

Pour contribuer à réduire ces incertitudes, une étude expérimentale des écoulements sur pente en escalier équipée d'éléments de macro-rugosité est menée dans un canal à pente moyenne ($\simeq 1.7H : 1V$) et à pente faible ($\simeq 3H : 1V$). Celles ci représentent la gamme habituelle des pentes des ouvrages en remblai.

Trois types de revêtement en marches d'escalier sont testés, des marches rectangulaires conventionnelles, des marches équipées de seuils à leur nez sur toute la largeur du canal et des marches recouvertes à leur nez de blocs espacés rectangulaires. Les variantes avec seuils sont caractérisées par différentes répartitions longitudinales alors que les systèmes de blocs présentent différentes distributions transversales.
Les essais sont menés pour les trois régimes en nappe, en transition et en mousse de l'écoulement. Les résultats sur modèle peuvent être extrapolés selon la similitude de Froude à des prototypes d'échelle 1/5 à 1/15 sans effet d'échelle significatif.

La hauteur d'eau, la concentration en air et la vitesse longitudinale sont mesurées avec une double sonde optique. Les pressions sur les faces des macro-rugosités sont prises à l'aide de mini capteurs piezo-résistifs. Les hauteurs conjuguées du ressaut hydraulique formé dans le bassin de dissipation au pied du canal sont mesurées avec des limnimètres à ultrason. Cette phase expérimentale de la thèse a contribué à:

- définir les paramètres hydrauliques de l'écoulement (régime, hauteur d'eau, distribution de vitesse et de concentration en air, forces hydrodynamiques) sur les systèmes testés,
- montrer que le mélange eau-air se décompose en:
  - une couche limite rugueuse influencée par le cisaillement mais surtout par les effets de forme (macro-turbulences) causés par les macro-rugosités,
  - une couche aérée homogène qui constitue la part principale de l'écoulement impliquée dans le mécanisme de dissipation d'énergie,
  - une couche de surface qui doit être prise en compte pour le dimensionnement des murs bajoyers,
- confirmer que l'énergie dissipée est surtout associée aux pertes de charge singulières,
- valider la méthode indirecte du ressaut hydraulique pour estimer l'énergie dissipée par les différents systèmes de macro-rugosités testés.

Les essais ont finalement montré que la variante optimale pour dissiper l'énergie de l'écoulement sur le parement aval consiste en un système de blocs espacés avec un écartement transversal plus grand que la largeur du bloc lui-même et fixés en ordre alterné sur le nez des marches.

L'ensemble des résultats expérimentaux reste par définition lié et limité aux conditions testées. C'est pourquoi, dans le but de généraliser les équations qui gouvernent les écoulements aérés sur des chutes en escalier équipées de macro-rugosités, une modélisation numérique des écoulements sur marches conventionnelles a été menée en collaboration avec le Laboratoire d'Hydrodynamique Appliquée et de Constructions Hydrauliques de l'Université de Liège. Un modèle numérique quasi-2D a été développé, basé sur la méthode des volumes finis. Ce modèle applique les équations simplifiées (termes de viscosité et de Coriolis négligés) de Navier-Stokes intégrées sur la hauteur à l'écoulement du mélange eau-air considéré incompressible et monodirectionnel.

Le processus d'auto-aération est modélisé par une équation de transport de la concentration en air moyenne alors que les structures turbulentes sont indirectement prises en compte par le coefficient de Boussinesq.

Cette première approche de la description semi-théorique des écoulements aérés sur marches d'escalier est testée pour un canal à 30^o avec une entrée contrôlée par vanne et pour le modèle réduit d'un évacuateur de crue à crête en ogive et de pente de 52^o. Le modèle numérique conduit à des résultats comparatifs réalistes tant du point de vue des hauteurs d'eau que des vitesses et concentrations en air moyennes ainsi que des amplitudes d'oscillation de la surface libre.

Finalement, sur la base des solutions récentes appliquées aux barrages en remblai réhabilités et des enseignements d'études antérieures, les présents résultats empiriques et numériques contribuent à étendre la connaissance des écoulements aérés sur macro-rugosités et fournissent des éléments pour optimiser un revêtement de surface en marches d'escalier avec macro-rugosités destiné à la sécurité des barrages en remblai.

Contents

List of Figures

List of Tables

List of symbols

Roman symbols

$\overline{C}$	Computed depth-averaged air concentration [-]
$\overline{H_{r,i}}$	Depth-averaged residual energy $[m]$
A	Cross section area $[m^2]$
B_f	Flume width [m]
b_r	Macro-roughness width $[m]$
B_{ba}	Stilling bassin width $[m]$
C	Depth-averaged or mean air concentration [-]
c	Local air concentration at the normal depth z [-]
C'	Mean true air concentration in homogeneous aerated flow [-]
c'	Local true air concentration according the intermittency approach [-]
c_b	Air concentration at the pseudo-bottom [-]
C_D	Discharge coefficient [-]
C_d	Drag coefficient [-]
C_e	Correction coefficient for broad-crested weir [-]
C_h	Air concentration at $Z = Z_h$ [-]
C_i	Depth average air concentration at the point of inception [-]
C_u	Air saturation concentration in the uniform region [-]
$c_{b,i}$	Air concentration at the pseudo-bottom at the point of inception [-]
$C_{u,s}$	Asymptotic value of the mean air concentration at saturation [-]
D'	Dimensionless coefficient for the advective diffusion model [-]
D_h	Hydraulic diameter $[m]$
d_p	Distance between the two tips of the optical probe [m]
d_r	Density of covering of the macro-roughness overlay $[-]$
D_t	Turbulent diffusivity $[m^2/s]$
E	Eötvös number [-]
E_f	Friction head loss [m]

e_r	Transversal space between two macro-roughness elements $[m]$
E_{ti}	Total mechanical energy at a point z_i on the normal axis $[J]$
E_{wall}	Wall pressure head (corrected hydrostatic pressure distribution) [m]
f	Darcy-Weisbach friction factor [-]
$F(c_j)$	Air concentration cumulative distribution [-]
$f(c_j)$	Air concentration density function [-]
F_0	Approach Froude number, $F_0 = q_w/\sqrt{g\cos\theta h_0^3}$ [-]
F_a	Frequency of acquisition of the pressure signal $[Hz]$
F_D	Drag force [N]
F_f	Filter frequency of the pressure signal $[Hz]$
F_i	Inception Froude number, $F_i = q_w/\sqrt{g(h_s/l_s)k_s^2}$ [-]
F_L	Lift force [N]
F_r*	Roughness Froude number [-]
F_s	Step Froude number, $F_s = q_w/\sqrt{g\sin\theta h_s^3}$ [-]
f_u	Darcy-Weisbach friction coefficient in the uniform region [-]
f'_u	Friction factor for effective homogeneous mixture flow in uniform region [-]
F_w	Clear water Froude number, $F_w = \frac{q_w}{\sqrt{(g\cos\theta Z_w^3)/\alpha}}$ [-]
$F_{*,\theta*}$	Equivalent Froude number for $m = 1/2$, $F_{*,\theta*} = q_w/\sqrt{g\cos\theta * k_T^3}$ [-]
$F_{*,\theta}$	Roughness Froude number including the slope effect, $F_{*,\theta} = q_w/\sqrt{g\cos\theta k_s^3}$ [-]
F_Θ	Froude number for steep slope [-]
$f_{c\ w,u}$	Colebrook-White friction factor in uniform region for equivalent clear water flow [-]
$f_{m,u}$	Darcy-Weisbach friction factor in uniform region for mixture flow [-]
$f_{w,u}$	Darcy-Weisbach friction factor in uniform region for equivalent clear water flow [-]
g	Gravity acceleration $[m/s^2]$
H'_r	Residual energy at the toe of the chute for the aerated homogeneous flow [m]
H_0	Head at the flume entrance or above the crest dam $[m]$
h_0	Opening of the jetbox [m]
h_c	Critical depth $[m]$
H_D	Total drop height of the structure $[m]$
h_d	Side wall height [m]
H_f	Flume Height [m]
h_m	Computed mean mixture depth $[m]$
h_n	Normal flow depth [m]

H_r	Residual energy at the base of the flume [m]
h_r	Macro-roughness height [m]
h_r*	Effective additional depth caused by the macro-roughness element [m]
h_s	Height of the step [m]
h_T	Total roughness height, $h_T = h_s + h_r$ [m]
H_u	Tailwater head at the dam crest [m]
h_v	Vertical length of the recirculating cells on the vertical step face [m]
H_{90}	Dimensionless mixture flow depth, $H_{90} = z/Z_{90}$ [-]
H_{ba}	Stilling bassin height [m]
$H_{r,m}$	Residual energy at the toe of the chute for aerated mixture flow [m]
$H_{r,NF}$	Residual energy at the toe of the chute for isolated nappe flow [m]
$H_{r,SF}$	Residual energy at the toe of the chute for skimming flow [m]
$H_{r,w}$	Equivalent clear water residual energy at the toe of the chute for skimming flow [m]
H_{r1}	Residual energy at the toe of the chute estimated by the hydraulic jump method [m]
H_{sr}	Residual energy for a smooth slope, in the developing region [m]
H_{su}	Residual energy for a smooth slope, in the uniform region [m]
$H_{Y,u}$	Specific energy at a level Y above the base of the chute for skimming flow [m]
k	Sand grain roughness [mm]
K'	Integration constant for the advective diffusion model [-]
K_3	Integration constant for the advective diffusion model [-]
k_r	Normal height of the macro-roughness element [m]
k_s	Normal height of the step [m]
k_T	Total normal macro-roughness height, $k_T = k_s + k_r$ [m]
L	Hydrostatic uplift [N]
l	Horizontal axis [m]
L_c	Equivalent distance from the ogee crest of a spillway to the jetbox of a gated flume of same roughness and slope characteristics [m]
L_e	Length of the crest of a broad-crested weir [m]
L_f	Flume length [m]
L_i	Longitudinal distance between the critical depth position on the crest of the dam and the horizontal face where the inception point is located [m]
l_r	Macro-roughness length [m]
l_s	Length of the step [m]
L_u	Longitudinal position from the dam crest of the beginning of the quasi-uniform region [m]

L_v	Horizontal length of the recirculating cells on the horizontal step face [m]
L_{ba}	Stilling bassin length $[m]$
L_{dr}	Length of influence of drag form such as internal transverse jet or jet caused by contraction [m]
L_{fr}	Length of place of friction caused by recirculating cells [m]
m	Dimensionless parameter to define the proportion of macro-roughness elements on steps, m=numb. of macro-roughness elements/numb. of steps [-]
N	Exponent of the velocity power law [-]
n	Manning coefficient $[s/m^{1/3}]$
$N*$	Number of conventional steps following a step equipped with endsill or block [-]
N_s	Number of steps along the chute $[-]$
p	Computed pressure field $[Pa]$
$p(z)$	Pressure at elevation z $[Pa]$
p_m	Measured local pressure $[PaA]$
q'_w	Computed water unit discharge for the homogeneous flow $[m^2/s]$
Q_w	Water discharge of the incoming flow $[m^3/s]$
q_w	Unit water discharge $[m^2/s]$
r	Cross correlation coefficient associated to the velocity estimation [-]
R_e	Reynolds number [-]
R_h	Hydraulic radius [m]
R_w	Clear water Reynolds number, $R_w = \frac{q_w}{\nu}$ [-]
S	Submergence factor [-]
s'	Dimensionless distance from the inception point, $s' = \frac{x - L_i}{Z_{w,i}}$ [-]
S_a	Term of the source of air of the air transport equation [-]
S_f	Friction slope [-]
T	Duration of a measuring sequence $[s]$
T_c	Time for a maximum cross correlation coefficient for velocity estimation [s]
T_{int}	Intermittency parameter [-]
U'	Mean homogeneous aerated flow velocity $[m/s]$
u_b	Longitudinal velocity component at the bottom $[m/s]$
U_m	Depth-average measured mixture flow velocity $[m/s]$
$u_m(z)$	Longitudinal component of the mixture flow velocity $[m/s]$
u_r	Air bubble rise velocity in the aerated flow over macro-roughness$[m/s]$
U_w	Equivalent clear water mean velocity $[m/s]$
u_w	Local longitudinal clear-water flow velocity $[m/s]$
$U_{1,2}$	Mean longitudinal velocity of the flow at the sides of the hydraulic jump $[m/s]$

U_{90}	Dimensionless mixture flow velocity, $U_{90} = u_m(z)/u_{90}$ [-]
u_{90}	Longitudinal flow velocity at 90 % of air concentration $[m/s]$
$u_{r,hyd}$	Air bubble rise velocity in hydrostatic pressure gradient flow $[m/s]$
V_e	Vedernikov dimensionless number [-]
w	Correction form coefficient for hydraulic diameter [-]
w_e	Height of a broad-crested weir [m]
w_m	Normal component to the main flow of the mixture velocity $[m/s]$
We	Weber number [-]
X_i	Dimensionless distance from the inception point, $X_i = (x - L_i)/Z_{m,i}$ [-]
x_r	Longitudinal space between two macro-roughness elements $[m]$
x_s	Longitudinal distance between two step corners $[m]$
x_v	Length of the friction interface recirculating cells/skimming layer [m]
Y_1	Upstream sequent depth of the hydraulic jump in the vertical direction [m]
Y_2	Downstream sequent depth of the hydraulic jump in the vertical direction [m]
z	Normal axis, perpendicular to the pseudo-bottom i.e to the mean slope of the chute
Z'	Effective homogeneous mixture flow depth [m]
$z*$	Modified normal axis, $z* = z + k_s$ $[m]$
z_b	Local bed elevation $[m]$
Z_h	Observed homogeneous aerated flow depth [m]
Z_j	Impact zone of the internal jet in the skimming layer [m]
Z_m	Mixture normal flow depth [m]
Z_v	Mixture flow depth estimated from the velocity profile [m]
Z_w	Equivalent clear water flow depth [m]
$Z_{90,u,m}$	Uniform mixture flow depth for any overlays m $[m]$
$Z_{m,i}$	Mixture depth at the point of inception [m]
$Z_{m,u}$	Mixture flow depth in the uniform region $[m]$
Z_{obs}	Mixture air-water depth deduced from visual observation $[m]$
z_{ref}	Vertical distance to the toe of the dam from a referenced datum [m]
$Z_{w,i}$	Equivalent clear water depth at the point of inception [m]
$Z_{w,u}$	Equivalent clear water flow depth in the uniform region $[m]$
g	Acceleration of gravity $[m/s^2]$]
$m = 1$	Every step equipped with an endsill
$m = 1/2$	Every second step equipped with an endsill
$m = 1/3$	Every third step equipped with an endsill
$m = 4$	Spaced alternated blocks

$m = 5$	Aligned alternated blocks
$m = 6$	Close-packed alternated blocks
$\overline{u_m}$	Computed mean mixture longitudinal velocity $[m/s]$

Greek Symbols

α	Kinetic energy correction factor [-]
α_m	Coriolis aerated correction coefficient [-]
β	Integration constant for the ADM for smooth slope [-]
β_r	Projected length on the pseudo-bottom of the macro-roughness element $[m]$
δ	Ratio of the density of the flow upstream and downstream of the hydraulic jump [-]
$\Delta H/H_0$	Relative energy loss [%]
$\Delta H_u/H_0$	Relative energy loss in the uniform region [%]
Δ_e	Upstream slope of a broad-crested weir $[^o]$
ϵ	Interfacial surface tension [N/m]
η_H	Correction factor for residual energy computed with hydraulic jump method [-]
η_m	Correction factor to take into account the influence of the endsill in the onset of flow regimes [-]
$\forall_r$	Volume of the macro-roughness elements $[m^3]$
$\forall_s$	Volume of the rectangular steps $[m^3]$
γ	Integration constant for the ADM for smooth slope [-]
κ	Von Kármán turbulent constante [-]
λ	Integration constant for the advective diffusion model [-]
λ_L	Length scale factor in Froude similitude [-]
ν	Kinetic viscosity $[m^2/s]$
ϕ_c	Chord length of the air bubble [m]
Π_m	Dimensionless head loss parameter [-]
ψ	Spacing roughness dimensionless parameter [-]
ρ_a	Density of the air $[kg/m^3]$
ρ_m	Density of the mixture air-water flow $[kg/m^3]$
ρ_w	Density of the water $[kg/m^3]$
$\rho_{1,2}$	Mean flow density at the sides of the hydraulic jump $[kg/m^3]$
ρ_{edge}	Correction coefficient of uneven vertical velocity profile at the step edge [-]
$\rho_{xx,m}$	Boussinesq aerated correction coefficient [-]
ρ_{xx}	Correction coefficient of uneven vertical velocity profile [-]
σ	Interfacial surface tension $[N/m]$

τ_0	Shear stress at the boundary $[N/m^2]$
τ_{bx}	Losses term projected along the x axis in the momentum equation $[N/kg.m]$
θ	Angle of the slope of the chute $[^o]$
$\theta*$	Equivalent slope inclination for $m = 1/2$ $[^o]$
ε	Proportion of energy lost per step [-]
ξ_u	Global dissipation coefficient [-]

Index

1	Characteristic of the upstream cross section of the hydraulic jump
2	Characteristic of the downstream cross section of the hydraulic jump
i	Characteristic of the inception point I
m	Mixture air-water flow characteristics
u	Characteristic of the fully developed region (uniform region)
w	Pure water characteristics

Abbreviations

RCC	Roller Compacted Concrete
VOF	Volume of Fluid
ADM	Advective Diffusion Model for air bubbles
ADV	Acoustic Doppler velocity meter instrumentation
CIRIA	Construction Industry Research and Information Association
EPFL	Swiss Federal Institute of Technology in Lausanne, Switzerland
HACH	Laboratory of Applied Hydrodynamic and Hydraulic Constructions, ULg, Belgium
I	Inception point
ICOLD	International Commission on Large Dams
LCH	Laboratory of Hydraulic Constructions
LMH	Laboratory of Hydraulic Machines at EPFL
OFEG	Federal Office for Water and geology (FOWG)
PIV	Particule Image Velocimetry instrumentation
ULg	University of Liège, Belgium
USACE	United States Army Corps of Engineers
USBR	U.S Bureau of Reclamation, Denver, CO, USA

Part I

Introduction

Chapter 1

Overtopping of dams: is it a real nowadays problem?

Energy control of aerated high velocity flows is one of the main challenges in the design of hydraulic structures. In fact, this type of flows is often observed in torrents, in drainage systems of urban areas, in industrial effluent evacuations and on spillways and overtopped dams.

For the later case, about 40 % of the recorded world failures without counting China [Lempérière (1993)] of embankment dams lower than 30 m are caused by uncontrolled overtopping during flood events. High energy of the overflow is indeed able to create dramatic damage as erosion of the downstream slope and scouring at the base of the chute which might lead to complete failure.

Nowadays, a great number of embankment dams have an under-designed spillway capacity since they were built at a period when hydrologic data, computation and measurements techniques were limited. They all could experience overtopping during severe flood events.

Then, as a reaction to these possible risks of dam failure, engineers become more and more interested in controlling overtopping with safe-time and economic solutions. As a consequence, important research activities have been conducted since the early eighties to develop downstream slope surface protection systems so-called overlays in the following.

Chapter 2

Why macro-roughness overlays can protect embankment dams during overtopping?

An efficient protection overlay consists in fitting the embankment slope with steps. This alternative is more and more developed since the eighties with the arrival of Roller Compacted Concrete (RCC) techniques. Steps behave like macro-roughness during overtopping: their height remains large compared to the overflow depth.

The main property of stepped overlay lies in its capacity to dissipate the flow along the slope which results:

- First, in the slowing down of bottom velocity and consequently in diminishing the risk of slope erosion.
- Secondly in a drastic decrease of the residual energy at the base of the chute. That leads to a reduction of scouring damage and also to a diminution of the dimension of the stilling basin.

Advantages of steps are not limited to their energy dissipation efficiency. In fact, they contribute also:

- to minimize the risk of cavitation thanks to the high aeration of the flow,
- to increase the spillway capacity of existing embankment dams because the steps tend also to stabilize the downstream slope [Matos, Pinheiro, Quintela & Frizell (2001)],
- to dissolve gas abatement since self-aeration process due to steps permits to regularly aerate the downstream river and then to "degase" partially the water [Ahmann & Zapel (2000)],
- to improve the quality of the wasted water or industrial effluents by re-aeration [Toombes & Chanson (2000)],
- to the safety of canoeists and rafters by reducing the dangerous reverse-flow region of a plunging flow in a inclined chute in a river [Yasuda & Ohtsu (2000)].

Chapter 3

Scope and organization of the study

Because of the high turbulence and the two-phase structure of the flow over stepped chutes, an accurate approach to estimate energy dissipation is still lacking. A better assessment strongly depends on a more precise description of the flow behaviour, especially the air-water structures. In fact, during the last international workshop on hydraulics of stepped spillways [at the Swiss Federal Institute of Technology in Zurich, Switzerland, (2000)], guidelines to design a stepped protection, such as friction coefficient, were scattered and confused. Furthermore, few studies are focused on optimization of macro-roughness overlays regarding energy dissipation and resistance.

In this context, the aims of this research project are:

- to extend the knowledge of two-phase structure of the flow over macro-roughness stepped chutes,
- to understand the contribution of the drag form effect caused by the macro-roughness in energy dissipation mechanism and to assess the relevant head losses,
- to propose an accurate method for estimation of residual energy,
- to investigate different stepped overlays to estimate the influence of geometry, size and distribution of the macro-roughness elements on energy dissipation,
- to furnish the bases for the recommendations and guidelines to design an optimal stepped macro-roughness overlay regarding flow depth, pressure field, air concentration, velocity and head loss.

Finally, this research project contributes to the reduction of the confusion regarding energy dissipation efficiency, to provide elements for an empirical guideline, to optimize surface protections for embankment dams and to introduce a numerical model of aerated flows over stepped chutes.

To attain these objectives, the project is developed in three steps, a literature review, an experimental and a numerical phases as illustrated with more details in Figure 3.1.

Figure 3.1: Organization of the research project

Part II

Existing lining protection techniques for overtopped dams: a summary

Chapter 4

Overtopped dams: a current problem

In addition to supply the volume and water head for hydroelectric energy production, dams have also often been constructed to store drinking, industrial and irrigation water and more and more used for the protection against floods. Embankment dams lower than $30\,m$ high are the most construction used structures due the low cost of construction, the facility of environmental integration and the techniques compared with concrete dams. This may explain the proliferation of embankment dams around the world, especially in developing countries. According to the last ICOLD statistics in 1995 [ICOLD (1997)], over the $145'000$ "large"[1] and "small"[2] dams in operation in the world, 93 % are lower than 30 m high, including around 90 % of earthfill dams.
The following literature review will thus focus on these embankment structures.

The very first embankment dams are already 2000 years old, but most existing dams were built in the fifties of the 20^{th} century. During this period, hydrology sciences were just starting and measurement techniques were limited. As a consequence, a great number of embankment dams have an under-designed spillway capacity and could experience overtopping as illustrated in Figure 4.1a for the spillway of Treig dam in Scotland.

Cofferdams during a construction period are also subject to overtopping since they are generally in operation for a short duration and thus designed for low flood events (see example of Cabora-Bassa cofferdam, Fig. 4.1b).

Uncontrolled overtopping during floods can be a real danger for the embankment safety. In fact, the high energy and velocity of the overflow are able to create dramatic damages such as erosion on the downstream slope and at the toe as well as breach formation which could lead to complete failure of the dam itself. This extreme situation concerns overall the earthfill or rockfill embankment dams which are built with natural material, not always well compacted and thus very vulnerable to erosion.
Uncontrolled overtopping is indeed a real problem since it is the cause of 40 % of the recorded world failures (without China) [Lempérière (1993)].

Until the beginning of the eighties, uncontrolled overtopping was absolutely rejected in safety dam programs. To prevent eventual damage, alternatives in masonry rehabilitation included either increasing the reservoir storage or enlarging the spillway capacity [ASCE (1994)]. It could consist in:

- raising the dam crest,
- increasing the crest length (by a Labyrinth weir, for instance),
- improving the discharge coefficient (by a refinement of the crest shape, for instance),
- adding spillways or outlets,
- using fuseplug embankments or submersible fusegates.

[1] "Large" dams, as defined by the ICOLD, are dams more than 15 m high, and dams between 10 m and 15 m high with a storage capacity larger than 1 hm^3, or more than 500 m long, or with a design discharge flood of more than 2 000 m^3/s

[2] "Small" dams are lower than 15 m with storage capacities less than 1 hm^3

These solutions are not always feasible, not only because of the cost and the techniques involved but also due to their requirements in space, in the topography, soil quality and their environmental impacts.

As a reaction to these overtopping events and to the burden of such techniques, engineers became more and more interested in controlling overtopping. This may be indeed a real time saving and an economic interest to rehabilitate the numerous likely overtopping dams. Important research activities have been then conducted since the early eighties, particularly in Russia, in the USA through a number of Federal agencies and private consulting firms (as an example, the USACE: United States Army Corps of Engineers) and the UK (as an example, the CIRIA: Construction Industry Research and Information Association). They intend to develop systems to ensure safe embankment dams during overtopping, in particular linings for the downstream slope protection. Notably, in parallel to this increasing interest in controlled overtopping and due to the encouraging results of the researches, legislation of dam safety has also evolved. Controlled overtopping is accepted for small dams for some countries such as the USA [Hagen (1982)], UK [Minor (1998)] and recently Switzerland [OFEG (2002)]. The conditions required to accept overtopping is that the crest, the downstream slope and the toe are equipped with protection systems.
However, due to the complexity of the turbulent aerated overflow behaviour, establishment of general design relationships for optimal protection systems are still lacking. As a consequence, controlled overtopping has not yet been widely adopted.

Though the crest and toe protections are important measures for dam safety, the following state-of-the art focuses mainly on the surface protection systems used to cover the downstream slope of embankment dams. As shown in the following, lining protections are required during overtopping because not only they avoid erosion of the downstream slope, but also they can contribute to diminish the residual energy at the toe of the chute.

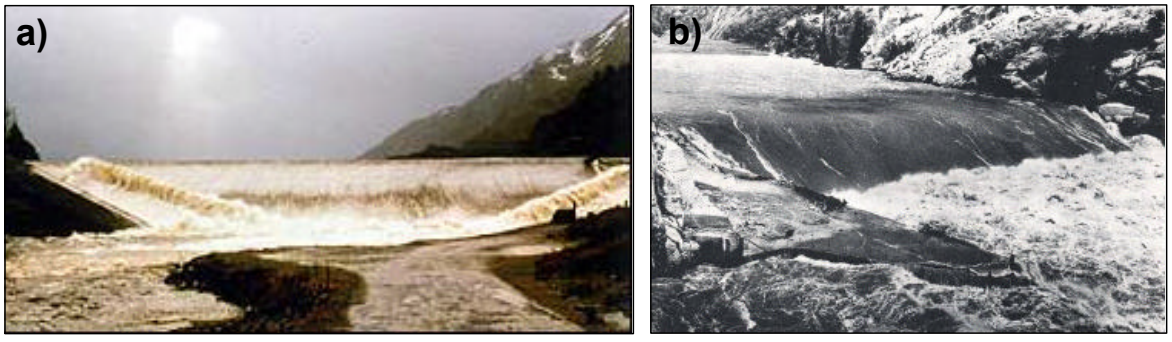

Figure 4.1: Overtopping of a) the spillway of the Treig dam near Fort William in Scotland [British dams organisation (2004)] ; b) upstream cofferdam of Cabora-Bassa, Africa, in 1972 [ICOLD (1984)]

Chapter 5

Erosion and failure processes during overtopping events

In order to develop reliable, efficient and adapted protection solutions, it is essential to understand the hydraulic behaviour of the overflow, its energy dissipation capacity and the consequences on the erosion and the failure processes of the structure during overtopping. Therefore overflow behaviour is briefly described in the following.

If hydraulic overflow is comparable to the hydraulic of flow over smooth steep chutes (as described in Appendix B), the behaviour of the overtopped embankment dam remains complex, involving interaction between a turbulent aerated flow and the erosion processes of granular or cohesive soils with a significant slope effect. As a consequence, the existing descriptions of embankment dam response during overtopping derive in general from history cases or from physical model studies performed in laboratories. They are then limited to their tested domain.

5.1 Hydraulics of the overflow

When the water level in the reservoir overtops the dam crest with a very shallow water depth, flow is lost in seepages due to the permeability of the downstream slope in case of earthfill or rockfill structures due to settlement cracks and joints. As the water level increases, flow starts to run over the downstream slope. As illustrated in Figure 5.1, the overflow can then be described in 3 zones [Gray (1991), Powledge, Ralston, Miller, Chen, Clopper & Temple (1989)], each of them characterized by the flow structure and regime and the energy gradeline (represented with the dotted line).

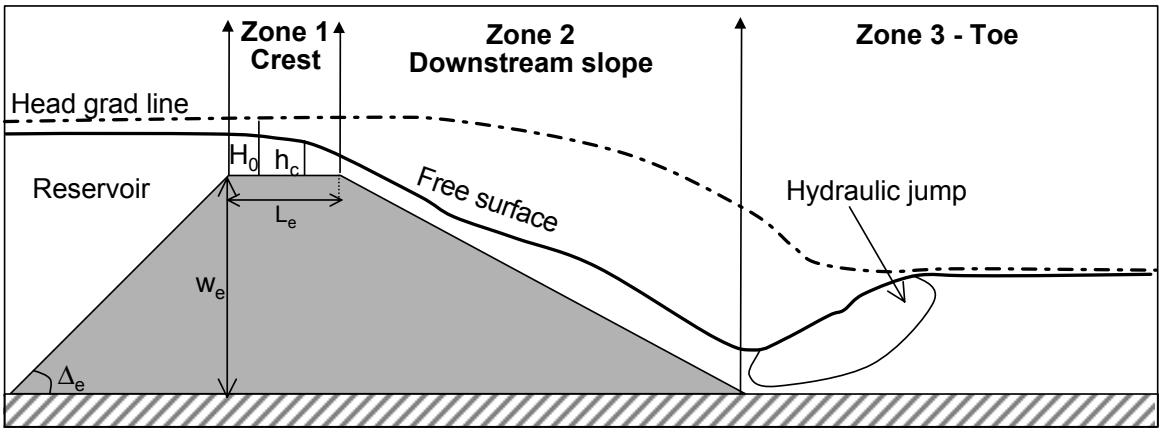

Figure 5.1: Sketch of flow zones over steep embankment slopes

5.1.1 Zone 1: Crest

The flow transits from a subcritical regime in the reservoir, with a very low approach velocity to a supercritical regime downstream from the crest through the critical depth, h_c, given by Eq. 5.1. Critical depth is located within the downstream third or fourth of the crest, depending on its shape and roughness as well as the overflow head.

$$h_c = \sqrt[3]{\frac{q_w^2}{g}} \tag{5.1}$$

where q_w is the unit discharge of the overflow and g the gravity acceleration.

The boundary layer is laminar upstream of the critical depth (low flow velocity) and the energy gradeline varies proportionally to the flow velocity. By consequence, the energy slope is insignificant and the tractive forces are negligible: only very highly erodible material can be moved.

The laminar flow condition transits to the turbulent flow regime downstream of the critical depth, with an increase of the flow velocity. Therefore, over a short distance, the energy head (proportional to the square of the velocity) and tractive forces increase significantly. Erosion has then to be expected at the downstream edge of the crest. In addition, if the angle between the crest and the downstream slope is sharp, the pressures decrease from hydrostatic pressure as the flow begins curving toward the slope, creating a separation of the nappe, with the formation of negative local pressures. This pressure gradient can be the origin of an erosion at the crest brink which can progress down the slope and lead to failures of the dam.

The depth and the head of the flow over the crest are respectively h_0 and H_0. They may be estimated with the broad-crested weir equations (Eq. 5.2, 5.3):
For no or low tailwater:

$$q_w = C_D C_e \sqrt{2g} H_0^{3/2} \tag{5.2}$$

For submerged crest:

$$q_w = C_D C_e \sqrt{2g} S H_0^{3/2} \tag{5.3}$$

with C_D, the discharge coefficient given by [Rehbock (1929)]:

$$C_D = 0.4023 \left[1 + \frac{0.135 h_0}{w_e}\right] \left[1 + \frac{0.0011}{h_0}\right]^{3/2}$$

C_e, a correction coefficient given by $C_e = 1 - \frac{2 sin\Delta_e}{9[1 + (\frac{H_0 - w_e}{L_e})^4]}$, and with $S = \sqrt{1 - (\frac{H_u}{H_0})^2}$, the submergence factor and H_u, the downstream or tailwater head (m). w_e, L_e and Δ_e are respectively the height of the weir, the length of crest and the angle of the upstream slope of the weir (Fig. 5.1).

5.1.2 Zone 2: Downstream slope

The flow down the steep slope accelerates rapidly until head loss equilibrium is reached and uniform flow is established. As represented in Figure 5.2, the flow down the chute can be divided into a number of distinct regions [Falvey (1980), Wood (1991)].

Non aerated flow :

Near the dam crest where there is no air entrainment, the turbulent boundary layer grows but has no significant effect on the water surface which remains smooth. In this *clear water region*, depth decreases according to drawdown curve. The flow velocity and energy level increase drastically, with a high erosion potential.

Aerated region :

When the turbulent boundary layer reaches the water surface, the turbulent energy

of the vortices is large enough to exceed the surface tension and gravitational forces: natural air entrainment starts to be developed at the so called inception point (I in the Figure 5.2). The free surface becomes wavy and white with ejection of spray. In this *developing aerated region*, mixture flow depth and mean air concentration increase down the slope. If the slope is long enough, an equilibrium between head loss and gravity is established. In this *uniform region*, air concentration (concentration at saturation), velocity and flow depth (normal depth h_n) are constant with distance. Pravdivets & Slissky (1981) proposed that the uniform regime would be attained at a distance at least 20 times the critical depth from the crest. However, this distance depends also on the slope and on the bottom roughness.

The presence of air has two principal positive effects for the embankment slope: the reduction of the cavitation risks since the mixture is more compressible as well as the decreasing of the shear stress [Wood (1991)]. However, for large overflows, the velocity and flow energy are so great that tractive forces are high enough to produce erosion and head cuts on the slope.
The flow characteristics over the downstream slope can be computed based on the standard step method [Chow (1959)], including air entrainment and friction relationship, such as proposed by Falvey (1980) (see Appendix B).

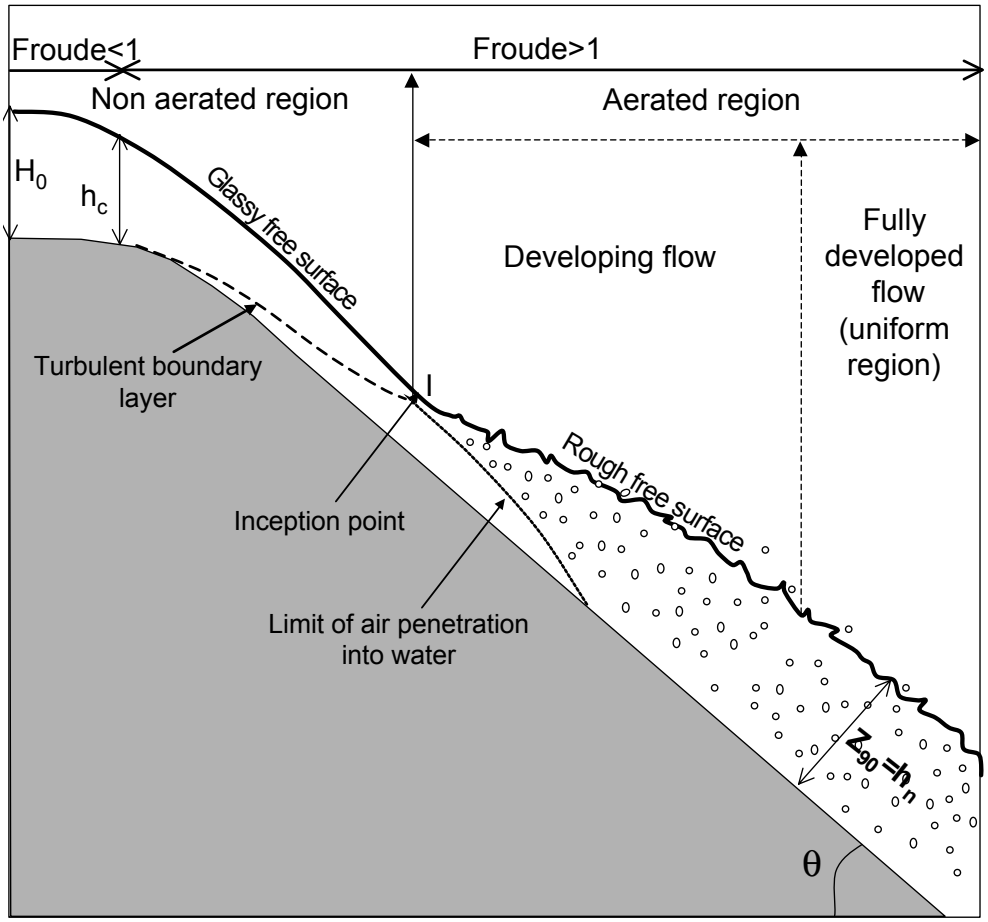

Figure 5.2: Regions of the aerated flow over steep slope

5.1.3 Zone 3: Toe of the chute

The residual energy at the toe of the chute is generally under-estimated because the friction is not properly computed. To take into account air effects, Wood (1991) proposed the following approximation of the residual energy.

♢ *In the developing region*

Based on the Aviemore dam measurements [Cain (1978)], the residual energy H_{sr} is estimated by Eq. 5.4.

$$H_{sr} = Z_w \cos\theta + \frac{1.09}{2g}\left(\frac{q_w}{Z_w}\right)^2 + z_{ref} \tag{5.4}$$

where Z_w is the equivalent clear water depth defined as $Z_w = (1-\overline{C})Z_{90}$ and Z_{90} the mixture flow depth at 90 % of air concentration, $\overline{C}$, the mean air concentration and where z_{ref} is the vertical distance to the structure toe from some datum.

♢ *In the uniform region*

The residual energy H_{su} can be expressed by Eq. 5.5:

$$H_{su} = Z_w \cos\theta + \frac{U_w^2}{2g} + z_{ref} \tag{5.5}$$

where U_w, the clear water flow velocity, is computed from the Darcy-Weisbach friction relation according to Eq. B.1, in Appendix B.

When the high velocity flow reaches the base of the dam, a hydraulic jump is developed (see Fig. 5.1). For low tailwater depth, the non-submerged hydraulic jump involves great local shear stresses as well as high pressure fluctuations. Therefore, if the base of the overtopped dam consists of erodible soil, scouring may occur. If it is lined with concrete slabs, significant uplift pressures may develop. That can cause failure. With increasing tailwater depth, the stresses are progressively reduced but in same time, the hydraulic jump dangerously moves up to the downstream slope of the dam. In this case, the pressure fluctuations and the high stresses applied on the slope itself can cause severe erosion.

5.2 Erosion and failure processes

Compared with concrete dams, embankment ones are more vulnerable and they are subject to:

- deformation due to settlement during and after construction,
- erosion, since they are fitted with natural materials with a low degree of resistance to shearing stress,
- infiltration due to their high permeability and to the presence of cracks resulting from settlement.

Therefore, the main failure mechanisms for earthfill and rockfill dams are the result of internal erosion of the filling material either in the embankment itself or along the foundation interface or also at the contact surface with an adjacent concrete structure. This process is responsible of about 30 % of the failures [Serafim (1981)]. External erosion of the downstream slope during overtopping, uplift pressures at the downstream crest edge and at the toe as well as in the foundation of the structure may also lead to failure.

5.2.1 Erosion mechanism

In general, experience of failure cases has shown that during overtopping the erosion mechanisms can be influenced by structural or hydraulic parameters such as [Powledge & Sveum (1988)]:

- Geometry of the dams (angle of the downstream slope and shape of the crest). A flatter slope would experience a lower erosion potential, and a smooth shape crest would involve lower uplift pressures.
- Quality of the filling materials for embankment dams (density, compaction and permeability). The more the earthfill is compacted and cohesive, the less erosion can be

developed. In addition, risks of infiltration would be limited for poorer permeable material.
In the particular case of concrete dams, it is the cement content which determines the resistance to abrasion when the degree of compaction influences the resistance to shear stress.

- Discontinuity over the downstream slope. Construction joints and bolt holes may cause local cavitation when the overflow velocity is very high (above 30 m/s, [Minor (2000)]) with local damage of the slope surface.

- Location of the hydraulic jump formed at the toe of the chute. It can induce uplift pressures and high shear stress.

- Drainage and sealing systems. They are essential to avoid percolation under-pressures and seepage uplift pressures, both for embankment and concrete dams. They also permit to avoid piping effect for earthfill dams.

- Duration of the overtopping. In fact, erosion depends not only on the velocity and the depth of the overflow but also on duration of the overtopping which has a great influence on the extent of the damages.

In most of the cases, erosion starts at the toe of the structure where the plunging overflow is highly turbulent and energetic. In addition, at this place, joints increase the risk of infiltration and uplift pressures. Then, the scouring and the local erosion developed at the toe tends to progress upstream until it reaches the dam crest. At the same time, due to its sharp shape, the crest may also experience undercutting and sub-pressures due to the wake of the flow which turns from the crest edge to the downstream slope.

A sketch of erosion mechanism for *homogeneous earthfill embankment dams* is given in Figure 5.3. As it can be seen in drawing a), for normal conditions, a water saturation line is established and seepage flow is collected by a drainage system at the dam toe.

During overtopping, the process of erosion can be divided into two mechanisms [Olivier (1967)] described in the following.

Internal mechanism :

If there is infiltration from the downstream slope, then a wet front progresses inside the embankment (Fig. 5.3b). If the saturation line is raised then infiltration water exits through the downstream slope, thus increasing uplift pressures in the embankment. That can produce slides. When the saturation line attains the slope surface at the toe of the structure, erosion and backcutting develop.

External mechanism :

If at the toe of the chute, velocity of the overflow and pressure fluctuations are large enough to exceed the material resistance or the weight of protection slabs, erosion starts at the base of the structure and progresses upstream if the overtopping lasts long enough (Fig. 5.3c).

Both erosion mechanisms may cause bank slides, removal of chunks, scouring of the slope, breaches of the embankment and at the last stage the failure of the dam itself.

If the *earthfill* dam is equipped with *an impermeable element* such as a clay central core, the embankment is divided into two regions during normal operation: upstream of the core where the earthfill is almost totally saturated and downstream of it where the region is dry. The stability of the dam strongly depends on this saturated/dry distribution. Therefore, during overtopping, in addition to the internal and external mechanisms described above, the progression of the wet downstream front by infiltration can dramatically and directly endanger the stability of the structure itself.
In addition, impermeable elements allow a delay of internal erosion progression during overtopping.

For *rockfill dams*, the failure process is quite comparable to earthfill ones with also an internal mechanism. However, due to the more permeable properties of the embankment material, infiltration spreads faster. The uplift pressures first wash out the finer particles, following by bank slides if seepages are not well drained [Olivier (1967)].

Concerning the external erosion, in this case, shear stress and uplift pressures may turn over rock boulders and remove them, leading to scouring and breaches.

Therefore, according to the failure process description, particular attention must be taken at the toe and slope protection to ensure the safety of embankment dams during overtopping. It may be concluded that both the impermeability of the slope and the reduction of the overflow velocity corresponds to the most relevant action to control overtopping.

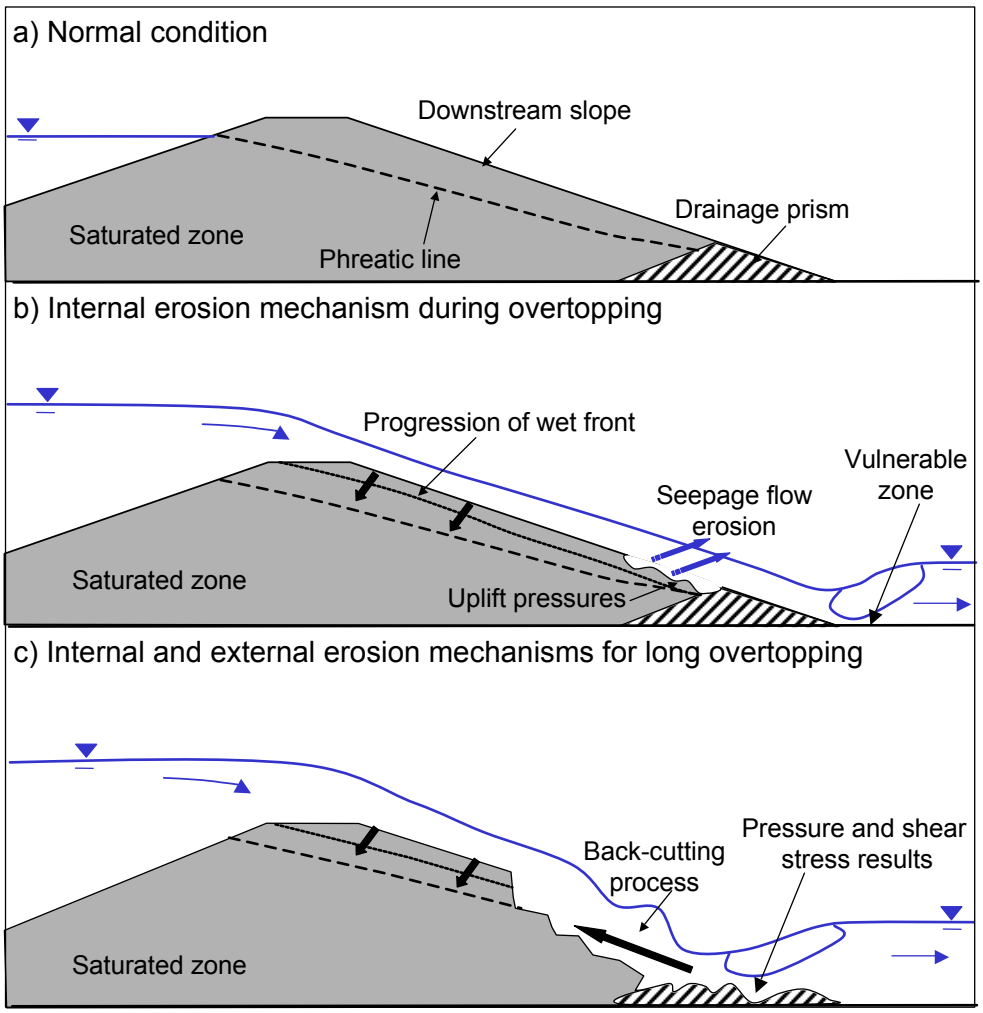

Figure 5.3: Sketch of the erosion processes during overtopping for homogeneous earthfill embankment dams

5.2.2 Dam failure examples

In order to highlight the consequences of uncontrolled overtopping, some historical failures of dams during overtopping, described by Powledge & Sveum (1988) and Powledge et al. (1989) are summarized in the following Table 5.1. In all cases, no information about drainage and sealing systems was available. A complete data base of all dam failures is available on the web-site of the United State Bureau of Reclamation [USBR (2004)]. The data concerning failures must be given more substance to be able to hold some design recommendations.

It can be noticed that no comparable criteria characterizing the overflow exists in literature. In fact, either the overtopping duration, or the maximum depth of the overflow, or even the specific discharge are given to define the phenomena, but never all of them. It is therefore difficult to compare the resistance response of dams in order to classify the safest structure.

Dams	Height (m)	Fill material	Overtopping: Max. depth (m) Duration (h) Unit discharge (m^2/s)	Damage
R.F. Bailey Ccofferdam, West Virginia (USA)	18.3	Well graded sand and sandstone	2.0 m depth and 4 h before breaching	Breached
Bloomington cofferdam, West Virginia (USA)	9.1	Clayed sand gravel	0.15 m depth and 1 h before breaching	Breached
B. Evertt Jordon cofferdam, North California (USA)	9.1	Silty-clay	0.3 m and duration more than 24 h	No significant damages
Little Blue River Levee (USA)	4.6	Vegetated clay	Overtopped in 1977 - No damage in 1982 : 0.3 m depth and 12 h before breaching	Breached
Jacksonport Levee, Arkansas (USA)	4.6	Clay	0.3 to 0.6 m depth and 1 week	No significant damage
Rocky Run Dam, Iowa (USA)	6.1	Loess	0.5 m and duration of 5 h	Moderate damages
Rocky Run Protection Levee, Iowa (USA)	2.7	Loess	0.6 m depth and duration of 6 h	Moderated damages
Elm Fork, Texas (USA)	11.0	Vegetated Clay	0.12 m and duration of 3 h	Moderate damage
Rainbow, Michigan (USA)	14.3	Clay	0.61 m and 12 h before breaching	Breached
W. Fork Pt., Arizona Remove Cr. Site 2 (USA)	10.7	Lean clay, gravel, and silty sand	0.37 m and duration shorter than 2 h	No significant damage
W. Fork Pt., Arizona Remove Cr. Site 4 (USA)	15.2	Lean clay gravel, and silty sand	0.3 m and duration shorter than 2 h	No significant damage
Randal RC+D CA-191-BH, South Dakota (USA)	6.7	Lean clay	0.3 m and duration shorter than 12 h	No significant damage

Dams	Height (m)	Fill material	Overtopping: Max. depth (m) Duration (h) Unit discharge (m^2/s)	Damage
Colorado Retarding structures, M-1, Colorado (USA)	11.6	Vegetated clayey sand	0.4 m and duration about 2 to 4 h	No significant damage
Colorado Retarding structures, S-1, Colorado (USA)	7.0	Vegetated clayey sand	0.23 m and duration about 2 to 4 h	No significant damage
Colorado Retarding structures, W-1, Colorado (USA)	14.9	Vegetated clayey sand	0.9 m and duration about 1 to 2 h	Moderate damage
Gibson dam, Montana (USA)	60.7	Concrete	1 m and 20 h	No significant damage
Mc Carty, Texas, USA	16.5	Sandy clay	Depth unknown, overtopped during 24 h before breaching	Breached
Kerrville Ponding Dam, Texas (USA)	6.4	Concrete-clapped clay	3 m depth	Damage of the concrete-capped on the downstream slope and of the embankment
Armando de Salles, Brazil	33.5 m	Earth fill	1.22 m depth and 0.3 h before breaching	Breached
Euclides de Cumba, Brazil	61.0	Earth fill	1.22 m and 7.5 h	Breached
Oros dam, Brazil	-	Classified rockfill	$q < 1m^2/s$	Breached
Hell Hole dam	30	Classified rockfill	-	Retrogressive erosion

- *no information*

Table 5.1: Selected overtopping events

Chapter 6

Downstream slope protection linings

The economical interest of controlling overtopping has enhanced research on alternative solutions to protect embankment dams. The understanding of failure mechanisms pointed out that the most vulnerable points during an overtopping of embankment dam concern:

- Uplift pressures at the downstream edge of the crest,
- Low resistance of granular and cohesive material as well as cavitation and uplift pressures risks on the downstream slope,
- High residual energy of the flow, fluctuations and uplift pressures at the toe.

Though the crest protection and the stilling basin design are of great importance to limit damage and though the drainage and sealing systems are essential to the good and efficient functioning of the whole protection system during overtopping, this literature review focuses on the downstream slope surface protection.

In this context, the proposed alternatives, described briefly in the following, result mainly from physical model studies. The principal aims investigated were :

1. to protect the slope surface against retrogressive erosion (initialization at the toe),
2. to increase the shear resistance of the surface,
3. to avoid infiltration in the downstream part of the dam,
4. to dissipate the energy along the structure itself in order to decrease the residual energy at the toe,
5. to reduce the risk of cavitation.

Their performances are summarized in the table in Fig 6.8. However, it is important to notice that among the collected examples, only a limited amount of information on the lining behaviour during overtopping could be obtained. Firstly this is due to the low probability of occurrence of an overflow observation. Secondly, in general the protected overtopped structures have not been followed up and were not the subject of scientific publications.

6.1 Protection linings without energy dissipation capacity

Established vegetation linings

This low cost solution is the most common system for protection against erosion of earthfill dams. Vegetation linings only require that the downstream slope be seeded with grass or another dense short vegetation.

However, this provides only limited erosion protection. Results of physical models and prototype observations have shown that well-established dense grass can provide moderate resistance during short overtopping (order of one hour), for overflow velocity up to 1.8 m/s for earthfill or 1.2 m/s for granular slope [Hewlett, Boorman & Bramley (1987)]. However, areas of poor grass covering, of non homogeneous distribution of grass or of holes, are responsible for earlier local erosion which can be spread over all the slope.

- Advantages
  Easy to fit and cheap.
  Self perpetuating.
  Good environmental integration.

- Disadvantages
  It needs a long duration to be fully developed (1-3 years) and a regular maintenance.
  This system is only efficient for reduced applications: short overtopping and flat slopes.
  It contributes to attract animals which can locally destroy the downstream slope.

- Recommendations
  To be effective, this system requires a regular maintenance by fertilizing, mowing, filling erosion spots.
  Alternative vegetation sowed over a fiber mattress fitted in the earth surface layer can improve the shear stress resistance of the slope due to the reciprocal action of the mattress which maintains the roots and inversely (see Fig. 6.1).

Figure 6.1: Establishment of vegetation within mattresses - [Maccaferri (2004)]

Armored earth

Armored earth consists in making a cohesive material by mixing pulverulent soils with armourings and in suppressing the downstream part of the structure. That leads thus to a vertical downstream slope of the embankment dam and then to a chute flow. By consequence, there is no question of surface erosion. However, particular attention must be taken with the toe protection since a great amount of energy is transmitted at the point of chute impact.
Armed earth has been observed for few dams lower than 40 m and subject to overflow lower than 12 m^2/s [Albert & Gautier (1992)].

- Advantages
  Armored earth can be constructed in narrow sites.
  Armored earth dams do not undergo overflow on the downstream slope.

- Disadvantages
  Corrosion of armorings can lead to loss of resistance quality of the armored earth.
  This system demands high quality of materials (resistance and impermeability).

- Recommendations
  The upstream slope can be protected by a sealing layer in order to avoid percolation which could initialize failures. A drainage between the embankment and the sealing protection is recommended to prevent uplift pressures due to possible seepage.
  At the base of an embankment dam, water mattress and toe protection are essential to ensure a protection against scouring and pressure fluctuations [Bollaert (2002)].

Geotextile covering

The main three types of geotextile systems encountered to protect downstream slope are:

- Two-dimensional woven meshes and fabrics, through which vegetation can grow.
- Three-dimensional open synthetic mats which are filled with topsoil and seeded (Fig. 6.2).
- Three-dimensional filed synthetic mats which are filled with asphalt or rock.

These system all behave as a seal and an erosion protection.
Physical tests [Hewlett et al. (1987), Chen, Anderson & Simons (1986)] and historic cases have shown that even for thick geotextile layers, the system resists short overflows with velocity up to 8 m/s. However, as soon as the overflow duration increases, seepages located between the topsoil and the fabric create uplift pressures at the interface, leading to geotextile failure.
The resistance to erosion of all these types of geotextile is tightly enhanced by covering them with a dense grass turf so that the geotextile is fully integrated with the subsoil by the root system.
The optimum system tested consists of an anchored three-dimensional open-textured mat geotextile layer, covered by dense grass. In fact, the open mats allow the roots to easily reach the subsoil and both anchors and roots limit the development of an underflow.

- Advantages
  Geotextile behaves both as a seal and an erosion protection layer.
  It is easily fitted on site.
  It can be completely integrated into the environment.
- Disadvantages
  Geotextile has poor anchorage and poor stretching capacities. It is limited for low velocity and short overflows because the system is vulnerable to wrenching and seepages.
  Geotextile is prone to vandalism.
- Recommendations
  Geotextile is more adapted to be used as a filter layer between the underlying topsoil and a protection system.

Soil cement overlay

This consists of a concrete layer of a minimum thickness of 30 cm placed from the upstream of the crest to the downstream toe of the embankment. This high resistance and water-tight protection can endure high overflow velocity [Powledge et al. (1989)]. However, seepage through joints or cracks can lead to great uplift pressures until failure and layer irregularities can initialize cavitation for high flow velocity ($> 30\ m/s$).

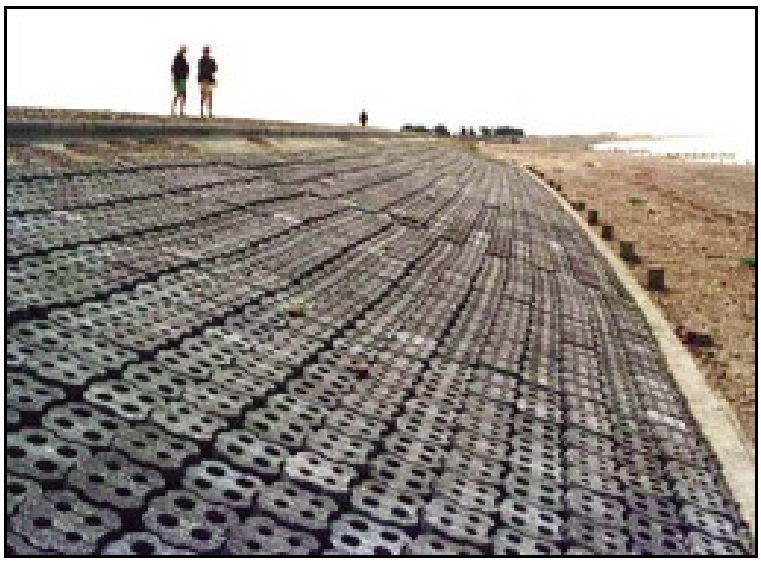

Figure 6.2: Example of a bank protection against flood with a 3D non-wowen polypropylene geotextile - [Website of Geofabrics company, England, (2004)]

- Advantages
  Resistant to high specific discharge, even for an important incoming head and a long overtopping duration.

- Disadvantages
  Risk of seepage in joints, of cracks because of settlement, risk of cavitation.
  It is prone to vibration under the overflow pressure fluctuations, that can rapidly lead to concrete fatigue.

- Recommendations
  Drainage layer is required for the possible seepages.
  To reduce vibration and to reinforce the armor layer, longitudinal armoring can be added in the concrete layer.

Cable-tied cellular concrete blocks

This consists of a layer of cellular concrete anchored blocks (minimum superficial mass of 135 kg/m^2), underlain with geotextile and covered with a minimum 25 mm thick seeded topsoil [Gray (1991)]. Open cell geotextile is preferable to allow penetration by grass roots which in turn enhances the anchorage system.
A schematic of the system is given in Figure 6.3.
Due to its high resistance and stability, this protection is stable for velocities up to 8.6 m/s.

- Advantages
  High degree of stability.
  Flexible and durable.
  Good environmental integration.
  Cost-effective.

- Disadvantages
  Negative hydrostatic pressures at the downstream edge of the embankment crest can lead to the displacement of blocks.
  Needs regular maintenance.
  Susceptible to vandales removing blocks (if non cabled).

- Recommendations
  Anchorage between the adjacent blocks and between the concrete armor and the subsoil has to be designed by taking into account the likely uplift pressures.
  The protection layer should be carried upstream on the embankment crest and also anchored upstream from the location of the critical depth to protect the structure against the negative pressures.
  For the same reasons, the layer should be extended downstream of the hydraulic jump position.

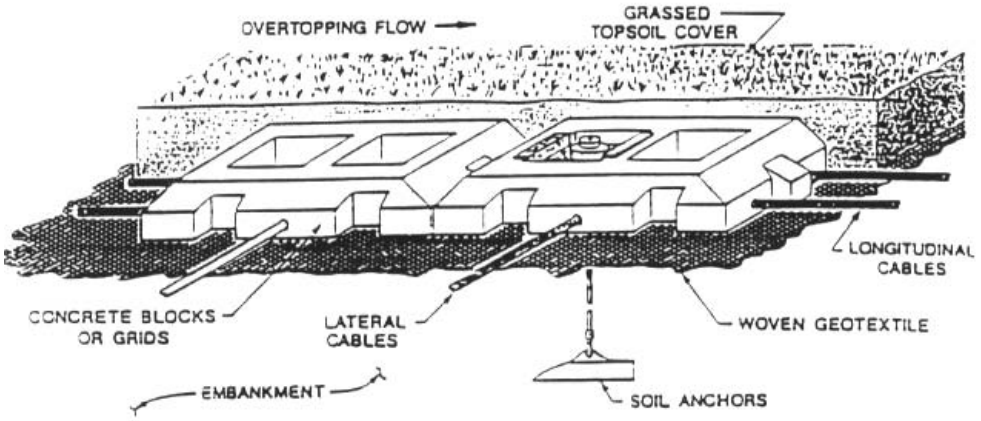

Figure 6.3: Typical cutaway of cellular concrete mat system [ASCE (1994)]

6.2 Protection linings with energy dissipation capacity

In addition to resisting to erosion, the following protection systems dissipate the energy along the slope due to their macro-roughness patterns. They contribute then to the diminution of the residual energy at the toe of the structure.

Furthermore, because these linings enhance the flow turbulence, self aeration process develops very near the crest. The risk of cavitation is then greatly reduced with this highly aerated overflow.

Riprap

Riprap placed on the downstream slope consist of two or more layers: filter and armor. These are generally used to protect cofferdams and small dams.
Fill block dimensions, gradation and distribution depend on the design specific discharge and on the slope. These characteristics are calculated based on empirical relationships as the Hartung and Scheuerlein equation, in Albert & Gautier (1992).
The material gradation (uniformity of the block sizes) has a significant influence on the erosion process: poorly-graded riprap presents a greater stability for overflows than well-graded riprap. However, it fails suddenly while well-graded resists sudden failures better [Wittler & Abt (1990)]. Nevertheless, in general, riprap do not resist long duration and high discharge overflows because the blocks start to overturn, then they move and finally are displaced out of the system by uplift pressures.

- Advantages
  The rough surface of riprap dissipates partially overflow energy.
  Riprap can be repaired easily by just replacing blocks if necessary.

- Disadvantages
  Design guidelines are still lacking because of the complex turbulent aerated flow involved. In addition, physical models of riprap protection are difficult to accurately produce because of scale effects with respect to granularity, shape, arrangement and permeability of the blanket.
  Riprap protection is not applicable everywhere since it needs a supply of large durable rocks (crystalline, basalt).
  It is not adapted for high overflow discharge and for overflow with floating debris. In fact, the later can accumulate between blocks during overtopping which can lead to an overload. This may endanger the stability of the blocks and reduce their dissipating function.

- Recommendations
  Since the riprap blanket is not a sealing protection, it should be underlain with a drainage layer or a sealing layer such as geotextile (see Fig. 6.4).
  Based on the results of tests at the Colorado State University [Abt & Johnson (1991)], the angular stones are more effective than the rounded-shape (unit discharge of failure is 40 % greater in the first case). In fact, angular stones tend to interlock and wedge.
  Because of the mobility of the rocks and the collection of floating debris, the riprap blanket should be inspected after each overtopping.
  The toe protection should be linked to the downstream slope protection because of uplift pressure and retrogressive erosion as well as sliding.

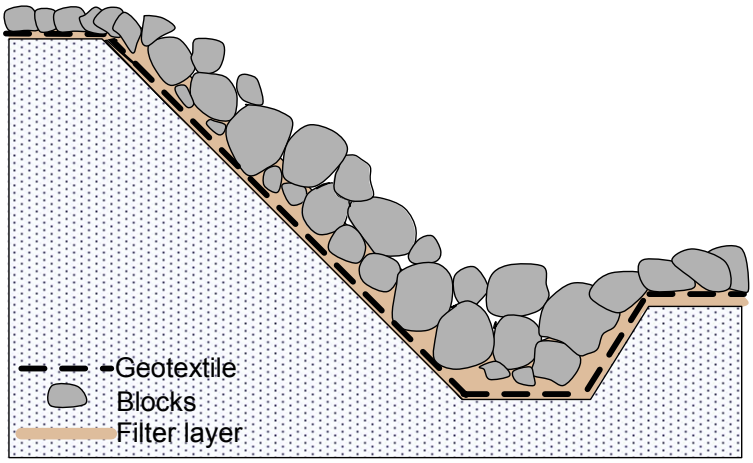

Figure 6.4: Schematic view of a Riprap protection over a downstream slope

Gabions

The Egyptians used a gabion system 7000 years ago to protect banks along the Nile river. As shown in Figure 6.5, gabions are rectangular baskets or mattresses of galvanized steel wire mesh woven in a uniform hexagonal pattern. Physical model studies have shown that the size of the compartments depends on the slope and on the hydraulic stresses. They are filled with angular rocks larger than 1.5 time the cells size to prevent lift. The edges of the baskets are laced together to form a large and heavy protection.
Gabions are mainly used for small earthfill dams and spillways. They can be fitted as a lining layer parallel to the embankment slope or as a stepped bottom over the downstream slope (Fig 6.5). In addition to prevent the slope erosion, stepped gabions provide a high degree of dissipation energy and offer a greater structural stability compared to lining gabions. This system is recommended due to its efficiency. It can sustain velocity up to 8 m/s. However, for long duration overflow, gabions can be rapidly damaged by erosion and/or abrasion and easily are deformed which leads to failure.

- Advantages
  The use of small blocks to fill the blankets makes material easily available at many places.
  Gabions involve light construction techniques and can be carried out on site, thus they can be cost effective if labor is cheap.
  Stepped gabions present mechanical stability as well as a good erosion resistance and an efficient rate of energy dissipation.
  Gabions can be easily repaired or replaced on site.

- Disadvantages
  Gabions are prone to vandalism.
  The rapid wear process of gabions (abrasion, erosion) limits their use to temporary protection cases. Then, they require maintenance to identify damaged baskets after overtopping.

Gabions are vulnerable to overflow transporting sediments (abrasion) and floating debris (damage of the mesh cells).

- Recommendations
  To prevent rapid failure due to uplift pressures between the mattresses and the subgrade, the gabion materials must be surely anchored, from the crest to the toe of the embankment.
  To reduce the migration of the rockfill and then the mesh deformation, the gabions must be tightly packed with angular stones at the surface layer.
  For loaded overflows, the exposed gabions can be protected with a 5 to 10 cm thick concrete layer to prevent abrasion [Peyras, Royet & Degoutte (1991)]. In case of discharge larger than 3 m^2/s, a reverse slope can be added to each step. This will enhance the gabions stability and the energy dissipation.

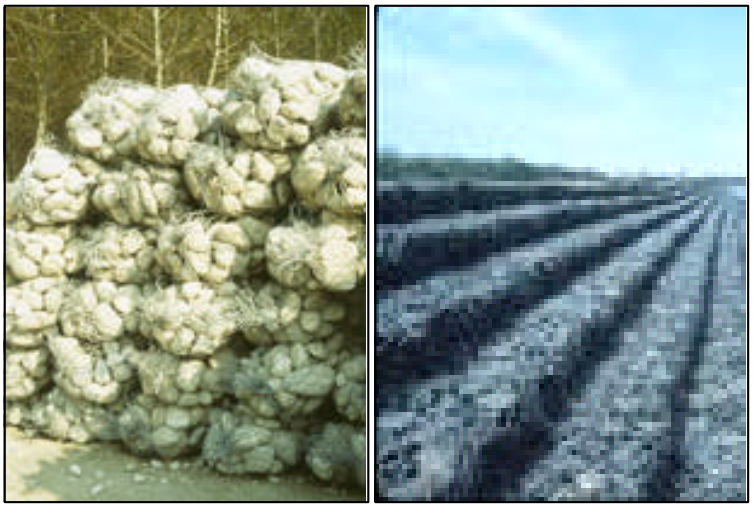

Figure 6.5: Left: Steel wire mesh baskets filled with stones; Right: Stepped Gabions protection - [Maccaferri (2004)]

Pre-cast concrete interlocked or cabled blocks

Concrete block can be fitted simply to interlock mechanically or can be secured together with cables. The block design varies from solid blocks to open cells to permit grass growth. Both interlocked or cabled types perform better if they are packed and when their interstices are filled with grass.
A new concept of stepped-block spillway has been developed in CIRIA, U.K, described in detail in the technical guide by Baker (1997).
Though this protection system is very efficient concerning resistance (overflow velocity up to 13 m/s), energy dissipation and stability, they require large block sizes and are expensive.

Pyramid shaped concrete blocks have been applied to protect an overtopped dam in Leithen, Austria (see Fig. 6.6). The stability of this system is ensured by the weight of the blocks itself [Bosshard (1991)]. Although the dam has not yet been overtopped, the stability of this

configuration was tested and confirmed in a steep laboratory flume at LCH-EPFL [Manso de Almeida & Schleiss (2002)].

- Advantages
  High resistance, stability and energy dissipation efficiency.
  Contrary to Riprap, physical models of pre-cast concrete blocks can easily be scaled to prototype dimensions using the Froude similarity.

- Disadvantages
  Heavy and large blocks are required, then this solution is not cost effective.
  Floating debris accumulated between the blocks can endanger the bloc stability and reduce the rate of dissipated energy.

- Recommendations
  As for riprap protection, blanket of pre-cast concrete blocks is permeable. Therefore, an underlining geotextile layer is recommended as a filter and sealing protection as well as a drainage layer [Baker (1997)].

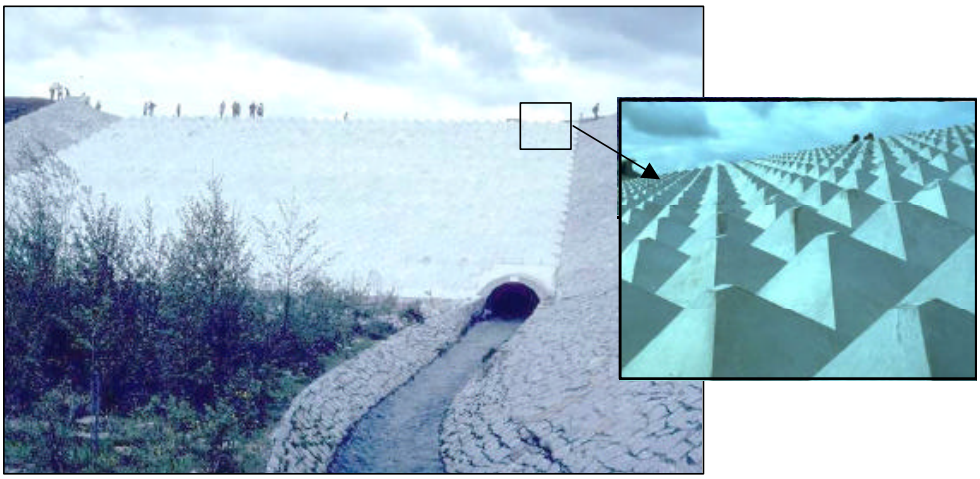

Figure 6.6: Pyramids lining of the downstream slope of the Leithen dam in Austria

Roller-Compacted Concrete linings

Since the early eighties, RCC technology has been used more and more not only for new dam constructions but also for the rehabilitation and the protection of embankment dams. In fact, since 1980, more than 50 RCC rehabilitation dams have been constructed in the USA (example figure 6.7). At the end of 1999, 195 large RCC dams were reported [Hansen (1989) and 2000].
Briefly, RCC consists of "a zero slump concrete that is transported, spread and compacted using traditional earth moving equipment" [Ditchey & Campbell (2000)]. The typical RCC system consists of placement from one abutment to the other in two or three about 0.3 m thick horizontal lifts in a stepped pattern (Fig. 6.7). More details about the alternative of RCC are also described in Ditchey & Campbell (2000). Generally, aggregates of the dam site are mixed with cement materials to produce the concrete. As a consequence of the method,

RCC techniques lead to fast and low cost construction.
The performance of overtopped RCC structures with respect to energy dissipation and slope protection was so effective that it was the driving force behind engineers and researchers to study the overflow behaviour over stepped slope. However, understanding and precise description of this complex aerated and turbulent flow is still not sufficient to provide a general design guideline for an optimal dimension of the steps.

Similar to Gabions system protection, RCC can be fitted in two ways: by slopping (directly next to and parallel to the downstream slope) or by stepped overlays (concrete layer compacted in horizontal lifts to form steps). The fundamental difference between these two systems lies in the energy dissipation capacity, the stepped linings being of course the most efficient.
Therefore, regarding stepped RCC, in addition to its high degree of resistance and stability, this system provides a high energy dissipation efficiency which will be discussed in Part IV. For example, flow velocities up to 29 m/s were observed for the 55^o gated RCC stepped spillway of the Dachaoshan project [Guo, Liu & Lu (2003)].

- Advantages
  RCC is time and cost effective compared to classical concrete construction.
  Because it is a rapid technique, RCC causes minimal project interruption.
  The protection is well integrated without requiring additional construction areas on site.
  Steps allow not only to greatly increase the energy dissipation rate but also to shift the onset of air entrainment (see chapter 14.1) upstream, near the dam crest. As a consequence, the length of the slope vulnerable to cavitation is significantly shortened.
  RCC steps are easier to be inspected.
  The mass of the step contributes to stabilize the whole structure against hydraulic uplift.

- Disadvantages
  RCC is not a watertight protection, thus uncontrolled seepage can lead to large uplift pressures.

- Recommendations
  Underlying drainage layers should be provided to avoid possible seepages through cracks or joints and which could lead to uplift pressures.
  For large overflow, formed steps and enriched concrete are recommended to avoid damage of the edges by abrasion.
  The toe protection is required to prevent uplift pressures at the downstream step which could then cause a slide of the entire system. Generally, for protection, RCC lifts are extended downstream the toe and upstream the slope (to protect the crest).

6.3 Summary of the lining protections performance

The performance of laboratory studies and a few case histories are summarized in Figure 6.8.

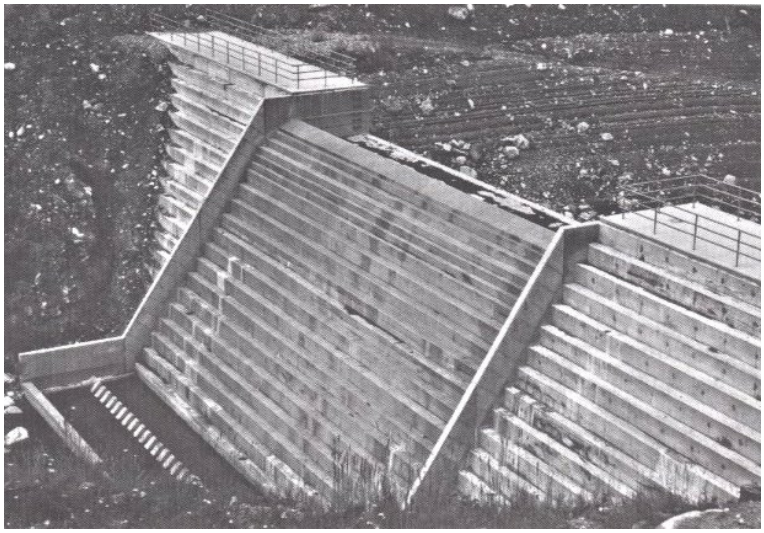

Figure 6.7: New Peterson RCC Dam. Colorado, USA (By courtesy of R.M. Boes)

System	Slope	Overtopping			Critical depth	Energy dissipation	Examples	Comments	References
		Duration	Velocity	Discharge					
Established vegetation	Granular $10° < \theta < 22°$ Cohesive $10° < \theta < 22°$	Short	< 1.2 m/s < 1.8 m/s	<2 m^2/s	-	No			Temple (1987) ICOLD (1997)
Armed earth	- Vertical slope - Dried friction angle >36°	-	-	- ≤12 m^2/s	≤ 1.0m -	Vertical jet: 100%	Vallon de Bîmes, France Taylor Draw Dam (USA)	Dam height : 9 m Dam height: 22.5 m	Albert *et al.* (1992) ICOLD (1997)
Geotextile	< 1V: 2H	Short	< 6.7 m/s	<2.25 m^2/s	-	No		Seeded with dense grass	Frizell *et al.* (1996) Hewlett *et al.* (1987)
Geo-membrane	1V:6H	Short	6-8 m/s	-	-	No			Timblin Jr. et al. (1988)
Soil cement	No limitation	Function of thickness	-	-	< 1.2 m	No		Laboratory results of USBR	Powledge *et al.* (1989) Frizell et al. (1996)
Cable tied concrete blocks	-	- -	7.9 m/s 8.6 m/s	-			Jackhouse Dam (UK)	135 -160 kg/m^2, geotextile under layer anchored, cohesive subsoil With grass covering and anchored	Powledge *et al.* (1989) Frizellet al. (1996)
Reinforced Riprap	< 1V:2H	Short	-	<3.7 m^2/s	-	Yes		Grain size: 15 – 60 cm	Frizell *et al.* (1996)
Slopping Gabions Stepped Gabions	1V:6H 1V:4H ≤1V:2H	Short	9.1 m/s ≤ 8 m/s	≤3.7 m^2/s ≤ 3 m^2/s	-	No 40% to 90%	Laboratory results	Compartments: 0.91x0.91x0.91 Anchored on the slope over filter bed -	Peyras *et al.* (1991) Frizell *et al.* (1996)
Precast concrete blocks	1V:6.5H 1V:4.5H 1V:6.5H 1V: 2 H		17 to 23 m/s ≤ 13 m/s	≤ 60 m^2/s ≤ 13 m^2/s ≤ 5 m^2/s ≤ 2.9 m^2/s	-	40% to 90%	- Dnieper Dam - Dneister cofferdam - Moscow water supply scheme, ex-URSS	3rd example was under 2 m^2/s during 1 month without damage (Dam height: 12 m)	Pradivets (1987) Frizell *et al.*(1996)
RCC	1V:0.7H	-	≤ 28 m/s	≤ 165 m^2/s	59 m	40% to 90%	Dachaoshan spillway, Chine	Gated stepped spillway	Guo et al. 2003
	-	4-5 days	-	≤ 10 m^2/s	4.3 m		Brownwood Country Club Dam, USA	Dam height: 5.79 m	Powledge *et al.* (1989)
	-		-	≤ 10 m^2/s	-		M'Bali Dam, USA	Dam height: 23.5 m	Albert et Gautier (1992)

Figure 6.8: Examples of protection systems for downstream slope of embankment dams

Chapter 7

Conclusions

The safety of embankment dams due to uncontrolled overtoppings is a real problem since they cause about 40 % of dam failures. The high velocity and energy of the overflow can in fact lead to dramatic damage by erosion and structural breaches, especially for long duration events.

However, in the early eighties, in parallel to the development of RCC techniques, researchers started to develop solutions to protect overtopped embankment dams against erosion and to control overflow.

Nevertheless, due to the complexity of the interaction processes between the aerated turbulent overflow and the rock, granular or cohesive embankment structures, protection systems have been mainly studied in hydraulic models or obtained from prototype cases.

The failure mechanism shows that the vulnerable points during overtopping concern:

- first the downstream edge of the dam crest prone to uplift,
- second, the base of the structure which undergoes very high energy flow impact and large pressure fluctuations,
- finally the whole downstream slope which experiences its own erosion in addition to the effect of the spread of the crest and toe erosions.

In this context, the brief state-of-the art focus on the surface lining protections of the downstream slope.

The cost-effective revetment surface lining such as vegetation and geotextile can be efficient for only mild slopes ($< \ 1V : 2H$), very short events (a few hours) with low flow velocities. Even cement or cellular cable-tied concrete blocks are not sufficient to avoid failure and erosion during overtopping. Though they increase the shear resistance of the slope for short duration events with velocity up to about 8 m/s, they finally fail due to internal seepages, anchorage or material resistance quality problems.

The only successful alternatives are those with an energy dissipation capacity in addition to high resistance and stability. Pre-cast concrete blocks and overall RCC steps are the most efficient solution in this regard. Due to their macro-roughness geometry, they increase head losses along the whole slope and thus reduce significantly the residual energy at the toe of the dam as well as the slope bottom velocity. Furthermore, they shift upstream near the crest the onset of aeration which greatly diminishes the zone of cavitation risk.

Finally it appears that macro-roughness alternatives are not only highly resistant to shear stresses (concrete surface), they are stable (weight of the steps/blocks) but they also **control the overflow velocity and energy**.

However, understanding of energy dissipation mechanisms and general flow behaviour relationships are still lacking. This lack has motivated the content of the research project as described in the following parts.

Part III

Background on the behaviour of high velocity aerated flow over stepped chutes

Chapter 8

Description of the aerated flow over stepped chutes

This literature review focuses in particular on the flow behaviour over slopes equipped with rectangular conventional steps. Indeed, this configuration will be the basis of the experimental study. Furthermore, very few investigations concerned other types of macro-roughness linings over steep slopes.

8.1 Flow regimes and structures

For a given slope, the general behaviour of the flow over a stepped chute is characterized by 3 different regimes, depending on the discharge.

Nappe flow (Figure 8.1a)

For low discharges, the flow drops from step to step. With flat chutes or long steps, a hydraulic jump can be developed partially or totally on the horizontal face [Pinheiro & Fael (2000)]. Otherwise, the free-falling nappe hits directly one step to be deflected to the next one downstream. An air cavity is trapped between the vertical face and the nappe, and if it is not aerated, pressure inside this cavity can drop below the atmospheric value [Sánchez-Juny (2001)]. Only a few authors studied the characteristics of this regime. In fact, the non homogeneity of the flow depth, the instabilities of the free surface due to the under-pressures inside the air cavities and the 3D pattern of the flow make direct measurements of flow parameters impossible.

Skimming flow (Figure 8.1c)

With larger discharges, the flow skims as a coherent stream over a pseudo-bottom formed by the outer edge of the steps. Beneath it, recirculating cells are trapped inside the step, rotating in a rounded triangular vortex [Diez-Cascon, Blanco, Revilla & Garcia (1991), Chanson (1994a), Chamani & Rajaratnam (1999), Pegram, Officer & Mottram (1999)]. The rotational velocity increases with increasing discharge. Recently, Ohtsu & Yasuda (1997), Matos (2000a), Sánchez-Juny (2001), Nariai, Ohmoto & Yakita (2001), have shown the 3D pattern of these vortices which turn not only in the mean flow sense but also in the transversal direction, over the width of the step. The water, after circulation in the vortex, is randomly ejected back into the main flow. Then, at the interface, a transverse internal jet insures an exchange between the filled pool inside the steps and the skimming layer. The pseudo-bottom is the place of the friction between these two flow layers.

Transition flow (Figure 8.1b)

The passage from nappe flow to skimming flow is gradual and continuous through a transition regime [Diez-Cascon et al. (1991), Ohtsu & Yasuda (1997)]. For this regime, the flow can appear as nappe flow (presence of air cavities) for some steps and as skimming flow (onset of vortices in a filled step) for the rest.

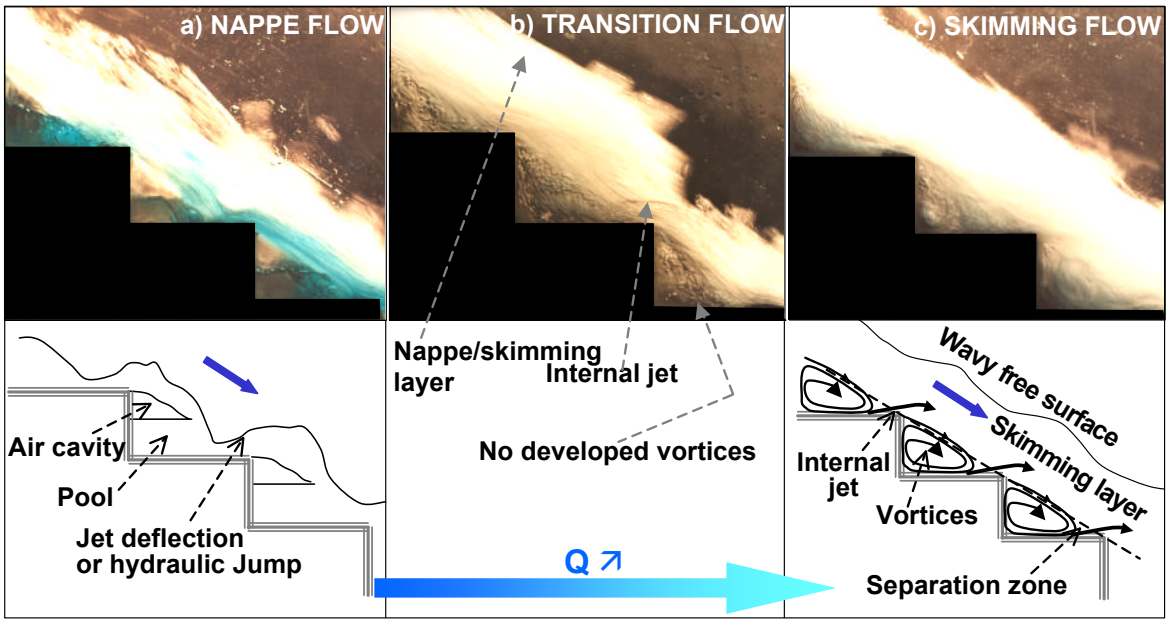

Figure 8.1: Definition sketch for nappe, transition and skimming regimes over a conventional stepped chute (flow over the 30^o stepped flume at LCH-EPFL)

Since the flow experiences different turbulence structures depending on the regime, flow depth, velocity, air concentration and overall energy dissipation efficiency are characterized differently according to these three regimes. It is therefore important for the designer to evaluate the likely flow regime for the design discharge. For this reason, the onset of the flow regimes have been subject of numerous laboratory studies. Dimensional analysis [Essery & Horner (1978), Peyras et al. (1991)] showed that the modification of the flow regime depends on the normalized critical depth h_c/h_s and on the dimensionless step geometry h_s/l_s with h_c, the critical depth, h_s and l_s respectively the height and length of the step. However, onset of regimes are determined by visual interpretation and thus are greatly subjective. This may explain the large scatter of the existing empirical criteria which are represented in Figure 8.2 and are defined in the following:

Onset of transition :

- Rajaratnam & Chamani (1995):

$$\frac{h_s}{l_s} = 0.405 \left(\frac{h_s}{l_s}\right)^{-0.62} \tag{8.1}$$

- Yasuda & Ohtsu (1999):

$$\frac{h_c}{h_s} = \frac{\left(1.4 - \frac{h_s}{l_s}\right)^{0.26}}{1.4} \tag{8.2}$$

Onset of skimming flow :

- Rajaratnam (1990)

$$\frac{h_c}{h_s} = 0.8 \tag{8.3}$$

- Chanson (1994a):

$$\frac{h_c}{h_s} = 1.057 - 0.465\frac{h_s}{l_s} \tag{8.4}$$

- Chamani & Rajaratnam (1999):

$$\frac{h_s}{l_s} = \sqrt{0.89\left[\left(\frac{h_c}{h_s}\right)^{-1} - \left(\frac{h_c}{h_s}\right)^{-0.34}\right] - 1} \tag{8.5}$$

- Yasuda & Ohtsu (1999)

$$\frac{h_c}{h_s} = 0.862\left(\frac{h_s}{l_s}\right)^{-0.165} \tag{8.6}$$

- Boes & Hager (2003b):

$$\frac{h_c}{h_s} = 0.91 - 0.14\frac{h_s}{l_s} \tag{8.7}$$

The two values of the slopes tested at LCH-EPFL, $\theta = 18.6^o$ and 30^o, are also shown in the Figure 8.2. The graph points out that for a given slope, the designer is confronted to a large range of possible discharges involving the onset of skimming flow.

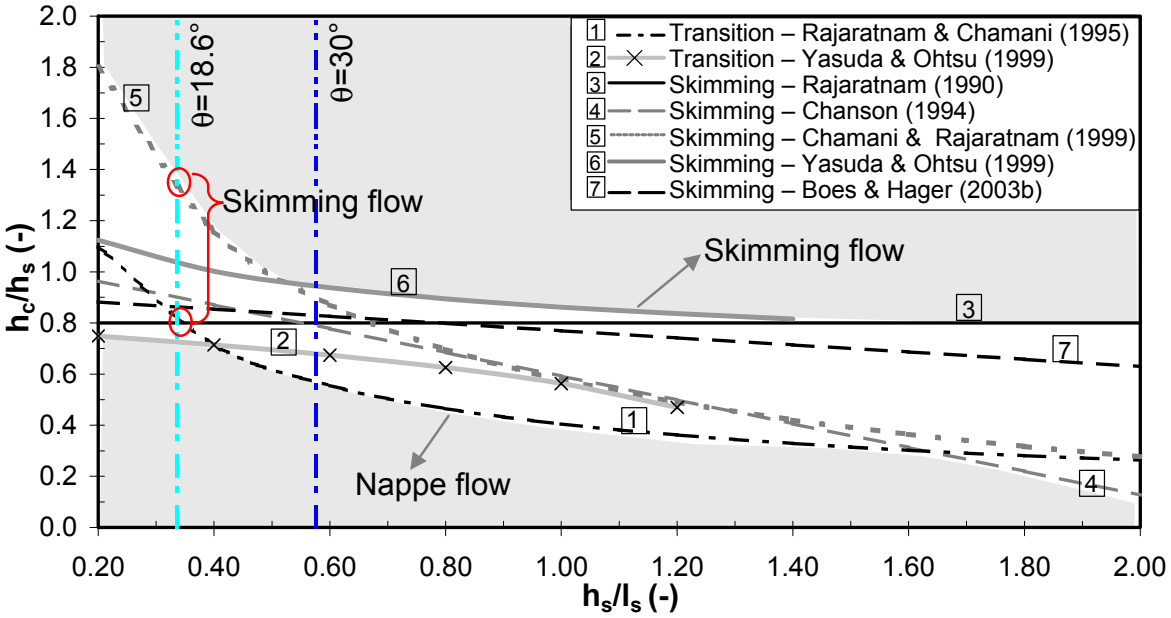

Figure 8.2: Comparison of empirical relationships to estimate the onset of transition and skimming flow regimes for conventional stepped chutes

8.2 Flow regions along the stepped slope

Because of its high velocity and turbulence, the flow over steep stepped slope is highly aerated. For the most likely observed flow regimes in prototype, namely the transition and skimming regimes, the flow along the chute can be divided into distinct regions as for smooth chutes [Falvey (1980), Wood (1991)].

Near the dam crest, in the *non-aerated region* (see Figure 8.3), the water flow accelerates and the turbulent boundary layer grows rapidly due to the macro-roughness effect. But this boundary has not a significant effect on the water surface which remains smooth. There is no air entrainment and the clear water flow depth Z_w decreases according to a drawdown curve [Hager & Boes (2000)].

When the turbulent boundary layer reaches the water surface, the turbulent energy of the vortices is large enough to exceed the surface tension and gravity effects: natural air entrainment starts at the so called inception point (I in Figure 8.3) characterized with its longitudinal position L_i from the dam crest, its mean air concentration C_i and the local mixture depth $Z_{m,i}$.

Downstream, in *the partially developing flow region*, the gradually increasing content of air swells the mixture air-water flow depth Z_m which progressively increases (backwater curve). The free surface becomes rough and wavy with white appearance and ejection of spray. That makes difficult to define its limit. However, as mentioned by Pegram et al. (1999), the undulation of the aerated free surface does not reflect the shape of the stepped bottom. In contrary it is out of phase, resulting from the macro-turbulence structures effect.

If the slope is long enough, an equilibrium between head loss and gravity is established. In this *fully developed aerated region*, it can be assumed that the quantity of air transported is the flow is near the maximum, namely at the saturation air concentration C_u. In fact, in this region the flow is "quasi-uniform" since mean air concentration, velocity and flow depth are constant from one to another similar step cross-section separated with a constant distance $x_s = h_s / \sin\theta$ with θ the angle of the chute. Inside the step, the flow characteristics are varying longitudinally due to the turbulent structures. This notion of uniformity has of course no sense for the random pattern of a natural macro-roughness such as rocks in a river bed.

With the nappe flow regime, the inception point concept is not applicable since air is trapped at the first steps down the crest. Air is transported in the flow at the point where the nappe impact the horizontal face or by the eventually developed hydraulic jump [Fratino, Amador, Valenzano, Renna, Sánchez-Juny & Dolz (2003)]. The notion of quasi-uniform flow has not yet been applied for this regime.

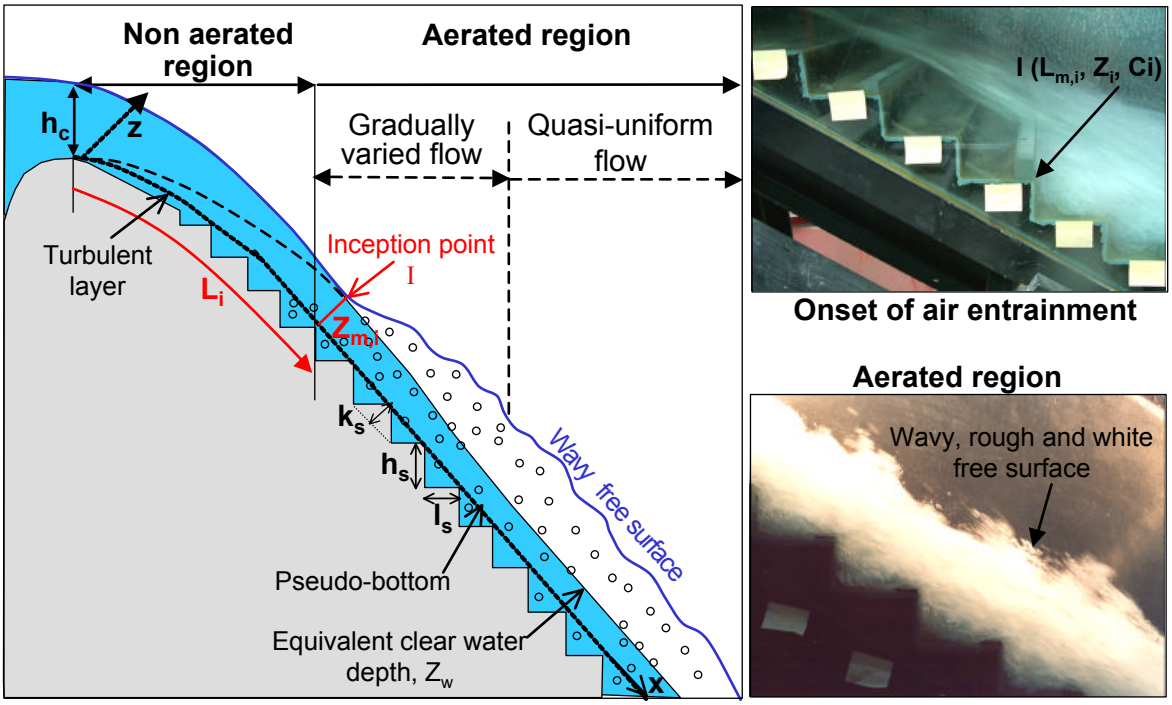

Figure 8.3: Sketch view of flow regions for transition and skimming flows over stepped chutes along with pictures of view from the 30^o stepped flume at LCH-EPFL

8.2.1 Location of the inception point

The location of the onset of air entrainment is significant for the designer of a stepped chute. It delimits the reach of the spillway or dam which can be prone to cavitation damage.

As mentioned, the inception point is located where the depth of the turbulent boundary layer equals the flow depth. In fact, it corresponds to that location where normal turbulent velocities near the surface are large enough to eject water slugs into the air. When falling back due to gravity, these droplets open the flow surface and break it in spray. Air is thus trapped in the water. Furthermore, if the normal component of the turbulent velocity overcomes both surface tension and air bubble uplift velocity, air is carried down the flow depth and transported by the high velocity of the flow.

For smooth slope the thickness of the boundary layer was assessed by different authors [Cain (1978), Falvey (1980), Wood (1991)]. Therefore the location of the inception point is determined theoretically. The inception point has not yet been located for stepped slopes because of the complexity of the turbulence pattern. Nevertheless, as mentioned by Chamani (2000), compared to smooth chute, the boundary layer grows faster, enhanced by the wakes, vortices as well as internal jet due to the steps themselves. Then, one positive effects of the steps is to shift up the inception point and to reduce the region vulnerable to cavitation.

The determination of the point of inception on stepped spillway is generally the subject of visually observations. The criteria are then subjective and different from an author to an other. Classically, the inception point corresponds to the step cross-section where the

water becomes intensively white, *i.e*, where the air bubbles remain significant and constante [Chanson (1994a), Chamani (2000), Matos (2000b), Mateos-Iguácel & Elviro-García (2000)]. Furthermore, empirical criteria for the determination of the inception point is proposed by [Boes & Hager (2003a)]: the air concentration at the pseudo-bottom at the inception point is defined by $c_{b,i} = 0.01$.

A large set of empirical laws existes to define the characteristics of the onset of air entrainment: the longitudinal position from the crest L_i, the mixture or clear water depth ($Z_{m,i}$, $Z_{w,i}$ respectively) and the mean air concentration (C_i). Some of these laws are presented in the following where $F_* = q_w/\sqrt{g \sin\theta k_s^3}$ is the roughness Froude number with $k_s = h_s \cos\theta$, the normal step height, $F_i = q_w/\sqrt{g(h_s/l_s)k_s^3}$ is the inception Froude number and $F_s = q_w/\sqrt{g \sin\theta h_s^3}$ is the step Froude number.

Chanson (1994a)
Crested stepped flume; $27^o < \theta < 52^o$

$$\begin{aligned} \frac{L_i}{k_s} &= 9.8(\sin\theta)^{0.080} F_*^{0.71} \\ \frac{Z_{m,i}}{k_s} &= \frac{0.40}{(\sin\theta)^{0.04}} F_*^{0.64} \end{aligned} \tag{8.8}$$

Chamani (2000)
Ogee crest; $50^o < \theta < 60^o$

$$\frac{L_i}{k_s} = 8.29 F_i^{0.85} \tag{8.9}$$

Matos (2000b)
Crested stepped flume; $\theta = 53^o$

$$\begin{aligned} \frac{L_i}{k_s} &= 6.289 F_*^{0.734} \\ \frac{Z_{w,i}}{k_s} &= 0.361 F_*^{0.606} \\ C_i &= 0.163 F_*^{0.154} \end{aligned} \tag{8.10}$$

Boes & Hager (2003a)
Tests on gated stepped flume but results extended for crested stepped spillway; $26^o < \theta < 55^o$

$$\begin{aligned} \frac{L_i}{k_s} &= \frac{5.90(\cos\theta)^{1/5}}{\sin\theta} F_*^{4/5} \\ \frac{Z_{m,i}}{h_s} &= 0.40 F_s^{0.60} \\ C_i &= 1.2.10^{-3}(240 - \theta) \end{aligned} \tag{8.11}$$

These formula show that the step height as well as the slope have a small effect on the onset of air entrainment whereas the discharge (or flow depth) is the dominant parameter. This results will be discussed in Part IV, Chapter 14.1.

Equations 8.8 to 8.11 are compared for slope $\theta = 50^o$ and a step height of $h_s = 0.06\ m$ in Figure 8.4 for both stepped and smooth slopes. The later location is derived from the formula of Wood (1983):

$$\frac{L_i}{k_s} = 13.6(\sin\theta)^{0.0796} F_*^{0.713} \tag{8.12}$$

Figure 8.4 illustrates the discrepancy of the empirical formula based on visual observation just mentioned above, especially for large discharges. For a specific discharge of $q_w = 0.25\ m^2/s$ the relative difference between the computed value from Chamani and Matos is large as 31.5 %. Therefore, there is still no objective criterion for the determination of the inception point. It can also be observed that, as already mentioned, the steps shift drastically the inception point up to the crest. That confirms the previous observation of Lane (1939) for smooth slope who suggested that the position of the inception point depends mainly on the roughness of the spillway surface and on the flow depth.

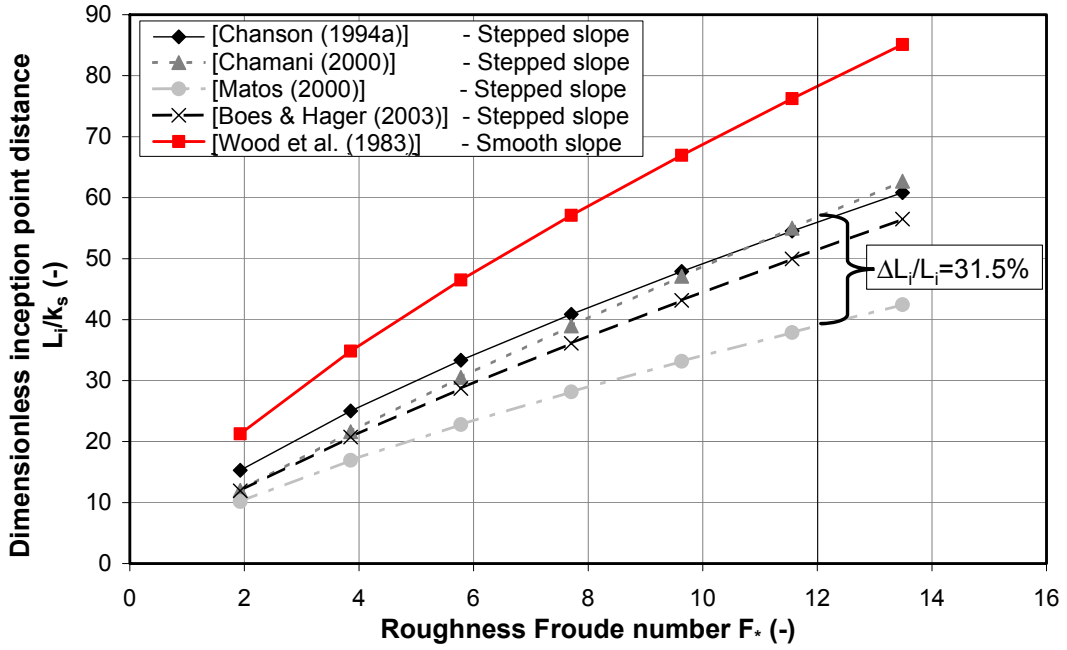

Figure 8.4: Comparison of empirical formula defining the longitudinal location of the inception point from the crest of a 50^o stepped and smooth chutes

Particular case of a jetbox entrance condition

Lane (1939) mentioned that the turbulence development on a spillway crest had a significant effect on the inception point characteristics. Indeed, the development of the turbulent boundary layer is also influenced by the turbulent initial condition and the initial acceleration of the flow controlled by either the shape of the crest or the opening of the gated entrance. For this reason, Hager & Boes (2000) who studied aerated flow behaviour in a gated stepped flume developed an analytical relation which defines the flow backwater and drawdown curves (Eq. 8.13). The relationship allows to calculate the inception point location for a crested spillway based on a jetbox entrance configuration (see Part IV, Chapter 11.1.1). It gives thus

the equivalent distance upstream of the jetbox to the crest L_c and the equivalent spillway height H_D (see Figure 8.5).

$$\frac{Z}{Z_u} = \left[1 - \left(1 - \frac{Z_u}{h_0}\right) Exp\left(-\frac{10}{3}\frac{x(Z_u^2 \sin\theta)}{h_c^3}\right)\right]^{-1} \tag{8.13}$$

with h_0 the opening of the jetbox corresponding at $x_0 = 0$. For $x < L_i$ (non aerated region), the flow depth $Z = Z_w$ and the uniform flow depth $Z_u = Z_{w,u}$. For $x \geq L_i$ (aerated region), $Z = Z_m$ and $Z_u = Z_{m,u}$.

However, the application of this formula is limited since it assumes that:

- The roughness of the reach from the equivalent crest to the jetbox is the same as the roughness between the jetbox and the inception point.
- The jetbox has no influence on the development of the turbulent boundary layer and that it is finally comparable to a cross section of depth h_0 in the clear water region with a Froude number $F_0 = q_w/\sqrt{g\cos\theta h_0^3}$. This is in disagreement with Lane's (1939) observations.
- The uniform conditions are reached.

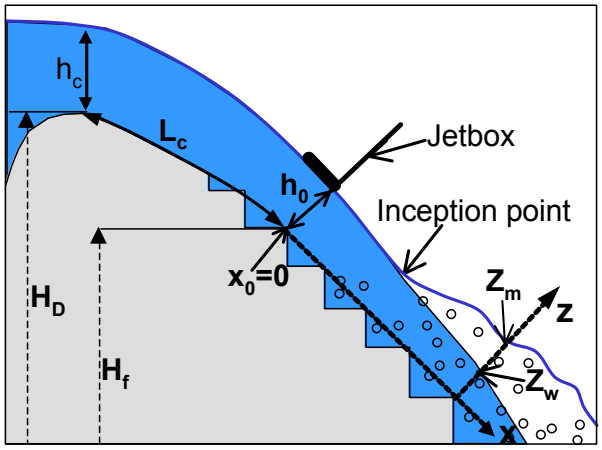

Figure 8.5: Sketch of the entrance with of an ogee crest or a jetbox configuration

8.2.2 Location of the uniform region

According to Christodoulou (1999), for a crested stepped chute with a slope angle $25^o < \theta < 55^o$, the uniform region is attained at the distance L_u:

$$L_u = \frac{8.60 q_w^{0.713}}{k_s^{0.0695} (\sin\theta)^{0.277}} \tag{8.14}$$

with q_w, the unit water discharge and $k_s = h_s \cos\theta$, the normal step height. This formula emphasizes that the attainment of the uniform condition mainly depends on the discharge and is slightly sensitive to the slope and independent of the macro-roughness height. This

relationship is in agreement with the recent analysis of Boes & Minor (2000) who estimated that the fully developed flow region depends only on the slope (Eq. 8.15):

$$\begin{aligned} \frac{L_u}{h_c} &= \frac{15}{\sin\theta} \qquad for \quad \theta = 30^o \\ \frac{L_u}{h_c} &= \frac{35}{\sin\theta} \qquad for \quad \theta = 50^o \end{aligned} \tag{8.15}$$

where h_c is the critical flow depth.

These two formulas show that position of uniform region is an approximation since for a same structure, the difference between the location of the uniform flow is about 1.3 to 1.8 times $h_c^{0.356}/(\sin\theta)^{0.723}$. In both cases it's of same order of magnitude as that of a smooth slope.

Chapter 9

Flow characteristics

9.1 Air entrainment

Downstream of the inception point I defined above, air is entrained at the free surface. Then, due to the turbulence, air is gradually transported inside the flow depth which becomes rapidly highly aerated with a mean air concentration varying from about 60% to 30 % depending on the chute slope and on the discharge. The compressible nature of the flow renders the classical hydraulic governing equations such as Bernoulli invalid. However, it was shown that the compressiblilty of the flow may be neglected [Cain (1978), Chen, Dai & Liu (2002)]. The flow can be considered as a single fluid with a mean density, ρ_m according to Equation 9.1

$$\begin{aligned} \rho_m(x,t) &= \rho_w(1-C) + \rho_a C \\ &\simeq \rho_w(1-C) \end{aligned} \tag{9.1}$$

with ρ_w, ρ_a the water and air density respectively and C the mean air concentration.

This high quantity of air in the flow has a positive effect such as to protecting the slope against cavitation damage. However, air invalidates the classical laws from hydraulics of the rivers. Indeed, air tends not only to swell the flow depth but also to reduce the energy dissipation efficiency of the steps. Chanson (1993) showed that air bubbles reduce the drag effect of the steps which was confirmed by the results of Tozzi (1994). Measurements in a closed conduit of air flow showed that the general friction factor was significantly reduced due to the air presence near the pseudo-bottom.

For these reasons, the longitudinal and vertical distributions of the air concentration have been the subject of many experimental studies. The main results are described in the following.

9.1.1 Mean air concentration in the quasi-uniform region

At any cross section along the slope, the mean air concentration C is derived from the depth-averaged of the vertical profile from the bottom to the free surface considered at the depth Z_{90} where the local air concentration is equal to 0.9 (see paragraph 9.2):

$$C = \frac{1}{Z_{90}} \int_0^{z_{90}} c(z) dz \tag{9.2}$$

Model studies showed that for skimming flow regime, when equilibrium between air entrainment and detrainment is established, the mean air concentration is constant along the slope. This definition of uniformity is true only from one step outer edge to the other then in the skimming layer. Inside the step, due to the 3D pattern of the flow, only a few measurements are available. Ohtsu, Yasuda & Takahasi (2000) found that in the vicinity of the pseudo-bottom (for $z/Z_{90} < 0.25$), the air concentration values are larger at the inner corner of the step than at the outer edge. This was explained by the presence of the recirculating cells which were assumed to transport a large quantity of air bubbles. This was confirmed by the profiles measured inside the step with a fiber-optical probe by Boes (2000a). Therefore, even for equilibrium condition, the mean air concentration varies along the slope.

At the outer step edge, the saturation air concentration depends mainly on the slope. In fact, if the macro-roughness has an effect on the location of the onset of air entrainment, it has no significant contribution on the concentration at the equilibrium. Furthermore, many authors found that the saturation air concentration, C_u, for skimming flow over stepped chutes

has the same order of magnitude as that for smooth chutes. Then C_u can be estimated by the experimental results proposed by Straub & Anderson (1958) or the following empirical relationship of Hager (1991):

$$C_u = 0.75(\sin\theta)^{0.75} \tag{9.3}$$

However, experimental results by Chamani & Rajaratnam (1999) were not in good agreement with the other authors and showed that the mean air concentration in stepped spillway is larger than the expected values for smooth chute. They proposed the following equation:

$$C_u = 0.93log\left(\frac{(\sin\theta)^{0.1}}{q_w^{0.3}}\right) + 1.05 \tag{9.4}$$

The difference may be explained by the different instrumentation used to measure the air concentration or because the uniform region wasn't strictly attained during the measurements.

In any case, this point will be discussed in the experimental Part IV, Chapter 14.1.2, for different cross-section locations.

For the nappe flow regime, no relationships are available.

9.1.2 Longitudinal variation of the mean air concentration

Downstream of the point of inception, the mean air concentration increases rapidly from value of about 20 % to the equilibrium value C_u which ranges between 30 % to 60 % depending on the chute slope.

For steep slope ($\theta = 53^o$), Matos (2000b) suggested that a good representation of the mean air concentration (C) development along a conventional stepped chute can be obtained from Equations 9.5 and 9.6, depending on the dimensionless distance from the inception point $s' = \frac{x - L_i}{Z_{w,i}}$ with x the distance from the crest.

- For $0 < s' < 30$

$$C = 0.210 + 0.297\exp[-0.497(\ln s' - 2.972)^2] \tag{9.5}$$

- For $s' \geq 30$:

$$C = \left(0.888 - \frac{1.065}{\sqrt{s'}}\right)^2 \tag{9.6}$$

As it can be observed in Figure 9.1, this development of the air concentration is quite different from that proposed by Boes (2000a):

$$C(X_i) = C_u\left[1 - \exp\left[-0.05(x + p)\right]\right] \tag{9.7}$$

where $p = 25$ for $\theta = 30^o$ and $p = 12$ for $\theta = 50^o$, $X_i = (x - L_i)/Z_{m,i}$. The later development is in better agreement with the characteristics of the quasi-uniform region, L_u according to Christodoulou (1999) and C_u from Hager (1991).

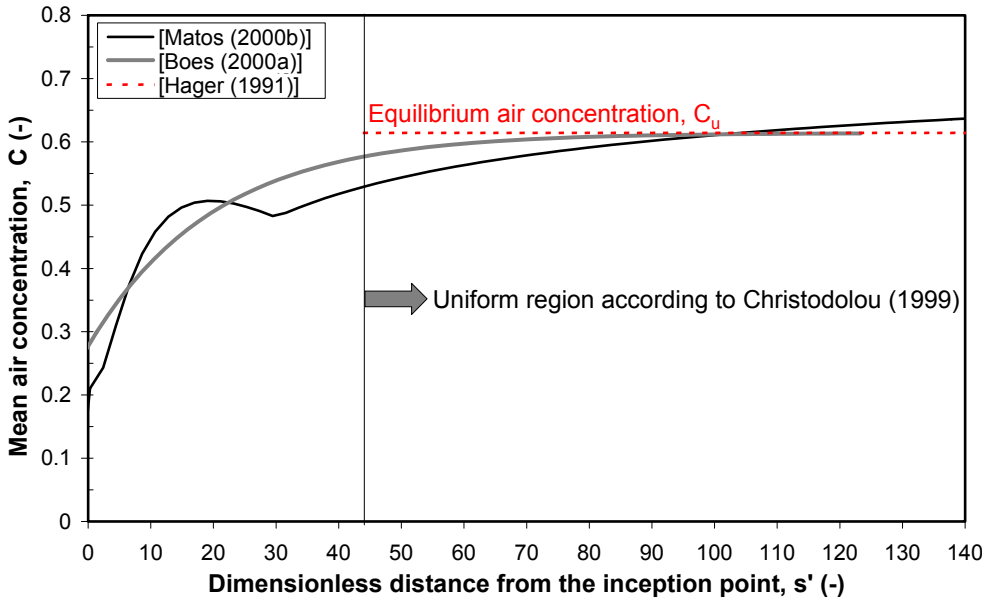

Figure 9.1: Computed longitudinal variation of the mean air concentration according to Matos (2000b) and Boes (2000a) for a 50^o slopping stepped chute ($h_s = 6\ cm$, $q_w = 0.16\ m^2/s$, L_i, $Z_{w,i}$ and $Z_{m,i}$ calculated according to Equations 8.10 and 8.11)

9.1.3 Vertical distribution of the air concentration

The nature of the air concentration profiles for nappe flow has not been studied in details.

For skimming flow regime, most of the authors found that air concentration distribution at the outer edge of the step, in both developed and uniform aerated regions, showed a smooth continuous profile. These vertical profiles are also comparable to those measured for smooth chutes which confirms the observations that the step height has no significant effect on the mean air concentration. However, for a given slope, when comparing the profiles of smooth chute based on Straub & Anderson (1958) measurements, the profiles of stepped chute indicate a difference for the values in the first 1.5 cm. This may correspond to the presence of an air concentration boundary layer [Matos (2000a)].

Furthermore, Chanson (2000) proposed an air bubbles advective diffusion theoretical model (Equation 9.8) for skimming flow regime which fits well with numerous laboratory models as well as prototype measurements at the step outer edges:

$$c(z) = 1 - \tanh^2\left(K' - \frac{\frac{z}{Z_{90}}}{2D'}\right) \tag{9.8}$$

with z the normal axis to the pseudo-bottom, $K' = arctanh(\sqrt{0.1}) + [1/(2D')]$ an integration constant deduced from the boundary condition where $c = 0.9$ for $z = Z_{90}$.
$D' = D_t Z_{90} \cos\theta / u_{r,hyd}$ is a dimensionless coefficient which is function of the turbulent diffusivity D_t normal to the flow direction, of the slope and of the air bubble rise velocity in hydrostatic pressure gradient $u_{r,hyd}$. The later depends on the bubbles size. If the diffusivity is unknown, D' can be deduced from the mean air concentration in the uniform region according

to Equation 9.9:

$$C_u = 2D' \left[tanh\left(arctanh(\sqrt{0.1}) + \frac{1}{2D'} \right) - \sqrt{0.1} \right] \tag{9.9}$$

For the transition flow regime, Chanson & Toombes (2001b) suggested that for the case of $C > 0.45$, the vertical distribution of the air concentration at most of the step outer edges may be better fitted by:

$$c(z) = K_3 \left[1 - \exp\left(-\lambda \frac{z}{Z_{90}} \right) \right] \tag{9.10}$$

with K_3 and λ depending on the mean air concentration and derived from the two following relationships: $K_3 = \frac{0.9}{1 - \exp(-\lambda)}$ and $C = K_3 - \frac{0.9}{\lambda}$.

9.1.4 Air concentration at the bottom

The minimal air concentration required next to the bottom to avoid cavitation damage to concrete surfaces is about 8 % [Peterka (1953)]. Downstream of the inception point, measurements at the step outer edge [Matos, Quintela, Sánchez-Juny & Dolz (2000), Boes & Minor (2000)] showed that the self-aeration of the flow over the steps fulfills this criterion. The development of the pseudo-bottom air concentration c_b along the stepped chute ($26^o < \theta < 55^o$) is given according to Equation 9.11 [Boes & Hager (2003a)]:

$$c_b(X_i) = 0.015 X_i^{\sqrt{tan\theta}/2} \tag{9.11}$$

It has however to be noted that this relationship was fitted for air concentration values measured the closest at 1.5 mm to 2 mm above the step outer edge.

9.2 Flow depths

The mayor difficulty encountered when studying flow over macro-roughness lies in the determination and the measuring of the flow depth. This is not without consequence since flow depth is the essential parameter for designing a safe stepped spillway, not only for the height of the training-walls but also for the size of the dissipation basin at the base of the chute.

For all regimes, both turbulence and aeration create a free surface that is difficult to define. Furthermore, the flow depth can be divided in several layers depending on the fluid structure. This complexity leads to the definition of different flow depths which characterize the flow behaviour.

9.2.1 Zoom on the side view of the mixture flow

For nappe flow regime, it is quite impossible to define the flow depth since it is a free-falling nappe, not homogeneous over the flume width.

However, for transition and skimming regimes, Pegram et al. (1999) gave a good detailed description of a cross section of the flow between two step outer edges. Over the pseudo-bottom, flow layer is quite comparable to the description given for the smooth spillway of the Aviemore dam (Waitaki river, New Zealand, [Cain (1978)]). Both divide the flow cross section into three layers as illustrated in Figure 9.2.

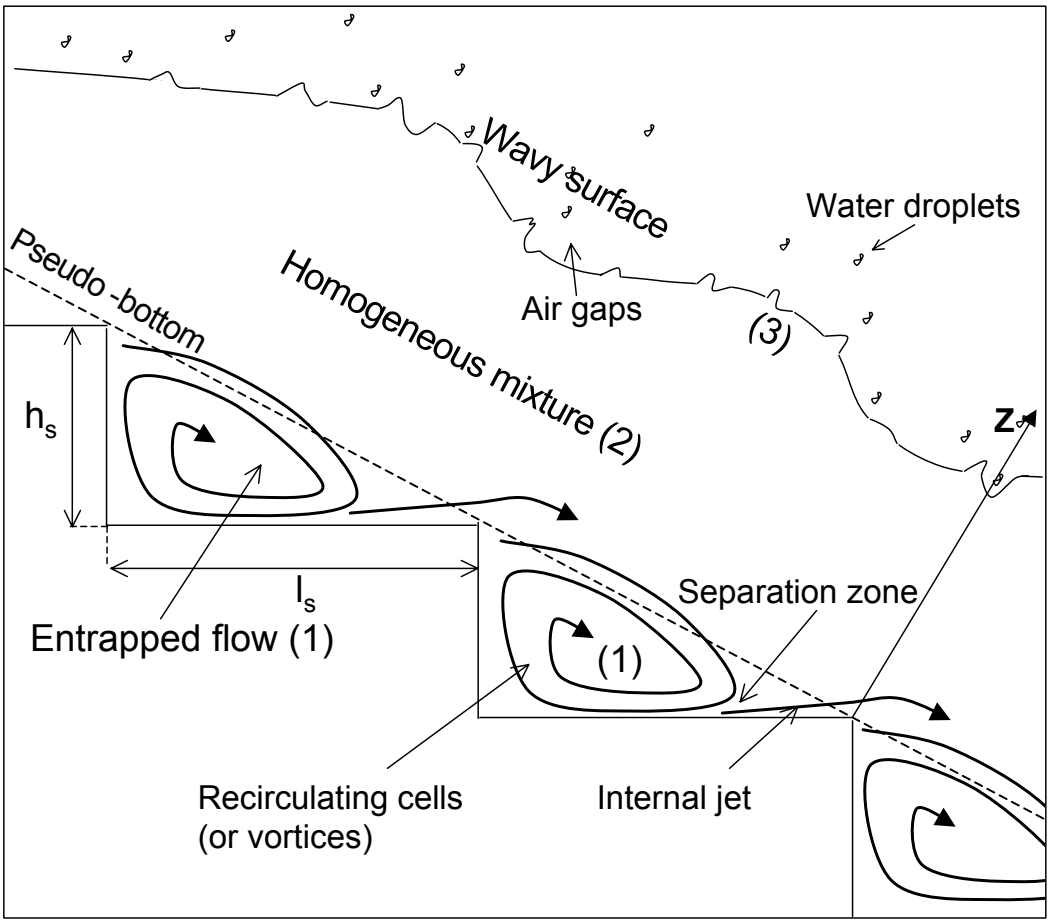

Figure 9.2: Schematic cross section of the skimming flow over a stepped chute

(1) Below pseudo-bottom layer :

Below the pseudo-bottom, slightly aerated water is trapped inside the steps. Depending on the discharge, a circulation flow is developed. The resulting triangular shaped vortices are spread over almost the whole step length and the whole step height. The water is ejected back in the principal flow through internal jets, transverse to the mean flow direction. That creates a flow exchange through the pseudo-bottom. On the horizontal step face, a separation zone is created between this vortex and the jet.

(2) Homogeneous skimming layer :

This layer close to the step is characterized by an homogeneous air-water mixture fluid flowing down parallel to the mean slope. It contains air bubbles with a size ranging from 0.5 to 3 mm. The mean air concentration in this layer remains as high as 0.5 [Cain (1978), Chanson & Toombes (2001b)].

(3) Rough water surface layer :

This layer, far from the pseudo-bottom, is characterized with a mixture of droplets of water with various size which travel through the air as well as air gaps between two consecutive waves. The high air concentration in this layer can be also attributed to the

presence of large air bubbles in the water (up to 10-20 mm in prototypes).

The two last layers are separated by a continuous surface according to Pegram et al. (1999) named as the free surface. The later is characterized by an irregular and turbulent wavy interface that is not well defined as already seen in Figure 8.3.

Based on this description, the three commonly techniques used to estimate the different characteristic flow depths are described in the following.

9.2.2 Direct method of estimation

With the direct method, the depth is measured in the flowing fluid along the chute. Three methods can be distinguished.

- *The normal mixture air-water flow depth*, $Z_m = Z_{obs}$ is measured either by a point gauge or with an electrode instrumentation such as the probe developed by Killen (1968). The electrodes are connected when the tip is in contact with water. This mixture depth can also be estimated by measurements on photos taken with high velocity camera or video [Chamani (2000), Sánchez-Juny, Pomares & Dolz (2000)].
  Any of the measurements based on visual observations are not very accurate since it is difficult to estimate the location of the free surface of the flow in this sparkling mixture. In addition, due to the viscosity and surface tension stress effects, the flow depth observed at the side-wall is slightly higher than in the chute axis.

- *The normal mixture and equivalent clear water depths* are estimated from air concentration profile measurements. This method is an extrapolation of the definition applied for aerated flow over smooth spillways, developed in particular by Cain (1978) and Wood (1991).

  Flow mixture depth, $Z_m = Z_{90}$ is characterized by the depth of the flow where the air concentration attains $c = 90\%$.

  Clear water depth, Z_w (see Figure 8.3) represents the equivalence of pure water (subscript w) of the mixture flow depth and is defined by Eq. 9.12.

$$Z_w = \int_0^{Z_m} (1 - c) dz = (1 - C) Z_{90} \tag{9.12}$$

  where z is measured perpendicular to the pseudo-bottom and c and C are respectively the local and mean air concentrations.

- *The mixture flow depth* is based on the velocity vertical profile as it was investigated by Tozzi (1994). In this case, the flow depth Z_v corresponds to the point where the local longitudinal velocity is maximum and above which the velocity remains constant. Above this limit, the velocities measured with a Pitot tube in the high air content flow layer are not accurate.

Finally, the mixture flow depth considered by Pegram et al. (1999) does not correspond to height at 90 % of air concentration but to a lower concentration in the range of 70 % to 80 %.

9.2.3 Indirect method of estimation

The mixture or clear water flow depth is estimated indirectly from the measured sequent depths of a hydraulic jump forced in a stilling basin at the base of the chute. This method assumes that the flow depth at the downstream end of the slope is equal to the upstream sequent depth of the hydraulic jump. Diez-Cascon et al. (1991), Tozzi (1994), Pegram et al. (1999), Boes (2000a) and Yasuda & Ohtsu (2000) have applied this method for their model studies in stepped chutes.

The principle consists in measuring the downstream sequent depth, Y_2 (subscript 2 for the downstream cross section of the jump) in the non-aerated tailwater of the hydraulic jump to estimate the upstream sequent depth Y_1 , from the mass and momentum conservation equations. A schematic view of hydraulic jump is given in Figure 9.3.

In order to simplify the calculation, it is normally assumed that:

- a hydrostatic pressure distribution and an uniform velocity distribution, upstream and downstream of the hydraulic jump,
- a negligible wall friction
- no effect of density of the incoming aerated flow then:
  $\rho_1 \simeq \rho_2 = \rho_w$, with ρ_w the density of the water.

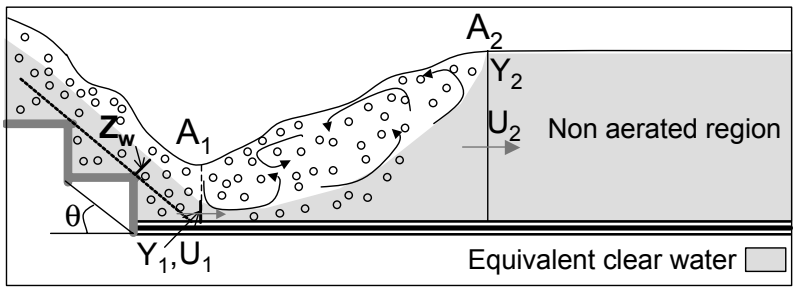

Figure 9.3: Schematic side view of a hydraulic jump at the base of a stepped chute

Then the following simplified conservation equations can be applied at the upstream and downstream section of the jump, A_1 and A_2:

Momentum conservation :

$$\rho_1 \frac{q_w^2}{gY_1} + \rho_1 \frac{Y_1^2}{2} = \rho_2 \frac{q_w^2}{gY_2} + \rho_2 \frac{Y_2^2}{2} \tag{9.13}$$

Mass conservation

$$\rho_1 U_1 Y_1 = \rho_2 U_2 Y_2 \tag{9.14}$$

Continuity

$$q_w = U_1 Y_1 = U_2 Y_2 \tag{9.15}$$

where $U_{1,2}$ are the mean velocities of the flow.

After simplification, these equations yield to:

$$Y_1^2 + Y_1 Y_2 - 2Y_2 \frac{U_2^2}{g} = 0 \tag{9.16}$$

and the solution Y_1 is given by:

$$Y_1 = \frac{Y_2}{2}(\sqrt{1 + 8Fr_2^2} - 1) \tag{9.17}$$

with $Fr_2^2 = \frac{q_w^2}{gY_2^3}$, the Froude number of the downstream section.

Assuming that the local head losses where the flow turns from the slopping chute to the stilling basin are not significant, then the clear water depth at the toe of the chute is derived from $Z_w = Y_1$.

Though this method is an reasonable alternative for estimating the depth without encountering the difficulty of measuring the very aerated, turbulent and wavy fluid surface, it is limited since it only provides the local depth at the toe of the chute.

9.2.4 Uniform flow depth

When the fully developed flow conditions are attained, from one step cross section to the other, both mixture and equivalent clear water depths remain constant. Recently, Boes & Hager (2003b) proposed an empirical relationship to determine these depths for any discharges and slopes between 26^o to 50^o (Eq. 9.18, Eq. 9.19).

Mixture normal depth

$$\frac{Z_{90,u}}{h_s} = 0.50 F_s^{(0.1 \tan\theta + 0.5)} \tag{9.18}$$

where $F_s = q_w / \sqrt{g \sin\theta h_s^3}$ is the step Froude number and h_s the height of the step.

Equivalent normal clear water depth

$$\frac{Z_{w,u}}{h_c} = 0.215 (\sin\theta)^{-1/3} \tag{9.19}$$

with $h_c = \sqrt[3]{q_w^2/g}$ the critical flow depth. It is surprising to note that according to Boes the equivalent clear water in the uniform region varies only with the chute slope and the discharge, independently of the height of the steps. It will be discussed in the Part IV, Chapter 14.2.

9.3 Flow velocity

According the literature review, the measurement of the flow velocity concerns only the longitudinal component, parallel to the mean slope. Double fiber-optical [Boes & Hager (1998), Matos, Frizell, André & Frizell (2002)] and double-tip conductivity probe [Chanson (1995)] are at the moment the more efficient intrusive instrumentation to measure the mixture flow velocity. In fact the often used Prandtl tube [Chamani & Rajaratnam (1999)] or back-flushing Pitot tube [Frizell, Ehler & Mefford (1994), Matos (2000a)] are limited to low aerated flow *i.e.* for air concentration lower than 0.7. In addition, new Particule Image Velocimetry (PIV) techniques [Amador, Tembleque, Sánchez-Juny, Puertas & Dolz (2002)] which would allow to measure all the 3 components of the flow velocity are not yet available for aerated flow.

9.3.1 Vertical distribution of the flow velocity

In light of the above, the following concerns the longitudinal component velocity u_m of the air-water mixture flow for skimming flow.

Logarithmic law distribution

In analogy with the studies of uniform turbulent rough flow for steep gravel beds in mountain streams, a few authors [Sayre & Albertson (1963), Chamani & Rajaratnam (1999)] suggested that above the pseudo-bottom, the homogeneous air-water flow (layer (2) in Figure 9.2) agrees with the rough boundary layer theory. However, because of the high relative roughness of the steps, the 3D pattern of the macro-turbulence structures as well as the drag around the steps, the classical logarithmic equation as proposed by Karman-Prandtl (Eq. 9.20) is not fully applicable.

$$\frac{u(z)}{\sqrt{\tau_0/\rho_w}} = \frac{2.30}{\kappa} log\left(\frac{z}{k}\right) + C1 \tag{9.20}$$

in which κ is the von Kármán turbulence constant determined experimentally between 0.40 and 0.42, $C1$ an integration constant, k the equivalent roughness size and $\tau_0 = \rho_w g S_f R_h$ the shear stress at the boundary, with S_f the slope of energy gradient and R_h the hydraulic radius.

Nevertheless, it could be used when properly fitting the constants A and B (Eq. 9.21) by the experimental data.

$$\frac{u_m(z)}{\sqrt{\tau_0/\rho_m}} = Alog\left(\frac{z*}{k_s}\right) + B \tag{9.21}$$

where ρ_m and u_m are respectively the density and velocity of the mixture flow, $z* = z + k_s$ where $k_s = h_s \cos\theta$ the normal height.

- For skimming flow regime over a 30^o stepped chute and for $z/Z_{90} < 0.7$, Chamani & Rajaratnam (1999) found $A = 5.75$ and $B = 8.5$.

- In the particular case of rectangular sheet baffles over a very flat slopping chute, Sayre & Albertson (1963) established that $A = 6.06$ and $B = 2.6$ but with k_s substituted by a roughness parameter $\psi = \frac{h_r b_r}{x_r(e_r + b_r)}$. This parameter takes into account not only the baffles height h_r but also their spatial pattern with b_r, e_r and x_r respectively the width of the baffles and the transversal and longitudinal space between two baffles. It should be noted that in this case the fluid was not aerated.

Power law distribution

Nevertheless, most of the researchers proposed that above the pseudo-bottom the local mixture velocity depends, as for smooth chutes, on the maximum velocity and that the velocity distribution of the quasi-1D flow in the skimming layer follows a power law given by Equation 9.22:

$$U_{90} = DH_{90}^{1/N} \tag{9.22}$$

in which $U_{90} = \frac{u_m(z)}{u_{90}}$, is the dimensionless mixture flow velocity and $H_{90} = \frac{z}{Z_{90}}$ the dimensionless mixture flow depth. D and N are coefficients obtained from experiments.

The exponent N is shown slightly affected by the slope [Boes & Hager (2003a)]. However, depending on the tested discharges or on the portion of flow layer considered in the empirical fitting, several power laws have been proposed with different coefficients:

- Chanson (2001) proposed that $D = 1$ and $N = 5$ to $N = 6$ for skimming flow over stepped chute without limiting the flow layer.
- Based on the Chamani & Rajaratnam (1999) data for a 30^o slope, Boes (2000b) suggested $D = 1$ and $N = 6.3$ for $0.04 \leq H_{90} \leq 0.5$.
- For their own experiments, Boes & Hager (2003a) found that for $26^o \leq \theta \leq 55^o$, $U_{90} = 1.05 H_{90}^{1/4.3}$ with $0.04 \leq H_{90} \leq 0.8$.
- This above result is greatly different from the values of Yasuda & Chanson (2003) who founded $N = 9$ for $0.05 \leq H_{90} \leq 1$ and a 15.6^o slope.

These experimental studies did not define the limiting values of H_{90} (minimum and maximum) to determine the flow layer which follows the power law.

The influence of the step height on the power law coefficients was not investigated.

9.3.2 Mean velocity

Based on the continuity equation, the mean velocity of the equivalent clear water flow is defined as:

$$U_w = \frac{q_w}{Z_w} \tag{9.23}$$

This definition assumes an uniform distribution of the velocity which is not accurate regarding the measured velocity profiles. In doing so, there is a tendency to over-estimate the flow velocity.

Another definition of the velocity could be directly derived from the velocity profile:

$$U_m = \frac{1}{Z_{90}} \int_0^{Z_{90}} u_m(z) dz \tag{9.24}$$

In this case, the air-water mixture flow velocity is considered.

Chapter 10

Energy dissipation efficiency of the macro-roughness overlays

10.1 Methods for energy dissipation estimation

The amount of residual energy at the base of the structure is of special interest for the design of toe protections such as stilling bassin. Then, a particular attention must be focused on the validity and accuracy of the residual energy and dissipation rate estimation for aerated flows over steeped chutes.
In this context, different methods of estimating the energy dissipation can be found in the literature:

- "Direct" methods:
  - Estimation of the residual specific energy at a given level on the slope by using the Bernoulli equation. This method involves air concentration and flow depth measurements.
  - Estimation of the specific energy of the flow at any position of the slope from the friction and drag coefficients [Tozzi (1994), Boes & Hager (2003b)].
- "Indirect" method which consists in measuring the sequent depths of the hydraulic jump formed at the toe of the chute [Diez-Cascon et al. (1991), Tozzi (1994), Pegram et al. (1999)].

10.1.1 Direct methods

Nappe flow regime

For the nappe regime, due to the unstable structure of the flow, few assessments were made to estimate the residual energy. However, Chanson (1994a) proposed an analytical relationship to estimate the residual energy $H_{r,NF}$ at the toe of a chute, Equation 10.1, only valid for nappe flow with fully developed hydraulic jump (isolated nappe flow):

$$\frac{H_{r,NF}}{H_0} = \frac{0.54(\frac{h_c}{h_s})^{0.275} + \frac{3.43}{2}(\frac{h_c}{h_s})^{-0.55}}{\frac{3}{2} + \frac{H_D}{h_c}} \tag{10.1}$$

with, H_0 the head at the chute crest and h_c the critical flow depth at the crest.

Chamani & Rajaratnam (1994) proposed a more general relationship (for all kind of nappe flows) based on the estimation of the averaged energy loss per step. At the toe of the chute, the residual energy is given by:

$$H_{r,NF} = (1-\varepsilon)^{N_s}(h_s + 1.5h_c) + h_s\Sigma_{i=1}^{N_s-1}(1-\varepsilon)^i \tag{10.2}$$

where N_s is the total number of steps, and $8 \leq N_s \leq 30$, $0.03\ m \leq h_s \leq 0.45\ m$, and $0.421 \leq h_s/l_s \leq 0.842$. ε represents the proportion of energy lost on each step. This formula is fitted to the experimental data of Essery & Horner (1978):

$$\varepsilon = [0.30 - 0.35(\frac{h_s}{l_s})] - [0.54 + 0.27(\frac{h_s}{l_s})]\log(h_c/h_s) \tag{10.3}$$

Skimming flow regime

For this regime, the residual energy is considered at the step edge corner where the mixture flow is quasi-unidirectional and thus easier to measure.

♢ *Residual specific energy*

The residual specific energy is given by the total head at the last step outer edge of the flume. It is based on the general energy equation for a fluid with mean velocity U through a cross section A:

$$\frac{1}{UA}\int\int_A \left(\rho\frac{U^2}{2} + p(z) + \rho g z\right) u(z) dA \tag{10.4}$$

where $u(z)$ is the velocity component normal to A, z is the normal position and $p(z)$ is the pressure at the point z.

At the step outer edge, the fluid is assumed non-compressible with a mean density $\rho_m = (1 - C)\rho_w$ with ρ_w the water density. A hydrostatic pressure distribution and uniform flow conditions are assumed. Therefore, the specific energy $H_{Y,u}$ at a level Y above the base of the chute is derived from Equation 10.5:

$$H_{Y,u} = Y + Z_w \cos\theta + \frac{\alpha q_w^2}{2g Z_w^2} \tag{10.5}$$

with Z_w the equivalent clear water depth and $\alpha \simeq 1.1$, a kinetic energy correction factor that takes into account the non-uniform velocity distribution. Therefore, at the toe of the chute, the residual energy $H_{r,w}$ is given by:

$$H_{r,w} = Z_w \cos\theta + \frac{\alpha q_w^2}{2g Z_w^2} \tag{10.6}$$

Some authors [Tozzi (1994), Chamani & Rajaratnam (1999)] considered the mixture flow parameters (Z_{90} and U_m) instead of the clear water values in Equation 10.6:

$$H_{r,SF} = Z_{90} \cos\theta + \frac{U_m^2}{2g} \tag{10.7}$$

♢ *Residual energy based on the friction coefficient*

Some authors [Chanson (1994b), Boes & Hager (2003b)] estimated the relative energy loss in the uniform region $\Delta H_u/H_0$ for a chute of total drop H_D and with an initial head at the crest H_0 :

$$\frac{\Delta H_u}{H_0} = 1 - \frac{\left(\frac{f}{8\sin\theta}\right)^{1/3}\cos\theta + \frac{\alpha}{2}\left(\frac{f}{8\sin\theta}\right)^{-2/3}}{\frac{H_D}{h_c} + \frac{2}{3}} \tag{10.8}$$

with f the friction factor.

Recently, for non-uniform flow conditions, Boes & Hager (2003b) proposed for $20° \leq \theta \leq 50°$ and $H_D/h_c < 15 - 20$ an estimation of the relative residual energy $H_{r,w}/H_0$ using Equation 10.9

$$\frac{H_{r,w}}{H_0} = \exp\left[\left(-0.045(\frac{k_s}{D_{h,w}})^{0.1}(\sin\theta)^{-0.8}\right)\frac{H_D}{h_c}\right] \tag{10.9}$$

with $D_{h,w}$ the hydraulic diameter.

Transition flow regime

No formula was found to estimate the energy dissipation for this regime which combines characteristics of nappe and skimming flows.

10.1.2 Indirect methods

Global energy dissipation can be estimated by the so-called "indirect" method. It consists in measuring the sequent depths of the hydraulic jump formed at the toe of the chute (see above paragraph 9.2.3). This method, already applied by several researchers [Diez-Cascon et al. (1991), Pegram et al. (1999), Yasuda & Chanson (2003)] is an adequate alternative for estimating the residual energy without encountering the difficulty of defining a representative depth for the aerated wavy flow.

A schematic side view of the hydraulic jump at the toe of the stepped flume is given in Figure 9.3.
Assuming:

- a hydrostatic pressure distribution upstream of the hydraulic jump,
- a negligible wall friction,
- no significative head loss when the flow turns from the stepped chute to the basin

the residual energy at the toe of the chute, H_{r1} is given by:

$$H_{r1} = Y_1 + \frac{\alpha q_w^2}{2gY_1^2} \tag{10.10}$$

with Y_1 the upstream sequent depth of the hydraulic jump and α, the kinetic correction coefficient to take into account the uneven vertical velocity distribution. For turbulent flow, generally, $\alpha \simeq 1.1$.

The upstream sequent depth Y_1 is computed based on the momentum conservation at the upstream and downstream cross section of the hydraulic jump (see Figure 9.3). Most of the authors neglect the effect of the density of the incoming aerated flow in the basin ($\rho_1 = \rho_2 = \rho_w$). Y_1 is thus computed according to Equation 9.17.

Finally, the energy dissipation is given by:

$$\frac{\Delta H}{H_0} = \frac{H_0 - H_{r1}}{H_0} \tag{10.11}$$

where $H_0 = H_D + \frac{2}{3}h_c$ is the total energy head at the crest of the dam with H_D the total drop height of the structure and h_c the critical depth at the crest.

Although this method avoids the measurement of the aerated flow depth or velocity, it is nevertheless quite complex. The resulting residual energy is strongly influenced by the location of the hydraulic jump and by the accuracy of the measurement of the downstream sequent depth Y_2. As highlighted by Pegram et al. (1999), H_{r1} varies approximately with the fourth power of Y_2. According to Diez-Cascon et al. (1991) and Pegram et al. (1999), the upstream limit of the hydraulic jump should be located as close as possible but not drowning the last step.

10.1.3 Comparison of methods

Unfortunately, only very few authors have performed comparison tests between these different methods of estimation of the residual energy. Among them, Tozzi (1994) found a maximum difference of 15 % between the residual specific energy $H_{r,SF}$ at the toe of the flume and the result in the basin H_{r1}.
In any case, it is obvious that $H_{r1} \leq H_{r,SF}$ due to the local head loss at the chute/basin transition. Since some authors used the clear water flow parameters, others used mixture flow values or the indirect method, the results of relative residual energy are scattered even for similar stepped spillway models. Therefore, different methods for energy dissipation estimation are compared in details in Part IV (Chapter 15).

10.2 Significant parameter for the energy dissipation process

From previous experimental studies it was suggested that the energy dissipation rate is depending on:

- the number of steps (N_s),
- the slope (θ),
- the regime of the flow,
- the relative critical depth (H_D/h_c) where H_D is the total drop height of the structure.

10.2.1 Flow regimes

Most of the authors agree that, depending on the flow regime, the energy of the flow is mainly dissipated:

Nappe flow :
through jet break-up in the air, jet impact on the horizontal step face as well as by the eventually partially or fully developed hydraulic jump. This regime is found the most dissipative.

Skimming flow :
by the development of the recirculating cells under the skimming layer, by the shear stress between the recirculating cells and the skimming layer and by the friction at the interface cells/horizontal-vertical step faces.

The transition regime has not been the subject of profound assessment. Because it follows both characteristics of nappe and skimming flow, researchers have assumed that the resulting head losses are a mixture of shear stress due to the not well-developed vortices and due to the impact of jet.

A study of stepped chute filled with triangular fillets inside the step cavity showed that the elimination or attenuation of the recirculating vortices do not reduce significantly the energy dissipation [Ahmann & Zapel (2000)]. Similar experiments were performed recently by Yasuda & Ohtsu (2003). These lead to the same results: the energy loss of skimming flow is independent of the step-cavity area. It has to be noted that the energy dissipation

was estimated in both studies by the hydraulic jump method. The schematic position of the hydraulic jump indicated that it is located quite downstream of the toe of the last step. For this reason, the negligible difference between the residual energy with or without recirculating cells could also be affected by the position of the jump. Therefore, the affirmation of the non-effect of the recirculating cells is not so obvious and is discussed in Part IV.

10.2.2 Number of steps and step height effects

Yasuda & Ohtsu (2000) measured the shortening of the hydraulic jump at the toe of a slopped chute due to the stepped linings. They noticed that the height of the steps has no significant effect on the length of the hydraulic jump region which bears indirectly on the energy dissipation rate. Boes & Minor (2000) also concluded about the negligible effect of step height in the energy dissipation efficiency.

The comparison of same slopping stepped chutes but with different number of steps shows that the energy dissipation is higher with a smaller number of steps for nappe flow regime.

10.2.3 Slope effect

Experimental results [Peruginelli & Pagliara (2000)] show that the effect of the slope is inverse, depending on the flow regimes: for nappe flow, the relative energy dissipation increases for flatter slopes while for skimming regime, it increases for steeper slopes. This result is however opposite to that by Fratino & Piccinni (2000) who measured better dissipation efficiency for the flatter slopes, for transition and skimming flows.

10.2.4 Macro-roughness elements fixed on steps

Most of the previous studies focused on the flow behaviour over conventional steps. Very few results concerned the effect of additional macro-roughness elements and their optimization. One of the most relevant were tests by Peruginelli & Pagliara (2000) who compare the energy dissipation of the same chute (1V:2H) with the same number of steps. However, either all steps are covered with an additional carpet of plastic grass or they are equipped with endsills. The results highlight that:

- For nappe flow, the endsills increase the energy dissipation rate in almost the same order of magnitude than with the steps covered with carpet. There is no significant difference if the whole steps or only the horizontal face are covering.
- For skimming flow, endsills or carpet have a negligible effect on the energy dissipation.

Sayre & Albertson (1963) studied the influence on flow resistance of rectangular alternate baffles along a very low slope. The tests were performed for several distributions and sizes of the sheet baffles but with non aerated flows. Their results concluded that the energy dissipation was greatly influenced by the density of distribution and the orientation of the macro-roughness elements. However, in agreement with numerous other researchers, they found that the height of the baffles had only little influence on the head losses.

Part IV

Experimental study of aerated flow over macro-roughness

Chapter 11

Experimental installation and test procedure

Because of the complexity of the flow (bi-phase air-water structure and high turbulence) and the great number of parameters which characterize the flow behaviour and which contribute to the energy loss, experimental study in a laboratory model has seemed to be an appropriate and suitable way to reach the goals of the project.

11.1 Experimental facility

The experimental tests were conducted in a steep stepped flume assembled at the hydraulic laboratory of LCH-EPFL (Figure 11.1). The downstream end of the facility lies on a trolley that permits a horizontal movement of the flume in order to adjust to slope changes of up to $60°$.
The chute consists of four modules of $2\,m$ long and $0.5\,m$ wide (B_f) with acrylic sidewall of $0.6\,m$ high to allow the visual observation of the flow. The flow runs over a section of $7.68\,m$ long (L_f).

An electromagnetic flow meter regulates the water discharge (Q_w) distributed by a feed pipe set in the axis of the flume that insures a uniform lateral distribution of the incoming flow. The maximal unit discharge (q_w) provided by the supply pump was up to $0.28\,m^2/s$ with a precision of about $\pm 0.005\,m^2/s$. Thus, the scale of tested discharges covers the three flow regimes, namely the nappe, transition and skimming flows (see chapter 8.1).

Tested slopes

The final aim of the research was to define macro-roughness overlays in order to rehabilitate and protect potential overtopped embankment dams. The review of existing projects [McLean & Hansen (2000), Matos (2002)] reveals that the most common slopes of such structures are 2:1 (26.6^o) and 3:1 (18.4^o), with a slight occurrence of other slopes. Then, in order to cover the range of embankment inclined chutes the experimental study focuses on the two limit slopes $\theta = 30^o$ ($\simeq 1.7:1$) and $\theta = 18.6^o$ ($\simeq 3:1$).

Height of the steps

The height of the step has been considered as the limitation parameter regarding the length scale of the model. Considering the step heights commonly found on prototypes, namely 0.30 to $0.60\,m$ for embankment dams or 0.60 to $0.90\,m$ for RCC dams [Ditchey & Campbell (2000)] and to conserve a relatively small scale factor, lower than 1:15 for scale effect consideration (see paragraphe 11.3), the height of the step (h_s) was fixed at $0.06\,m$. The normal height of the step ($k_s = h_s \cos\theta$), defined as the step height perpendicular to the mean flow direction that is normal to the pseudo-bottom depends on the chute slope.

As mentioned in paragraph 10.2, the height of the step has been the subject of previous studies which showed that this parameter has a negligible effect on the energy dissipation rate. However, recirculating cells inside the step have been identified as a significative source of energy dissipation.
Based on these results, it has been decided to conserve the same step height for the two tested slopes but to vary their length (l_s) in order to modify the size of the vortices and to assess their effect. This choice means also to have a different number of steps (N_s) from one slope to the other which could also have an effect on the energy dissipation.

Finally, the bottom of the chute consists of aluminium steps which can be fitted with PVC

macro-roughness elements of the following sizes:

30^o **inclined chute** :
$N_s = 64$ steps, $h_s = 0.06\,m$, $k_s = 0.052\,m$ and $l_s = 0.104\,m$, with a chute height of $H_f = 3.85\,m$

18.6^o **inclined chute** :
$N_s = 42$ steps, $h_s = 0.06\,m$, $k_s = 0.057\,m$ and $l_s = 0.178\,m$, with a chute height of $H_f = 2.45\,m$

The stepped bottom formed with conventional rectangular steps is considered as a reference bottom for comparison. Steps are also equipped with different macro-roughness elements to understand the flow behaviour and to improve the efficiency of the protection overlays.

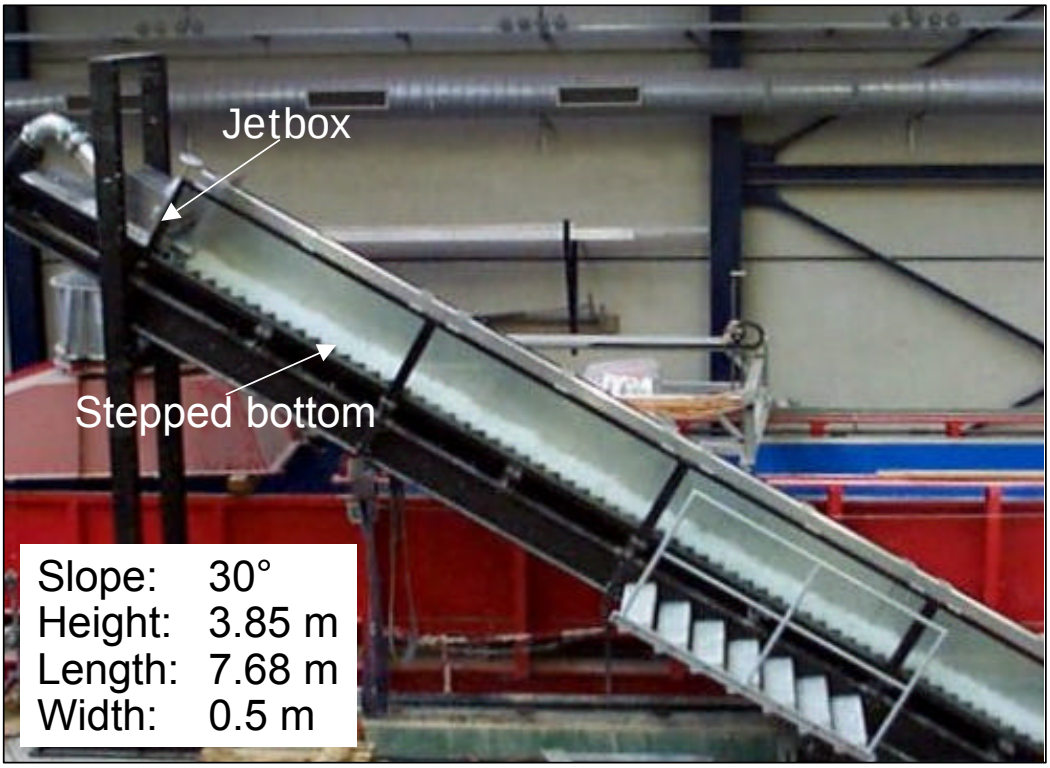

Figure 11.1: Stepped steep flume assembled at the LCH-EPFL for $\theta = 30^o$

11.1.1 Entrance condition: jetbox

In contrary to the most embankment dams which are equipped with either ogee or broad crested weirs, the entrance conditions of the chute model consists in a jetbox. This later was developed by Schwalt & Hager (1992). It transforms the high velocity pressurized approach flow to a free surface flow. The flow is then supercritical at the entrance of the chute, without passing through critical depth.

The opening of the jetbox, h_0, up to $18\,cm$, allows the approach Froude number, $F_0 = q_w/\sqrt{g\cos\theta h_0^3}$ (where g=acceleration of gravity) to be controlled, and to ensure a homogeneous velocity and depth distribution over the width of the flume. For high discharges, the jetbox cushions pressure fluctuations of the pump.
In addition, the jetbox is very useful in case of flumes in laboratory that is often limited in length. In fact, it shifts the onset of air entrainment upstream and shortens the transition (or developing) region of the flow. As a consequence, in contrast to some existing other models of stepped chute, fully developed flow conditions were reached for all step geometries and for the highest tested discharge.

11.1.2 Stilling basin at the toe of the chute

The amount of the residual energy at the base of the structure is important to design the toe protection such as stilling basins. Particular attention is focused on the validity and accuracy of the residual energy and dissipation assessment for the tested macro-roughness slopes. Therefore, three different methods of energy estimation were tested and confirmed.

A stilling rectangular and horizontal basin of width $B_{ba} = 0.5\,m$ was fixed at the toe of the stepped flume, at the base of the last step (see the schematic view in Figure 11.2) to use the "indirect method" (see chapter 10.1). Local head losses were minimized where the flow turns from the stepped flume to the basin: $B_{ba} = B_f$ (no contraction effect) and there is no sharp change of direction of the flow.

For both inclined chutes, at the downstream end of the $6\,m$ long basin (L_{ba}) with $1\,m$ high training-walls (H_{ba}), an adjustable gate allows a hydraulic jump to be formed at the toe of the stepped flume (Fig. 11.2).
It is important to note that the accuracy of this method to estimate the energy dissipation depends on the position of the hydraulic jump compared to the toe of the flow runs. A sensitivity study on the effect of this position is described in Chapter 15. Based on preliminary tests and according to Diez-Cascon et al. (1991) and Pegram et al. (1999), it has been concluded that the upstream limit of the hydraulic jump should be located as close as possible but not submerging the last step, just at the intersection of the flow impact with the horizontal bottom of the bassin as shown in Figure 11.2. Hence with this present facility, the residual energy has been estimated indirectly by measuring the downstream sequent depth (Y_2) of the hydraulic jump.

11.1.3 Macro-roughness overlays

In light of the literature review, a solution to obtain an optimal efficiency to dissipate energy would be to design the steps to retain, as long as possible, the nappe flow regime. In fact, it has been measured that under nappe flow conditions, the quasi-total dissipation of the incoming head could be achieved. However, in most of the cases, limitations due to environment, due to structural points and due to the overflow characteristics ($i.e$ design discharge) render such a solution technically impossible.

Another ideal alternative would consist in reproducing conditions as observed in the mountain streams. The best efficiency for dissipating the energy of the torrents naturally is in the random distribution of rock boulders of different size and spacing. This is also confirmed by studies of flow over high gradient gravel bed, as Canovaro, Paris & Solari (2003) who observed that random distribution leads to greater values of drag induced shear stress. But obviously,

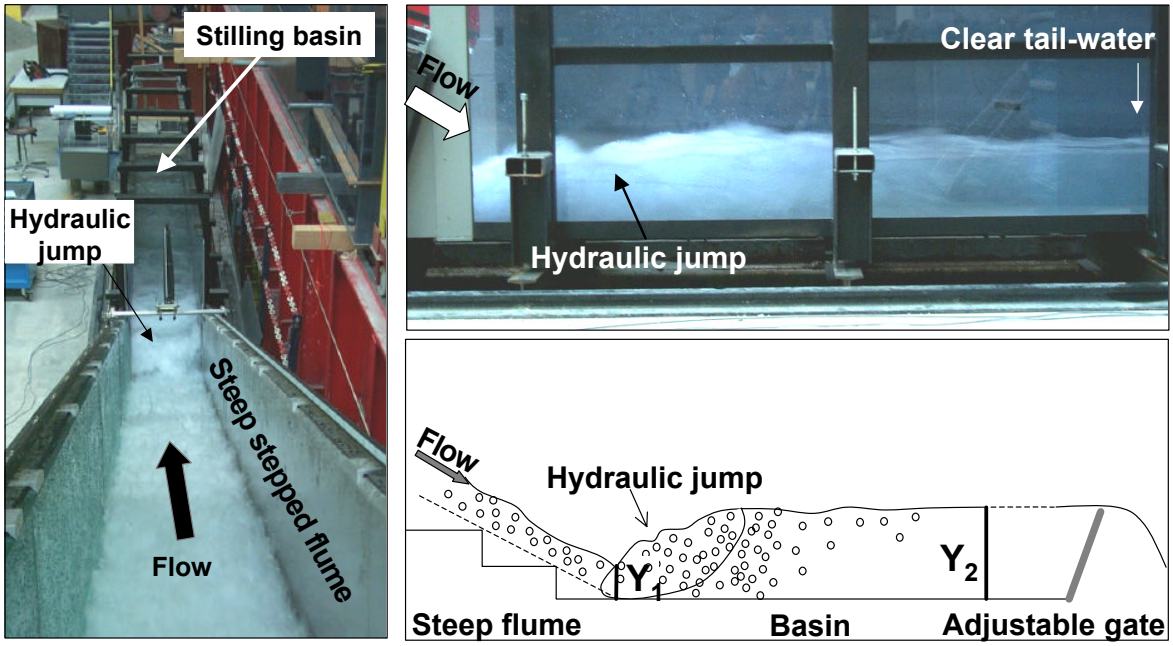

Figure 11.2: General view of the facility (left) and schematic side view of the rectangular stilling bassin along with a picture of wavy inclined jump (right) at the toe of the 30^o inclined chute

a random design is the contrary of what an engineer could expect to achieve technically and economically with normal construction techniques.

Therefore, rather simple configurations were tested in order to:

1. Understand the energy dissipation process
2. Delay the onset of skimming flow
3. Exploit to the maximum the friction and drag form created by the macro-roughness elements
4. Create different distribution of obstacles to the flow
5. Consider simple and realistic macro-roughness elements

This lead to the overlay configurations represented in Figures 11.3 and 11.4 and tested over the 30^o and 18.6^o inclined chutes.
The tested configurations have been firstly characterized with a simple dimensionless parameter (m) to represent the proportion of additional macro-roughness elements compared to the conventional rectangular steps as a reference:

$$m = \frac{number\ of\ macro - roughness\ elements}{number\ of\ steps} \tag{11.1}$$

The tested macro-roughness overlays have also been divided into two groups:

"2D-overlays" (Fig. 11.3.b, c, d) which consists in endsills fixed on the downstream of the horizontal face of all (m=1), every second (m=1/2) and every third (m=1/3) steps, over the entire width of the flume. Endsills are made of PVC, with 0.03 x 0.026 x 0.5 m dimensions. A chamfer at their upstream edge avoid sharp and sensible angle at the jet impact zone.

"3D-overlays" (Fig. 11.4.e, f, g) which consists in rectangular blocks with 0.03 x 0.026 x 0.05 m dimensions with also a chamfer edge, fixed with different spacings at the downstream of the horizontal face. Overlays are named in the following as spaced alternated blocks for m=4, aligned alternated blocks for m=5 and close-packed alternated blocks for m=6. To facilitate moving the blocks, they are fitted on a Velcro band of 0.026 m width of high resistance, attached at the downstream end of each step.

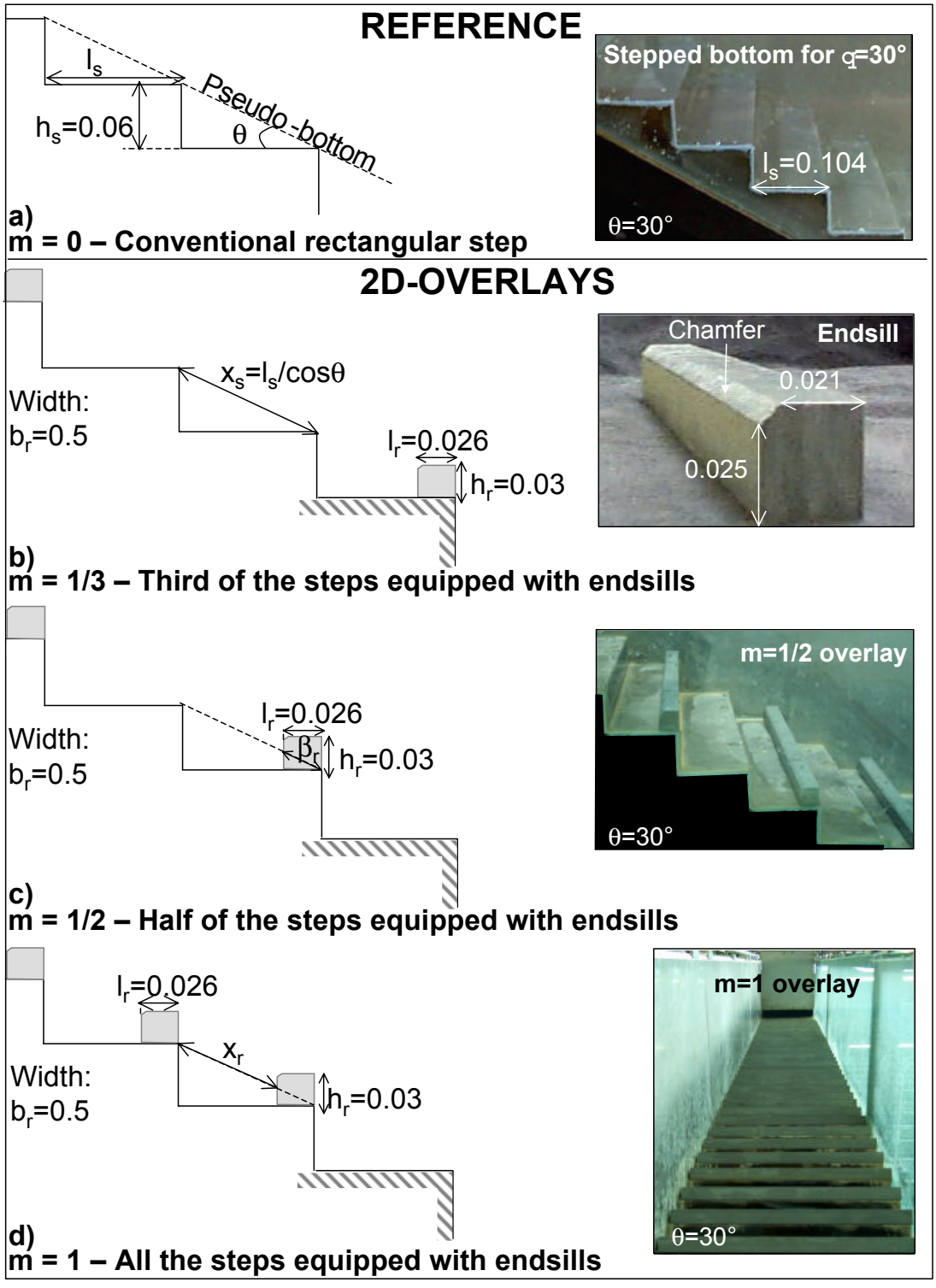

Figure 11.3: Sketch of the tested stepped macro-roughness overlays: conventional steps and steps equipped with endsills (dimensions in m)

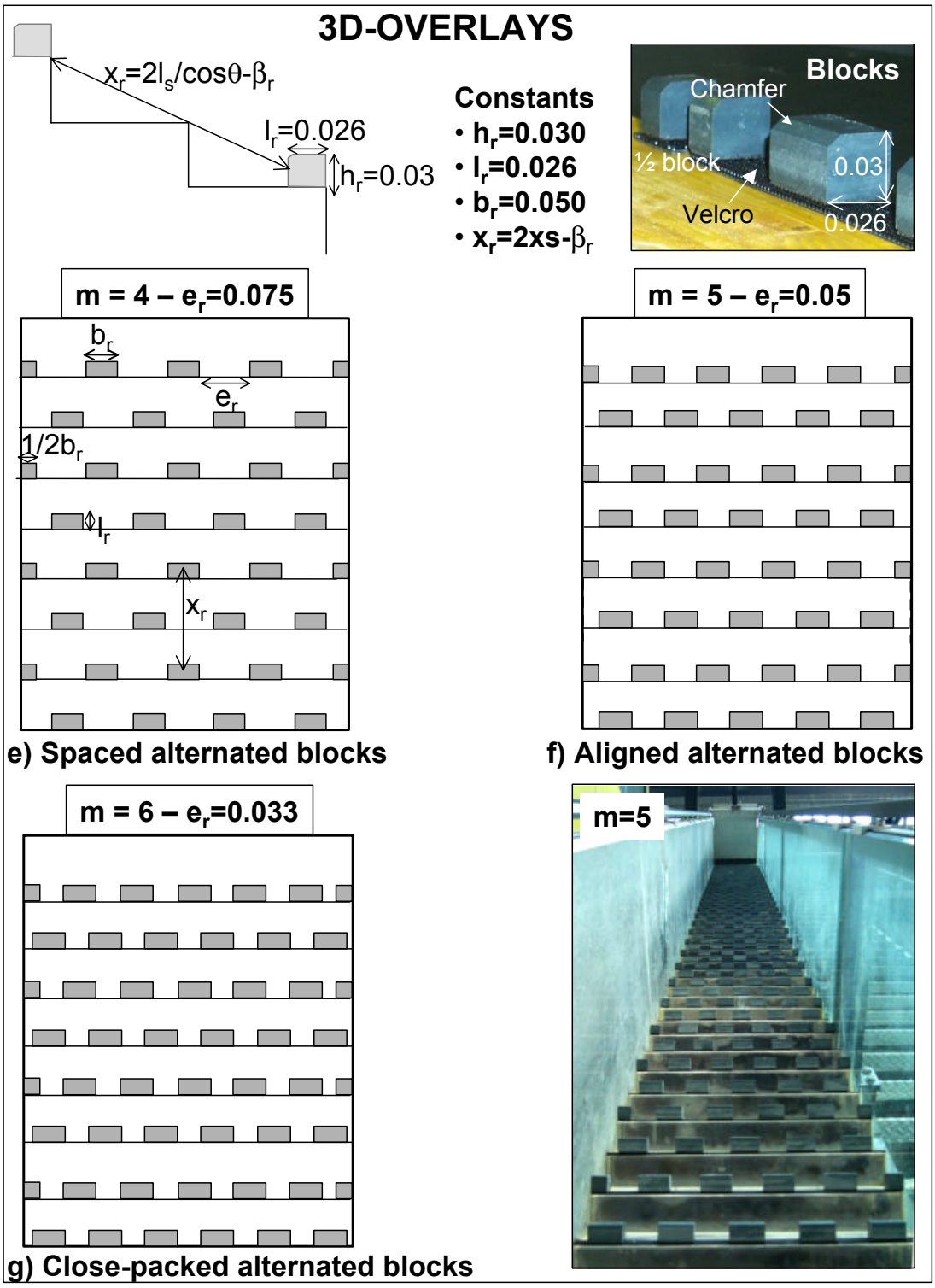

Figure 11.4: Sketch of the tested stepped macro-roughness overlays: steps equipped with rectangular blocks (dimensions in m)

In addition, to represent the macro-roughness pattern, a dimensionless parameter was defined that takes into account the elements distribution. Thus, a density of covering (d_r) is defined in Equation 11.2 as the ratio of the volume of the elements over the volume of the referencing steps,

$$d_r = \frac{N_r \forall_r}{N_s \forall_s} = m \frac{h_r b_r l_r}{h_s B_f l_s} \tag{11.2}$$

where $\forall_r$ and $\forall_s$ are respectively the occupation volume of the macro-roughness elements and the conventional steps. For the tested configurations, for all cases, ratios $h_r/h_s = 1/2$ and $l_r/l_s = 1/4$ are constant then:

$$d_r = \frac{m}{8} \frac{b_r}{B_f}$$

The overlays can be then classified according to their density, which gives the following scheme, Figure 11.5.

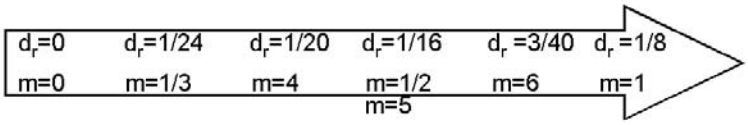

Figure 11.5: Classification of the macro-roughness overlays according to their density

A relevant study of roughness spacing of rigid baffles fixed in open channel with very low slope [Sayre & Albertson (1963)] defined a roughness density ratio (ψ) taking into account the shape and geometry as well as the distribution of the elements, defined according to Equation 11.3:

$$\psi = \frac{h_r b_r}{x_r (e_r + b_r)} \tag{11.3}$$

This definition gives rise to the same classification of the macro-roughness overlays.

In the following, it will be shown that the efficiency of the overlays is obviously not related to the density parameters such as d_r, ψ or the normal height of the roughness element k_r. A dimensionless parameter that is a function of the roughness pattern and of some other drag from parameters induced by the elements needs to be defined. This parameter would represent a characteristic effective roughness *i.e* one that really contributes to the friction and singular head losses of the flow (see chapter 16.3).

11.2 Measuring instrumentation

In order to characterize and define the hydraulic behaviour of the air-water mixture flow as well as the head losses along the slope, a set of relevant flow parameters are required. They can be measured directly in the flow but without disturbing the fluid structure. In this regard, the experimental tests involved:

1. Assessment of the flow two-phase structure and the flow resistance: air concentration, bubble sizes, characteristic flow depths and longitudinal flow velocity. These parameters have been measured at several cross sections along the slope by an optical-fiber probe described in paragraph 11.2.1.

2. Calculation of the surface forces applied to a control volume formed by steps, to estimate the forces on the macro-roughness elements and to observe the sensible zones. This can be achieved as a result of pressure measurements in the fully developed region, on horizontal and vertical faces of the elements equipped with micro-pressure sensors (see in paragraph 11.2.2).

3. Estimation of a global energy dissipation balance for each overlay by measuring the sequent depths of the forced hydraulic jump at the toe of the chute with ultra-sound sensors (see in paragraph 11.2.3).

The measurement sections are shown in Figure 11.11. The measurements were supported by visual observations of tracers, from pictures at different shutter speeds and videos.

11.2.1 Flow velocity, air concentration and air bubble size

♢ Background

Several measurement techniques are currently used to determine the velocity in air-water flows. Briefly, the most common instrumentation is:

- *Back-flushing Pitot tubes* developed by the U.S Bureau of Reclamation (USBR) and used both for large outdoor flumes [Frizell et al. (1994)] and laboratory models [Chamani & Rajaratnam (1999), Matos & Frizell (2000)].
  This instrumentation is based on the principle of a classical Pitot tube but includes a flushing system (developed at first by Viparelli (1953) then Wood (1983)) which eliminates the disturbing air bubbles. Previous experiments showed that this instrumentation has a limited range of application, with a significant underestimation of the velocity for large air concentrations in the flow (for $C > 0.7$, Matos (2000a)).

- *Acoustic Doppler velocity meter* (ADV), tested by Frizell (2000).
  The technology is based on the variation of the sonic velocity with the state of the water (its density) and the change in frequency of the emitted pulse of sound. The ADV provides 3-D dimensional velocity measurements. Even though, its application is limited to very low bubbly flows ($C < 0.08$, Matos et al. (2002)). Its application is recommended in the vicinity of the inception point or near the pseudo-bottom where the air concentration is low.

- *Single or Double-tip conductivity probes*, also developed by the USBR.
  This probe has been the object of a pioneering prototype study by Cain (1978) in the Aviemore dam spillway. The same type of instrumentation had also been developed and widely used by Chanson (1995). If one of the wires of the probe is in contact with an air bubble, the current between the two conductors is interrupted. Then the single-tip probe provides the time-average air concentration in the flow. A cross-correlation analysis of the two signals of the double-tip probe allows the longitudinal component of the velocity of the flow to be estimated.

The availability of other techniques such as digitized flow video sequences [Sánchez-Juny et al. (2000)] or high speed camera haven't yet been proven. A study is in progress [Amador et al. (2002)] to develop a promising future application of the Particule Image Velocimetry (PIV). This is a non intrusive technique for measuring the 3D velocity components distribution of

flow over stepped chute, but limited to the section upstream of the inception point.

Finally, the recent development of the double fiber-optical probe has provided a available technique to measure air concentration, air bubbles size and instantaneous longitudinal velocity of highly aerated flow.
More detailed comparisons of back-flushing Pitot tube and ADV instrumentation along with the optical probe are given in Matos et al. (2002).

♢ Fiber-optical probe

The double fiber-optical probe, developed in the nineties by RBI Instrumentation (Meylan, France) had its first applications in nuclear and chemical two-phase flows. This probe was used as a velocity measurement instrument for free surface aerated flow by Robert Boes [Boes & Hager (1998)] who proved its capacity to provide accurate data even with high air concentrations [Boes (2000a)]. These results lead to the choice of the double fiber-optical probe for assessing the aerated flow characteristics over macro-roughness.

The measuring principle of the probe is based on the Descartes refraction law in optics that takes into account the different light refraction indices of the air and the water.

⋆ *Composition of the equipment*

The fiber-optical device is composed of three components as represented in Figure 11.6:

1. The opto-electronic amplifier module
   The module emits light and transmits it into the probe through 2 optical fibers connected to the 2 probe tips which are located in the flow. It also receives the reflected optical signal and converts it to electrical information by means of photosensitive diode. After amplification, the raw analog signals is converted with two thresholds into a TTL digital signals corresponding to the air (5 volts) or water (0 volt) in the vicinity of the probe tips.
   The two thresholds, a upper to delimit the gas phase and a lower for the water phase, have to be selected to eliminate the noise without losing any information about the phases. The accuracy of the approximation of the time-development of the phases and then of the final results on air concentration and velocity is directly dependent on the selection of these thresholds.
   Because light is used as compared to conductivity probes, the signal transfer (emission and response) is much faster. The acquisition system is characterized with a very short response time or resolution of $0.033\,\mu s$ instead of $10\,\mu s$ with the conductivity probe.

2. The double tip fiber-optical probe
   As shown in Figure 11.6, the probe comprises a transmission part - the two optical-fibers protected in rigide tube, and a sensitive part corresponding to two sapphire tips of a diameter of roughly $80\,\mu m$. Each tip is sharpened into an optical prism through which a fraction of the light escapes, the rest being reflected according to the reflection index of the phase at the probe. The rate of reflection is proportional to the difference between the sapphire refraction index ($= 1.62$) and the indices of the measured phase. Thus, in clear water (refraction index of 1.33), a very tiny portion of light is reflected, whereas in dry air (refraction index of 1.00) all light is reflected.
   At the moment when the tip enters in contact with an air bubble, ideally, the change of

phase water-air (or inversely when the tip is out of a bubble) should be instantaneous marking by a sharp step in the time-signal response. In fact, because of the viscosity and inertia of the fluid as well as the curvature of the bubble interface, the piercing by the tip of a bubble is not instantaneous. The change of phase experiences a transition period instead of a step signal. For this reason, after amplification, the signal is passed through a threshold level in the opto-electronic module to be transformed into a TTL-signal, with 0V for the water phase and 5 V for the gas phase.
The size of the tip is considerably smaller as compared to the conductivity probe. This allows very small bubbles to be detected. The study conducted by Stutz (1996) concluded that the detection is limited to the bubbles with a size around 3 times larger than the diameter of the tip. In the present tests, the probe can detect bubbles larger than 0.25 mm. Furthermore, this small tip size limits the disturbance of the bubbles themselves and of the flow streamline.
The design of the submerged part of the probe was a compromise between a shape intending to minimize the disturbance of the flow and a good hydrodynamic behaviour. This design reduced the induced errors of the responding signals and yet was strong enough to resist the high velocity of the flow.
The technique assumes that the probe tips are aligned along the mean streamline in order to measure the longitudinal flow velocity (Fig. 11.6). To be able to catch a representative scale of air bubbles in the flow, the distance $d_p = 2.5\,mm$ between the two tips was fixed. In fact, few years ago, no study could provide the scale of the bubbles size for flow over stepped flume. Nevertheless, an impressive study of bubble size measurements for the smooth Aviemore dam spillway [Cain (1978)] had confirmed the Killen (1968) results for smooth laboratory flumes : for homogeneous bubbly flow corresponding to $\overline{C} \leq 0.5$, bubble chord length (ϕ_c) ranged between 0.5 to 3 mm. Assuming that the air structure was similar in the stepped chute, a distance of $d_p = 2.5\,mm$ appeared as a good compromise to accurately measure the velocity of displacement of an air bubble between the two tips. Later, Chanson & Toombes (2001a) obtained the same results for laboratory stepped flume.

3. Computer interface board
The TTL-signals are collected in an acquisition card developed by RBI and which allows a large sampling frequency in the range of MHz.
The resulting file corresponds to a discrete time development of the Volt values. A data reduction program developed by RBI provides the principal local characteristics of the mixture flow : air concentration, velocity and the corresponding correlation factor, bubble Sauter diameter and their time-development, as well as the bubble sizes.

⋆ *Resulting flow parameters*

In the following, the principle and the assumptions of the concept supporting the data reduction are presented.

Air concentration :

The local air concentration ($c(z)$) or void fraction measured at a depth z is determined as the proportion of time that the probe tip is in contact with air. Although the air concentration can be obtained in both probe tips, only the value of the leading probe tip is considered. In fact, the unavoidable disturbance caused by the intrusion of the leading probe may reduce the accuracy of the trailing probe tip data in the wake influence of the

first one. Calibration experiments by Stutz (1996) concluded that the air concentration difference between the two tips may be as large as 15 % for high velocity flows.
In the present study, the air concentration values are always given from the leading tip with a maximum error of ±3%.

Flow velocity :

The measurement of velocity is based on the successive detection of air-water interfaces by the two tips. This technique assumes that the probe tips are aligned along the mean streamline (corresponding to the pseudo-bottom direction) and that air bubbles or droplets are not significantly affected by the leading tip. Under ideal conditions, the signals from the two tips would be identical but separated by a time delay. In practice they differ because the leading probe slightly disturbs the flow. Thus the most likely time delay is estimated by cross-correlating the two signals.
The resulting local air-water velocity at the depth z is given by $u_m(z) = d_p/T_c$, where d_p is the distance between tips and T_c the time for which the cross correlation coefficient (r) is maximum.
For 1D-flow, RBI suggests that when the cross correlation coefficient is lower than 0.7, the signals are not well correlated and that the resulting velocity value has to be used with caution. For the highly turbulent flow over macro-roughness, in the two first centimeters above the outer corner of the step or the endsill, the flow is strongly affected by an internal jet (see paragraph 12.2). In this region, the normal (along the z axis) component of the velocity should be significant which could disturb the longitudinal trajectory of air bubbles. As a consequence, only a few percent of bubbles experience the longitudinal velocity and the two signals are quite different. The maximal cross correlation factor is generally lower than 0.7. This implies that the flow direction is also important in the normal direction. Based on this interpretation, it has been suggested to fix the critical value of r at 0.5 instead of 0.7.
Obviously, this analysis assumes that the velocity of the air bubbles is of same order of magnitude as the velocity of the flow in the mean direction parallel to the alignment of the tips. In fact, similarly to aerated flow over smooth chute [Wood (1991)], in the homogeneous part of the flow (*i.e* the portion of the water flow where air bubbles are transported), the air bubbles are surrounded by water. Because of their very law density compared to the water density, of their little drag effect due to their very small size, their velocity in the direction down the slope should be very close to the water velocity. Near the wavy free surface region, this assumption is no longer strictly valid since the flow is slightly disturbed by the drag of the projected water droplets ejected by turbulence. Furthermore, the bubble size is much larger, of about 10 mm or more [Cain (1978)]. Nevertheless, due to the high velocity of the flow, the velocity of the bubbles should be consider with confidence of same order of magnitude as the fluid velocity.
Finally, the maximum error in the velocity is about $\pm 0.20 m/s$.

Air bubble chord length :

Except to assess the different flow layers in order to determine a characteristic flow depth (see Chapter 13), the chord length or the distribution of the air bubbles has not been an item of interest in this project.

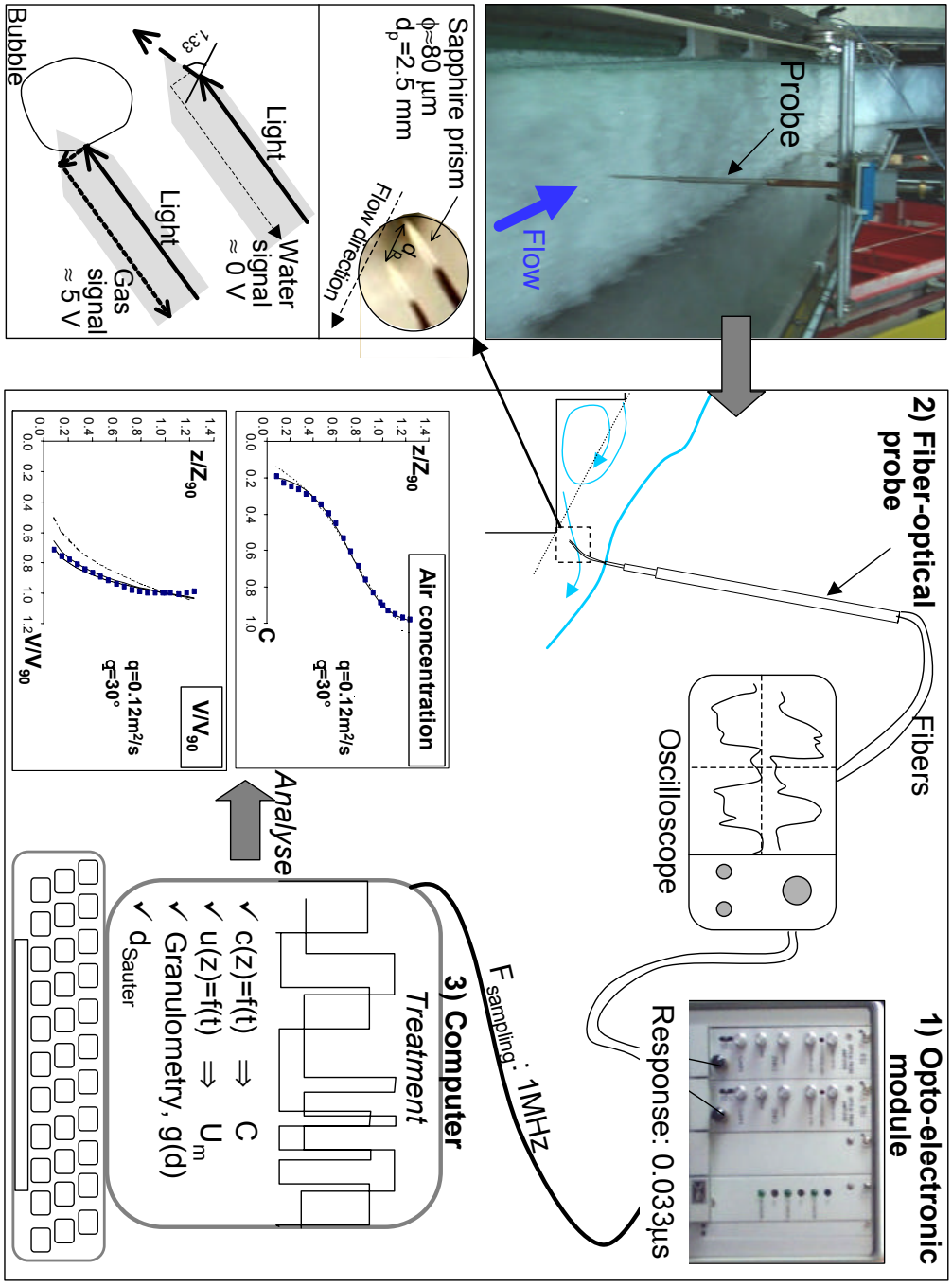

Figure 11.6: Schematic of the double fiber-optical probe, RBI, along with the acquisition line

11.2.2 Dynamic pressures

The distribution of pressure forces on the boundary of the control volume considered along the macro-roughness slope must be known to apply the momentum equation. In addition, the high velocity flow which encounters sharp corner when flowing over steps, endsills or blocks suggests that risk of cavitation may likely occur in some regions of the slope. Without speaking about

the design interest to estimate the dynamic forces and fatigue which the macro-roughness elements should experience during a flood. These information should be provided by pressure measurements.

Few pressure measurements have been the subject of study, except the recent work on pressure distributions over stepped flume by Sánchez-Juny (2001). He pointed out that the typical pressure signals consisted in weak pressure fluctuation with local negative pressure peaks. On this basis, highly sensitive and accurate sensors were chosen herein to minimize the noise and to detect negative pressures. The Kulite sensors developed by Kulite international SARL, France, that were chosen are also resistant to high velocity jet impacts.

◇ Description

The XTL-140M KULITE silicon over silicon piezo-resistive micro-sensor is shown in Figure 11.7. The full scale of these 2.6 mm diameter pressure sensor cells corresponds to 0-1.7 absolute bars with very high sensitivity (between 50 and 70 mV/bar). It can resist to peak of pressure up to 3.4 bA and it has a resonance frequency at about 300 kHz, which is much higher than the frequency of the measuring phenomenon. Both the non-linearity and hysteresis errors represent 0.1 % of the full scale. The accuracy of the sensor is then of $\pm 1.7 mb$. The compensated temperature ranging between $10^o\,C$ to $30^o\,C$ avoids variations in the pressure signal during the measuring sequence in a water with a temperature close to $15^o\,C$.

In order to ensure the waterproofness of these sensors that are normally designed for medium without humidity, they have been covered by a layer of silicon over the connected part between the sensor and the transmission cable. Calibrating tests conducted at the Laboratory of Hydraulic Machines (LMH) at EPFL confirmed that the accuracy and sensitivity of the sensors were not affected by the silicon layer.

A set of 8 sensors can be simultaneous fixed directly at the surface of the step or macro-roughness elements along the flume axis, as shown in Figure 11.7.

◇ Data acquisition

The 8 sensors are connected to a data acquisition box which includes the acquisition card developed by LMH. This card, with an accuracy of about the double of the sensors one (then of roughly $3.4\,mb$), includes a hard filter which can be adjusted from $60\,Hz$ filter frequency to $7500\,Hz$. It also offers the possibility to amplify the response signal by a factor of 10 or 100 and to shift the zero of $\pm$ 5 V. This contributes to increase the sensor sensitivity. The resulting output signal is limited between $-10\,V$ to $10\,V$ and it is transmitted to the computer via an ARCNET link at 2.5 MB. The acquisition frequency can vary between $100\,Hz$ to $20\,kHz$, with a limitation of the resulting data files at around 6500 points.

A brief analysis of the phenomenon to be measured by the pressure sensors, namely the rollwaves with a frequency of 0.5 to $2\,Hz$, the recirculating cells with frequency of 5 to $10\,Hz$ and the jet impact suggested that the acquisition should be in the range of the low frequencies. Finally, after a set of preliminary tests concentrated on the noise of the rough signal and on the frequency spectrum, where both filter and acquisition frequencies were tested for several values, lead to the following specifications:

- Filter: $F_f = 60\,Hz$

- Acquisition frequency: $F_a = 120\,Hz$

- Duration of the measuring sequence: $T = 60s$

The rough pressure signal is then statically treated with LabVIEW (National Instruments) to provide the mean pressure, the positive and negative peaks, the variance and standard deviation. A spectral analysis gives the energy frequency spectrum.

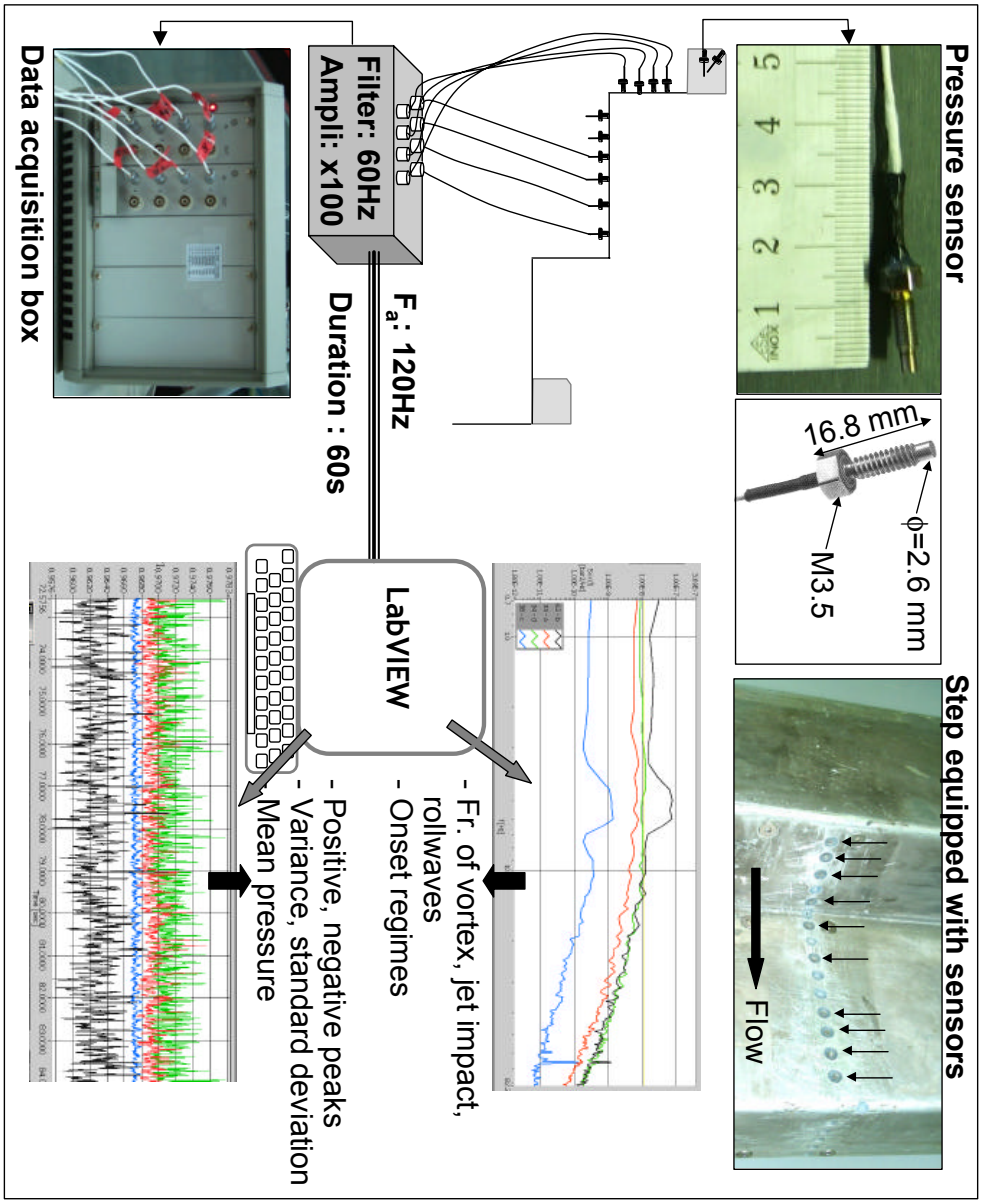

Figure 11.7: Sketch of the Kulite pressure instrumentation along with the acquisition line

11.2.3 Sequent depths in the dissipating basin

As already mentioned, the global energy dissipation of the macro-roughness chute is estimated from the characteristics of a hydraulic jump that is forced in the rectangular stilling basin at the base of the flume. The residual energy is calculated on the basis of the upstream sequent depth (Y_1) of the hydraulic jump, assuming that it is of same order of magnitude than the depth at the toe of the chute (see chapter 15). Figure 11.2 shows that it is almost impossible to accurately measure Y_1 due to the high aeration, the instability, the undulation and ejections in the jump.

The solution consists in measuring the downstream sequent depth (Y_2) and calculating Y_1 from the momentum equation. For this purpose, two automatic ultrasonic analog cylindrical sensors (Baumer electric, Switzerland) are fixed in the stilling basin (see Figure 11.8) at a distance long enough to be in the non-aerated tailwater of the jump. Their location was chosen out of the influence of the mobile gate. Based on the acoustic velocity in the water, these sensors provide an acoustic signal with a frequency of $230\,kHz$.

Because of the high velocity of the incoming flow, the front face of the hydraulic jump is disturbed by slugs creating by intermittent and small rollers, leading to waves and then to an undulating tailwater. For this reason and in order to obtain repeatable and stabilized data, the duration of the measuring sequence was fixed at $120\,s$ and the acquisition frequency was limited to $4\,Hz$. After calibration, the rough signal is filtered with a standard deviation criterion to render a representative signal (see Fig. 11.8). Mean and extreme sequent depth values are then extracted with a precision of about $\pm 0.5\,mm$.

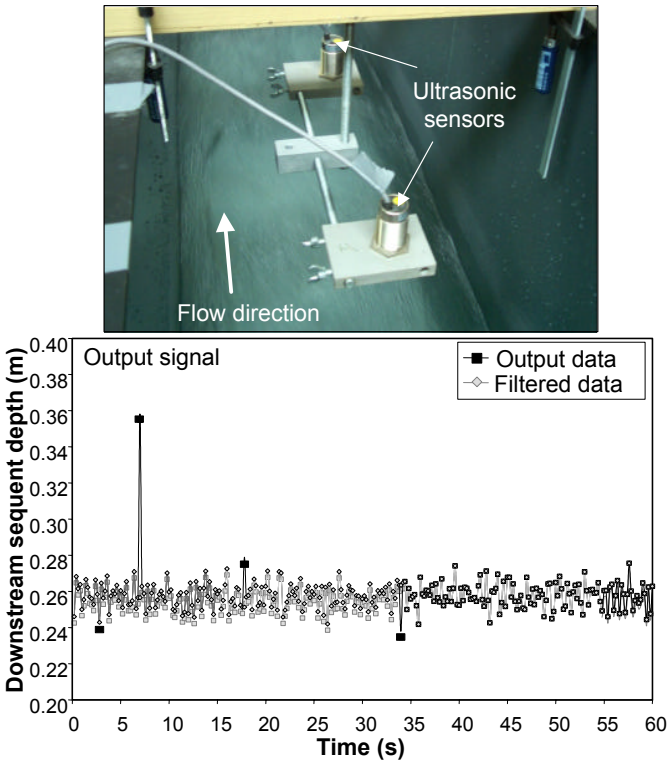

Figure 11.8: Above) Ultrasonic sensors at the tail water of the hydraulic jump - Below) Time-development of the rough and filtered signals

11.3 Similarity and scale effects

To represent accurately the behaviour and characteristics of the *free-surface*, highly *turbulent* and *self-aerated* flow in the scale model, three similarity laws would have to be fulfilled simultaneously:

- Froude similarity, for the effect of the gravity forces, where the Froude number is defined for the clear water flow as:
$$F_w = \frac{q_w}{\sqrt{(g \cos\theta Z_w^3)/\alpha}} \tag{11.4}$$
where α is the kinetic energy correction factor due to the non uniform velocity distribution (see paragraph 14.3.3). It has to be noted that the tested slopes are large enough to have an effect on the wall pressure head and hence on the Froude number which explains the angle correction $\cos\theta$. As mentioned by Chow (1959), the effective pressure starts to be affected by the steepness for $\theta > 6^o$.

- Reynolds similarity, for the important role of the viscosity, with the clear water Reynolds number given by:
$$R_w = \frac{q_w}{\nu} \tag{11.5}$$
where ν is the kinematics viscosity ($\nu \simeq 1.020.10^{-6}\ m^2/s$ for the flume water).

- Weber similarity, for the non-negligible interfacial tensile force. The Weber number is defined as:
$$We = \frac{U_m}{\sqrt{\sigma/(\rho_w x_s)}} \tag{11.6}$$
where σ is the interfacial surface tension ($\sigma \simeq 0.072\,N/m$ for the water of the flume), and $x_s = h_s/\sin\theta$, the longitudinal distance between two step corners.

This condition cannot be fully satisfied at the scale model due to the facility limitations. Because the gravity forces remain the dominant effect, the tests are conducted in the **Froude similarity**.

Scale effects

The air bubble sizes are proportionally too large in the model and as shown by Kobus (1984), the air transport capacity tends to be lower than for an equivalent prototype.

However, Boes & Hager (2003a) analyzed scale effects on air entrainment and velocity for flow over stepped chutes. They showed that scale effects can be rendered negligible for Reynolds and Weber numbers as well as scale length (λ_L) in the range of the criteria mentioned in table 11.1.

These results are in good agreement with some previous studies of scale effect for aerator spillways. They concluded that for correct aeration model, the scale length should be lower than 1:15 [Vischer, Volkart & Siegenthaler (1982), Pinto (1984)] and the Weber number larger than 110 [Rutschmann (1988)]. Pegram et al. (1999) also assessed that there was no significant scale effect for energy dissipation of stepped chute for $\lambda_L \leq 15$. Kobus (1984) suggested a $R_w \geq 10^5$ to mitigate the viscous effects.

	Criterion
λ_L	≤ 15
We	≥ 100
R_w	$\geq 10^5$

Table 11.1: Dimensionless criteria according to Boes & Hager (2003a) to minimize the scale effects due to Froude similarity

In light of the above and considering the step height commonly found in prototypes, namely 0.30 to 0.60 m for embankment [Ditchey & Campbell (2000)], the model data of the present study with step height of $0.06\,m$ can be extrapolated to 1:5-1:10 scaled prototypes using the Froude similarity.

Furthermore, for the tested discharges and macro-roughness overlays, the Weber number ranges between 100 and 207 which is above the recommended value. The Reynolds number is larger than 10^5 for discharges larger than $0.1\,m^2/s$ (or $50\,l/s$). Nevertheless, for low discharges, its value remains higher than 2.10^4, with depth of the nappe larger than 2 cm. Therefore, based on these verifications together with the length scale, it may be concluded that the model results can be applied with confidence to prototypes, with a possible exception for the very low discharges ($q_w < 0.04\,m^2/s$) where $R_w = [2.10^4 - 4.10^4]$ and the flow depth is between 2 and $3\,cm$.

No previous study of the scale effect on the pressure measurements have been found in the literature. Because the effects are mitigated on the velocity and air concentration, it may be assumed that they are also negligible on the pressures.

Particular case of the jetbox entrance condition
In addition to the respect of the length scale and dimensionless numbers criteria, to be able to transpose the experimental laboratory data to prototype, care must be taken about the effect of the jetbox.

When comparing with an equivalent gated spillway, no problem are encountering. However, to generalize with whatever broad-weir or ogee crested entrance, it is necessary to calculate the equivalent height of the dam or spillway. In fact, as seen in paragraph 11.1.1, the jetbox modifies the position of the inception point and the length of the developing region compared to ungated prototypes. An analysis of the backwater and drawdown curves shows that, assuming that the roughness between the jetbox and the inception point is the same than from the crest to the inception point, the equivalent length downstream the jetbox can be estimated in similar condition to those with an ungated structure. The total height (H_D) can then be easily calculated.

This analysis has been presented in details by Hager & Boes (2000). It will be applied and compared for the conventional steps data and adapted for the other set of macro-roughness overlays in the chapter 14.1.

11.4 Description of the set of experimental tests

To be able to compare the tests from one configuration to another, the entrance conditions, for a given discharge, are maintained identical. Indeed, as already mentioned, the jetbox has

an effect on the onset of air entrainment and on the flow regions position. Then, the jetbox openings (h_0), given in Table 11.2, are fixed so that the box is just pressurized.

Discharges (l/s)	10	15	20	30	40	60	80	100	120	130
h_0 (m)	0.01	0.015	0.019	0.023	0.033	0.046	0.054	0.063	0.072	0.078
F_0 for $\theta = 18.6^o$ (-)	6.6	5.4	5.0	5.6	4.4	4.0	4.2	4.1	4.1	3.9
F_0 for $\theta = 30^o$ (-)	6.9	5.6	5.2	5.9	4.6	4.2	4.4	4.3	4.3	4.1

Table 11.2: Entrance conditions: openings of the jetbox in function of the water discharges for both 18.6^o and 30^o inclined chutes with the corresponding approaching Froude number

In order to have a global view of the tests performed, the following table in Figure 11.9 gives the main conditions and configurations tested during the experimental phase in the stepped flume. The location of the cross sections of the measurement of the air concentration and velocity of flow are shown in Figure 11.11 whereas the position of the pressure sensors are represented in Figure 11.10.

Measuring \ Configurations	m=0	m=1/3	m=1/2	m=1	m=4	m=5	m=6
Air concentration, velocity, bubbles size							
Developing region	▲		▲	▲			
Uniform region	● ▲		● ▲	● ▲		●	
Inside step	▲						
Pressure							
Over the step	● ▲	▲	● ▲	▲	▲	▲	▲
Over the elements		▲	● ▲	▲			
Sequent downstream depth	● ▲	● ▲	● ▲	● ▲	● ▲	● ▲	● ▲
Observations							
Inception points	● ▲	● ▲	● ▲	● ▲	● ▲	● ▲	● ▲
Mixture depths	● ▲	● ▲	● ▲	● ▲	● ▲	● ▲	● ▲
Rollwaves	● ▲	● ▲	● ▲	● ▲	● ▲	● ▲	● ▲

● θ=18.6° ▲ θ=30°

Discharges ranging : Q_w (l/s) =[10-15-20-30-40-60-80-100-120-140]

q_w (m^2/s)=[0.02 – 0.28]

Figure 11.9: Summary of the measured parameters and tested macro-roughness configurations

It has to be noted that :

- For the optical probe, to respect a certain homogeneity and confidence of the measurements, the data result of an average of three measuring sequences of 60 s with a systematic control of the corresponding standard deviation.

- In case of pressures, due to the great number of sensors, the measurement is taken twice for each discharge, with a duration of 60 s.
- As for the downstream sequent depth, the resulting values are extracted from 2 x 2 (2 sequences by 2 ultrasonic sensors) measuring sequences of 120 s.

For each case, repeatability was verified during each daily set of tests.

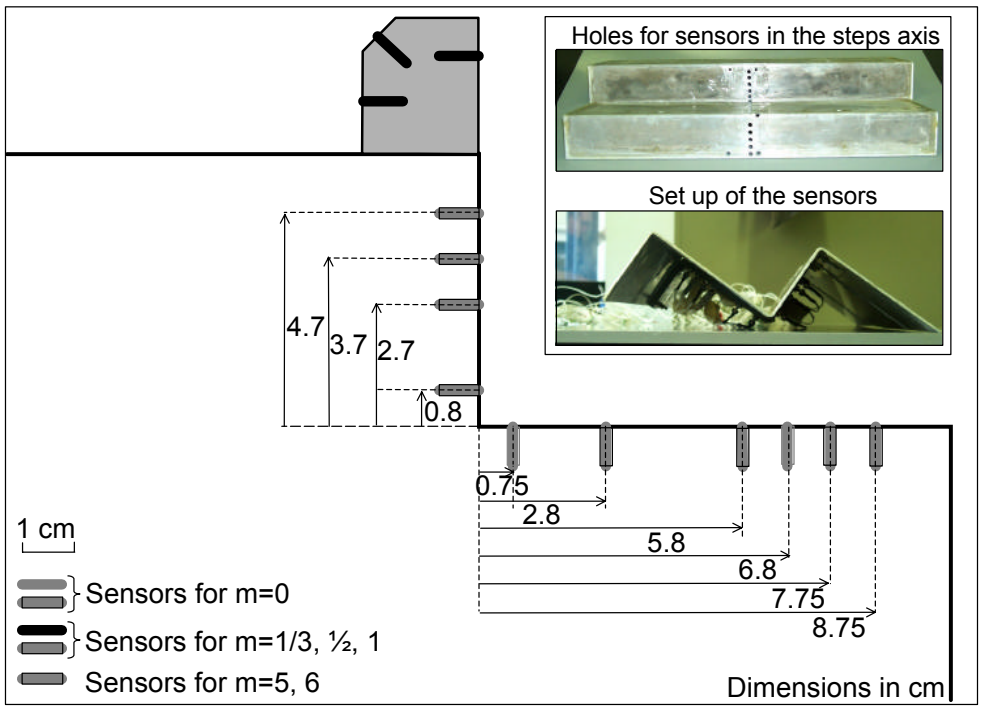

Figure 11.10: Location of the pressure sensors along the flume axis, in the uniform region, between $x = 5.52\,m$ and $x = 5.64\,m$

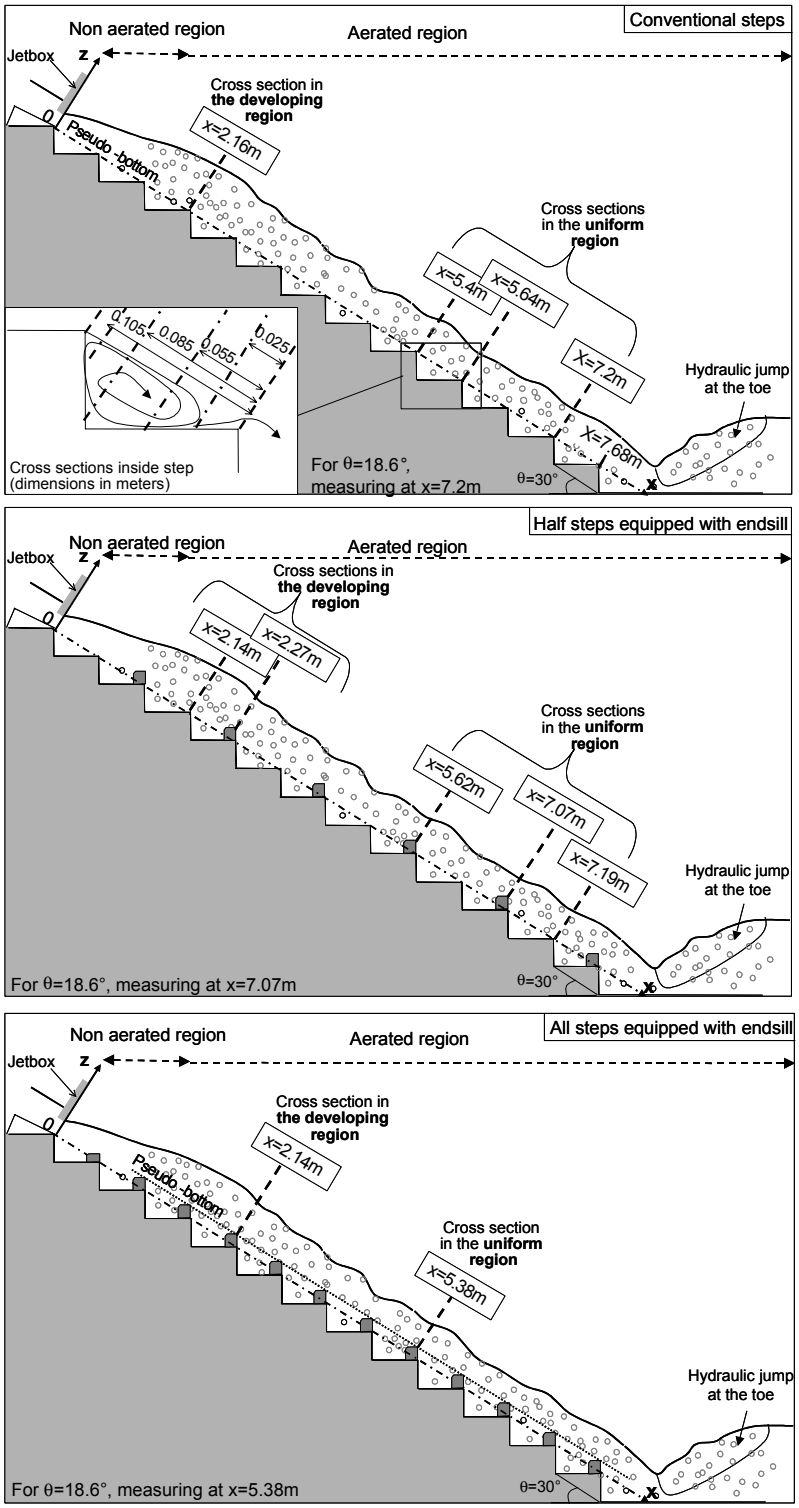

Figure 11.11: Cross sections of optical probe measurements along the slope

Chapter 12

Description of aerated flow over macro-roughness

12.1 Quasi-uniform flow region

For the tested slopes and overlays, it was observed that downstream of the point of inception the mean air concentration gradually increases until it attains the quasi-uniform region.

According to Christodoulou (1999), it was expected that in the experimental facility the quasi-uniform region would be reached at the toe of the conventional stepped flume. Indeed, from Equation 8.14 (Part III, Ch. 8.2.2), the longitudinal distance from the entrance of the flume to the onset of the quasi-uniform region, L_u can be estimated to about: $L_u \simeq 4.9\ m$ for $\theta = 30^o$ and $L_u = 5.5\ m$ for $\theta = 18.6^o$ for the largest tested discharge. These values are probably overestimated since this relationship was established for a crested spillway entrance. With the jetbox, the super-critical flow entering in the flume is already accelerated which reduces the required length for the flow to be fully developed. Moreover, it was found that the height of the roughness has an insignificant effect on the location of the uniform region. Then, it was expected that the uniform region would be attained for all tested stepped overlays.

The equilibrium conditions are fulfilled if depth average mean air concentration C_u, mean velocity U_m as well as both mixture depth Z_{90} and equivalent clear water depth Z_w are constant between two steps (or endsills or blocks) outer edge. Variations of these four flow parameters with unit discharges were plotted for the measuring cross sections in the developing and quasi-uniform region for the 30^o slope. The conservation of the values between the two measuring cross sections at the downstream end of the flume (see Fig 11.11) shows that indeed the quasi-uniform conditions are attained. The scattering of the data lies within the error scale. According to Christodoulou (1999), it can be assumed that the quasi-uniform region is also reached for the flat slope of $\theta = 18.6^o$.

12.2 Flow regimes

12.2.1 Influence of the macro-roughness elements on the flow structure

The macro-structures associated with the three flow regimes for aerated flows over conventional steps, namely the nappe, transition and skimming flow, have been described in detail in Chapter 8.1, Part III. In order to observe the influence of the macro-roughness elements, the side views of the five configurations $m = 0$, $m = 1$, $m = 1/3$, $m = 1/2$ and $m = 4$ are given respectively in the following Figures 12.2, 12.3 and 12.4 for the 30^o slope.

The observations show that the main macro-structures are similar for all the tested configurations and for both slopes:

- Nappe flow is characterized by the presence of a non aerated static water pool on the horizontal face where the flow plunges down. Air cavities are trapped between the step or step+endsill/block vertical face and the falling nappe.
- Skimming flow is characterized by well-developed rotating triangular vortices under the skimming layer and internal jets at the corner of steps, endsills or blocks. The size of the recirculating cells appear independent of discharge.

However the distinct effects of endsills fixed over the whole step width ($m = 1/3,\ 1/2,\ 1$) and those related to the blocks ($m = 4,\ 5,\ 6$) as well as the slope angle can be noticed.

Slope effect on the macro-structures for conventional steps

For conventional steps, the development of a hydraulic jump was observed only in the case of the 18.6^o slope, for low discharges. It corresponds to the so called isolated nappe flow [Pinheiro & Fael (2000)]. With the increasing slope, the hydraulic jump disappears (partial nappe flow): only a part of the nappe strikes the downstream end of the step face to be deflected to the next step.

The slope does not influence the spreading of the recirculating cells for skimming flow. In fact, for both slopes and all discharges, the vortices are spread over almost the whole step height and over the 2/3 of the horizontal face. For $\theta = 30^o$, $L_v \simeq 7\ cm$ with L_v the length of the vortex on the horizontal step face whereas $L_v \simeq 12\ cm$ for $\theta = 18.6^o$.

Regarding the internal transverse jet, for both slopes, this singularity is well developed and impacts about the first 1.5 cm above the step outer edge for all discharges. Moreover, between the vortex and the internal jet, visual observations indicate a separation zone trapped under the skimming layer. A schematic of the macro-structures for the skimming flow is given in Figure 12.1.

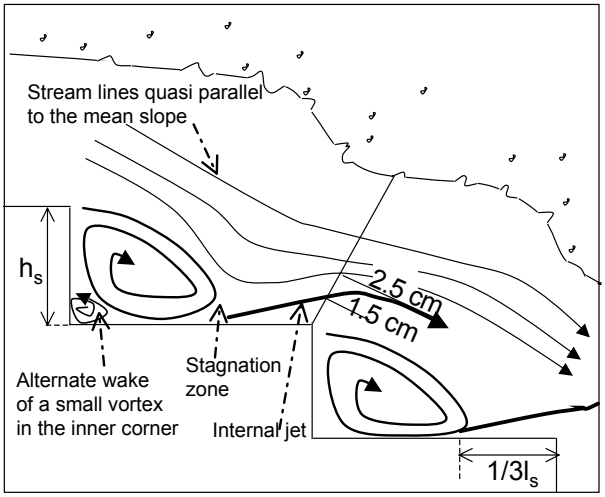

Figure 12.1: Sketch of macro-structures during skimming regime for $\theta = 18.6^o$ and $\theta = 30^o$ and for conventional steps

Endsill and block effects on the macro-structures

For the 2D overlays (m=1/2 m=1/3 and m=1), the endsills do not contribute to a major modification of the flow macro-structures. However, for transition and skimming regimes, the sizes are slightly modified [André, Matos, Boillat & Schleiss (2004)]. This has a direct effect on the contact length between recirculating cells and step faces as well as on the impact zone of the internal jet. With endsills, the vertical length of the vortex increases from $h_v = h_s$ to $h_v = h_s + h_r$ while the horizontal length is extended to the toe of the endsill. For steps without endsill (for $m = 1/2$ and $m = 1/3$), the vortices impact the entire vertical and horizontal step faces.

In the skimming layer, the zone under the influence of the internal jet becomes thinner at the endsill outer edge as compared to the case of the step corner.

For the particular case of $m = 1/3$, the two steps downstream the step equipped with the endsill remain empty, skipped by the flow for a large range of discharges. As an example, for the 30^o slope, it's only for $q_w = 0.16\ m^2/s$ that the second step is filled with a rotating vortex. For $q_w = 0.20\ m^2/s$, a recirculating cells starts to be developed in the cavity of the first step (see Fig. 12.3).

The blocks fixed on steps lead to an increase of the 3D flow features, due to their alternate position over the flume width. In fact, when passing between two blocks, the flow is contracted and deflected in the transverse axis [André, Matos, Boillat & Schleiss (2004)]. As a consequence, in addition to the internal jet, blocks create a succession of transverse jets and the 3D pattern of the recirculating cells is thus increased. In addition, local vortices are developed at the downstream and upstream ends of the blocks corners.

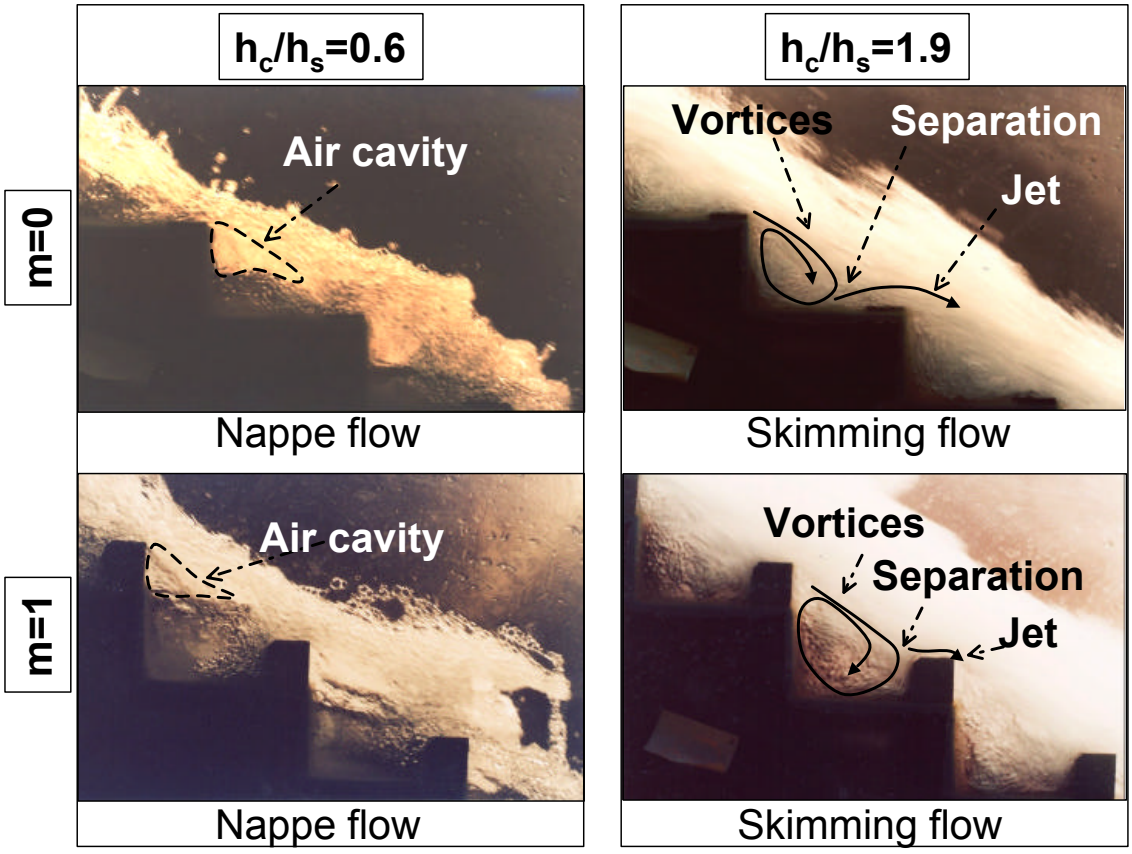

Figure 12.2: Side view of fully developed aerated flow over conventional steps ($m = 0$) and all steps equipped with endsills ($m = 1$) - $\theta = 30^o$

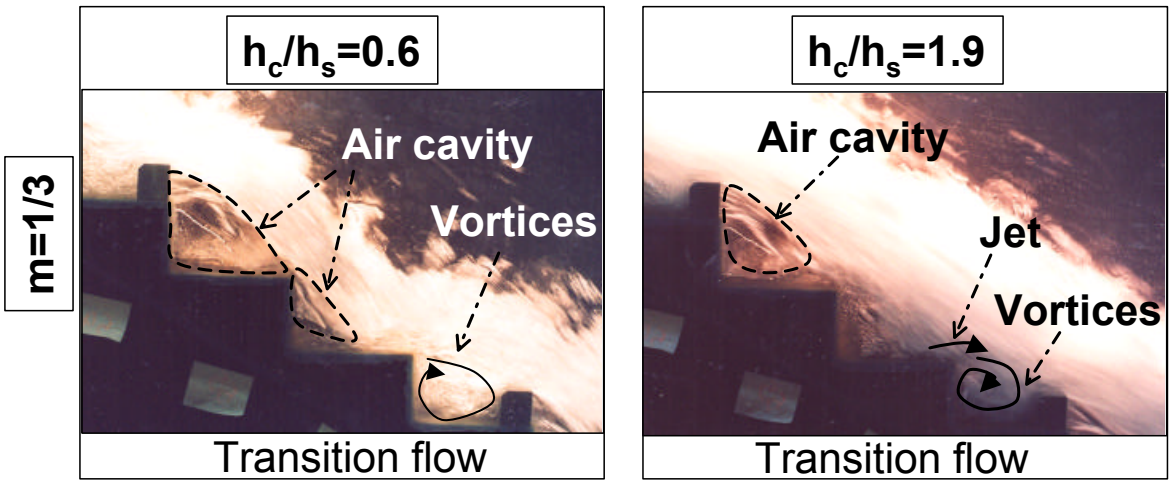

Figure 12.3: Side view of fully developed aerated flow over steps with endsill on every third step ($m = 1/3$) - $\theta = 30^o$

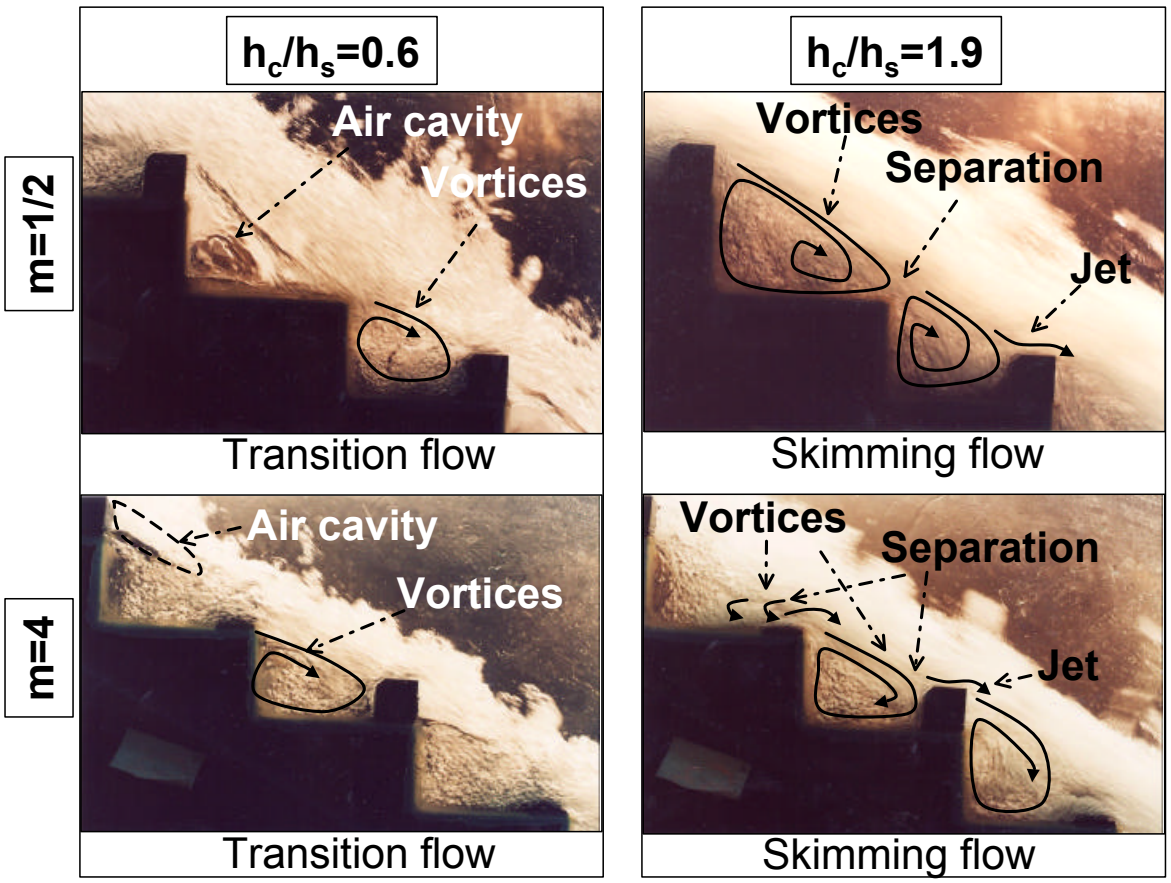

Figure 12.4: Side view of fully developed aerated flow over steps with endsills on every second step ($m = 1/2$) and all steps equipped with spaced alternate blocks ($m = 4$) - $\theta = 30^o$

12.2.2 Influence of macro-roughness elements on the onset of the flow regimes

The criteria used to distinguish the flow regimes are similar to those proposed by Matos (2001):

- Nappe flow: when there is an air pocket within each step cavity,
- Skimming flow: when all step or step+endsill/block cavities are completely filled, when vortices are well developed and when the width of the skimming layer is significant compared to the boundary layer influenced by the internal jet,
- Transition flow: when nappe and skimming flows characteristics are observed on alternate steps or when the characteristics of the skimming flow are not permanent and only fulfilled in some steps.

On this basis, the conditions for their occurrence are given in Table 12.1, where h_c is the critical depth and h_s, l_s, the height and length of the conventional step.

Overlays (as in Figures 11.3, 11.4)	m=0	m=1/3	m=1/2	m=1	m=4	m=5	m=6
$h_s/l_s = 0.58$							
Onset of transition flow (h_c/h_s)	0.85	0.40	0.50	0.85	0.60	0.60	0.80
Onset of skimming flow (h_c/h_s)	1.15	2.70	1.90	1.15	0.95	0.95	1.10
$h_s/l_s = 0.34$							
Onset of transition flow (h_c/h_s)	1.00	0.45	0.60	1.00			
Onset of skimming flow (h_c/h_s)	1.40	3.00	2.50	1.40			

Table 12.1: Measured onset of transition and skimming flows for $h_s/l_s = 0.58$ and $h_s/l_s = 0.34$

Effect of macro-roughness elements

When comparing the results with those for conventional steps, the following observations can be drawn:

- Endsills on all steps ($m = 1$) do not appear to modify the onset of transition and skimming regimes. They have an effect similar to a displacement of the pseudo-bottom by a distance equal to the normal height of the endsill, $k_r = h_r \cos\theta$.
- Endsills on half of the steps ($m = 1/2$) or on third of the steps ($m = 1/3$) significantly influence the onset of the skimming flow. In fact, the flow is subject to a larger acceleration prior to hitting the next endsills, where it is deflected. As a result, the air pocket in the subsequent downstream step (without endsill), remains in the cavity for higher unit discharges.
- Alternate blocks with a large dimensionless space $e_r/b_r \geq 1$ ($m = 4$ and $m = 5$), present quite the same criteria as for $m = 1/2$ for the onset of transition flow. However, the onset of skimming flow is attained sooner as compared to the other overlays. It is judged that air cavities are rapidly filled with water because the flow is free to circulate between blocks.
  For the configuration $m = 6$ when the space between the blocks decreases ($e_r/b_r < 1$),

both onset of transition and skimming regimes become closer to the criteria for the overlay $m = 1$ or $m = 0$.

Effect of slope

All conditions of onset of transition and skimming regimes are shown in Figure 12.5 to highlight the effect of the slope. The following observations can be made for conventional steps and steps equipped with endsills:

- Nappe flow regime occurs for a larger range of discharges for flatter slope.
- Skimming flow starts for higher discharges for the 18.6^o inclined chute.
- The duration of the transition regime is similar for both slopes.

Finally the influence of the slope is identical for all the configurations and can be summarized by a shift up of the onset of transition and skimming regimes when the slope is decreasing.

Comparison with existing empirical relationship

For conventional steps or endsills on all steps, the onset of regimes are slightly different when comparing against the envelop curves of the relationships presented in Part III (see Fig. 8.2). The scatter of the results is surely a consequence of the subjectivity lying in the visual criteria to distinguish the regimes. However, it will be shown furthermore that the present discharges visually estimated for the onset of regimes are in fact validated by another more objective criterion: the type of the air concentration vertical profile measured in the fully developed aerated region (Chapter 9.1.3).

Finally, it appears that the slope effect on the values are well represented by a relationship such as proposed by Yasuda & Ohtsu (1999):

$\frac{h_c}{h_s} = a\left(\frac{h_s}{l_s}\right)^{-b}$

in which a and b are empirical constants.

Therefore, the following relationships are proposed for $18.6^o \leq \theta \leq 30^o$.

Onset of transition flow:

$$\frac{h_c}{h_s} = 0.743\left(\frac{h_s}{l_s}\right)^{-0.244} \tag{12.1}$$

Onset of skimming flow:

$$\frac{h_c}{h_s} = 0.939\left(\frac{h_s}{l_s}\right)^{-0.367} \tag{12.2}$$

For the other configurations, results show that the criteria based on the slope h_s/l_s and on h_c/h_s can not be obviously extrapolated. In fact, the notion of a pseudo-bottom parallel to the mean slope of the chute has no sense for the alternate topography. Besides, for example for $m = 1/2$, if h_s is replaced by $h_T = h_s + h_r$ (see Fig. 12.5), the condition of h_T/l_s is completely wrong.

Nevertheless, for both slopes, the onset of transition flow $(h_c/h_s)_{m=0} \simeq 1.7(h_c/h_s)_{m=1/2}$ and $(h_c/h_s)_{m=0} \simeq 2.1(h_c/h_s)_{m=1/3}$. For the onset of skimming flow the displacement of the value of h_c/h_s is inversely proportional (1/1.7 for $m = 1/2$ and 1/2.1 for $m = 1/3$). Therefore, to account for the effect of the endsills, based on the available data, the following relationships

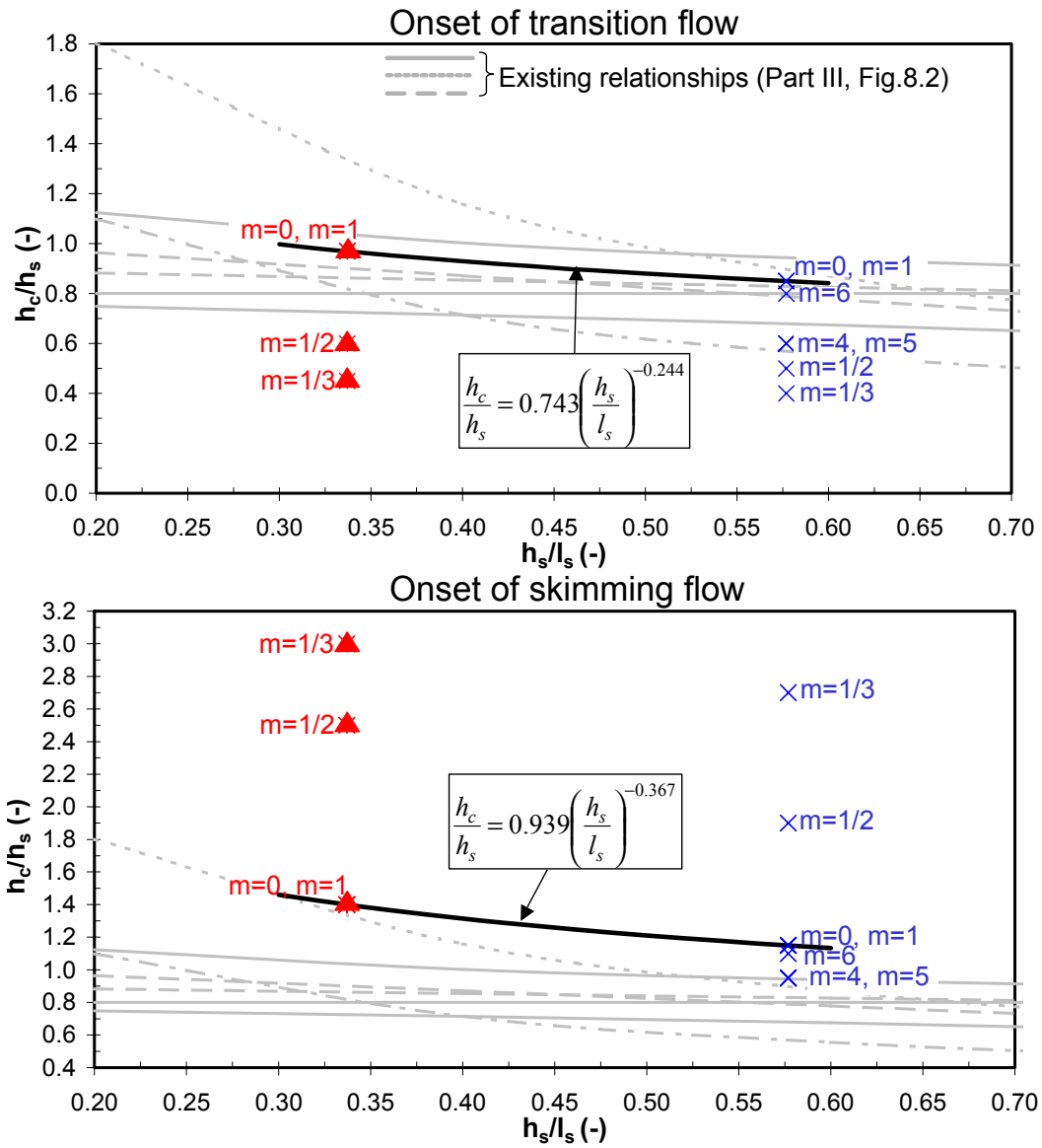

Figure 12.5: Onset conditions for all tested overlays on the 18.6^o ($\triangle$) and 30^o ($\times$) inclined chutes

are suggested:
Onset of transition flow:

$$\frac{h_c}{h_s} = \left(\frac{0.743}{\eta_m}\right)\left(\frac{h_s}{l_s}\right)^{-0.244} \tag{12.3}$$

Onset of skimming flow:

$$\frac{h_c}{h_s} = 0.939\eta_m\left(\frac{h_s}{l_s}\right)^{-0.364} \tag{12.4}$$

where η_m is a correction coefficient for the endsills overlays. For $m = 1 \Rightarrow \eta_m = 1$, for $m = 1/2 \Rightarrow \eta_m = 1.7$ and for $m = 1/3 \Rightarrow \eta_m = 2.1$. Therefore, for 2D overlays such as

endsills and for $1/3 \leq m \leq 1$:

$$\eta_m = -\ln m + 1 \tag{12.5}$$

12.2.3 Conclusions

Understanding of the development of the flow with macro-structures is essential to interpret furthermore the energy dissipation efficiency of the different macro-roughness overlays and the contribution of head losses in the friction and drag coefficients.

The macro-structures caused by the macro-roughness topography of the bottom equipped with endsills or blocks is the same as that for conventional steps.
For the case of the alternate blocks additional transverse contraction jets develop between the elements as well as local vortices at the corners of the elements.

The sizes and the numbers of these macro-turbulent structures are influenced by the spatial pattern of the macro-roughness elements. As it will be discussed in Chapter 16, these changes have a direct effect on:

- the horizontal and vertical friction lengths (L_v and h_v) under the recirculation cells,
- the friction length at the interface recirculating cells/skimming layer (x_v),
- the impact zone of the internal jet in the skimming layer (Z_j),
- the number of singular contraction effects of the flow between blocks,
- the number of vortices create upstream and downstream the blocks

The onset of regimes are unchanged with endsills on all steps compared to conventional stepped chutes. For all the other tested configurations, the macro-roughness elements influence the onset of flow regimes. This is important for the design of the elements. In fact, as it will be shown, the behaviour of flow depth, air concentration, energy dissipation and bottom pressures varies depending on flow regimes.

12.3 Rollwaves

Rollwaves were clearly observed for low discharges over the 30^o slope. Though rollwaves were not investigated in this study, their existence can not be ignored regarding the design of the structure. Rollwaves have indeed an important influence on the wavy pattern of the flow, on the air entrainment and also on the pressure fluctuations. But their principal consequence lies in an important local increase in the flow depth which must be considered for the design of the training-walls of the chute.

Among the previous studies, rollwaves were rarely mentioned since the length of the experimental flumes were generally to short to permit their development and observations.

Some practical criteria are proposed to determine the instability conditions which lead to rollwaves. Among them, there are:

- the Froude number, $F_0 = q_w/\sqrt{g \cos\theta h_0^3} > 2$ for rough turbulent flow [Albertson (1960)],
- the Vedernikov number, $V_e = \frac{1}{2} F_0 \geq 1$ [Chow (1959)]

In the 30^o conventional stepped chute, rollwaves with frequencies between 2 to 5 Hz were observed for unit discharges up to about 0.06 m^2/s. The minimum Froude number at the jetbox corresponds to $F_0 = 4.9$ and thus $V_e = 2.45$. Then, the above criteria are fulfilled. Nevertheless, it seems that the ratio between the flow depth and amplitude of the instability is a relevant parameter to explain the development of the rollwaves.

Development of rollwaves were also observed when endsills or blocks are fixed on the steps. The influence of these macro-roughness elements on the characteristics of the instabilities (frequencies and amplitude of the wave) was not investigated.

Finally, for all cases, local elevation up to 3.5 time the mixture flow depth was measured due to rollwaves. These instabilities have then to be considered for the design of the mixture flow depth.

Chapter 13

Definition of an effective homogeneous aerated flow

Residual energy at the toe of an overtopped embankment dam is necessary to design protection alternatives to ensure the safety of the structure. Estimation of friction factor has been therefore the aim of many research efforts. Different methods for estimating the friction factor are based mostly on either the flow depth or the mean flow velocity. They all result in widely scattered values: Chanson, Yasuda & Ohtsu (2000) highlight that for same hydraulic conditions, the derived friction factor could vary with a factor 100 depending on the study. Accurate approaches of head losses estimation are then still lacking and a better assessment strongly depends on a more accurate description of the air-water structures of the flow. Two main questions arise:

1. Which part of the wavy aerated flow effectively contributes to the "dissipation" forces?

2. Is the energy dissipation mainly dominated by the friction or the drag forces?

To answer these questions, the existence of a homogeneous flow region is introduced. This homogeneous flow is shown to be the main portion of the aerated flow effectively involved in momentum transport, mass conservation and energy dissipation. This concept is developed for the case of a flow over conventional steps (m=0) in the uniform region and for $\theta = 30^o$. This definition has sense only for transition and skimming regimes since for nappe regime, the flow is a thin non homogeneous falling nappe.

13.1 Characteristic flows

13.1.1 Classical flow definitions

Two ways were proposed in literature to characterize the aerated flow structure (see Part III, Chapter 9.2).

1. 90 % mixture flow approach:
   This description of the flow is based on the concept of a mixture fluid characterized by the depth Z_{90} where the air concentration reaches 90 % [Tozzi (1994), Chamani & Rajaratnam (1999)]. The flow considered to transport the momentum and to participate to the energy dissipation process is then represented by the mean air concentration, $C = \frac{1}{Z_{90}} \int_0^{Z_{90}} c(z)dz$, and the mean velocity $U_m = \frac{1}{Z_{90}} \int_0^{Z_{90}} u_m(z)dz$ where z is the normal position, c the local air concentration and u_m the longitudinal component of the local mixture flow velocity. The depth Z_{90} is represented in Figure 13.1.

2. Equivalent clear water approach:
   For smooth chute, Cain & Wood (1981) proposed the notion of equivalent clear water flow: the behaviour of the aerated flow is similar to a clear water fluid but with a shallow depth $Z_w = (1 - C)Z_{90}$ and a mean velocity $U_w = q_w/Z_w$. This approach was widely adopted for stepped chutes [Matos (2000b), Boes & Hager (2003b)].

13.1.2 Homogeneous effective aerated flow

By definition, concentration represents the amount of a specified substance in a unit amount of another substance. Applied to aerated flow, the "true" air concentration should be defined as the volume of air in a volume of water. However, in highly turbulent flow over stepped

chutes, due to its wavy behaviour and to spray (see Fig. 13.1), the water surface is not well defined.

The concept of Wilhelms & Gulliver (1989) is therefore well adapted for such a flow. In fact, they divided the aerated flow into a homogeneous mass of air in water which they call "entrained air" and air that flows between waves which they call "entrapped air". If it is applied to flow over conventional steps, for transition and skimming regimes, the homogeneous flow layer is characterized by air bubbles entrained in water whereas the free surface layer contains a lot of air gaps between the waves and water ejections.

During experimental tests performed in the 30^o stepped flume, it was observed that for local air concentration of about 90 %, the tips of the fiber-optical probe in the wavy free surface were most of the time completely outside the flow. They were within air gaps or they skimmed the crest of the waves and sometimes they were in contact with water droplets. For this reason, the notion of the depth at 90 % of air raised some questions and discussions. Thus, the original approach of Cain (1978) to define the flow layers was applied in this study.

13.2 Intermittency approach

The first concept which distinguished the two different origins of air in the two-phase fluid was proposed by Killen (1968) who defined the notion of intermittency parameter T_{int}. Cain (1978) and Falvey (1980) developed and applied this concept for prototype smooth spillways.

The optical probe for measuring the air concentration does not distinguish between an air bubble in the flow or an air gap above the flow. For this reason, the concept of intermittency parameter has been applied to the present case of flow over conventional steps. Under this condition, T_{int} corresponds to the proportion of time that the probe tips are within the bubbly flow which appears homogeneous. Therefore, for a measuring sequence of duration T:

- During the interval $0 \leq t \leq T_{int}$, the tips are assumed to be inside the homogeneous aerated skimming layer (layer (2) in Fig. 9.2, Part III).

- During the interval $T_{int} \leq t \leq 1$, the tips are assumed to be intermittently in large air gaps (layer (3), figure 9.2, Part III).

According to Cain (1978), T_{int} is derived from the density function $f(c_j)$ (Eq. 13.2), calculated on the basis of the time evolution signal of the local air concentration $c(t)$ at each depth of the flow. The procedure of the statical analysis is summarized in the following.

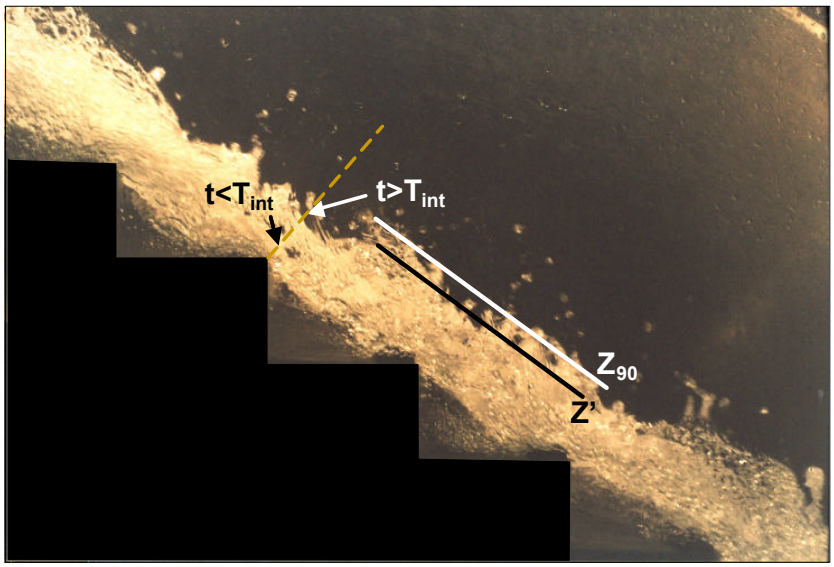

Figure 13.1: Wavy aerated flow for transition regime over the 30^o stepped flume - Z_{90}: mixture flow depth, Z': homogeneous flow depth, T_{int}: intermittency parameter

1. Air concentration signal, $c(t)$
   The local air concentration is extracted from the probe measurements as a function of time (figure 13.2a).

2. Cumulative distribution function, $F(c_j)$
   Derived from $c(t)$, this function represents the probability, P, that, at any instant t, the air concentration is less than c_j, a given concentration (figure 13.2b).

$$F(c_j) = P(c < c_j) \tag{13.1}$$

3. Probability density function, $f(c_j)$
   $f(c_j)$ (figure 13.2c), derived from $F(c_j)$, represents the proportion of time that the air concentration is equal to c_j during the measuring period.

$$f(c) = \frac{dF(c_j)}{dc_j} = \lim_{dc_j \to 0} P(c_j \leq c \leq c_j + dc_j) \tag{13.2}$$

The intermittency parameter is thus calculated according to:

$$T_{int} = \int_0^{0.7} f(c) d(c) \tag{13.3}$$

Cain showed that for $c > 70$ % probe was at the upper limit of the homogeneous flow. In fact, during the measurements with the optical probe in the LCH-flume, the upper limit of the observed homogeneous flow, *i.e.* the visual limit where the tips of the probe are still inside the flow, was also found for $c < 70$ to 75 % (see values of C_h in Fig. 13.3).

The real air content c' in the homogeneous flow is therefore :

$$c' = \frac{c - (1 - T_{int})}{T_{int}} \tag{13.4}$$

and:

$$T_{int} = \frac{1 - c}{1 - c'} \tag{13.5}$$

13.3 Definition of an effective homogeneous flow

It was shown that air decreases the shear stress at the bottom and thus friction factor [Wood (1991), Tozzi (1994)]. However, the air gaps trapped between waves at the free surface have no effect on the flow boundary layer where shear stress and singular head loss take place (see Chapters 9.3.1 and 16.3). For transition and skimming regimes, considered all the flow portion up to Z_{90} may then induce errors in determining the friction and drag reductions. For this reason, an **effective homogeneous flow** is defined on the basis of the intermittency approach. It corresponds to the homogeneous aerated flow which is effectively transported along the slope and which is involved in the dissipation process. Its characteristics are defined in the following.

- Effective mixture depth Z'
  Z' is determined for the value of z where $c'(z) = 0$. Depths higher than Z' correspond to times when the tips of the probe are in air gaps above the flow (when $T_{int} \ll 1$).

- Mean effective air concentration C' :

$$C' = \frac{1}{Z'} \int_0^{Z'} c'(z) dz \tag{13.6}$$

  with $c'(z)$ according to equation 13.4. The duration of time for which the tips are in the air gaps is not taken into account for the effective time-average air concentration.

- Mean effective mixture velocity U' :

$$U' = \frac{1}{Z'} \int_0^{Z'} u_m(z) dz \tag{13.7}$$

  with u_m, the local mixture flow velocity

The characteristics of the homogeneous flow are given in Appendix A for conventional steps (m=0) but also for all steps with endsills (m=1) and for $\theta = 30^o$.

13.4 Verification of the intermittency approach

In order to verify the physical significance of the effective homogeneous flow:

- The effective depth Z' is compared with the observed depth Z_h when the tips of the fiber-optical probe get inside the wavy free surface and spray ejections.

- The bubble sizes are compared in the homogeneous flow and the wavy surface regions.

- The relative error on the unit discharge is calculated for the effective homogeneous flow.

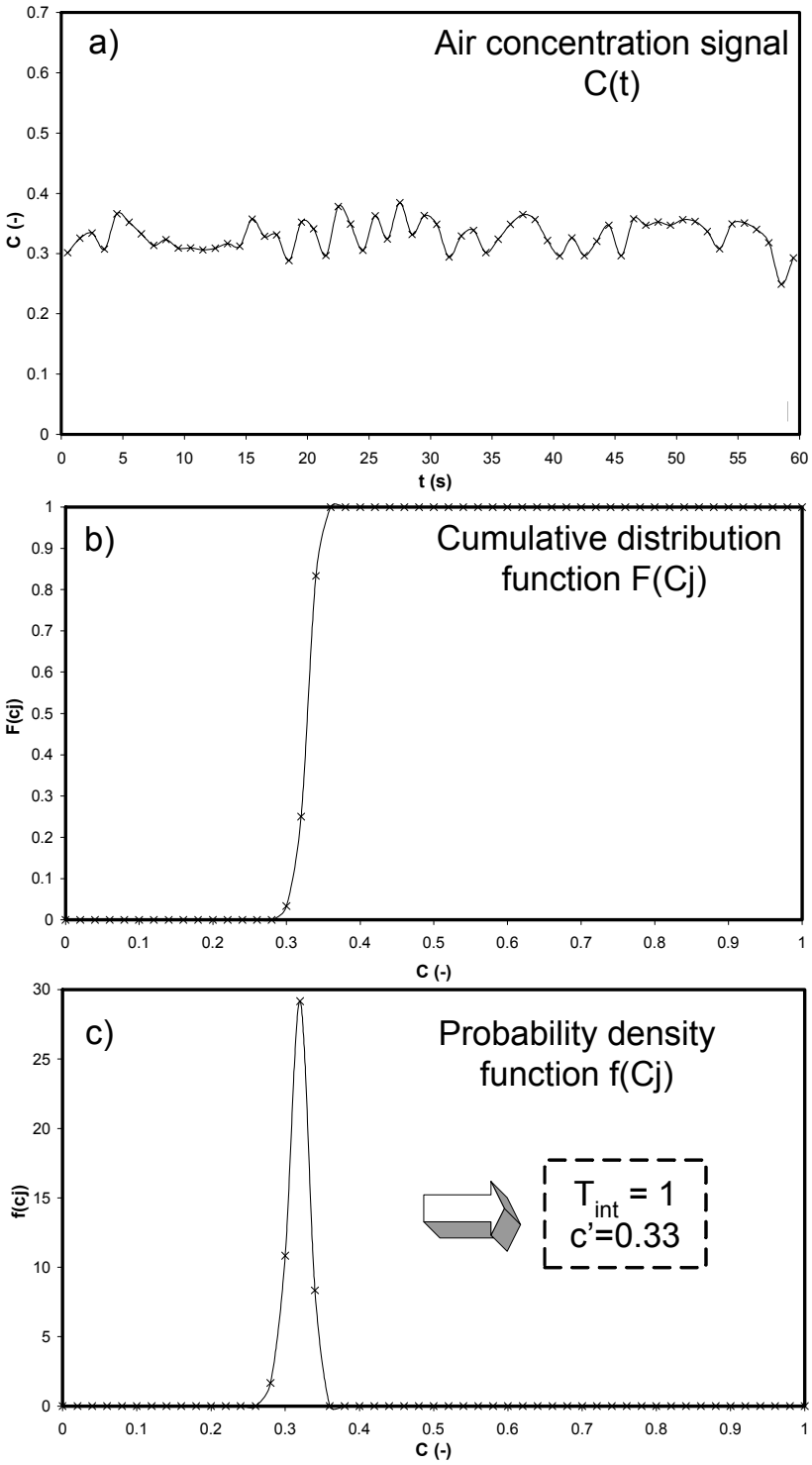

Figure 13.2: Derivation of probability density function and intermittency parameter for an air concentration measuring sample of skimming flow in fully developed region ($q_w = 0.12\ m^2/s$ and $z/Z_{90} = 0.37$)

Effective depth

The Figure 13.3 represents the effective depth Z' versus the observed homogeneous depth, Z_h and versus the homogeneous depth according to Tozzi (1994). Tozzi defined the mixture flow depth based on velocity vertical profile. It corresponds to the point just above a constant velocity (see Part III, section 9.2.2). The air concentration C_h associated to the observed depth Z_h is also plotted in Figure 13.3.

From this Figure, it can be noticed that in the range of uncertainty, Z' is in the same order of magnitude than the observed and the Tozzi's depths, with a correlation coefficient $R^2 = 0.98$.

The higher difference between Z' and Z_h, of about 14%, corresponds to low discharges for the transition regime and the beginning of the skimming flow, when the free surface of the flow is greatly wavy.

For well developed skimming flow, this intermittency approach provides an homogeneous depth quite representative of the observed homogeneous flow.

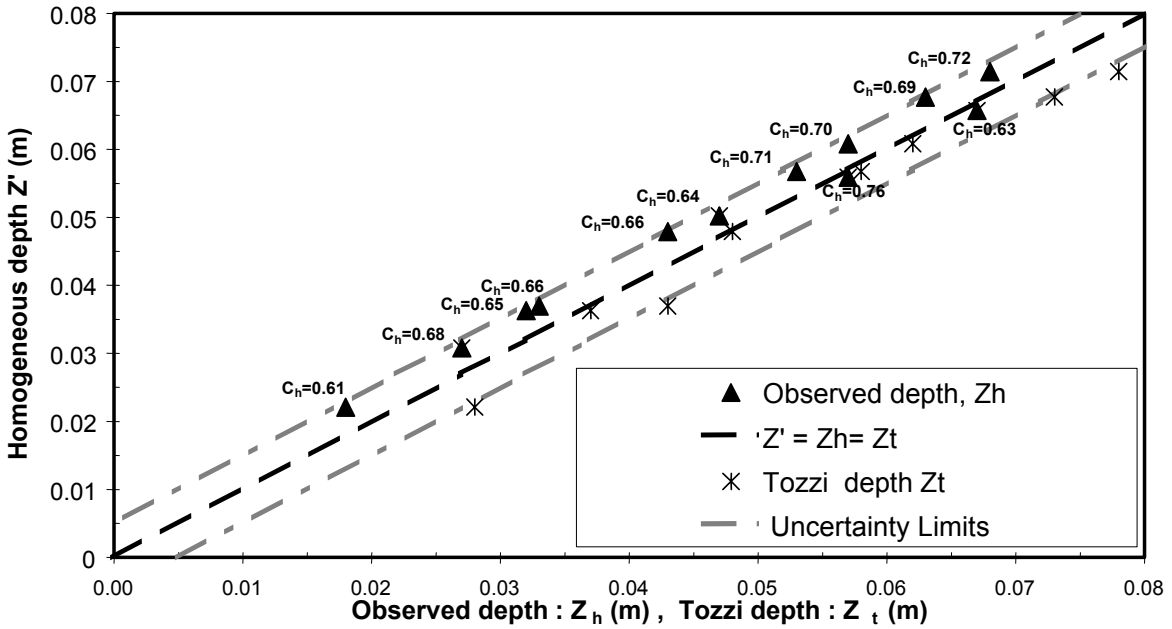

Figure 13.3: Effective homogeneous flow depth Z' (intermittency approach) versus observed homogeneous depth Z_h and mixture flow depth Z_t according to Tozzi (1994) - Transition and skimming flows over a 30^o conventional stepped chute ($q_w = 0.0606$ to 0.2416 m^2/s)

Bubble sizes

The fiber-optical probe measures the mean chord length ϕ_c of air bubbles in contact with the tips.

In the uniform region, for transition and skimming regimes, the bubble sizes are within the range:

- for $z \leq Z_{50}$ then for $c \leq 0.5 \Rightarrow$

$\phi_c = [2 - 4]$ mm

- for $Z_{50} < z \leq Z'$ then for $0.5 < c \leq 0.7 \Rightarrow$
  $\phi_c = [4 - 10]$ mm

- for $Z' < z \leq Z_{90}$ then for $0.7 < c \leq 0.9 \Rightarrow$
  $\phi_c =]10 - 50]$ mm

These results are in good agreement with Cain (1978) or Killen (1968) observations for smooth chute but also with those of Chanson & Toombes (2001a) for stepped chutes. They measured that below the surface region corresponding at air concentration less than 0.5, the bubbles size are about 0.5-3 mm and that the largest bubbles in the homogeneous flow are about 10-20 mm.

The effective depth Z' delimits indeed the homogeneous flow with air bubbles to the surface flow mostly constituted with air gaps ($\phi_c > 10mm$) and spray.

Unit discharge

Unit discharges $q'_w = \int_0^{Z'} [1 - c'(z)] u_m(z) dz$ of the effective homogeneous flow in the uniform region are given in Table A.1, Appendix A.
The relative error $(q_{pump} - q'_w)/q_{pump}$ (where q_{pump} is the water discharge provided by the pump) or the relative error considering the depth integration limit up to Z_{90} ($q_w = \int_0^{Z_{90}} [1 - c(z)] u_m(z) dz$) are quite identical. This shows that discharge is quite completely represented by the portion of the flow characterized with Z' and C'.

13.5 Conclusions

Flows over stepped chutes are characterized by highly turbulent, wavy and greatly aerated free surface. For these reasons, confusion still exists to characterize the flow. In fact, arbitrary flow depths relating to the percent of air measured, fixed between 90 % and 99 % or equivalent clear water depth $Z_w = (1 - C) Z_{90}$ have been developed.

As a consequence, the resulting mean flow velocity, friction factor and residual energy are quite scattered, depending strongly on the measured air concentration analysis and on the chosen flow depth. In light of the above, a better assessment of the flow behavior seems to strongly depend on a more accurate approach of the air concentration estimation and on a definite computed flow depth.

In this aim, the intermittency approach [Killen (1968), Cain (1978), Falvey (1980)] distinguishes:

- the portion of air which is effectively transported downstream through bubbles by the mass of water and then which constitutes the true air concentration of the homogeneous flow,

- the portion of air which is trapped between splashing waves, rollwaves and ejections, above the free surface of the mass of air-water mixture.

That leads to the definition of an homogeneous flow, characterized by a definite mixture depth Z' and a true air concentration C' which is significantly lower than the measured percent of air C: C' is within the range 35 % to 40 % instead of 45 % to 65 % for C for the same tested discharges.

Regarding shear stress or drag form effect at the step faces, it seems reasonable to assume that these head losses are not influenced by air gaps trapped between the crest at the wavy free surface. Thus energy dissipation mechanism might be concerned mainly by this aerated homogeneous portion of flow. Furthermore, the effective homogeneous flow parameters are applied to estimation of the residual energy (Chapter 15) and friction coefficients (Chapter 16.3). It will allow to determine the portion of the flow which has to be taken into account to establish head loss law for aerated flow over macro-roughness.

Chapter 14

Influence of the macro-roughness on the flow characteristics

14.1 Air entrainment

14.1.1 Onset of air entrainment

The location of the point of inception, L_i, is determined visually. It is defined as the cross section at the step outer edge where the presence of air bubbles is permanent and well distributed inside all the step and over the whole flume width (see an illustration in Fig. 14.1).

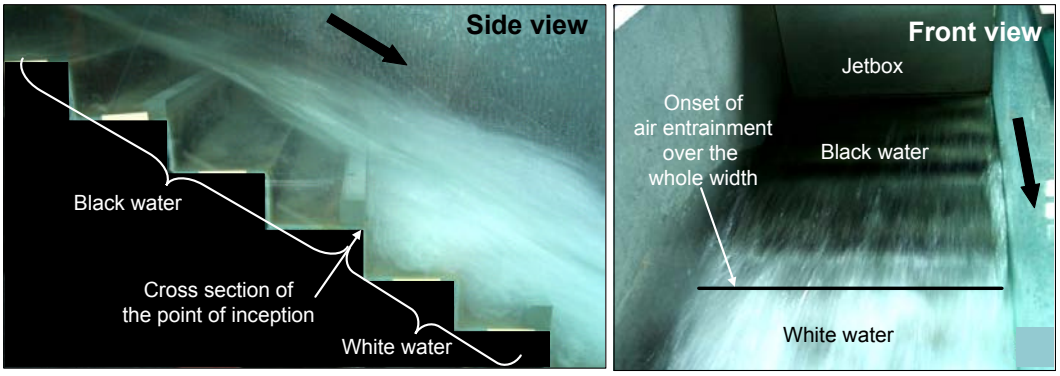

Figure 14.1: Side and front views which show the limit of black and white water regions and the location of the point of inception for a 30^o slope with endsills on every two steps ($m = 1/2$)

Conventional steps

In order to compare the observed location of the inception point in the gated laboratory flume (jetbox entrance) with the existing results for a crested entrance, L_i has been computed according to Equation 8.13 Part III, for an equivalent crested flume with the same roughness and slope.

For the 30^o inclined stepped chute, the data of L_i/k_s for jetbox condition and equivalent values for a crested entrance are plotted versus the roughness Froude number F_* in Figure 14.2. The data are compared with the relationships described in Part III, Chapter 8.2.1.

This shows that the measured data are within the range of magnitude defined by the Boes, Chamani and Chanson empirical relationships, and they display the same trend with increasing discharge. The inception point is displaced downstream as q_w increases. This can be explained by the combined effect of increasing flow depth and longitudinal velocity. First, due to the large flow depth, the turbulent boundary layer intersects the free surface further downstream. Second, due to the high longitudinal velocity compared to the vertical component, the air bubbles trapped just at the surface are transported rapidly down the slope without sinking into the flow column.

For large discharges ($F_* > 8$), when $h_c/k_s > 3$, the characteristics of the inception point become closer to smooth slope spillway values. This may be explained by the cushioning of the step drag form effect by the large skimming layer.

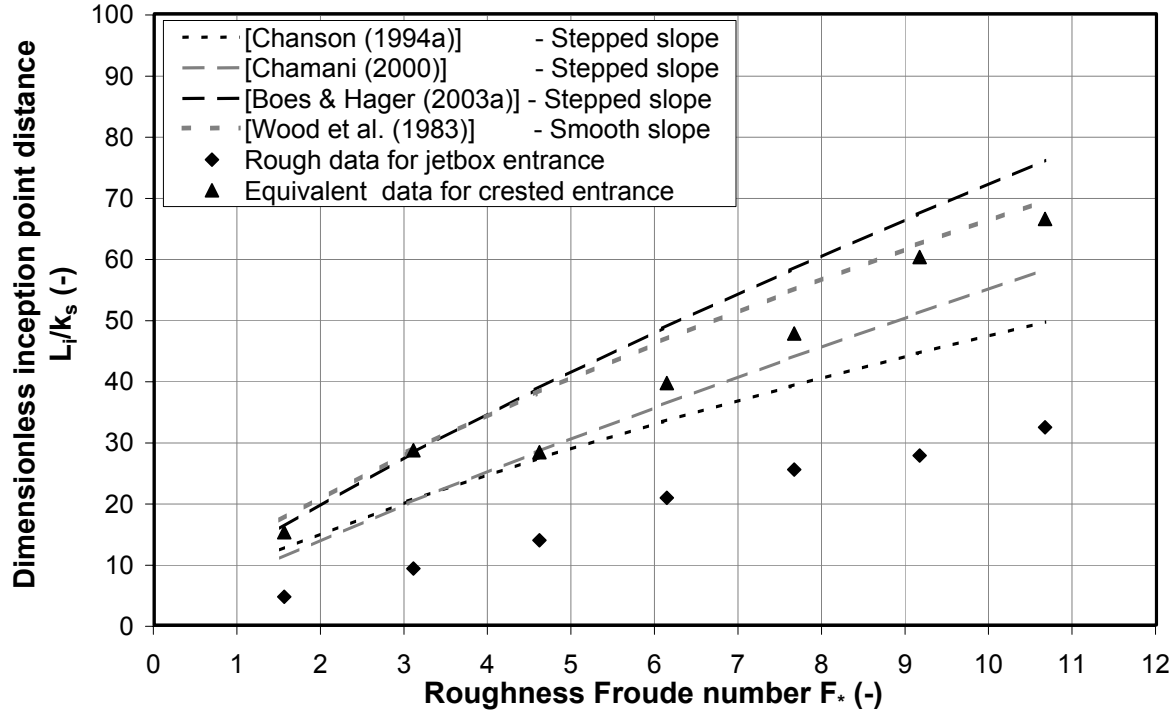

Figure 14.2: Comparison of rough (jetbox entrance) and equivalent (crested entrance) data of the dimensionless location of the inception point, L_i/k_s, according empirical formula of Wood et al. (1983), Chanson (1994a), Chamani (2000) and Boes & Hager (2003a). Data for the 30^o slope equipped with conventional steps ($m = 0$)

A comparison of the data between 18.6^o and 30^o slopes which have identical step heights highlights the fact that if the flow depth (or discharge) is the principal parameter that controls the onset of air entrainment then the slope also has a significant effect (see Fig. 14.3). The inception point is displaced towards to the crest for steeper slopes, a behaviour which is increasingly marked for high discharges. In fact, in the non aerated region, the clear water flow depth for a flat slope at a given discharge is larger than for a steep chute.

The expected location of the inception point for an equivalent crested embankment dam ($18.6^o < \theta < 30^o$) equipped with conventional rectangular steps can be described with a good correlation ($R^2 = 0.982$ for $\theta = 30^o$ and $R^2 = 0.967$ for $\theta = 18.6^o$) by the following Equation 14.1 (see Fig. 14.3):

$$\frac{L_i}{k_s} = \frac{8.0}{\tan\theta} F_{*,\theta}^{0.730} \tag{14.1}$$

with $F_{*,\theta} = q_w/\sqrt{g\cos\theta k_s^3}$, the roughness Froude number corrected for the slope effect according to Chow (1959). With $\theta = 53^o$, $\frac{L_i}{k_s} = 6.03 F_{*,\theta}^{0.730}$ which is similar results as the proposed relationship of Matos (2000b) (Eq. 8.10, Part III).

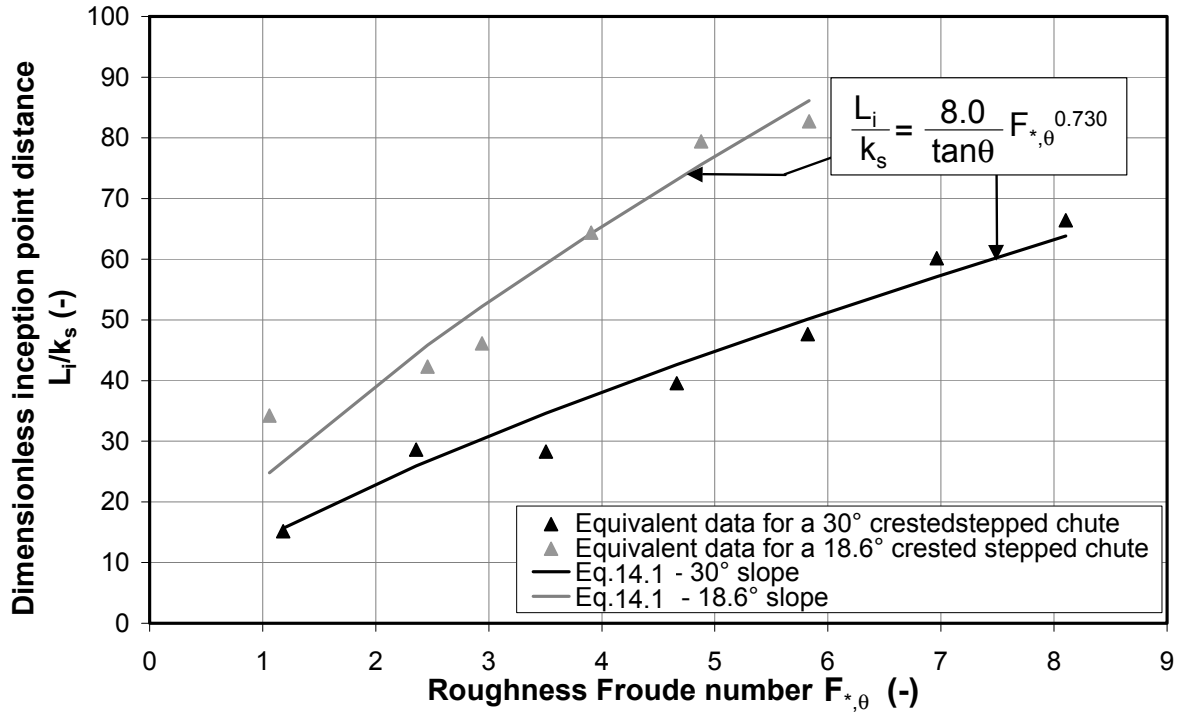

Figure 14.3: Dimensionless location of the inception point L_i/k_s versus roughness Froude number $F_{*,\theta}$ for the 18.6^o and 30^o slopes equipped with conventional steps ($m = 0$)

Influence of the macro-roughness

The dimensionless distance of the inception point from the jetbox, for all tested endsill and block configurations, is plotted versus the roughness Froude number $F_{*,\theta}$, for the 30^o slope in Figure 14.4.

In agreement with previous studies performed on crested spillway models, the height of the macro-roughness has no significant effect. Indeed, results indicate that when endsills or close-packed blocks are added on each step ($m = 1$, $m = 5$ and $m = 6$ respectively), the location of the inception point remains identical for all tested discharges.

However, in the case of alternated endsills ($m = 1/2$) and spaced blocks pattern ($m = 4$), a displacement of the inception point can be observed for well established skimming flow regime, when $F_{*,\theta} \geq 4$. The onset of aeration for these two overlays is at the same position and is nearer to the crest compared to the other macro-roughness systems. This difference may not be the result of a different relative flow depth $Z_{90,u}/k_T$ with $k_T = k_s + k_r$ since the values are quite similar for all the overlays. However, the longitudinal spatial distribution for $m = 1/2$ ($x_r/x_s = 2$) as well as the transverse pattern for $m = 4$ ($e_r/b_r = 1.5$) are the largest compared to other overlays. The resulting **effective roughness**, *i.e.* the roughness which has a real significant effect on the flow behaviour, is larger for these two particular configurations ($m = 1/2$ and $m = 4$) than for the others. And as mentioned by Lane (1939), this results in an earlier onset of air entrainment.

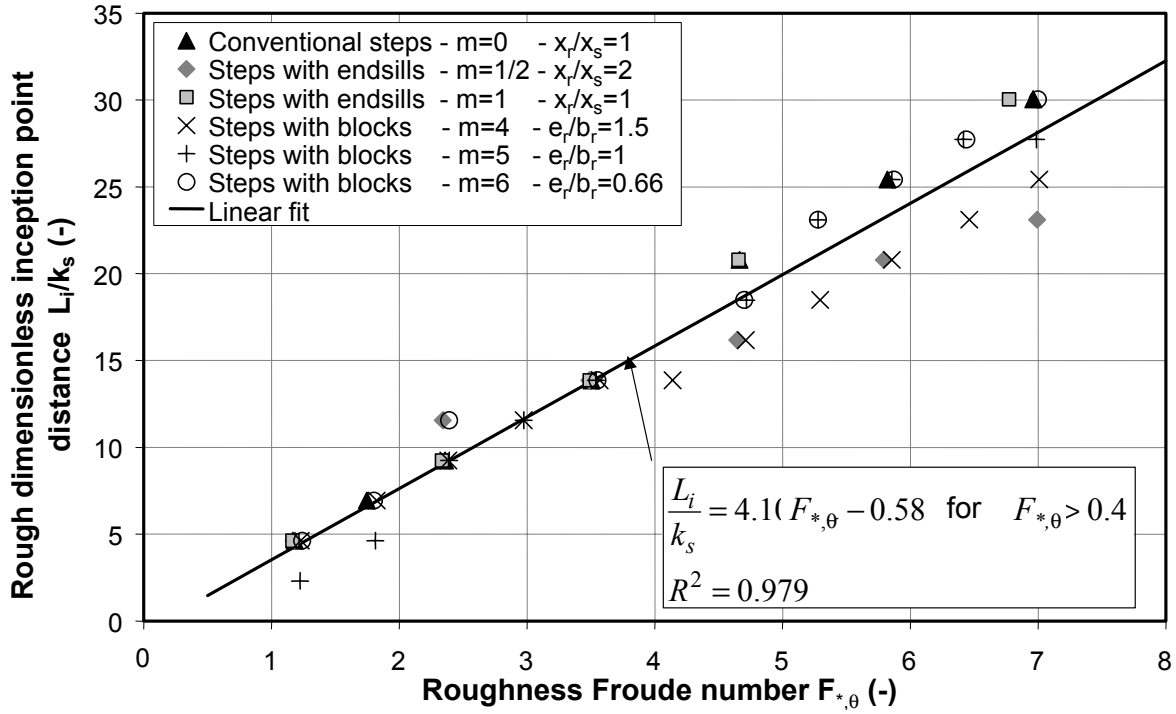

Figure 14.4: Rough data (jetbox entrance) of the dimensionless location of the inception point versus $F_{*,\theta}$ for the 30^o slope with conventional steps ($m = 0$), steps equipped with endsills ($m = 1/2$ and $m = 1$) and steps equipped with blocks ($m = 4$, $m = 5$, $m = 6$)

14.1.2 Effect of the macro-roughness on the mean air concentration in the uniform region

Conventional step

For conventional steps ($m = 0$), the variation of the mean air concentration C_u in the uniform region with the roughness Froude number $F_{*,\theta}$ is shown in Figure 14.5.

The figure shows that C_u varies with the flow regime. The mean air concentration value decreases drastically for the nappe and transition flow regimes to reach an asymptotic value $C_{u,s}$ for $F_{*,\theta} = 4$, when the skimming flow is well developed.
For nappe regime the fluid is highly aerated due to the great air entrainment when the free-falling nappe breaks on the step face. Whereas for transition and skimming regimes, the air entrainment is mainly the result of free-surface exchange.

In contrast to the suggestions of Boes & Minor (2000), the asymptotic value is not systematically attained for the onset of skimming flow. The data indicate that the air concentration remains constant regardless of the discharge values when the skimming layer is large compared to the normal step height. That is, $Z_{90,u} \simeq 1.3k_s$ or $h_c \simeq 2h_s$.
For the 30^o slope, a good representation of the mean air concentration can be given by Equations 14.2 and 14.3.

For $F_{*,\theta} \leq 4 \quad (R^2 = 0.963)$

$$C_u = 0.55 F_{*,\theta}^{-0.12} \tag{14.2}$$

For $F_{*,\theta} > 4$ $\quad (R^2 > 0.997)$

$$C_u = C_{u,s} = 0.81 \sin\theta^{0.81} \tag{14.3}$$

Therefore, compared to smooth chute, steps enhance the onset of air entrainment and slightly increase the mean air concentration $C_{u,s}$.

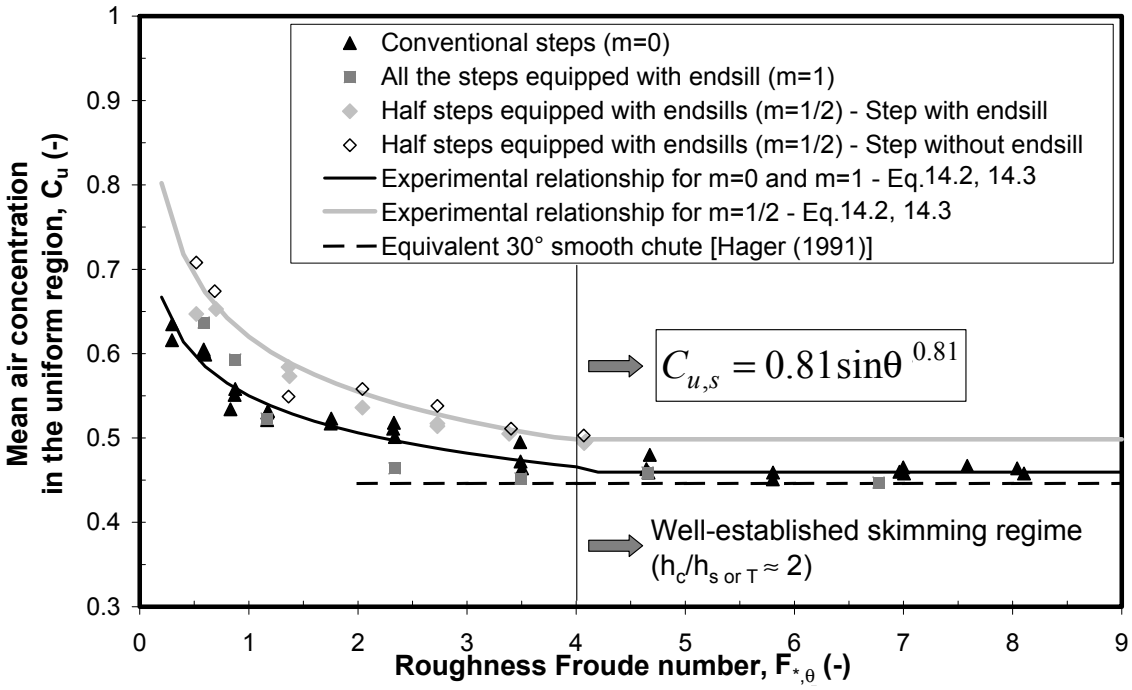

Figure 14.5: Mean air concentration in the quasi-uniform region versus roughness Froude number for the 30^o chute with conventional steps ($m = 0$), an endsill on all steps ($m = 1$) and an endsill on every second step ($m = 1/2$)

Effect of the endsills

♢ *Stepped chute with endsills on all steps ($m = 1$)*

The presence of endsills on each step does not cause significant changes in mean air concentration. This result is not surprising as both the onset criteria of flow regimes and the characteristics of the point of inception for $m = 0$ or $m = 1$ were found to be identical. The only change lies in the displacement of the pseudo-bottom defined by the endsill outer edges by a distance of $k_r = h_r \cos\theta$. That does not significantly affect mean air concentration. This behaviour agrees with the suggestions of Boes & Minor (2000) who mentioned that mean air concentration is independent of step height.

Therefore, it is suggested that the mean air concentration for $m = 1$ can also be derived from Equations 14.2 and 14.3, with the height of the roughness equal to k_s in the roughness Froude number $F_{*,\theta}$.

♢ *Stepped chute with an endsill on every second step ($m = 1/2$)*

The situation is different for the overlay where every second step is equipped with an endsill

($m = 1/2$). In this case, the notion of pseudo-bottom parallel to the mean slope has no sense since the topography is irregular along the slope.

The discharge limitations of the experimental set up did not allow a verification that if $C_{u,s}$ remains constant for large $F_{*,\theta}$. Nevertheless, it can be inferred that the mean air concentration follows the same variation behaviour with respect to flow regimes as $m = 0$. Indeed, in the present case skimming flow starts for $q_w = 0.12\ m^2/s$ compared to $q_w = 0.06\ m^2/s$ for $m = 0$ and $m = 1$.

However, the mean air concentration remains about 4 to 5 % larger for all discharges. The discontinuity pattern of endsills seems to involve more air entrainment when the nappe falls from one step with a vertical face of height $h_T = h_s + h_r$ to the following one with an height that is h_s.
Data presented in Fig. 14.5 also indicates that in the uniform region, the depth-averaged air concentration is quite constant from one conventional step to the following one quipped with an endsill.

Finally, for mean air concentration values in the uniform region, the overlay behaves like a slope of angle $\theta* = 33.3^o$ equipped with equivalent steps of normal height $k_T = (h_s + h_r)\cos\theta*$ (see Fig. 14.6). In fact, this equivalent configuration leads to a behaviour comparable to conventional steps with :
For $F_{*,\theta*} < 4$ with $F_{*,\theta*} = q_w/\sqrt{g\cos\theta * k_T^3}$:

$$C_u = 0.62 F_{*,\theta*}^{-0.16} \tag{14.4}$$

For $F_{*,\theta*} \geq 4$

$$C_u = C_{u,s} = 0.81 \sin\theta*^{0.81} \tag{14.5}$$

It can be noted here that the criterion of $F_{*,\theta*} = 4$ corresponds also in this case to $h_c/h_T \simeq 2$ or $Z_{90,u}/k_T \simeq 1$, when the macro-turbulence effects seem cushioned by the large skimming layer.

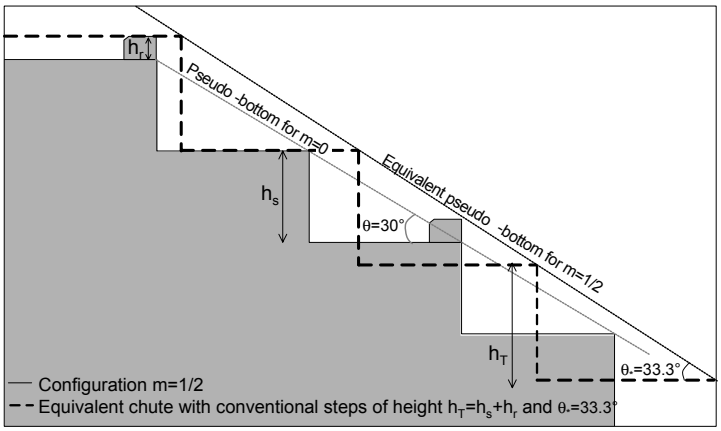

Figure 14.6: Definition of the equivalent slope condition implemented in the mean air concentration formula (Eq. 14.4, 14.5 for the configuration $m = 1/2$)

14.1.3 Vertical distribution of the air concentration

Chanson (2000) proposed that the vertical air concentration profile in the quasi-uniform region depends upon flow regimes.

For the skimming regime, profiles were derived from the solution to the continuity equation of the mixture air-water flow including the balance between the turbulent diffusivity and the bubble rise velocity. For the transition regime, the profile resulted from empirical fitting (details in Part III, Chapter 9.1.3). No information were available for nappe flow regime.

Air concentration were measured for the 30^o inclined chute equipped with conventional steps ($m = 0$) and steps with endsills ($m = 1/2$, $m = 1$) in the developing and equilibrium regions (see Fig. 11.11). The following results show the influence of flow regimes, flow regions and macro-roughness elements on the vertical air distribution of the air concentration.

Advective diffusion air bubble model for conventional steps

♢ *Skimming flow regime*

◇ *In the equilibrium region*

Air concentrations measured at the leading tip of the fiber-optical probe are plotted in Figure 14.7 versus the dimensionless depth $H_{90} = z/Z_{90}$ (where Z_{90} is the depth at 90 % of air content) for skimming flow regime.

Air concentrations at the step outer edge have smooth continuous profiles for the whole depth of the flow. For all tested discharges, the vertical distribution of $c(z)$ correlates well with the advective diffusion air bubble model (ADM) of Chanson (2000) given by Eq. 9.8 in Part III.

The profiles also highlight that:

- For a same discharge, the 3 tested cross sections ($X_1 = 5.4$ m, $X_2 = 5.64$ m, $X_3 = 7.2$ m in Fig. 11.11) are effectively in the quasi-uniform region since within ± 1 %, $c_1(z) = c_2(z) = c_3(z)$ (with $c_1(z)$ the local air concentration at the distance z above the step outer edge located at X_1).
- For a well-developed skimming flow ($q_w > 0.12$ m^2/s), the profiles are identical which is as expected since the mean air concentration remains constant.

◇ *In the developing region*

The air concentration is lower in the developing region (see Fig. 14.7) for identical discharges as expected. However, the profiles indicate that there is no difference in the air concentration distribution for these two aerated regions. In the developing region, the aeration mechanism also follows the advective diffusion model. Under this condition, the turbulent diffusive constant D' is computed by Eq. 9.9, Part III, but with the equilibrium air concentration substituted by the depth-averaged, C.

Finally experimental results show that the advective diffusion model remains valid even if the equilibrium between air entrainment and detrainment is not attained. The mechanism of aeration is therefore independent of flow regions.

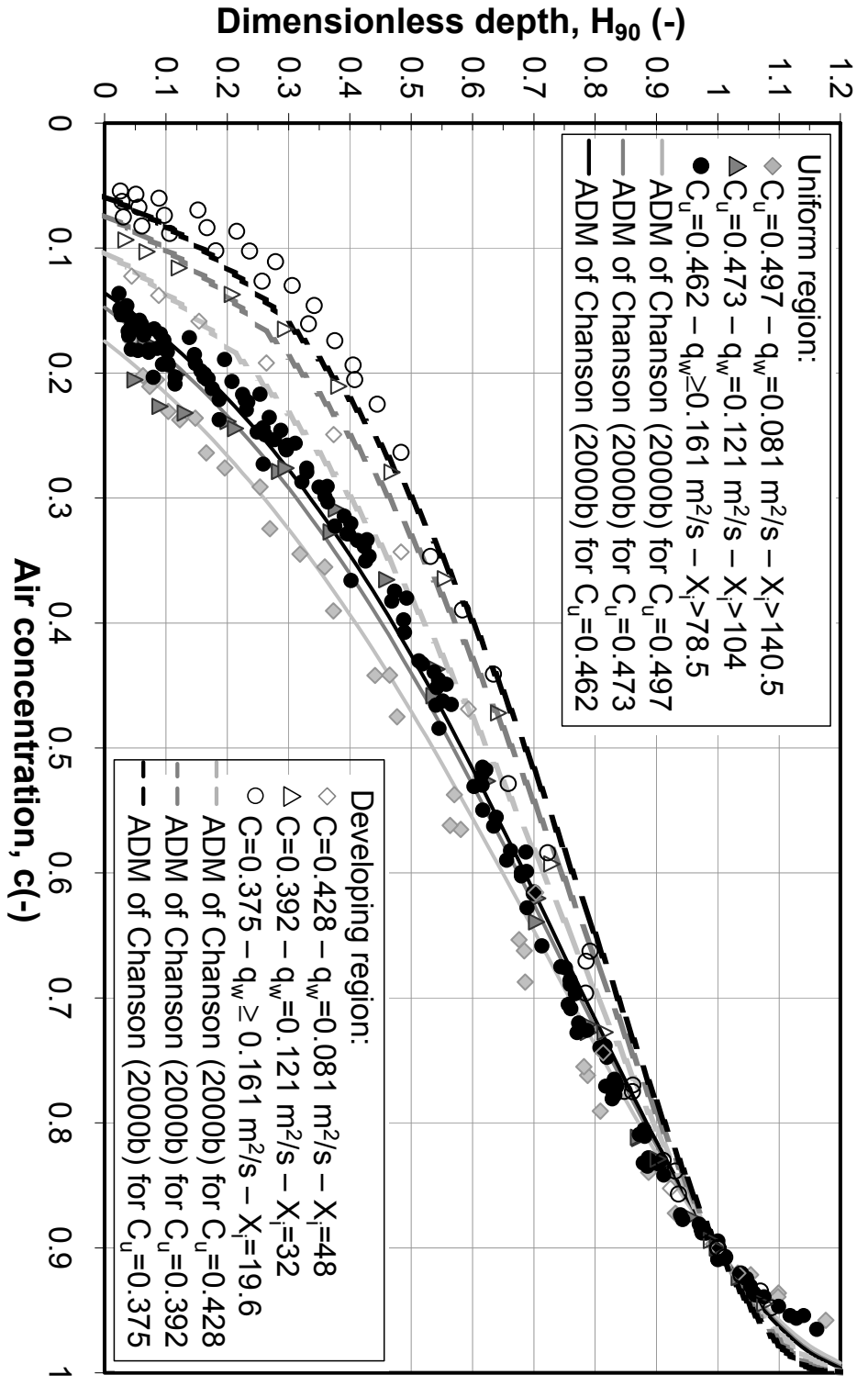

Figure 14.7: Vertical distribution of air concentration measured in the developing region (C) and in the equilibrium region (C_u) for skimming flow over the 30^o conventional stepped flume. Comparison with the advective diffusion model of Chanson (2000b)

◊ *Transition flow regime*

As already mentioned in Chapter 12.2, compared to skimming regime, the visual observations for transition flow above the pseudo-bottom do not indicate significant changes in the aerated flow structure. Except that the skimming layer is thinner and more influenced by topographical effects such as the internal jet. Therefore, the amplitudes of the wavy free surface are larger but with the same ejection of water droplets. Below the pseudo-bottom, until the onset of rotation of the well-developed vortices, the pool of water is practically non aerated.

In light of the above, it is not surprising to see in Figure 14.8 that the vertical distribution in both equilibrium and developed regions also show continuous and smooth profiles which follow the advective diffusive model for $c(z) < 0.7$. This portion of flow corresponds to the homogeneous aerated flow as described in Part III, Fig. 9.2, layer 2.
However, for $c(z) \geq 0.7$, the measured air concentration is larger than predicted by ADM profiling. This difference may be attributed to the influence of the waves. In fact, the tip of the fiber-optical probe which detects the change between air and water phases in the flow, does not distinguish air bubbles in the water from air gaps between two wave crests. In the latter case, the value of $c(z)$ does not characterize the "true" air concentration of the mixture air-water resulting from the self-aeration advective-diffusive process. This notion of true air concentration has been discussed in detail in Chapter 13.

Therefore, in transition flow regimes, for both developing and quasi-uniform aerated regions, the vertical distribution of the air concentration can be predicted with a good correlation from the following equations:

- In homogeneous flow, for $c(z) < 0.7$

$$c(z) = 1 - tanh^2\left(K' - \frac{\frac{z}{Z_{90}}}{2D'}\right) \tag{14.6}$$

  where K' and D' are computed from the mean air concentration has described in Part III, Chapter 9.1.3.

- In the wavy rough free surface layer, for $c(z) \geq 0.7$

$$c(z) = 1.25\left[1 - \exp\left(-1.25\frac{z}{Z_{90}}\right)\right] \tag{14.7}$$

For tested discharges in the transition flow regime, the portion of air in the free surface layer of the flow is constant. The air gaps between the waves contribute significantly to the increase of measured air concentration in this portion of the flow.

Finally, from the Figure 14.8, it can also be inferred that for the 30^o conventional stepped chute, the model proposed by Chanson & Toombes (2001b) (Eq. 9.10, Part III) concerning transition regime does not satisfactorily describe the measured data. This model predicts no aeration in the first millimeters above the step outer edge and leads to an over-estimation of the air concentration in the homogeneous flow. Moreover, large instabilities, vibration and ejections of numerous water droplets in this regime were not observed for this particular regime, contrary to the observations of Chanson.

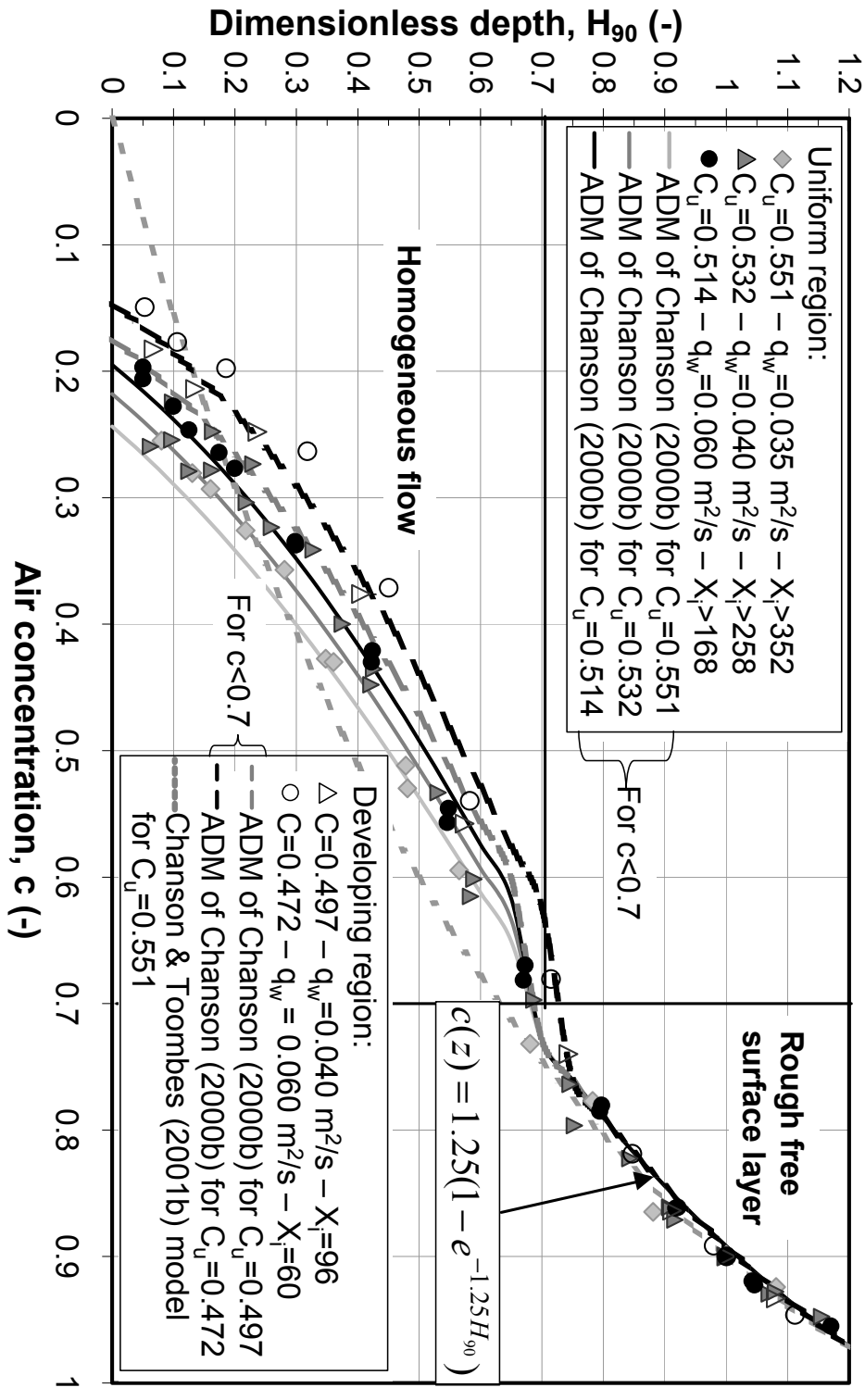

Figure 14.8: Vertical distribution of the air concentration measured in the developing (C) and equilibrium regions (C_u) for transition flow over the 30^o conventional stepped flume. Comparison with the empirical model proposed by Chanson & Toombes (2001b)

♢ *Nappe flow regime*

Due to the non homogeneity of the nappe and due to instabilities such as rollwaves, it was difficult to visually ascertain if the tips of the fiber-optical probe were effectively inside the flow during the measurement sequences. Therefore, the air concentration values do not distinguish if air is effectively trapped in the water or in gaps between two waves or in falling jets. Nevertheless, in Figure 14.9, the data is plotted versus the dimensionless depth $H_{90} = z/Z_{90}$ for two discharges in nappe flow ($q_w = 0.010\ m^2/s$ and $q_w = 0.020\ m^2/s$) and one discharge at the limit of onset of transition regime ($q_w = 0.030\ m^2/s$). Data for a well-developed skimming flow is also plotted in order to highlight the differences in behaviour depending on flow regime.

The measured profiles clearly indicate that the distribution of air concentration in nappe regime is different than in skimming regime for $0.25 \leq H_{90} \leq 1$. As expected, in this portion of the flow, air concentrations do not follow the advective diffusion model, being larger than the predicted values. This may be explained by the high rate of air trapped when the falling nappe is broken at the downstream corner of the horizontal step and by the non homogeneity of the nappe and the air gaps between two crests of rollwaves.

Finally, for well defined nappe flow, as illustrated in Figure 14.9, at $H_{90} \geq 0.25$, the vertical distribution of the air concentration follows the exponential empirical law (Eq. 9.10) proposed by Chanson & Toombes (2001b) (see Part III, Chapter 9.1.3) though this relation was basically developed for transition regime. Definition of transition regime must be different for these authors compared to herein.

Then for $z/Z_{90} \geq 0.25$ $\quad c(z) = K_3[1 - \exp(-\lambda H_{90})]$

where K_3 and λ are derived from the mean air concentration and the concentration at 90 %. This confirms that for this regime (as observed by Fratino et al. (2003)) intense aeration is the result of the plunge nappe breaking close to the step outer edge as opposed to transition and skimming regimes where the air entrainment process is governed by turbulent diffusion of the air bubbles trapped at the free-surface. In the inner layer, for $H_{90} \leq 0.25$, which corresponds to the first 5 mm above the step outer edge, the data shows that air concentration is comparable to the ADM profile as for the two other flow regimes.

At onset of transition regime (triangles in Fig. 14.9), the exponential profile tends toward the ADM profile in the homogeneous portion of the flow ($c < 0.7$), although air concentration in the wavy free surface layer remains larger than for the skimming layer, with a gradient governed by Eq. 14.7.

Thus, the change of flow regime between nappe, transition and skimming flows can be objectively determined by air concentration profile variation. That sustains the onset criterion for transition and skimming flows used in Chapter 12.2.

Finally, for all tested discharges, the air concentration values lie between the two curves plotted in Figure 14.9 and given by:

(1) : For $H_{90} < 0.25$: $\quad c(z) = 1 - tanh^2\left(1.077 - \frac{H_{90}}{1.334}\right)$

For $\quad H_{90} \geq 0.25$: $c(z) = 0.96[1 - \exp(-2.76 H_{90})]$

(2) : $\forall H_{90}$ $\quad c(z) = 1 - tanh^2\left(1.655 - \frac{H_{90}}{0.754}\right)$

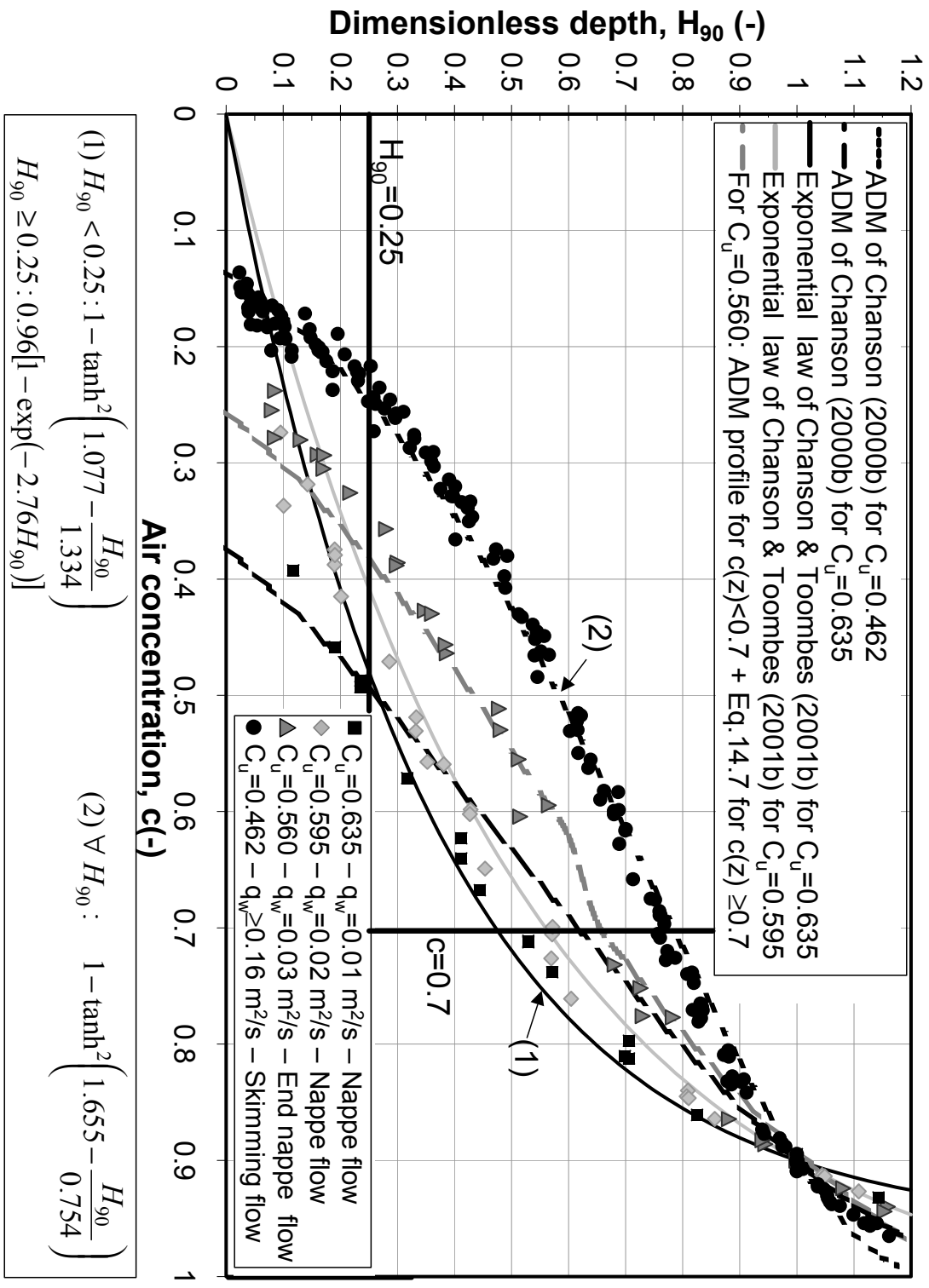

Figure 14.9: Vertical distribution of the air concentration measured in the equilibrium region (C_u) for the nappe flow regime over the 30^o conventional stepped flume. Comparison with the ADV profile [Chanson (2000b)] and the empirical relation proposed by Chanson & Toombes (2001b)

Influence of the endsills

◇ *Stepped chute with an endsill on every step ($m = 1$)*
Mean air concentration and onset of air entrainment were not significantly affected by the addition of an endsill at the end of each step. It is therefore not surprising to see that the vertical distribution of the air concentration above the endsill outer edge is more or less identical to the conventional step case.
For transition and skimming flows, the vertical distribution of air concentration correlates well with the advective diffusion model profile, confirming that this overlay ($m = 1$) amounts to a displacement of the pseudo-bottom by a distance $k_r = h_r \cos\theta$, without significant effect on self-aeration.

◇ *Stepped chute with an endsill on every second step ($m = 1/2$)*
For this particular configuration, no measurements were possible during nappe flow which occurs only at very low discharge. That was difficult thus to stabilize with the hydraulic pump system used.

Concerning the steps equipped with endsills, the aerated flow above the endsill outer edge shows the same behaviour as for conventional steps or as the overlay $m = 1$ but based on a higher mean air concentration (see Paragraph 14.1.2). Thus, for skimming flow ($q_w \geq 0.12$ m^2/s), the vertical distribution of air concentration globally follows the ADM profile. Furthermore, for transition regime, in the homogeneous layer (up to $c(z) = 0.7$), the aeration process is also governed by the ADM profile whereas, measured air concentration in the free surface layer is larger than predicted and follows the exponential relationship given in Equation 14.7.

The air concentration distribution in the cross section above the outer edge of the steps without endsills shows a different behaviour. From Figure 14.10, it can be observed that in the uniform region, if the mean air concentration is constant from one cross section at the step outer edge to the following cross section at the endsill outer edge, the vertical distribution of air concentration is quite different.
In the first two centimeters above the step corner, for $H_{90} \leq 0.25$, $c(z)$ is about 5 % to 8 % lower than values measured at the same points for $m = 0$. In fact, as it can be observed in Figure 14.11b, for m=1/2, the inner layer of the flow ($H_{90} \leq 0.25$) defines a zone where the flow separates into two recirculating cells, one in each of the following steps. The turbulent normal velocity in this stagnation region is expected to be very low explaining the difficulty for air bubbles to be entrained downwards in this layer.

For skimming flow and $H_{90} > 0.25$ ($H_{90} > 0.25$ corresponding to the pseudo-bottom formed by the endsills outer edges), the skimming layer is highly aerated compared to the equivalent layer above the endsill. For this portion of flow, the air concentration distribution can be derived from the advective diffusion profile but the turbulent diffusive constant D' must be calculated based on the depth-average air concentration taken between $H_{90} = 0.25$ and $H_{90} = 1$.

For transition regime, the flow structure in the step without endsills is identical to nappe flow over conventional steps (see Fig. 14.11a). The air concentration values follow the expo-

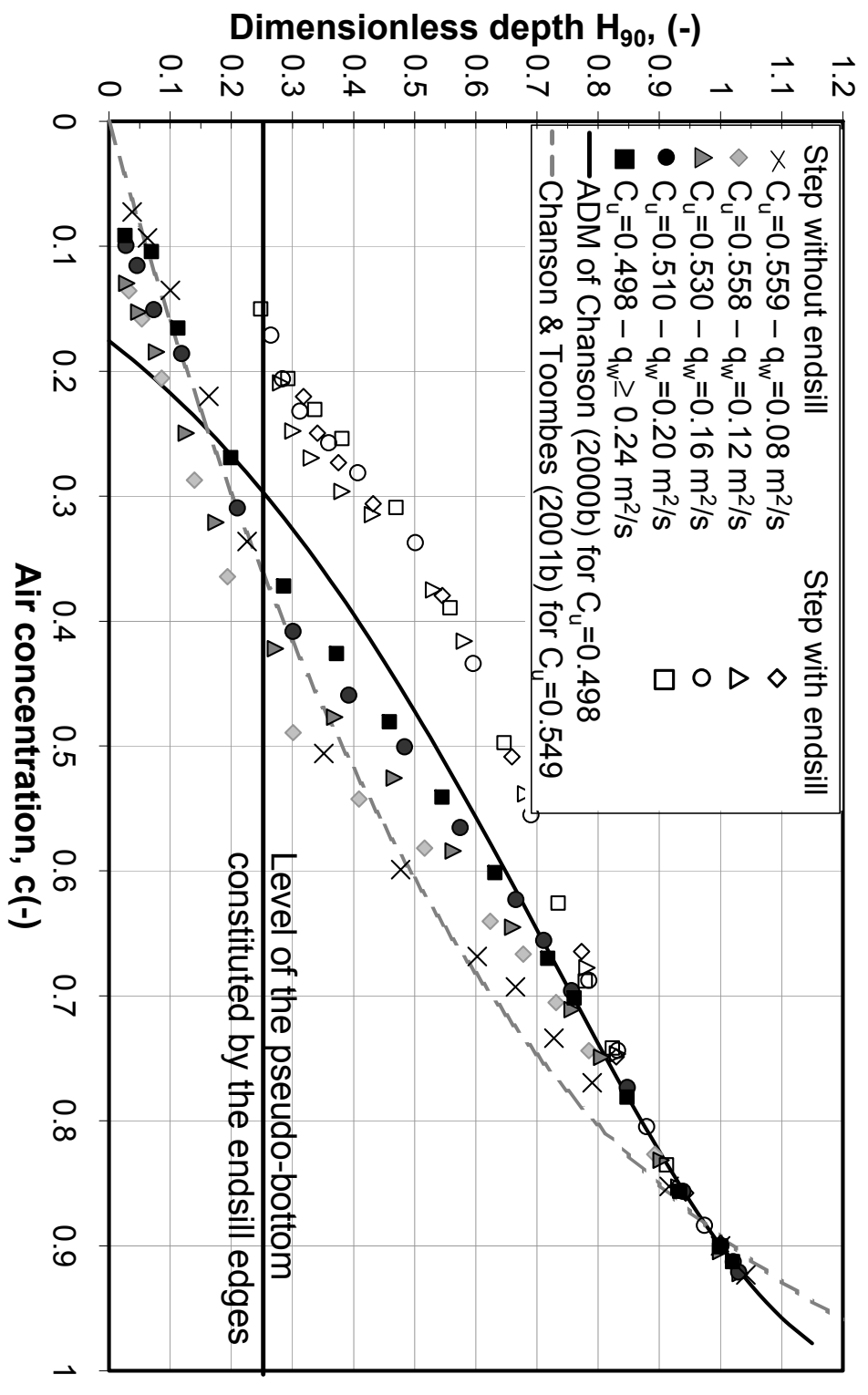

Figure 14.10: Vertical distribution of the air concentration for $m = 1/2$ measured in the equilibrium region (C_u) for skimming ($q_w \geq 0.12m^2/s$) and transition flows ($q_w = 0.08m^2/s$) over the 30^o inclined chute. Comparison with the ADM profile [Chanson (2000b)] and the empirical relation proposed by Chanson & Toombes (2001b)

nential profiles proposed by Chanson & Toombes (2001b) for the tested discharges, described by Equation 9.10, Part III: $c(z) = K_3 \left[1 - \exp\left(-\lambda \frac{z}{Z_{90}}\right)\right]$ with K_3 and λ derived from the mean air concentration. As it can be seen in Figure 14.10, by comparing transition regime profiles to profiles for onset of skimming flow and for skimming flow itself, the change of regimes can be determined by the shape of the vertical distribution $c(z)$.

In conclusion, the configuration $m = 1/2$ provides higher aeration in the homogeneous flow. The impact of the macro-roughness elements is then more significant than for the configurations $m = 0$ and $m = 1$. The induced turbulent forces may then be globally greater than in the two previous cases.

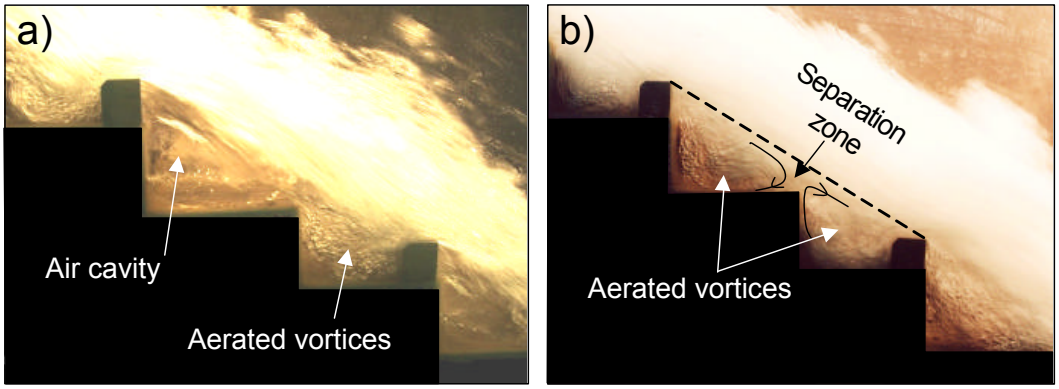

Figure 14.11: Flow structure for a) $q_w = 0.04$ m^2/s (transition regime) and b) for $q_w = 0.12$ m^2/s (skimming regime) over the 30^o stepped flume equipped with an endsill on every second step ($m = 1/2$)

Air concentration boundary layer

Analysis of the vertical distribution of air concentration for conventional steps in transition and skimming flows, yields two important facts concerning the flow layers:

1. The confirmation that portion of the homogeneous flow characterized by air concentration lower than 70 % is governed by advection, turbulent diffusion and transport of air bubbles trapped at the free surface. This point is then in agreement with the Cain's intermittency concept developed in Chapter 13.

2. The existence of an air concentration boundary layer

Indeed, for the later point, air concentration profiles can be compared with the advective diffusion model developed by Wood (1991) based on the Straub & Anderson (1958) data. When applied to an equivalent smooth chute with an identical mean saturation air concentration, the air concentration can be computed as:

$$c(z) = \frac{\beta}{\beta + \exp(\gamma \cos\theta \frac{z}{Z_{90}})} \tag{14.8}$$

where γ is a constant depending on the mean air concentration in the equilibrium region. It can be empirically determined according Wood (1991). β is calculated using a free surface boundary condition given by $\beta/(\beta + e^{\gamma \cos\theta}) = 0.9$.

In the upper layer of the flow, for $H_{90} = z/Z_{90} > 0.25$, air concentration distributions for smooth and stepped chutes are comparable (see Fig. 14.12). However, for $z/Z_{90} \leq 0.25$, the data for $m = 0$ is lower than expected for equivalent smooth chute. In agreement with Matos (2000a), these results indicate the presence of an air concentration boundary layer which may characterize the drag form influence of the step in the turbulent boundary layer. In the equilibrium region, for transition and skimming regimes, it was also visually observed that this portion of flow within the first 1.5 to 2 cm above the step outer edge is strongly disturbed by internal jet.
The data for transition and skimming regimes shows that the thickness of the boundary layer remains constant up to $H_{90} = z/Z_{90} \leq 0.25$, regardless of discharge.

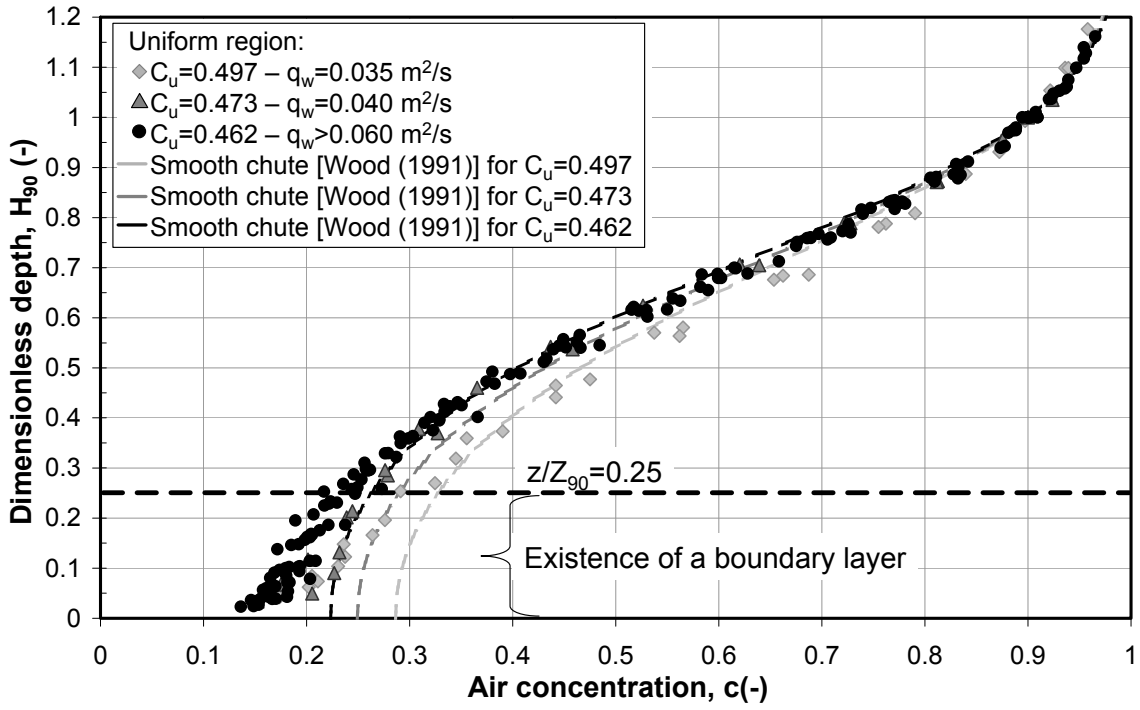

Figure 14.12: Comparison of the vertical distribution of the measured air concentration in the equilibrium region with the computed values for an equivalent smooth chute according to Wood (1991). Data for skimming flow regime over the 30^o conventional stepped flume

In skimming flow, for both configurations $m = 1/2$ and $m = 1$, the vertical distribution $c(z)$ above the endsill outer edge was also compared with the equivalent profiles for smooth slopes.

For $m = 1$, the intersection of smooth and ADM profiles is displaced to $H_{90} = 0.20$. Above endsills corners, the boundary layer is then thinner. Whereas, for $m = 1/2$, the intersection between the two distributions corresponds to $H_{90} \simeq 0.3$ to 0.35.

Therefore the higher concentration value as well as the thicker air concentration boundary layer observed for the macro-roughness system $m = 1/2$ may suggest that the global equivalent roughness of this overlay is larger than for $m = 0$ and $m = 1$.

14.1.4 Pseudo-bottom air concentration

Due to the fragility of the diamond tips of the fiber-optical probe, the measurements were taken at a distance of 2 ± 0.2 mm above the outer edge of the step or of the endsill. If the data give the air concentration *near* the step face, it appears premature to conclude that they are representative of the values in the inner layer at the bottom where cavitation mechanism may occur.

For these reasons, the "pseudo-bottom" values of air concentration were not used to investigate the macro-roughness effect on the risk of cavitation.

14.1.5 Conclusions

♢ *Self-aeration mechanism*
For nappe flow regime, air is mainly entrained at the plunging point where the nappe is broken or when hydraulic jump is developed.

For transition and skimming regimes, self aeration is initiated at the free surface: air bubbles are trapped at flow surface when turbulent forces overcome superficial tension and bubble rise velocity. Air entrainment and detrainment are governed by the mixture flow continuity equation:

$$\frac{\partial}{\partial z}\left(D_t \frac{\partial c(z)}{\partial z}\right) = \cos\theta \frac{\partial}{\partial t}[u_r c(z)] \tag{14.9}$$

where D_t is the turbulent diffusivity characteristic of the flow density and u_r is the air bubble rise velocity.

♢ *Onset of air entrainment*
For the 18.6^o and the 30^o slope, compared to equivalent smooth chutes, the roughness due to the macro-roughness elements (steps and endsills) displaces the onset of air entrainment closer to the crest chute which reduces the reach of the dam slope prone to cavitation.

For crested slope equipped with conventional steps, a good approximation of the longitudinal location of the point of inception is given by Eq. 14.1

$$\frac{L_i}{k_s} = \frac{8.0}{\tan\theta} F_{*,\theta}^{0.730}$$

For well developed skimming flow, the two overlays $m = 1/2$ and $m = 4$ lead to a displacement of the point of inception upstream.

♢ *Mean air concentration*
For conventional 30^o stepped chutes or stepped chutes equipped with endsills, the mean air concentration depends on flow regimes. The mean equilibrium air concentration C_u decreases exponentially from nappe flow to skimming flow :

$$C_u = A F_{*,\theta}^{-b}$$

with $F_{*,\theta} = q_w/\sqrt{g\cos\theta k_*^3}$ the roughness Froude number, A and b experimentally fitted constant and k_* the equivalent normal height of the effective macro-roughness element, i.e., the roughness height which has a significant effect on the self-aeration.
The mean air concentration becomes independent of discharge for well developed skimming flow, corresponding to $h_c/h_* \simeq 2$.

$C_u = 0.81\sin\theta_*^{0.81}$ then depends principally on the equivalent pseudo-bottom slope.
Data shows that for conventional steps ($m = 0$) and all steps equipped with endsills ($m = 1$), $h_* = h_s$ and $\theta_* = \theta = 30^o$ whereas for steps equipped with alternating endsills ($m = 1/2$), $h_* = h_s + h_r$ and $\theta_* = 33.3^o$.

$\diamondsuit$ *Vertical air concentration distribution*
The shape of the profile is the same as for endsills configurations.

For nappe flow regime, the profiles are predicted by the exponential relationship (Eq. 9.10) experimentally established by [Chanson & Toombes (2001b)]:

$$c(z) = K_3\left[1 - \exp\left(-\lambda\frac{z}{Z_{90}}\right)\right]$$

where K_3 and λ depend on the corresponding mean air concentration and are derived from the two following relationships: $K_3 = \dfrac{0.9}{1-\exp(-\lambda)}$ and $C = K_3 - \dfrac{0.9}{\lambda}$.

For transition and skimming flow regimes, the homogeneous portion of the aerated flow is accurately described by the ADM profile developed by Chanson (2000), Eq. 9.8 :

$$c(z) = 1 - tanh^2\left(K' - \frac{\frac{z}{Z_{90}}}{2D'}\right)$$

with $K' = arctanh(\sqrt{0.1}) + [1/(2D')]$ and $C_u = 2D'\left[tanh\left(arctanh(\sqrt{0.1}) + \frac{1}{2D'}\right) - \sqrt{0.1}\right]$.
This analytical profile remains valid for the developing aerated flow.

$\diamondsuit$ *Air concentration boundary layer*
For conventional steps, the vertical distribution of the air concentration indicates the presence of a boundary layer in the portion of the flow below $z/Z_{90} = 0.25$, for all discharges during transition and skimming regimes.

When endsills are added to all steps (m=1), the results are similar and the configuration has no effect on this inner layer of the flow. However, for $m = 1/2$ a thicker air concentration boundary layer ($z/Z_{90} \leq 0.3 - 0.35$) is observed.

14.2 Flow depth

In Chapter 13, different flow depths have been defined to describe the flow behaviour. Herein, interest is focused on the mixture flow depth Z_{90}. In fact, bulking (spray, water drop ejections) and wavy characteristics of the aerated flow over macro-roughness must be taken into account for the design of the training walls of an overtopped structure.

14.2.1 Influence of macro-roughness on free surface shape

For all stepped macro-roughness overlays and for both tested slopes, the shape of the free surface reflects the drag form effect caused by the bottom topography. A plot of the free

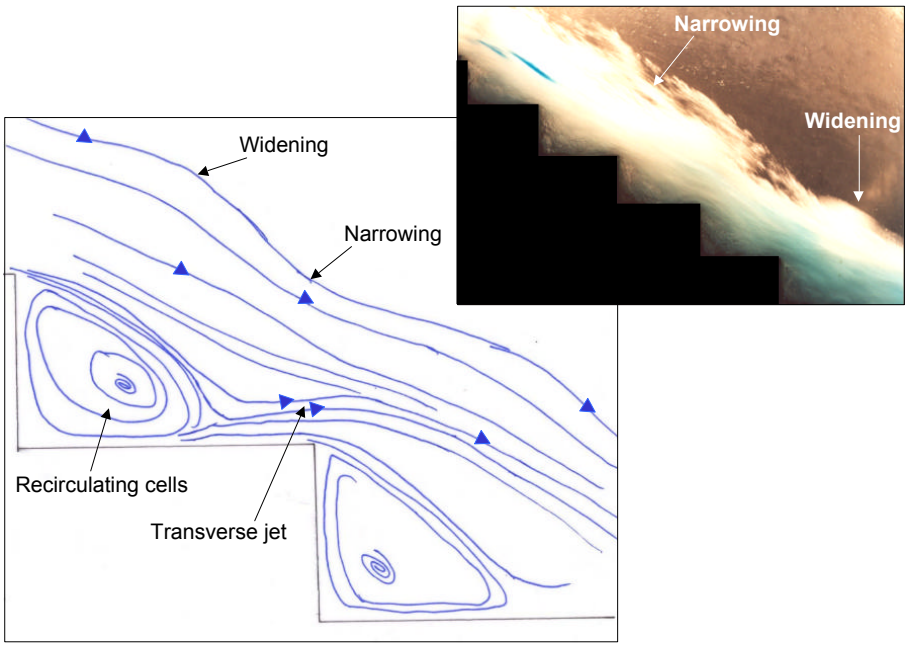

Figure 14.13: Schematic of wavy free surface for skimming flow ($q_w = 0.12\ m^2/s$) over conventional step - Uniform region

surface with tracing paper (see Fig. 14.13 for $q_w = 0.12\ m^2/s$ and conventional step overlay) for transition and skimming flows shows that the mixture flow layer:

- is narrowed at the point of separation between the recirculating cells and the transverse jet, therefore just upstream of the step or endsill or block outer edge,

- is widened at the point where the transverse jet becomes transported by the 1D-skimming layer. It corresponds roughly at the inner step corner.

This behaviour suggests that the vertical pressure distribution is non hydrostatic. Indeed, the form effect caused by the steps such as recirculating cells and transverse jets must create an additional pressure component. At the separation zone, where the vertical shear stress between vortex and transverse jet is significant, a depression could be developed (narrowing). Whereas, the significant vertical velocity component at the transverse jet may result in a overpressure (widening). Furthermore, these assumptions would be verified with a 2D numerical model where the vertical velocity component would be implemented. It is one of the numerical tests in progress which were performed in collaboration with HACH-ULg (see Part V).

The amplitude of the waves decrease with the swelling of the skimming layer. The influence of the macro-roughness on the free surface thus diminishes to zero for well developed skimming flow characterized by $Z_{90}/k_s = 1.5$ for $m = 0$ and $m = 1$ and for $Z_{90}/(k_s + k_r) = 1.5$ for $m = 1/2$ (where $k_s = h_s \cos\theta$ and $k_r = h_r \cos\theta$ and h_s and h_r are respectively the step and the endsill or block height).

14.2.2 Influence of macro-roughness on mixture flow depth

Conventional steps

Boes & Hager (2003b) proposed that for conventional steps and $30^o \leq \theta \leq 50^o$, the uniform mixture depth $Z_{90,u}$ above the pseudo-bottom can be computed by Equation 14.10:

$$\frac{Z_{90,u}}{h_s} = 0.50 F_s^{0.1 \tan\theta + 0.5} \tag{14.10}$$

This formula is compared with the data measured in the conventional stepped flume for $\theta = 30^o$ and $\theta = 18.6^o$ in Figure 14.14.

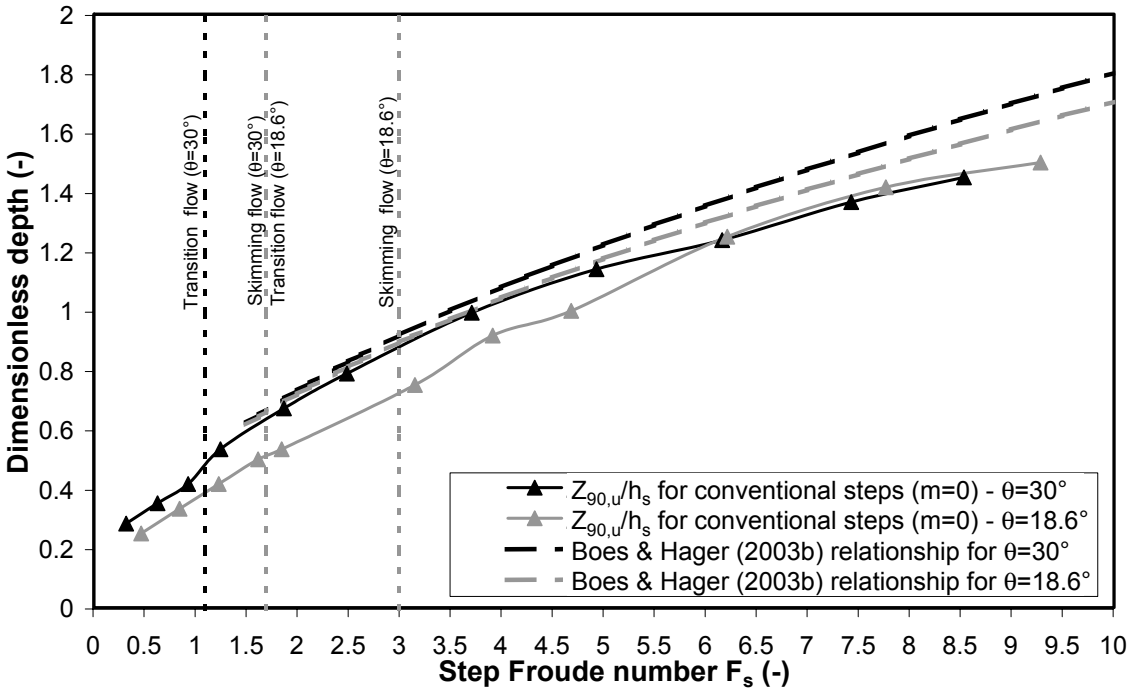

Figure 14.14: Dimensionless mixture depth $Z_{90,u}/h_s$ versus step Froude number $F_s = q_w/\sqrt{g \sin\theta h_s^3}$

It can be seen that Equation 14.10 fits the data well for the mild slope ($\theta = 30^o$) but it is not accurate for the shallow slope ($\theta = 18.6^o$).

In addition, for $\theta = 30^o$ and for high discharges ($F_s > 5$ or $Z_{90,u}/k_s \geq 1.5$), the mixture depths measured in the flume are lower than the predicted one. This indicates again that when the skimming layer becomes large compared to the step normal height k_s, the influence of the drag form effect are weaker. In addition, the mean equilibrium air concentration becomes constant with discharge which also has an effect on the swelling of the flow depth.

In order to define a more accurate relationship, the dimensionless depth $Z_{90,u}/k_s$ has been plotted versus the roughness Froude number $F_{*,\theta} = q_w/\sqrt{g \cos\theta k_s^3}$. This yields to a good correlated following relationship:

For $18.6^o \leq \theta \leq 30^o$ ($R^2 = 0.995$) and conventional steps:

$$\frac{Z_{90,u}}{k_s} = 0.58 F_{*,\theta}^{0.6\cos\theta} \tag{14.11}$$

Steps equipped with endsills or blocks

According to equation 14.11, the height of the step and the slope angle have a significant effect on the flow depth. To verify if the macro-roughness height has indeed an effect, the uniform mixture depth for any overlay m, $Z_{90,u,m}$, is compared with the uniform mixture depth for conventional steps $Z_{90,u,0}$, for $\theta = 30^o$. The resulting values are plotted versus the unit discharge in Figure 14.16.

Except for the particular case $m = 1/3$, the curves indicate that for $0.04 < q_w < 0.12\ m^2/s$, when the free surface is perturbed by the drag form effect, the uniform mixture depth is at maximum 2 times higher than for conventional steps, independently of the macro-roughness additional elements. For thicker skimming layer ($q_w > 0.12\ m^2/s$), the difference is in the order of 1.4. Nevertheless, the configuration $m = 1$ presents the lower swelling of the mixture depth (around 1.3). In fact, as seen in the above section, for this configuration the mean air concentration is unchanged compared to conventional steps as well as flow regimes. The effect is as if the pseudo-bottom is displaced up at a distance of $k_r = h_r \cos\theta$. For $m = 1$, the mixture depth taken above the pseudo-bottom formed by the endsills outer edges is equal to the mixture depth above the pseudo-bottom formed by the steps outer edges for $m = 0$.

For low discharges ($q_w < 0.04\ m^2/s$), the flow corresponds in most of the case at a non-homogeneous highly aerated falling nappe. The associated uniform mixture depths are then to be taken with care since they are very complex and difficult to measure.

For the particular case of $m = 1/3$, the mixture flow depth presents a lot of instabilities and large slug ejections (see Fig. 14.15). That results from the important deflection of the nappe which greatly accelerates over a distance of $3x_s$ to hit again the next endsill. This alternative is a bad design since it involves high and unstable flow depth.

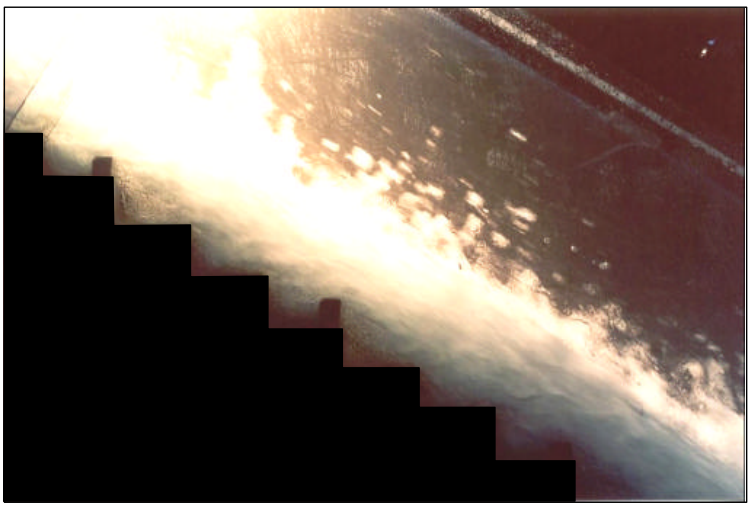

Figure 14.15: Side view of aerated flow over a 30^o inclined chute for $m = 1/3$

Finally, mixture depths for the different blocks overlays (m=4, m=5, m=6) have been compared. This shows that there is no significant effect of the transverse distribution of the blocks (e_r/b_r) on the mixture depth in the uniform region.

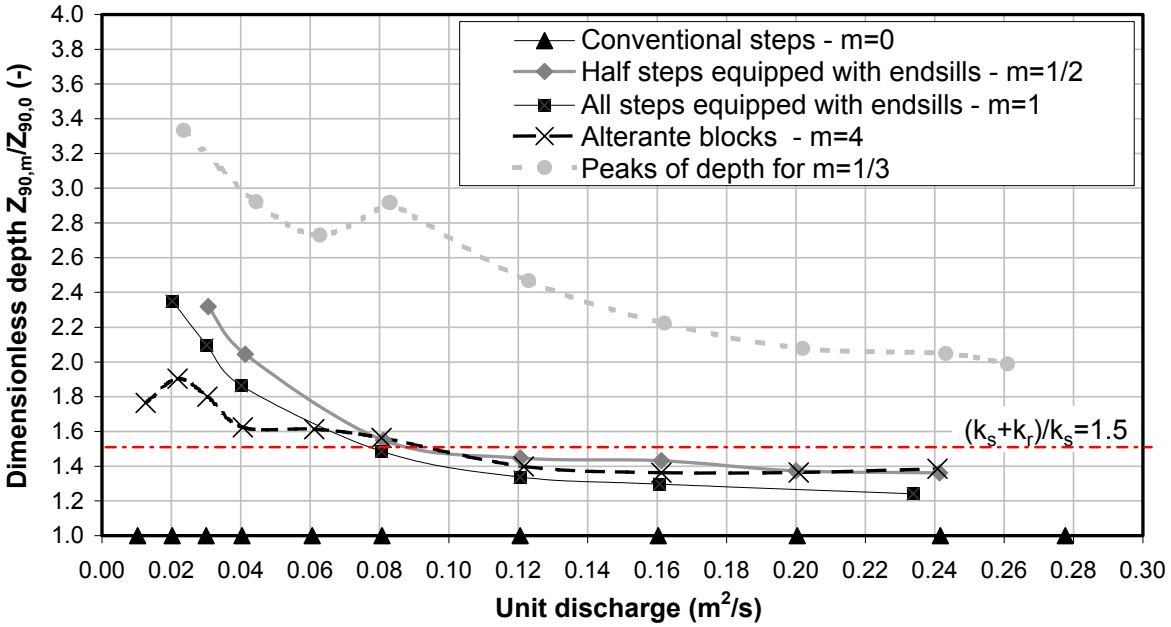

Figure 14.16: Dimensionless depth $Z_{90,u,m}/Z_{90,u,0}$ for the 30^o inclined chute equipped with steps with endsills (m=1/3, m=1/2, m=1/3) and with steps with blocks (m=4) versus unit discharges (uniform region)

14.2.3 Conclusions

For $q_w \geq 0.08\ m^2/s$ (transition and skimming regimes), the configurations consisting in either every second step equipped with an endsill (m=1/2) or all steps equipped with alternate blocks (m=4, 5, 6) present quite the same mixture flow depths in the uniform region.

The alternative $m = 1$ behaves similarly to conventional step but with a displacement by a distance $k_r = h_r \cos\theta$ of the pseudo-bottom.

The results show also that the longitudinal distribution of the endsills (x_r/x_s) have an influence on the swelling of flow depth whereas the transverse distribution of blocks has a negligible effect on it.

Based on the tested discharges and slopes ($18.6^o \leq \theta \leq 30^o$) for conventional steps, the mixture flow depth can be estimated by Equation 14.11 (see Fig 14.17):

$$\frac{Z_{90,u}}{k_s} = 0.58 F_{*,\theta}^{0.6\cos\theta}$$

For steps equipped with endsills, flow uniform mixture depths follows the same variation with discharges but with a slight shift up for the alternate distribution (m=1/2).

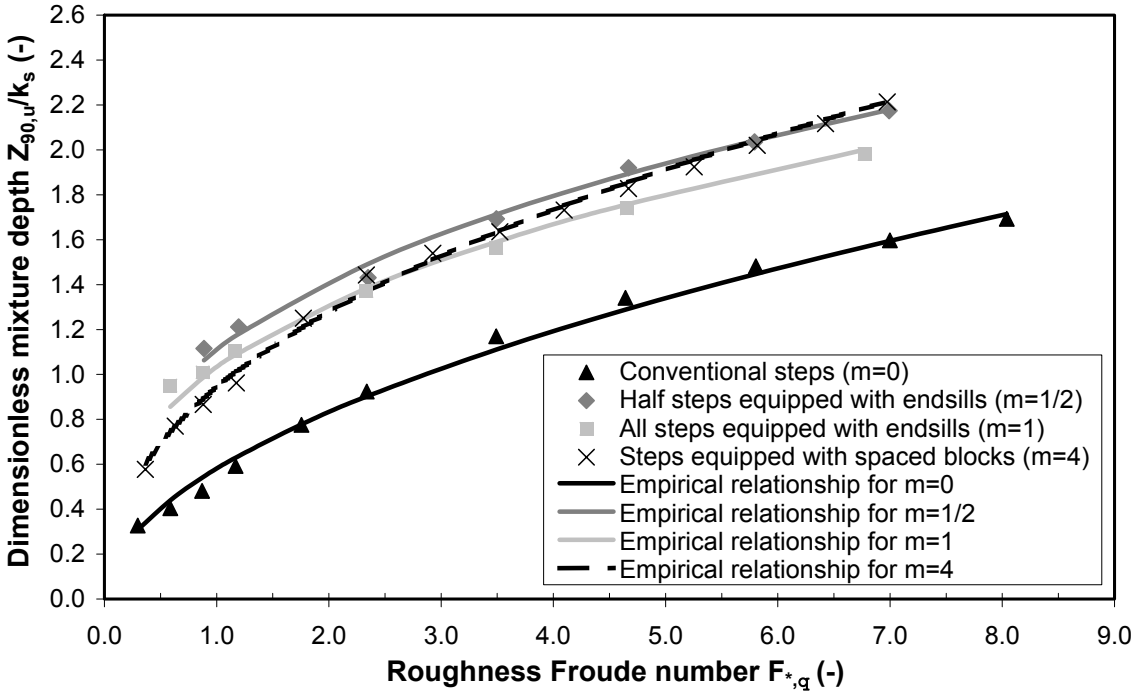

Figure 14.17: Dimensionless uniform mixture flow depth $Z_{90,u}/k_s$ versus roughness Froude number $F_{*,\theta}(k_s)$ for $\theta = 30^o$

For $\theta = 30^o$, $Z_{90,u}$ can be derived according to Equations 14.12 and 14.13 with $F_{*,\theta} = q_w/\sqrt{g\cos\theta k_s^3}$:
For m=1/2 ($R^2 = 0.993$):

$$\frac{Z_{90,u}}{k_s} = 1.109 F_{*,\theta}^{\frac{2}{3}0.6\cos\theta} \tag{14.12}$$

For m=1 ($R^2 = 0.996$)

$$\frac{Z_{90,u}}{k_s} = 1.030 F_{*,\theta}^{\frac{2}{3}0.6\cos\theta} \tag{14.13}$$

For steps equipped with blocks, the variation of the uniform mixture flow depth is a little bit different, following Equation 14.14 for $\theta = 30^o$.
For m=4, 5, 6 ($R^2 = 0.994$):

$$\frac{Z_{90,u}}{k_s} = 0.942 F_{*,\theta}^{0.51\cos\theta} \tag{14.14}$$

14.3 Flow velocity

Flow velocity is required to estimate the residual energy at any section of the chute. Moreover, velocity is necessary for the friction and drag coefficient computation. In this study the mixture flow longitudinal velocities, u_m, are measured with a double optical-probe instrumentation at different cross sections in the developing or quasi-uniform flow (see Fig. 11.11).

14.3.1 Vertical distribution of flow velocity

For conventional steps, most of the authors conclude that above the pseudo-bottom, for skimming flow, the velocity follows a power law profile as in case of smooth chutes: $U_{90} = DH_{90}^{1/N}$ where $U_{90} = u_m(z)/u_{90}$ and $H_{90} = z/Z_{90}$. Index 90 indicates the flow parameters at a air concentration of 0.9 and index m, the mixture flow values.

According to Boes & Hager (2003a), the exponent N is not affected by the slope nor by the discharge or the flow regions. However, as already mentioned in Part III, Chapter 9.3.1, experimentally obtained values of N show large scatter. In fact, Boes & Hager (2003a) obtained a power law with N=4.3 for $0.04 \leq H_{90} \leq 0.8$. Based on Chamani & Rajaratnam's (1999) data for a 30^o slope, Boes (2000b) suggested $N = 6.3$ for $0.04 \leq H_{90} \leq 0.5$. Yasuda & Chanson (2003) found $N = 9$ for $0.05 \leq H_{90} \leq 1$ and a 15.6^o slope. Chanson (1994a) recommended $N = 3.5$ to 4 based on model experiments.
Therefore, it is not clear which criterion should be used to define the portion of the aerated flow which follows a velocity power law. In the author's view, the difference between the several proposed power laws might result from the portion of flow layer considered in the empirical fitting as well as from the strong dependence of the exponent on discharge. This will now be discussed. A summary of this discussion is given in André, Boillat & Schleiss (2004).

Definition of a lower and upper flow layers for conventional steps

In Figure 14.18, dimensionless velocity data U_{90} are plotted versus dimensionless depth H_{90} for one cross-section in the developing aerated region (cross dots) and three in the uniform aerated region (grey dots) for skimming flow over a 30^o slope. The approximated power law proposed by Boes & Hager (2003a), Equations 14.15 and 14.16, established for skimming flow on conventional stepped chutes ($30^o \leq \theta \leq 50^o$) in both partially and fully developed regions is also shown.
For $0.04 \leq H_{90} \leq 0.8$:

$$U_{90} = 1.05 H_{90}^{1/4.3} \tag{14.15}$$

For $H_{90} > 0.8$:

$$U_{90} = 1 \tag{14.16}$$

It can be seen that:

- For $H_{90} \leq 0.2$, almost all the velocity data are below the curve of Boes & Hager. The gradient of velocities in this region is smaller than the expected one. The scattering of the points decreases for increasing H_{90} when the stream becomes more and more unidirectional, parallel to the pseudo-bottom.

- There is a more significant effect of the flow region on the mixture velocity for $H_{90} \leq 0.8$ than in the homogeneous portion of the flow. This difference on the velocity distribution in the developed and the quasi-uniform regions should be expected since both air concentration and flow depth are also varying before reaching equilibrium conditions.

In light of the above and regarding the conclusions on the air concentration distribution, *i.e.* the existence of an air concentration boundary layer, the emphasis is put on the definition of flow layers.

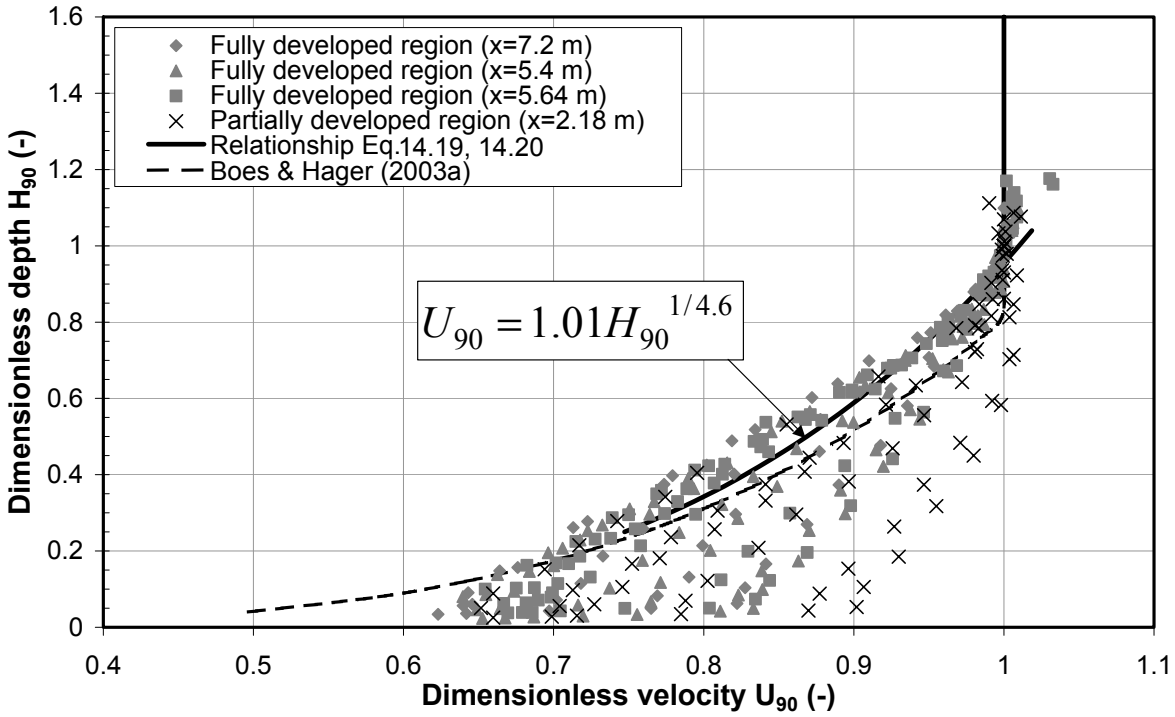

Figure 14.18: Comparison of the dimensionless velocity data with Boes & Hager's (2003a) power law for skimming flow ($q_w > 0.057\ m^2/s$) over the 30^o inclined stepped chute at cross-sections in the partially and fully developed aerated regions

Based on the analogy to studies of uniform turbulent rough flow for steep gravel beds, it is suggested that the aerated flow over stepped chutes can be divided into a lower and upper layer.

♢ *Logarithmic velocity profile in the lower flow layer*

In the lower flow layer, as observed by Sayre & Albertson (1963), Bathurst (1988), Chamani & Rajaratnam (1999) and Canovaro et al. (2003), the flow in the rough boundary layer theory is affected by the shear stress and the drag around the macro-roughness. In this lower portion of the flow, the velocity gradients are expected to experiment a logarithmic profile. This is really the case of the dimensionless values measured below $H_{90} \leq 0.2$ to 0.3. However, as already mentioned in Part III, Chapter 9.3.1, because of the high relative roughness of the steps, of the 3D macro-turbulence flow structures such as recirculating cells and internal jets, the classical logarithmic equation as proposed by Karman-Prandtl, may not be completely satisfied. For this reason, the logarithmic Equation 9.21 (Part III) is fitted with the experimental data in the uniform region:

$$\frac{u_m}{\sqrt{\tau_0/\rho_m}} = A log\left(\frac{z*}{k_s}\right) + B$$

with $z* = z + h_s \cos\theta$, $\rho_m \simeq (1-C)\rho_w$ the mixture density and the shear stress $\tau_0 = \rho_w g \sin\theta Z_{w,u}$ and $Z_{w,u}$ the equivalent clear water depth in the uniform region.
Only the velocities with the cross-correlation coefficient $r > 0.5$ are considered (see Chapter 11.2.1). Note that sometimes, due to the low value of r, the logarithmic law was fitted only with 3 experimental data.

For skimming flow over the 30^o inclined conventional stepped chute, data in the uniform region best fit Eq. 9.21 ($R^2 = 0.8$ to 0.99) with $A = 3.1$ to 5.9 thus $\overline{A} = 4.14$, and $B = 6.9$ to 9.0 thus $\overline{B} = 7.6$. The variation of the coefficients versus the roughness Froude number $F_{*,\theta} = q_w/\sqrt{g \cos\theta k_s^3}$ is given in Figure 14.19. It indicates, considering the uncertainty of the data, that the coefficient A is independent of discharge whereas B varies until a well established skimming flow ($q_w > 0.16$ m^2/s). These values are comparable to those proposed by Chamani & Rajaratnam (1999): A=5.75 and B=8.5.

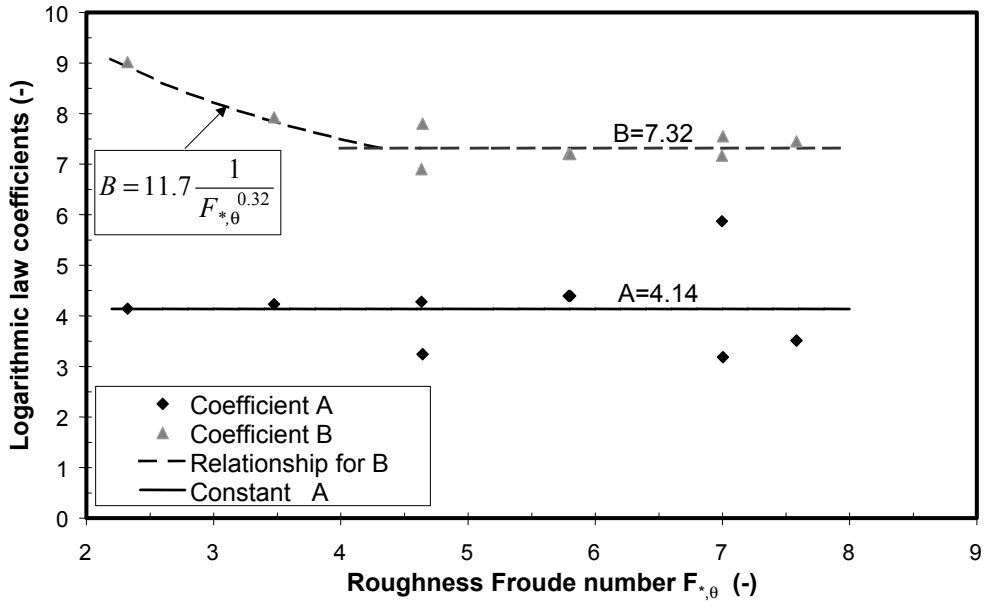

Figure 14.19: Variation of the coefficients A and B of the logarithmic law $\frac{u_m}{\sqrt{\tau_0/\rho_m}} = A log\frac{z*}{k_s} + B$ for skimming flow over the 30^o inclined stepped chute in the uniform region - Lower layer of the flow

♢ *Power law in the upper flow layer*

Above this boundary layer, the rough turbulent flow theory indicates that the upper flow layer is not influenced by the roughness. The local mixture velocity depends, as for smooth chutes, on the maximum velocity. Then, the velocity gradient follows a power law:

$$U_{90} = D H_{90}^{1/N}$$

Because of the pronounced effect of the flow region, the power law is first assessed in the uniform region. In order to define the limit of application of this law, the exponent N was estimated for different lower and upper limits of H_{90} (see Fig. 14.20) for all the data concerning the skimming flow.

It can be seen that the coefficient D is not significantly affected by the limits of H_{90}. However, N strongly varies for $H_{90} \leq 0.2$. This explains that below $H_{90} = 0.20$, there is large scatter on the velocity data. In fact, as already mentioned, for transition and skimming regimes, it was visually observed that the portion of the flow within the first 1.5 to 2.5 cm over the step outer edge (corresponding roughly to $H_{90} \leq 0.2$ to 0.3) is strongly disturbed by the internal jet (see Figure 12.1).

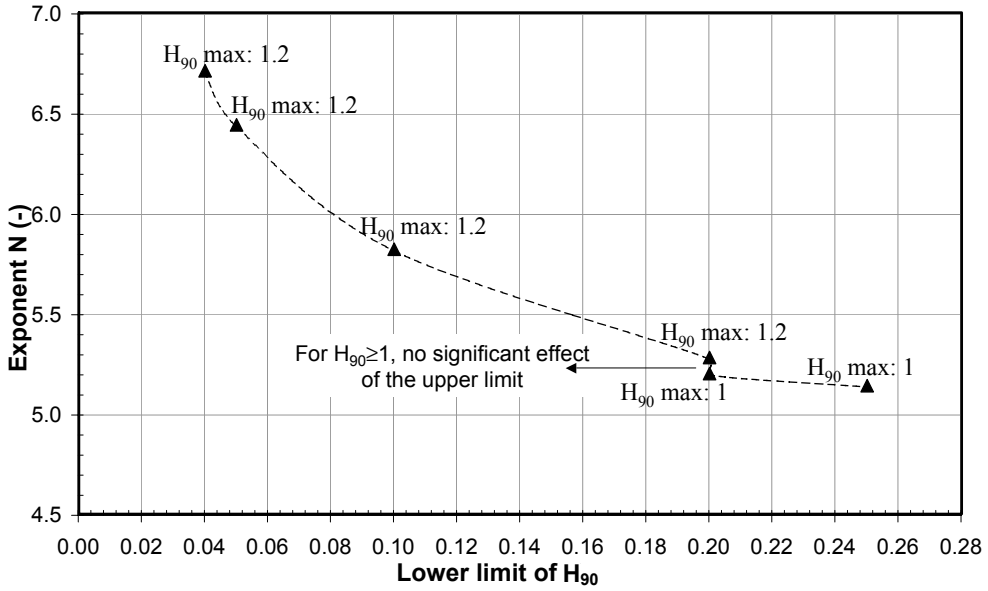

Figure 14.20: Variation of the exponent N of the power law $U_{90} = H_{90}^{1/N}$ with the lower and upper depth limits of the upper flow layer - Skimming flow over the 30^o inclined stepped chute in the uniform region ($H_{90,max}$=upper limit of the flow layer used to fit the power law)

To underline these observations, the cross-correlation coefficients r of velocities obtained from the probe signals (see Matos et al. (2002) for details) have been plotted versus the dimensionless depth H_{90} in Figure 14.21. It can be seen that below $H_{90} = 0.25$, correlation coefficients for all data are lower than 0.7, which corresponds to the recommended criterion by the probe manufacturer for an accurate velocity estimation. It has to be noted that this threshold was established for unidirectional aerated flow in tubes. However, for all the tests up to 0.20 m^2/s, unit discharge derived from the measurements ($q_w = \int_0^{Z_{90}} (1-c) u_m(z) dz$) lead to accurate results: $\Delta q_w/q_w$ remains lower than 7 % which is in the range of the errors due to measurements and facility. Based of this, for such greatly turbulent flow the threshold for reasonable accurate velocity measurements is fixed at $r = 0.5$. Below $H_{90} = 0.25$, the low values of r may be explained by the existence of a significant vertical velocity component due to the internal jet.

Therefore, to be out of the macro-roughness influence, it is suggested to take $H_{90} = 0.25$ for the lower limit of the upper flow layer, rather than 0.2 as normally used to define the boundary layer of flow over gravel beds.

Regarding the upper limit of application of the power law, the velocity is constant ($U_{90} = 1$) for most of the data above $H_{90} = 0.9$ and 0.95 (Fig. 14.18). Thus, the power law could be extrapolated up to the limit of $H_{90} = 0.95$.

♢ *Conclusions*

Visual observations, concentration and velocity vertical profiles, variation of the cross-correlation coefficients as well as the previous studies on streams over gravel beds lead to the same conclusion. During skimming regime in the uniform region the aerated flow over conventional

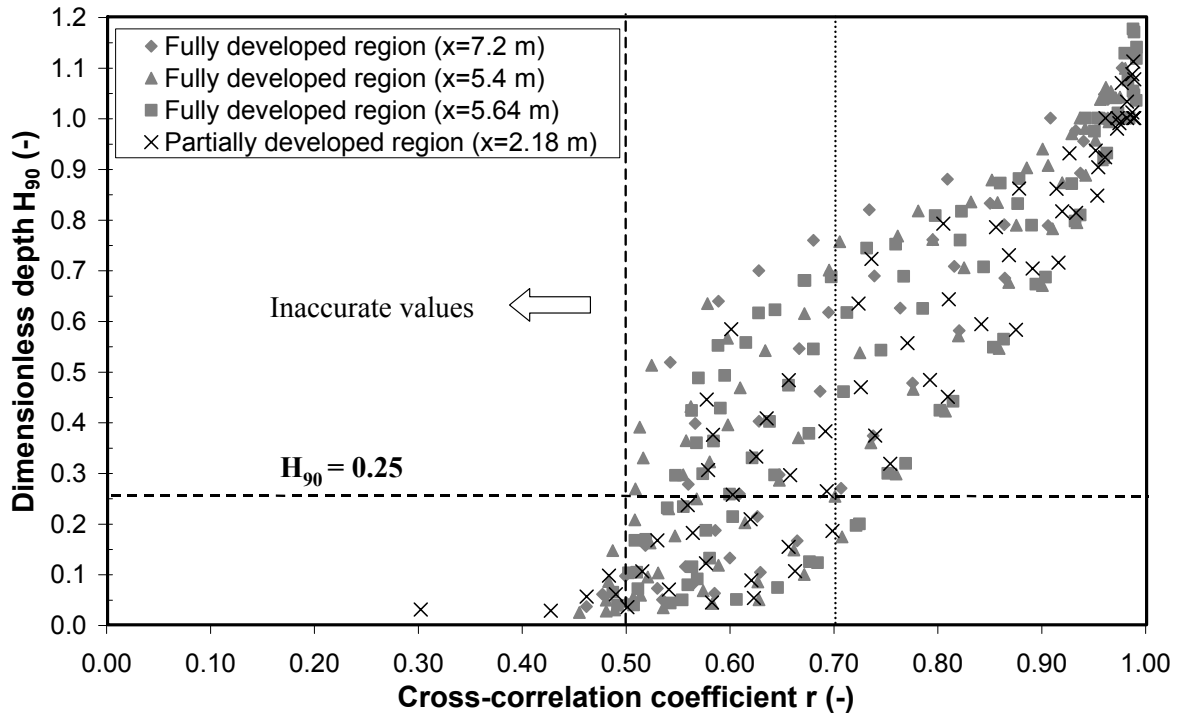

Figure 14.21: Vertical distribution of the cross-correlation coefficient associated to the velocity measurement with the double fiber-optical probe signal, for skimming flow over the 30^o conventional stepped chute

steps are characterized by two layers above the pseudo-bottom:

- **The rough boundary layer** or lower layer in the portion $0 < H_{90} < 0.25$ which is under the influence of the shear stress in the first millimeters and under the form effects due to the steps in the first centimeters in the model scale. Herein, the flow experiments a logarithmic velocity profile:
  For $1.7 \leq F_{*,\theta} \leq 4$ and $\theta = 30^o$ ($R^2 = 0.99$),

$$\frac{u_m(z)}{\sqrt{g \sin\theta Z_{90,u}}} = 4.14 \log\left(\frac{z}{k_s} + 1\right) + \frac{11.7}{F_{*,\theta}^{0.32}} \tag{14.17}$$

  For $F_{*,\theta} > 4$ and $\theta = 30^o$,

$$\frac{u_m(z)}{\sqrt{g \sin\theta Z_{90,u}}} = 4.14 \log\left(\frac{z}{k_s} + 1\right) + 7.32 \tag{14.18}$$

- **The upper layer** which depends on the surface velocity. Herein, the flow, quasi-parallel to the pseudo-bottom, follows a power law. An approximation for the skimming flow over the 30^o inclined conventional stepped chute in the uniform region can be given by:
  For $0.25 \leq H_{90} \leq 0.95$ ($R^2 = 0.93$):

$$U_{90} = 1.01 H_{90}^{1/4.6} \tag{14.19}$$

For $H_{90} > 0.95$:

$$U_{90} = 1 \tag{14.20}$$

In the partially developed region, based on one tested cross section, the velocity distribution can be described by:
For $0.25 \leq H_{90} \leq 0.95$ ($R^2 = 0.82$):

$$U_{90} = 1.01 H_{90}^{1/7.8} \tag{14.21}$$

and for $H_{90} > 0.95$, $U_{90} = 1$.
However, more cross sections would be required to obtain a general relationship in this region.

Influence of flow regimes on the velocity power law

♢ *Skimming flow*
Regarding the upper layer, if D is a constant, exponent N of the power law varies significantly with the unit discharge. In fact, the power law has been fitted in the uniform region for the different discharges with skimming regime up to 0.28 m^2/s.

For $0.25 \leq H_{90} \leq 0.95$, $U_{90} = 1.01 H_{90}^{1/N}$ was obtained with a good correlation ($R^2 > 0.99$) for N varying from 8 to 3.9. For high discharges ($q_w \geq 0.25$ m^2/s, $F_{*,\theta} \geq 7.5$) and therefore low relative roughness ($Z_{90,u}/k_s > 1.6$), N tends to a constant value of about 3.9.
In Figure 14.22, the variation of N with the roughness Froude number $F_{*,\theta}$ is plotted. For the tested configuration (30^o slope, 0.6 m step height, uniform region), N may be computed as:
For $1.7 \leq F_{*,\theta} < 7.5$ ($R^2 = 0.960$):

$$N = \frac{11.2}{F_{*,\theta}^{0.52}} \tag{14.22}$$

For $F_{*,\theta} \geq 7.5$:

$$N = 3.9 \tag{14.23}$$

♢ *Transition and nappe flows*
For the transition regime, the velocity distribution follows also a power law in the upper layer of the aerated flow, estimated as:
For $0.25 \leq H_{90} \leq 0.95$ ($R^2 = 0.991$):

$$U_{90} = 1.01 H_{90}^{1/8} \tag{14.24}$$

and for $H_{90} > 0.95$, $U_{90} = 1$.
It appears that the maximum exponent of the power law is about 8 and that N in Eq. 14.22 attains an asymptotic value at $N = 8$.

In the lower layer, the limited data fit the logarithmic law, Eq. 14.17. Therefore, in agreement with the air concentration behaviour, the velocity distribution reveals that the flow structure is similar above the pseudo-bottom for both skimming and transition regimes.

However, the power law is no longer applicable for nappe flow. Due to the instability of the plunging nappe, the velocity data are quite scattered.

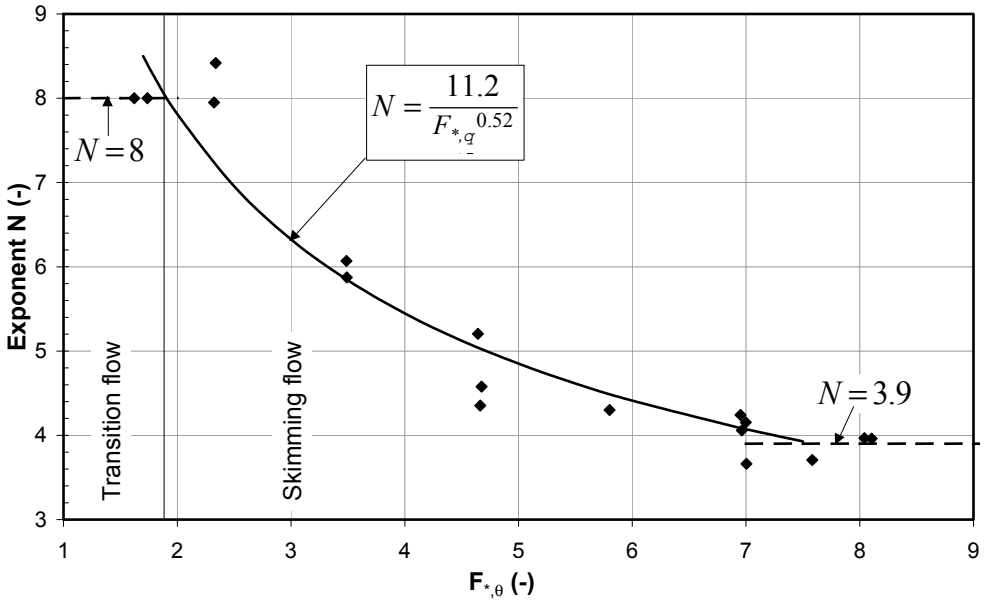

Figure 14.22: Variation of the exponent N of the velocity distribution power law $U_{90} = 1.01 H_{90}^{1/N}$ with the roughness Froude number $F_{*,\theta}$ for transition and skimming flows over the 30^o inclined stepped chute - $0.25 \leq H_{90} \leq 0.95$ in the uniform region

Effect of the macro-roughness elements on the velocity distribution

The following describes the uniform region. The tendency is identical in the partially developed region.

♢ *Stepped chute with an endsill on every step*

For transition and skimming flows over all steps equipped with endsills ($m = 1$), the data clearly indicate that the velocity distribution is unchanged compared with conventional steps. In addition, it appears that the lower region influenced by the macro-turbulence, is thinner and delimited by $H_{90} = 0.20$. In fact, velocities between $0.20 \leq H_{90} \leq 0.25$ also follow the power law (see Fig. 14.23). For the vertical air concentration distribution, the same order of magnitude of the thickness of the boundary layer was observed. All converge to indicate that the influence on flow resistance of endsills for $m = 1$ is less important than for conventional steps.

♢ *Stepped chute with an endsill on every second step*

For the alternate configuration, $m = 1/2$, above the endsill edge, the upper layer of the flow experiments also a power law profile. Similarly to $m = 1$, the relationship can be accurately applied for the upper portion of the flow between $H_{90} = 0.20$ and $H_{90} = 0.95$. However, the exponent of the power law is lower.

For $0.20 \leq H_{90} \leq 0.95$:

$$U_{90} = 1.01 H_{90}^{1/6} \tag{14.25}$$

and for $H_{90} > 0.95$, $U_{90} = 1$.

This difference can be attributed to the influence of the extreme aeration of the flow which

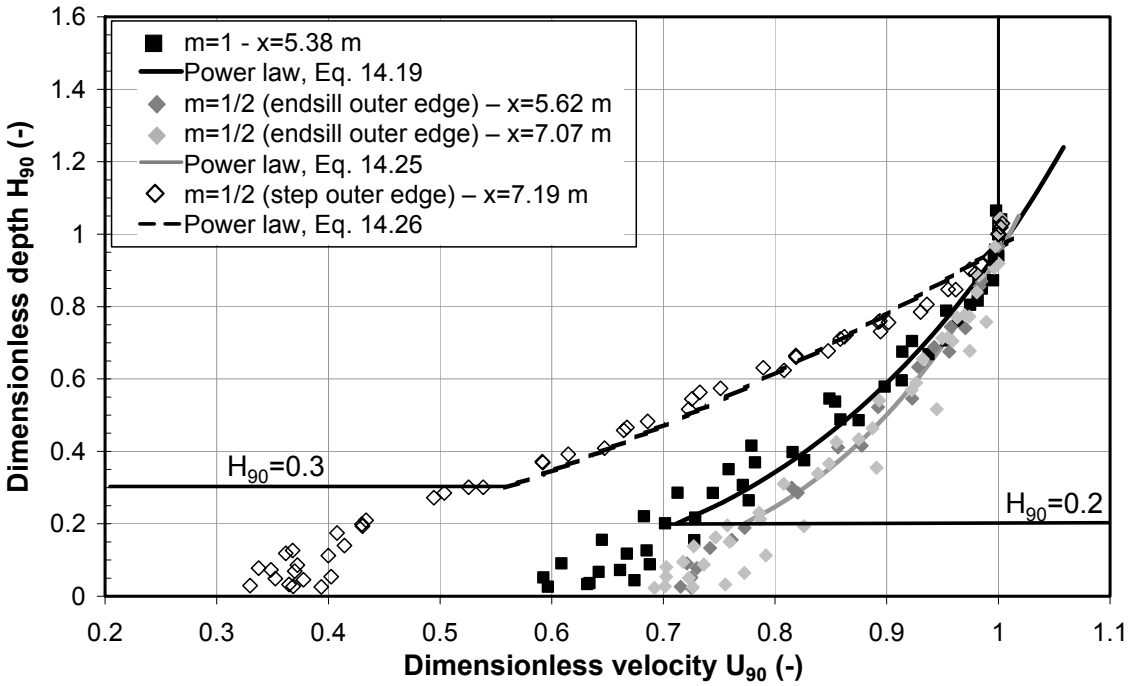

Figure 14.23: Vertical distribution of the dimensionless velocity U_{90} along with the corresponding power law, for the aerated flow over the 30^o chute with all steps equipped with endsills (m=1) and every second steps equipped with endsills (m=1/2) - Uniform region

tends to decrease the flow resistance. Nevertheless, since the flow structure above the outer edge of the endsill is not modified compared the other configurations, the additional head losses with this configuration more dissipative (see Chapter 16) must lie in the step without endsill.

Velocity profiles above the step outer edge (without endsill) present indeed more significant differences. Contrary to the stream above the endsill, the skimming layer above the step is affected by the change of topography which creates a broken slope from one step with the endsill to the following without endsill. It adds singularity such as widening and narrowing which reduces locally the velocity.

In fact, as illustrated in Figure 14.23, the limit between the lower and upper flow layers is at about $H_{90} = 0.3$. In the upper layer (which corresponds to the layer above the pseudo-bottom formed by the endsills outer edges), velocity distribution is well approximated ($R^2 = 0.992$) by Equation 14.26.
For $0.30 \leq H_{90} \leq 0.95$, in the uniform region:

$$U_{90} = 1.02\sqrt{H_{90}} \tag{14.26}$$

In the inner region, the layer above the step corner follows a logarithmic law ($R^2 = 0.900$) as in case of rough turbulent flow, up to $H_{90} = 0.30$:

$$\frac{u_m}{\sqrt{\tau_0/\rho_m}} = 7.47log\left(\frac{z}{k_s} + 1\right) + 2.76 \tag{14.27}$$

In this case, the coefficients of the relationship are closer to those proposed by Sayre & Albertson (1963) which were established for alternate rectangular baffles on a flat flume.

♢ *Conclusions*
These results suggest that if the step height has no significant effect on the flow velocity (from comparison m=0 and m=1), the alternate longitudinal distribution of the endsills induces a significant additional drag form effect in the rough boundary layer. The parameter x_r/x_s and by extrapolation e_r/b_r (x_r, e_r respectively the longitudinal and transverse spaces between the elements and b_r the width of the elements) seems to be relevant to characterize the effective roughness of the macro-roughness system.

14.3.2 Mean flow velocity

Similarly to the flow depth considerations, definition of a representative mean velocity of the flow is the clue to estimate accurately the energy dissipation of flows over stepped macro-roughness overlays.

The equivalent clear water velocity $U_w = q_w/Z_w$ (where Z_w is the equivalent clear water depth), assumes a uniform velocity distribution and takes into account the air effect through Z_w.

The mean mixture flow velocity, U_m is directly computed from the measured velocity profile: $U_m = \frac{1}{Z_{90}} \int_0^{Z_{90}} u_m(z)dz$. Therefore, the non-uniform velocity distribution is directly integrated in the value.

As a consequence, it is expected that $U_w \leq U_m$.

Both mean velocities in the uniform region are represented versus the roughness Froude number $F_{*,\theta} = q_w/\sqrt{g \cos\theta k_s^3}$ for the tested overlays on the 30^o slope in Figure 14.24. The following observations can be drawn.

Influence of flow regimes

For all overlays, the mean velocities continually increased with discharge without discontinuity caused by the change of flow regimes.

For $F_{*,\theta} > 4.5$ (or $q_w > 0.16\ m^2/s$), the increase of the mean mixture flow velocity decreases. This behaviour, common for all the overlays is also observed in the partially developed region. A question arises: is this behaviour the result of a physical phenomenon or is it an artifact?
To have an idea of the accuracy of these particular values, the relative error on the unit discharge, $\Delta q_w/q_w = (q_{w,pump} - q_{w,meas})/q_{w,pump}$ (with $q_{w,pump}$ the unit discharge provided by the pump and $q_{w,meas} = \int_0^{Z_{90}} (1-c)u_m dz$) is given in Table 14.1.
The maximum relative error due to the combination of the pump uncertainty and the error due to the instrumentation has been estimated at 15 % for the nappe flow and 10 % for the transition and skimming flows.

For all overlays and for $q_w > 0.16\ m^2/s$, the large errors on the unit discharge are combined with quite low values of r even in the quasi-1D skimming layer. For these high discharges, the leading tip of the probe may create a significant wake downstream which perturbs the trailing tip. During a measurement, this may result in a large difference between the two probe TTL

Overlay	$F_{*,\theta}$ (-)	$\Delta q_w/q_w$ (%)	Overlay	$F_{*,\theta}$ (-)	$\Delta q_w/q_w$ (%)
$m = 0$	0.60	9	$m = 1$	0.59	9.1
	0.83	-0.2		0.87	3.7
	1.18	1.2		1.16	-3.0
	2.32	-3.6		2.33	0.6
	3.49	0.8		3.49	4.6
	4.68	7.3		4.66	12.4!!
	7.01	15 !!		6.77	18.8!!
	7.58	16.6 !!			
$m = 1/2$	0.87	12.8	$m = 1/2$	0.89	-19.9!!
at endsill corner	1.20	11.7	at step corner	1.18	-26.4!!
	2.33	6.7		2.33	-6.2
	3.49	4.5		3.49	7.2
	4.67	6.8		4.67	14.2!!
	5.79	12.1!!		5.82	16!!
	6.99	15.6!!		6.96	19.2 !!

Table 14.1: Relative error $\Delta q_w/q_w$ on the unit discharge associated to the velocity measurement in the uniform region for the 30^o chute equipped with conventional steps (m=0), every steps with endsill (m=1) and every second steps with endsill (m=1/2)

signals and consequently a low cross-correlation. It affects the portion of the homogeneous flow between about $0.3 < z/Z_{90} < 0.7$.
For these reasons, U_m can be underestimated for $F_{*,\theta} > 4.5$ or $q_w \geq 0.16\ m^2/s$.

Influence of macro-roughness elements

The computed mean velocities in the uniform region of aerated flow over an equivalent 30^o smooth slope (see appendix B) are also plotted in Figure 14.24. It indicates that all stepped macro-roughness overlays enhance significantly the flow resistance: mean velocities are reduced of about 20 to 30 % compared with an equivalent smooth slope.

Without surprise, there is no difference between the mean clear water and mixture velocities of flows over conventional steps and all steps equipped with endsill (see Fig. 14.24).

For the configuration of the alternate endsills overlay (m=1/2), above the endsill outer edge, the mean flow velocities remain of same order of magnitude as for the other configurations. There is no global effect of the endsills.

For the particular case of the velocity measured above the step outer edge, $\Delta q_w/q_w$ is large for all discharges though no signal problems with the optical probe occurred (see Table 14.1). As already mentioned for the air concentration results and as observed in Figure 14.11, the alternate repartition of the endsills develops a separation zone at the step outer edge, below $H_{90} = 0.30$. Due to the low values of both u_m and r in this zone, it is reasonable to consider that high vertical shear stress exists in between the two recirculating cells in the two consecutive steps. Locally, the longitudinal velocity component is negligible with respect to

the vertical one. But the probe does not measure this vertical component which may explain the very low values of r in this flow layer.

The mean mixture velocity above this separation zone (for $H_{90} > 0.30$) is almost equal to the mean velocity above the endsill outer edge (see Fig. 14.24). It also confirms the negligible velocity close to the step outer edge, in the boundary layer.

For this configuration, the mean air concentrations are quite constant from one step cross section to one endsill cross section, but the mean velocities are different. In order to fulfill the longitudinal momentum conservation between the two consecutive steps, the vertical distribution of the pressure and total drag and friction force must be quite different at these two cross-sections.

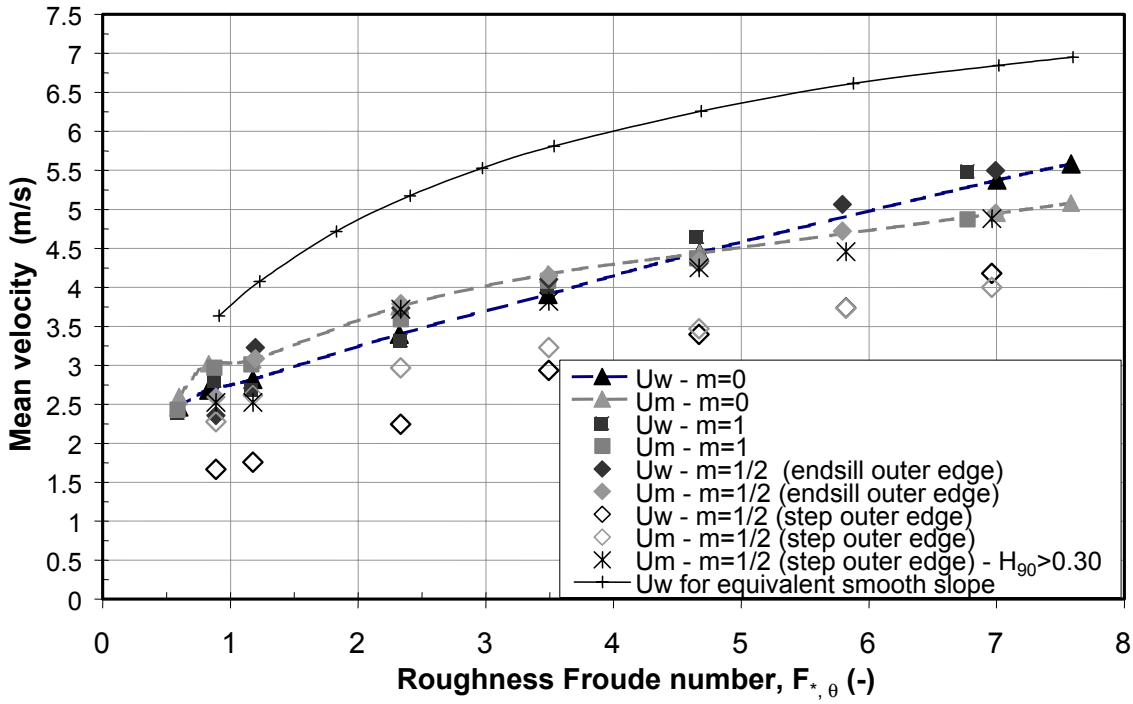

Figure 14.24: Clear water flow mean velocity U_w and mixture flow mean velocity U_m versus roughness Froude number in the uniform region over 30^o smooth slope and stepped macro-roughness chutes

Conclusions

For all tested configurations, the mean clear water or mixture flow velocity in the uniform region is identical above the pseudo-bottom formed either by the steps corners (m=0) or the endsills corners (m=1 and m=1/2). No significant influence of the endsills can be observed. Nevertheless, thank to these stepped macro-roughness overlays, the mean flow velocities are about 20 to 30 % lower than in case of an equivalent smooth chute.

Due to the assumption of uniform distribution of velocities, U_w remains lower than U_m with $U_w \simeq 0.90$ to $0.95U_m$. This difference would be amplified in the estimation of the residual energy which is proportional to the square of the velocity. Therefore, correction coefficients have to be considered in the energy dissipation assessment.

14.3.3 Kinetic energy and momentum correction coefficients

As a result of the non-uniform vertical distribution of the axial velocity over a cross-section A, the velocity head may be larger than the value derived from $U_w^2/2g$. This non-uniform distribution affects also the momentum through A per unit time, $\rho_w Q_w U_w$ with Q_w the water discharge.
Therefore, to represent the "true" kinetic head and the "true" momentum, Coriolis [Chow (1959)] proposed a correction energy coefficient also named Coriolis coefficient, α, such as $\alpha U_w^2/2g$. Boussinesq proposed also a correction momentum or Boussinesq coefficient ρ_{xx} such as $\rho_{xx}\rho_w Q_w U_w$.

For non aerated flow, in uniform region:

$$\rho_{xx} = \frac{\int\int_A u^2 dA}{U_w^2 A} \tag{14.28}$$

$$\alpha = \frac{\int\int_A u^3 dA}{U_w^3 A} \tag{14.29}$$

with U_w the mean velocity assuming a uniform distribution, u the axial component of the velocity and A the cross section. $1 \leq \rho_{xx} \leq \alpha$.
Based on experimental tests in fairly straight prismatic channel, for turbulent non aerated flows, the empirical values proposed by Kolupaila (1956) are given in Table 14.2.

	ρ_{xx}	α
Regular channels, flumes, spillways	1.03 to 1.07	1.1 to 1.2
Torrents	1.05 to 1.17	1.15 to 1.5

Table 14.2: Empirical values of Boussinesq (ρ_{xx}) and Coriolis (α) correction coefficients for non aerated flows, Kolupaila (1956)

For 1D turbulent flows, $\rho_{xx} \simeq \alpha \simeq 1$. The highest estimated values concerned the laminar flow in closed conduit where $\alpha = 2$.

For turbulent aerated flow over macro-roughness elements, the coefficients are thus defined as:
Boussinesq aerated coefficient, $\rho_{xx,m}$

$$\rho_{xx,m} = \frac{1}{U_w} \frac{\int_0^{Z_{90}} (1-C) u_m^2(z) dz}{\int_0^{Z_{90}} (1-C) u_m(z) dz} \tag{14.30}$$

Coriolis aerated coefficient, α_m

$$\alpha_m = \frac{1}{U_w^2} \frac{\int_0^{Z_{90}} (1-C) u_m^3(z) dz}{\int_0^{Z_{90}} (1-C) u_m(z) dz} \tag{14.31}$$

where C is the depth-averaged mean air concentration of the fluid characterized with a mean density $\rho_m \simeq (1-C)\rho_w$.
For skimming flows, Matos (1999) recommended a value $\overline{\alpha_m} = 1.16$ while Boes (2000a) recommended $\overline{\alpha_m} = 1.21$.
The resulting values of both coefficients in the uniform region for the three endsills overlays (m=0, m=1/2 and m=1) are given in Figure 14.25. The integration domain of the velocity concerns only the values of $u_m(z)$ for $r > 0.5$. The values are also compared with the coefficients for smooth spillway according to Wood (1991) and based on Aviemore dam data: $\rho_{xx} = 1.02$ and $\alpha = 1.09$.
The main trend observed from Figure 14.25 are described in the following.

Influence of flow regimes

Correction coefficients are influenced by flow regimes.

For nappe regime only, values increase with discharges. For conventional steps, coefficients are the highest with $\rho_{xx,m} = 1.17$ and $\alpha_m = 1.37$. It reflects indeed the greatly non-uniform velocity distribution where the plunging nappe is deflected at the step or endsill corners.

For transition and skimming flows, the variation is reversed. The values decrease with the diminution of the relative roughness. This shows that the turbulence effect is progressively cushioned by the quasi unidirectional skimming layer which becomes thicker and thicker. It could be expected that for well-developed skimming flow (for $Z_{90,u}/k_* \geq 2$ with $k_* = k_s$ for $m = 0,\ 1$ and $k_* = h_s + h_r$ for $m = 1/2$) the coefficients tend to the values related to equivalent smooth chute. It is not the case in Figure 14.25 where the coefficients become lower than 1 for all the macro-roughness overlays.

The question which arises is that whether this is due to a physical mechanism such as the aeration or to an artifact? Based on the Aviemore Dam data, Cain & Wood (1981) showed that the vertical velocity distribution is independent of the mean air concentration in the range of 0 to 50 %. For skimming flow over the 30^o slope, $C \leq 0.5$. Aeration may therefore not be the explanation. However, for $q_w \geq 0.16\ m^2/s$, mixture mean velocities seem underestimated which could explain the low values of both correction coefficients. It is therefore proposed not to consider these low kinetic and momentum correction coefficients in the following. In this condition, for transition and skimming flow in the uniform region, the mean kinetic coefficient for conventional steps is equal to 1.16 which is identical to the value proposed by Matos (1999).

Influence of the upper layer of the flow

If only the upper layer of the flow is considered to compute the momentum and kinetic energy coefficients, for the skimming regime, then the power law established just above can be included in Equations 14.30 and 14.31. It leads:

$$\rho_{xx,m} = (1-C)\frac{\int_0^1 (1-c) H_{90}^{2/N}\, dH_{90}}{\left[\int_0^1 (1-c) H_{90}^{1/N}\, dH_{90}\right]^2} \tag{14.32}$$

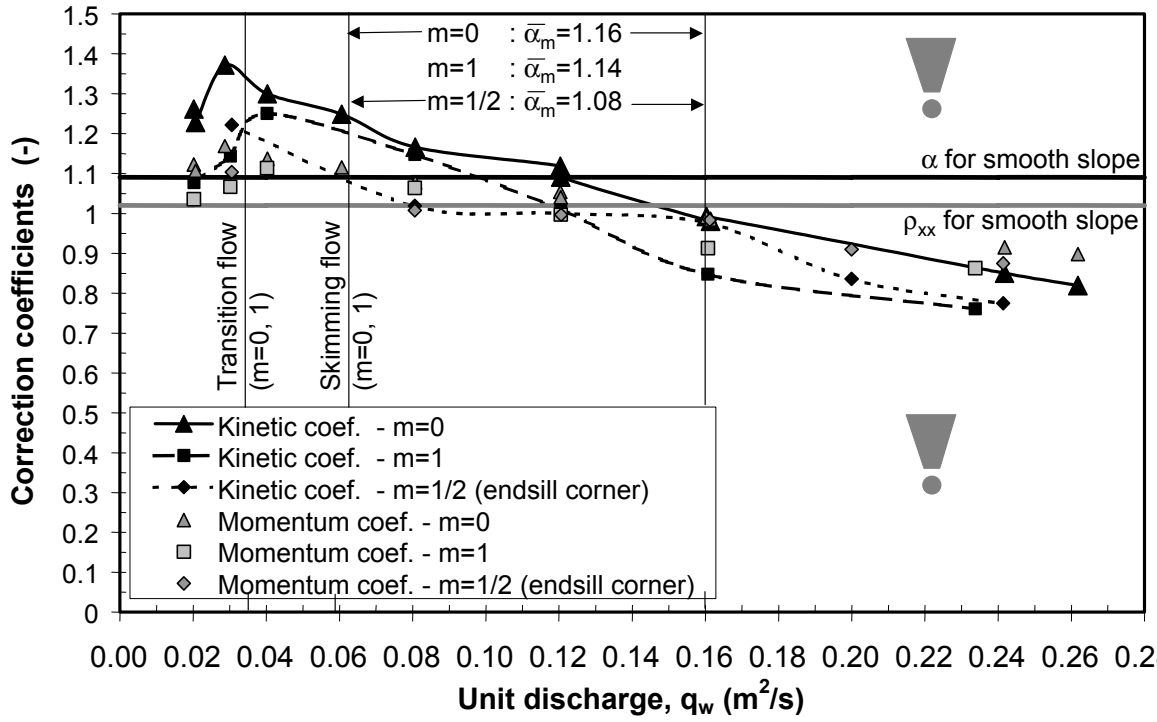

Figure 14.25: Variation of the momentum (grey dots) and kinetic (black dots) correction coefficients with unit discharges for the aerated flow over the 30^o conventional steps or steps with endsills - Uniform region

$$\alpha_m = (1-C)^2 \frac{\int_0^1 (1-c) H_{90}^{3/N} dH_{90}}{\left[\int_0^1 (1-c) H_{90}^{1/N} dH_{90}\right]^3} \tag{14.33}$$

For well developed skimming flow over conventional steps or all steps equipped with endsills, $C = 0.462$ and $N = 3.9$. The corrections coefficients are then $\rho_{xx,m} = 1.06$ and $\alpha_m = 1.16$. Comparison of these coefficients with the values computed over all the flow depth shows that the upper layer of the flow has a dominant influence on the global mean velocity and thus head velocity.

Influence of endsills

There is no significant difference between the Coriolis and Boussinesq coefficients for conventional steps or all the steps equipped with endsills except for nappe flow where the values for $m = 1$ are lower. This is in agreement with the above results concerning the shape of the velocity profile which is identical for these two configurations.

Based on the few available values for $m = 1/2$, it seems that both Coriolis and Boussinesq coefficients at the endsill outer edges are slightly lower than for the other configurations. This could be the influence of the high mean air concentration for the nappe, transition and beginning of the skimming flows (from 70 % to 50 %) which has for consequence to cushion the shear stress effect at the endsill face and therefore to accelerate the velocity.

Conclusions

For the estimation of the residual energy at any step outer edges (m=0) and at any endsill outer edges (m=1 and m=1/2) in the uniform region, it is suggested to consider the mean values of the Coriolis and Boussinesq coefficients proposed in the following Table 14.3.

	$\rho_{xx,m}$	α_m
Nappe flow		
m=0	1.15	1.30
m=1/2, m=1	1.05	1.15
Transition flow		
m=0, m=1	1.11	1.25
m=1/2	1.05	1.15
Skimming flow		
m=0	1.08	1.16
m=1/2	1.05	1.10
m=1	1.07	1.14

Table 14.3: Empirical values of Boussinesq ($\rho_{xx,m}$) and Coriolis (α_m) correction coefficients for aerated flow over the 30^o chute in the uniform region

14.4 Dynamic pressures

Silicon-over-silicon piezo-resistive micro-sensors have been fixed to the step, endsill and block surfaces, along the flume axis, in the uniform region (see Chapter 11.2.2). The development of the dynamic pressure with flow discharge (or normalized critical depth h_c/h_s) determines the effects of these macro-roughness elements. A summary of the main interesting normalized pressure variation $p_m/(\rho_w g h_s)$ (with p_m the measured pressure), is given in Figure 14.27 for aerated flow over conventional steps (m=0), in Figure 14.30 for every step equipped with endsill (m=1) and in Figure 14.31 for steps equipped with alternate blocks (m=4). The tests were performed for the three flow regimes (distinct flow regimes were separated by vertical lines) up to $q_w = 0.28\ m^2/s$. More details about pressure measurements are given in André, Boillat & Schleiss (2001) and André, Matos, Boillat & Schleiss (2004).
In the following observations, the positions of the sensors are given in the l axis on the horizontal face and on the y axis on the vertical face. Their origins are taken at the step outer edge (see schematic in Fig 14.26).

It is important to stress that for practical reason, the nearest sensor from the step outer edge is located at 0.75 cm on the horizontal face and at 1.25 cm on the vertical one. Therefore, no information are available directly downstream of the sharp corner.

The accuracy of the pressure measurements is about $\pm$ 3.4 mb.

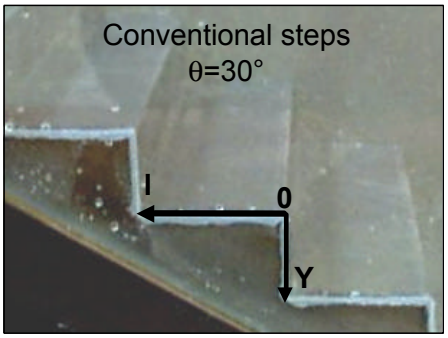

Figure 14.26: Definition of l and y axis on the horizontal and vertical step faces

14.4.1 Pressure field on conventional stepped chute ($m = 0$)

Pressures variation

- The position corresponding to the sensor located halfway from the outer step edge (Fig. 14.27-a1) appears to represent the region near the jet impact on the horizontal step face (nappe or transition flow) or the boundary region between the jet impact on the horizontal face and the recirculating vortex (transition or skimming flow). This can be explained by the high pressure fluctuations associated with the jet impact and the negative value of the mean pressure. It might indeed be attributed to the flow separation, as observed by Sánchez-Juny et al. (2000) for skimming flow over a 51 degree inclined stepped chute. However, in the latter situation and due to the steep slope, the extent of the impact region was smaller (*i.e.*, $l/l_s < 0.2$).

- The distribution of the dynamic pressure with the discharge, for $0 < l/l_s < l/2$ (Fig. 14.27-a2 and a3), is fairly similar. This should be representative of the region near the impact of the oscillating jet. The pressure fluctuations, the maximum pressure as well as the mean pressure for the position of the sensor located close to the step edge increase with the discharge, as one would expect due to the larger kinetic energy of the flow.

- The sensor located on the vertical face of the step (Fig. 14.27-a4) has a pressure that is practically constant and equal to zero. In the nappe or possibly the transition flow, the pressure is near atmospheric provided that the free-surface of the pool behind the jet is below the position of the sensor. In the skimming flow regime, the circulation of the main vortex should not influence the outer region of the vertical face (*i.e.*, $y/h_s < 0.2$).

- No significant negative pressure peaks have been measured.

- The standard deviation, representative of the pressure fluctuation reveals that the skimming flow regime has the highest pressure fluctuations measured. This may be the consequence of the interference between the oscillating jet impacts and the recirculating vortices. For nappe and transition regimes, the pressure fluctuations are lower. Contrary to the visual observations of Chanson (1994c), pressure measurements for transition regime do not indicate any vibrations or instabilities.

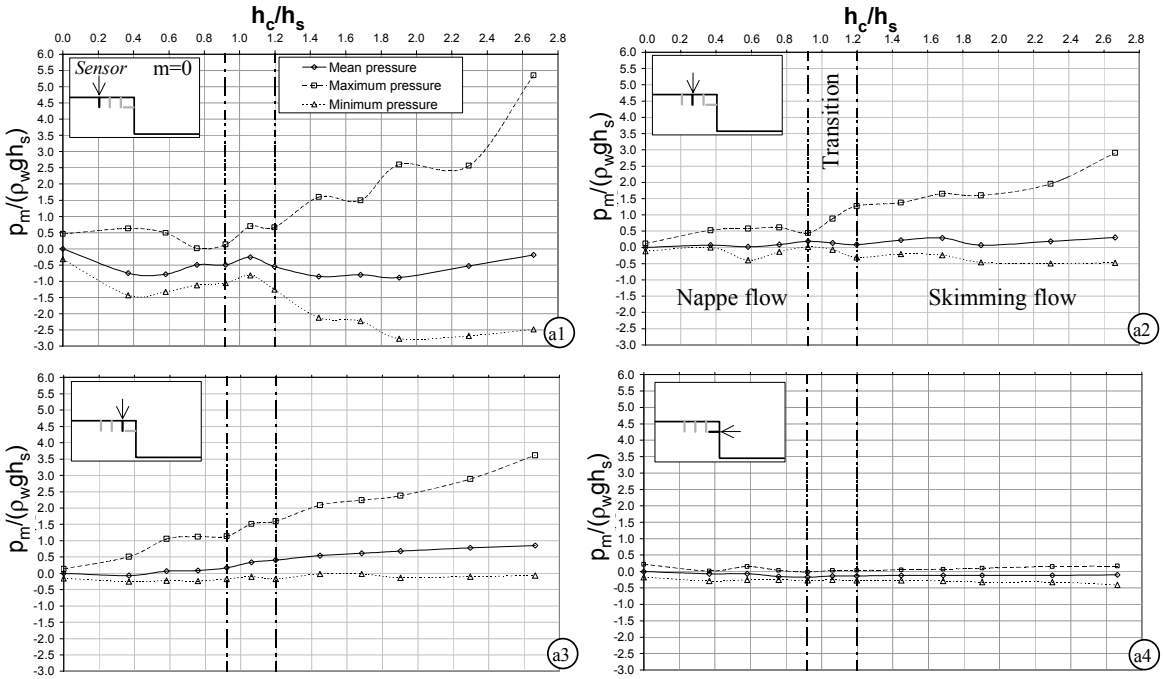

Figure 14.27: Evolution of the mean, maximum and minimum normalized pressure with the normalized critical depth for the 30^o inclined conventional stepped flume (m=0) - Uniform region

Frequency spectrum

Frequency spectrum measurements (LabVIEW treatment based on Bollaert (2002) program) have been established for the three flow regimes in order to study the influence of the flow regimes. Sensitive study with different combination of filter and acquisition frequency minimizes the noise. Some of these spectrum highlight the presence of peak frequencies depending on the regime.

Nappe flow :

Sensors below the jet impact ($0 \leq l/l_s \leq 0.25$) countain peaks of energy for frequencies in the range of 1 Hz to 2 Hz (see Fig. 14.28). They could be attributed to the plunging nappe impact or to instabilities such as rollwaves (see Chapter 12.3).

Transition flow :

Frequency energy peaks at 1 to 2 Hz have disappeared for this regime, due to the cushioning by the water trapped in the step cavity.

Skimming flow :

When the skimming flow is developed, peaks appear in the spectrum corresponding to all the sensors fixed below the recirculating cells on the horizontal face (for $1 < l/l_s < 1/3$) and on the vertical face. The peaks lie in the range of frequencies between 3 and 7 Hz (see Fig. 14.29). The signal of the sensors fixed from the step outer edge and $l/l_s < 0.25$ do not show these peaks.

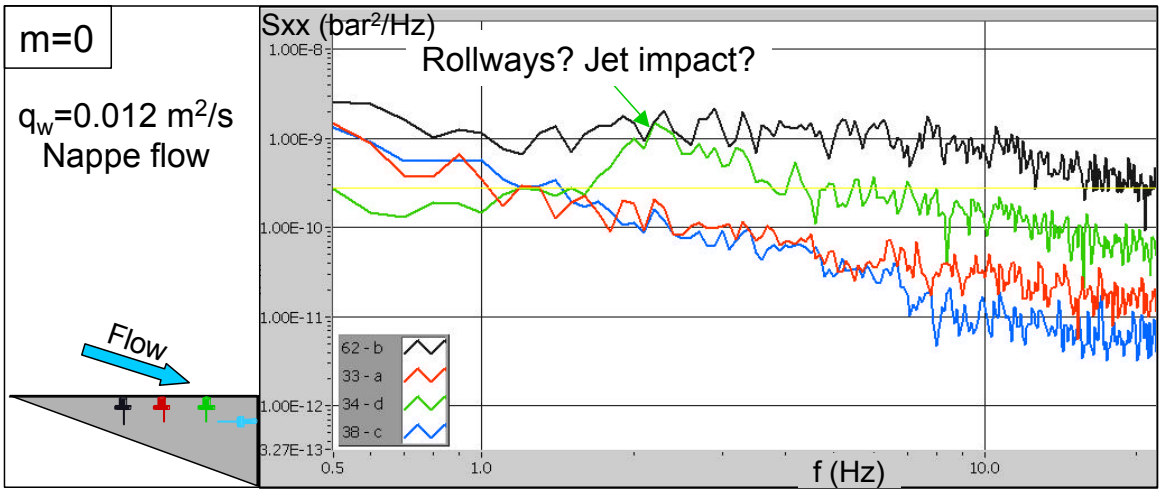

Figure 14.28: Energy spectrum for nappe flow ($h_c/h_s = 0.024$) over the 30^o conventional steps (uniform region)

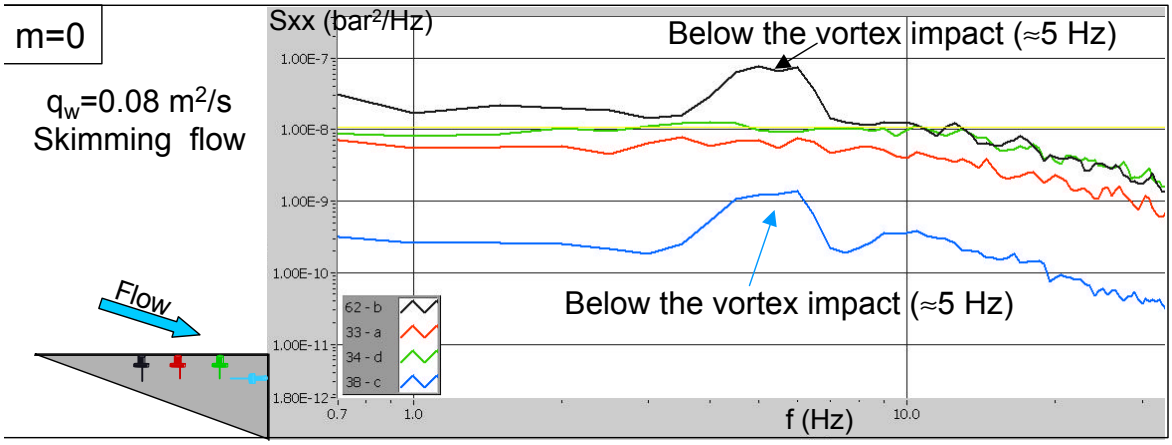

Figure 14.29: Energy spectrum for skimming flow ($h_c/h_s = 0.088$) over the 30^o conventional steps (uniform region)

Finally, the frequency spectra fellows the changes of regime. The onset of transition and skimming flow correspond to the values proposed in Chapter 12.2 and to values deduced from air concentration profile.
Moreover, the behaviour of the flow is characterized by low frequencies up to 7 Hz.

14.4.2 Pressure field on stepped chute with an endsill on every step ($m = 1$)

- The increase of the pool due to the larger step cavity reduces the pressure fluctuations on the horizontal face of the step (Fig. 14.30-b1 to b3).

- The positive pressures over the endsill and the maximum values (Fig. 14.30-b4) show that the flow strikes locally the macro-roughness, regardless of the discharge.

- No significant negative pressure peaks were measured.

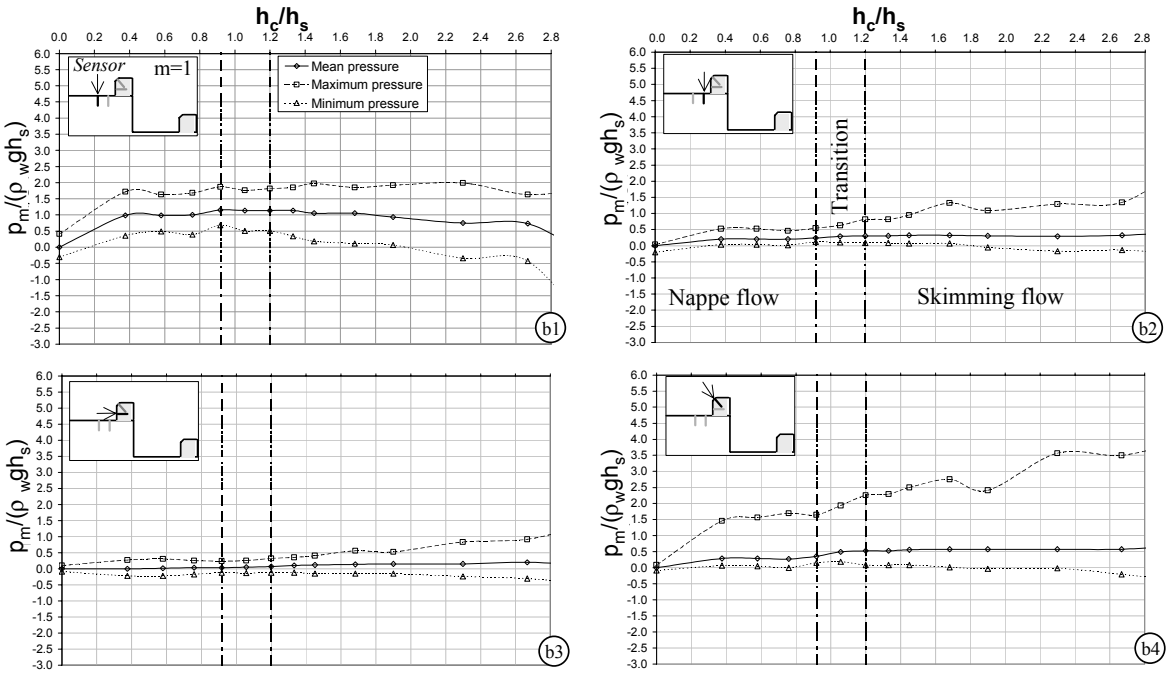

Figure 14.30: Evolution of the mean, maximum and minimum normalized pressure with the normalized critical depth for the 30^o inclined stepped flume equipped with endsill on all steps (m=1) - Uniform region

14.4.3 Pressure field on stepped chute with spaced blocks on every step ($m = 4$)

- A significant negative-pressure zone was observed at the upstream vertical face of the blocks (see Fig. 14.31a). In fact, both mean and minimum relative pressures are negative as soon as the skimming flow regime is attained. In the aerated region, if we extrapolated the air concentration values measured for the alternate endsill configuration (m=1/2) to the blocks overlay, the local air concentration may be assumed to about 15 % at two millimeters above the block outer edge. This is higher than the minimum values of 5 % to 8 % proposed by Peterka (1953) to avoid cavitation damage. Upstream and in the vicinity of the inception point, local air concentration is quite small. However, the computation of the cavitation index [Falvey (1990)] for unit discharges up to 0.26 m^2/s yields to minimal value larger than about 10. Based on these data and on these model experiments, the risk of cavitation may be considered negligible.

- The maximum load is located on the chamfer of the block. However, both the mean and the maximum pressures tend to reach an asymptotic value for well-developed skimming flow (Fig. 14.31c). This may be explained by the cushion of the jet impact due to the high submergence of the block (mixture air-water depth larger than $3k_r$).

  The maximum measured positive pressure corresponds to an equivalent pressure force of 3.6 kN per block of 50 cm length and 30 cm high, for $q_w = 8.3$ m^2/s in the prototype,.

- On the upstream vertical face of the block, the slight increase of the mean pressure (Fig. 14.31c) may be the result of the increasing kinetic energy transported in the recirculating cells. The pressure fluctuation is low, despite the presence of the vortices.

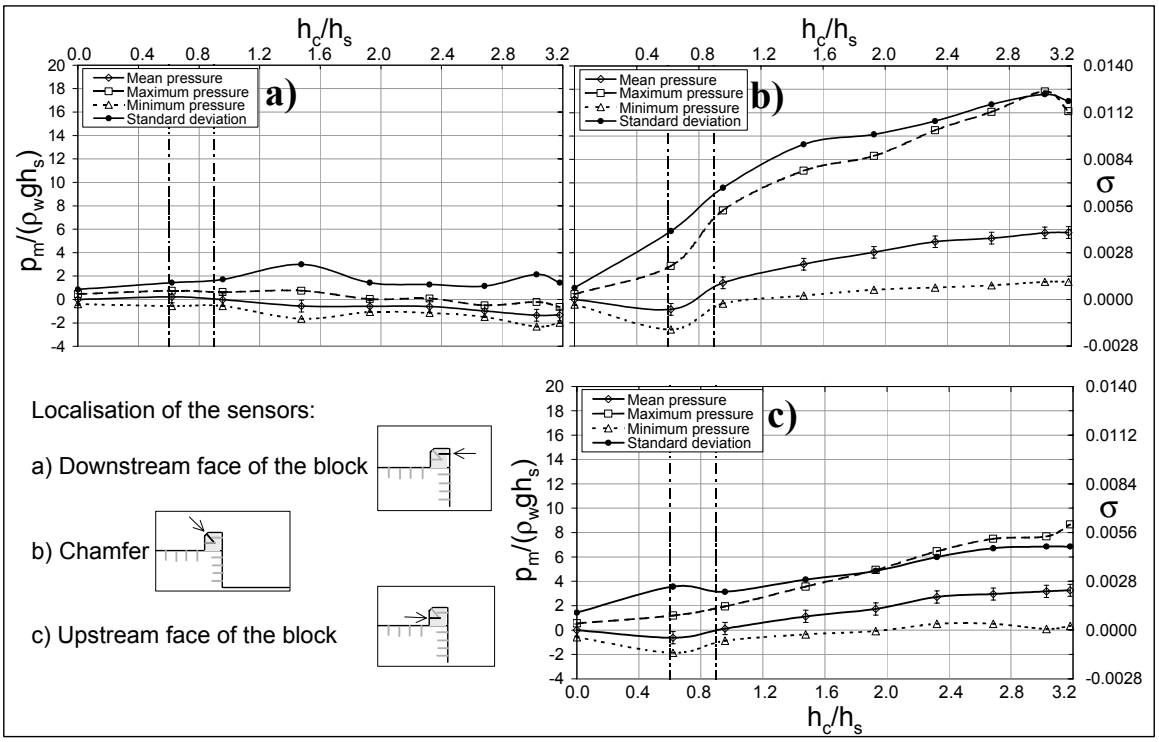

Figure 14.31: Mean, maximum and minimum normalized pressure with the normalized critical depth for the 30^o inclined stepped flume equipped with alternate blocks (m=4) - Uniform region

Finally, when compared to conventional steps, the present results show that blocks induce negative-pressure immediately downstream, but they are expected to be higher than the critical values for the onset of cavitation. They also contain pressure peaks about 3 times larger than those for conventional steps.

14.4.4 Hydrostatic and hydrodynamic forces on blocks

In the following, special attention is drawn to the order of magnitude of the loads on the blocks and to the verification that macro-roughness elements do not undergo large pressure fluctuation and negative pressures. The results focus on the alternate block system which is the most efficient system for energy dissipation (see Chapter 16 and [André, Boillat & Schleiss (2004)]).

The resultant of the pressure field acting on the block includes the hydrostatic uplift L, normal to the flow direction, and a force caused by the hydrodynamic pressure field which is composed by the drag force F_D parallel to the flow direction, and the lift force F_L normal to

the flow direction.

In the clear water region, the flow characteristics are given by density $\rho = \rho_w$, flow depth $Z = Z_w$ and mean velocity $U = U_w = q_w/Z_w$. In the aerated region, the mixture density is given by $\rho = \rho_m = (1 - C)\rho_w$, $Z = Z_{90}$ and the mean velocity is estimated as $U = \frac{q_w}{(1-C)Z_{90}}$.
Assuming a hydrostatic pressure distribution in the inclined channel flow and steady flow conditions, the hydrostatic uplift is normal to the slope and it can be roughly estimated as :

$$L = \rho g \cos\theta b_r l_r h_r \tag{14.34}$$

where b_r, l_r and h_r are respectively the width, length and height of blocks. The hydrodynamic lift force is assumed small compared to the resultant hydrodynamic force, the drag force will be parallel to the mean flow direction. The drag force can be thus estimated as:

$$F_D = C_d \rho b_r k_r \frac{U^2}{2} \tag{14.35}$$

where $k_r = h_r \cos\theta$ and C_d is the drag coefficient. For Reynolds number higher than 10^4, empirical tables give values of C_d ranging from 0.80 to 1.55 for $1 < l_r/b_r < \infty$. Considering the largest value of 1.55, the force values obtained for the maximum tested discharge are given in Table 14.4.

Forces per block (kN)	Clear water region	Aerated region
L: Uplift hydrostatic force	0.38	0.19
F_D: Hydrodynamic drag force	11.4	8.9

Table 14.4: Estimated prototype hydrostatic uplift and hydrodynamic drag forces on spaced alternate blocks (m=4) on the 30^o inclined stepped chute for a prototype unit discharges of $q_w = 7.6\ m^2/s$ (uniform region)

The results show that the force due to the peak of pressure on the chamfer of a block is relatively low compared to the drag force. In the aerated region, the high air content reduces considerably the mass of the mixture fluid, which contributes to a decrease of the impacting forces.

Finally, the measurements suggest that the blocks do not experience severe pressure fluctuations and related minimum and maximum pressures. The uplift hydrostatic force was found to be small compared to the weight of the block, whereas the hydrodynamic drag force is of the same order of magnitude. The forces acting on the blocks should not endanger their stability and resistance. More detailed study is needed to verify the reasoning for prototype application.

14.4.5 Conclusions

Dynamic pressure measurements were obtained for a 30 degree inclined stepped chute for conventional steps (m=0), endsills on every step (m=1) and alternate blocks (m=4).

For all overlays, the horizontal face of step has the largest load for skimming flow regime. The highest pressure fluctuations were measured for the nappe flow regime whereas the lowest ones were for the transition regime.

The configurations with endsills and blocks were found to attenuate the pressure fluctuations and particularly the maximum pressures on the measured points of the horizontal step faces. This fact is of interest for the hydraulic design.

Pressure fluctuations as well as negative and maximum pressures measured on the block faces and on the steps are not expected to be severe enough to produce cavitation or to destabilize the blocks.

The frequency spectrum highlights that the flow is governed by very low frequencies structures such as rollwaves (1 to 2 Hz) for nappe flow or recirculating cells for skimming flow (3 to 7 Hz).

Chapter 15

Comparison of methods for estimating residual energy

15.1 Brief review of methods for residual energy estimation

The previous chapters showed that measurement of flow depth and velocity may be complex and lead to inaccurate results. In addition, for alternate 2D or 3D macro-roughness overlays, the question still remains in where to take measurements (at the endsill or block outer edge or at the step outer edge?) to have a good estimation of the global residual energy. To avoid this difficulty, one indirect method consists of the sequent depths measurement of an forced hydraulic jump at the chute base.

Since the amount of residual force at the structure base is crucial to design of toe protection, particular attention is focused on the validity and the accuracy of this hydraulic jump method to estimate global energy dissipation of a stepped macro-roughness overlay. In addition the validation of the hydraulic jump method for conventional steps overlay also determines the energy dissipation for more complex macro-roughness systems such as steps equipped with blocks.

15.1.1 Direct methods

Summary of classical residual energy relationships

To clarify the existing estimation methods of residual energy and to see their influence on results, the different formulations exposed in Part III, Chapter 10.1 are applied to depth and velocity measurements obtained at the toe of conventional stepped flume for $\theta = 30^o$. A summary of these formula, along with their assumptions, are given in the following.

1. Mean residual energy for equivalent clear water fluid: $H_{r,w}$
   Assumptions: uniform flow conditions, hydrostatic pressure distribution, incompressible fluid

$$H_{r,w} = Z_{w,u} \cos\theta + \frac{\alpha_m q_w^2}{2g Z_{w,u}^2} \tag{15.1}$$

   where α_m is the kinetic energy correction coefficient derived from Equation 14.31, Chapter 14.3.3.

2. Mean residual energy for air-water mixture flow: $H_{r,m}$
   Assumptions: Uniform flow conditions, hydrostatic pressure distribution, incompressible mixture fluid

$$H_{r,m} = Z_{90,u} \cos\theta + \frac{U_m^2}{2g} \tag{15.2}$$

   with U_m the depth-averaged air-water mixture flow velocity.

3. Mean residual energy for homogeneous effective mixture flow (see Chapter 13.2): H_r'
   Assumptions: Uniform flow conditions, hydrostatic pressure distribution, only the homogeneous portion ($c \leq 0.7$) of mixture flow is considered

$$H_r' = Z_u' \cos\theta + \frac{U'^2}{2g} \tag{15.3}$$

   where Z_u' and U' are respectively depth and averaged velocity of the mixture homogeneous flow layer.

4. Residual energy for nappe flow according to Chamani & Rajaratnam (1994): $H_{r,NF}$
   Assumptions: $8 \leq N_s \leq 30$, $0.03\ m \leq h_s \leq 0.45\ m$, and $0.421 \leq h_s/l_s \leq 0.842$.
   For the tested case: $h_s = 0.06\ m$, $h_s/l_s = 0.58$ and $N_s = 64$
   Equation 10.2 (Part III) is assumed to be available for this high number of steps.

$$H_{r,NF} = (1-\varepsilon)^{64}(h_s + 1.5h_c) + h_s \Sigma_{i=1}^{63}(1-\varepsilon)^i \tag{15.4}$$

   According to Equation 10.3, $\varepsilon = 0.098 - 0.696\log(\frac{h_c}{h_s})$.

5. Residual energy for transition and skimming regimes according to Chanson (1994b): $H_{r,SF}$
   Assumptions: Uniform flow conditions, incompressible fluid and head losses characterized by the Darcy-Weisbach friction coefficient f at the pseudo-bottom.

$$H_{r,SF} = h_c\left[\left(\frac{f}{8\sin\theta}\right)^{1/3}\cos\theta + \frac{\alpha_m}{2}\left(\frac{f}{8\sin\theta}\right)^{-2/3}\right] \tag{15.5}$$

All these estimation methods assume a single-phase and incompressible fluid characterized by a mean density $\rho_m \simeq (1-C)\rho_w$.

Depth-averaged mechanical energy

Since both air concentration and longitudinal velocity profiles have been measured for conventional steps, the depth-averaged total mechanical energy is computed at the toe of the chute. This provides a means to verify if the incompressible assumption can be applied without significant error.

Total mechanical energy E_{ti} of a point z_i on the normal axis is given by (see notations in Fig. 15.1):

$$E_{ti} = \rho_i \frac{u_i^2}{2} + p_i + \rho_i g y_i \tag{15.6}$$

with p_i the local pressure and ρ_i the local density of the aerated flow at the elevation z_i. Divided by $\rho_i g$ yields the local total head H_i:

$$H_i = \frac{u_i^2}{2g} + Y_b + z_i\cos\theta + \frac{\int_{z_i}^{z_{90}}\rho_i dz}{\rho_i}\cos\theta(Z_{90} - z_i) \tag{15.7}$$

Therefore, the depth-averaged residual energy at any bottom reference Y_b above the chute base is derived from:

$$\overline{H_{r,i}} = \frac{1}{Z_{90}}\int_0^{Z_{90}} H_i dz \tag{15.8}$$

The methods are compared for the case of a 30^o conventional stepped chute.

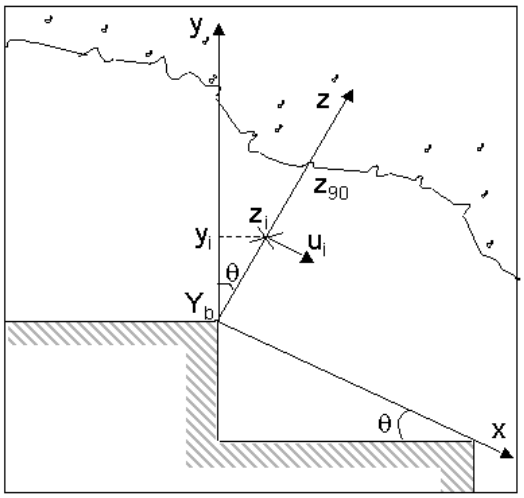

Figure 15.1: Notation used in the residual energy computation

15.1.2 Hydraulic jump method

The Froude number which characterizes the flow at the last step of flume is within the range of 7 to 10. According to Hager (1992), the forced hydraulic jump corresponds to either a stabilized or a choppy jump. Therefore, in most of the cases, hydraulic jump is very aerated and unstable. For this reason, as already mentioned in Paragraph 11.2.3, when the hydraulic jump is stabilized, downstream sequent depth Y_2 is measured with ultrasonic sensors at two different places in the axis of non aerated tailwater of jump. Sequences of measurements were fixed at $120s$ and a numerical filter eliminated anomalies.

The global residual energy at the toe of the chute is then assumed to be derived from:

$$H_{r1} = Y_1 + \frac{\alpha_m q_w^2}{2gY_1^2} \tag{15.9}$$

where Y_1 is the upstream sequent depth of the hydraulic jump and α_m is the kinetic energy correction coefficient.

15.2 Validation of hydraulic jump method

15.2.1 Influence of hydraulic jump position

The resulting residual energy varies significantly depending on the hydraulic jump position. A sensitive study was performed to estimate the optimal position of hydraulic jump. Two conditions are possible:

1. Last steps are submerged (Fig. 15.2a):
   The residual energy H_{r1} is over-estimated and thus the relative energy loss is drastically underestimated (about 15 % lower for two drowned steps),

2. Jump is far from the base of the last step (Fig. 15.2c):
   The flow is deaerated upstream of the hydraulic jump. Friction losses become significant.

The resulting residual energy is then under-estimated. The relative energy loss, which includes also the head loss in the basin, is then over-estimated (about 5 % higher).

The repeatability of the results is improved when the front of the hydraulic jump is located at the point where the plunging flow reaches the basin bottom as illustrated in Figure 15.2b.

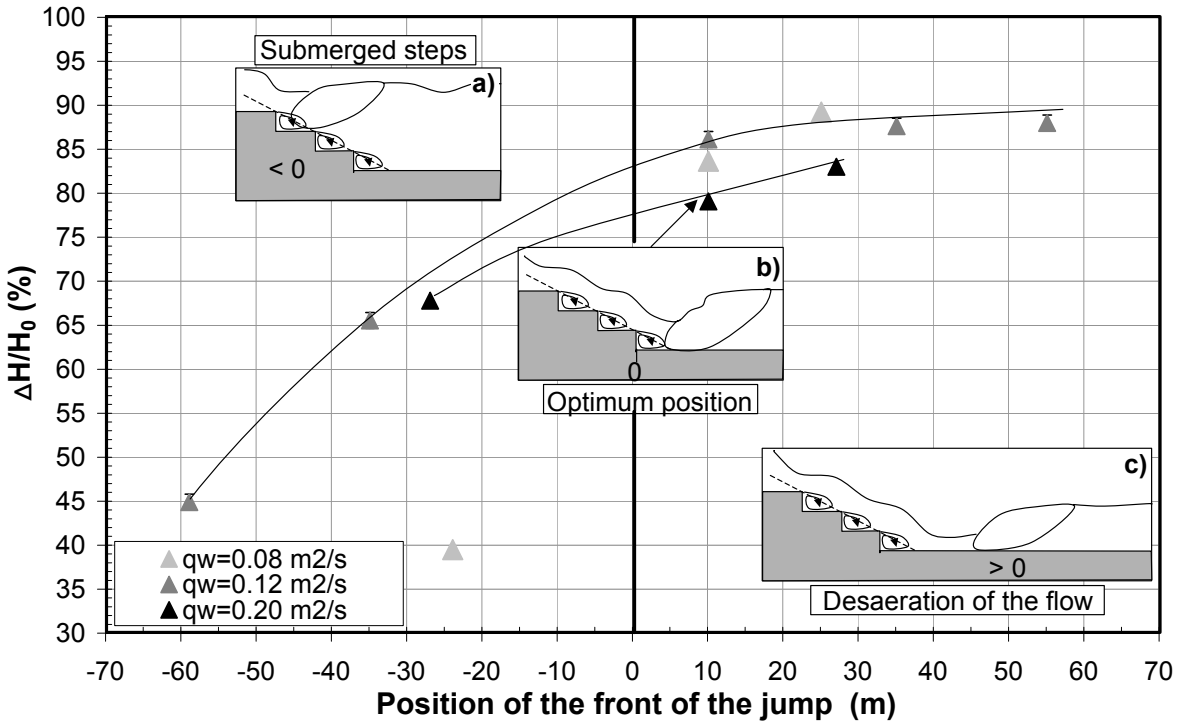

Figure 15.2: Effect of position of hydraulic jump on relative energy dissipation $\Delta H/H_0$ for the 30^o conventional stepped chute

15.2.2 Repeatability of measurements

In order to estimate repeatability of results, sequent depths Y_2 were measured several times for the same discharge. Tests were also performed with increasing and decreasing discharges. As shown in Figure 15.3, except for nappe flow where hydraulic jump is difficult to observe and to locate accurately, the difference on relative energy loss is about 0.5 % for the other regimes. It is smaller than the maximal relative error due to measurements uncertainty and estimated to be 1 %. Except for the lowest discharges, repeatability of measurements is therefore acceptable.

15.2.3 Influence of density assumption

The upstream sequent depth Y_1 is derived by measuring the downstream sequent depth Y_2 in the non aerated tail water of hydraulic jump. Most of the authors assumed that $\rho_1 \simeq \rho_2 \simeq \rho_w$ which yields to the Belanger formula, Equation 9.17, Part III:

$$Y_1 = \frac{Y_2}{2}(\sqrt{1+8Fr_2^2}-1)$$

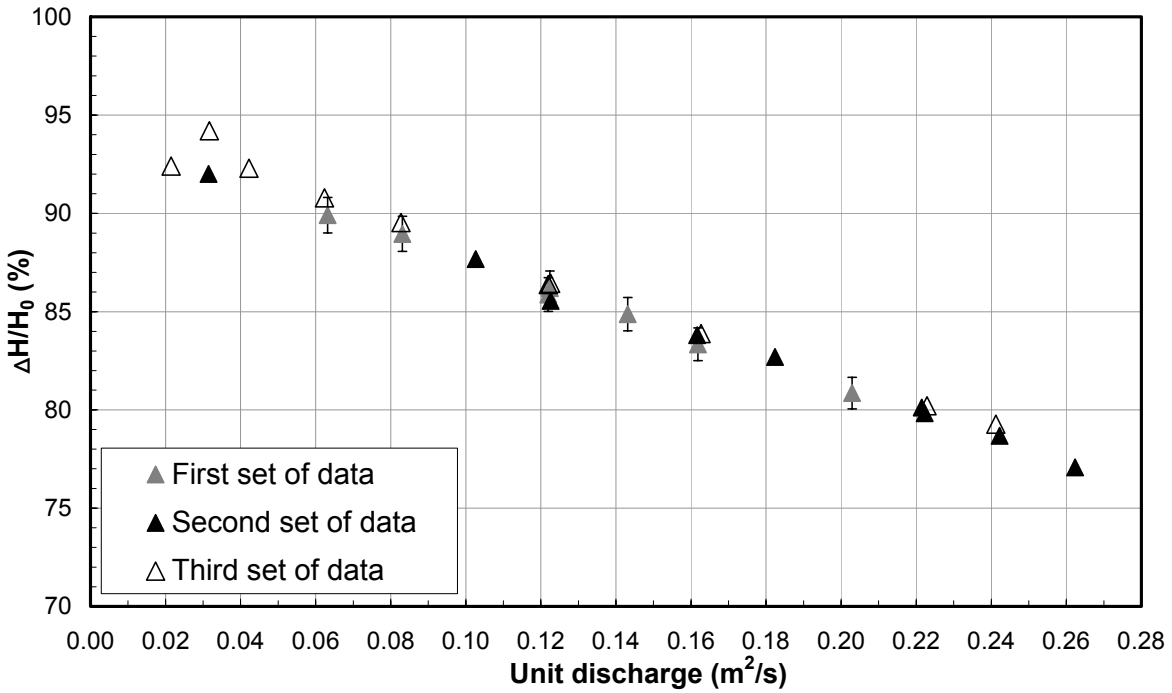

Figure 15.3: Repeatability of the relative energy loss estimated using the hydraulic jump method - 30^o conventional stepped chute

where $Fr_2^2 = q_w^2/(gY_2^3)$, ρ_1 and ρ_2 are the flow densities at the upstream and downstream of hydraulic jump.

However, this assumption on density does not seem to be realistic since the flow mean air concentration at the end of the chute can vary from 70 % ($\rho_1 = 300\ kg/m^3$) to 46 % ($\rho_1 = 540\ kg/m^3$) depending on flow regimes and macro-roughness overlays.

If $\rho_1 \neq \rho_2$ is conserved in both the momentum Equation 9.13 (Part III) and the mass conservation Equation 9.14 (Part III), a third degree equation is obtained (Eq. 15.10) and thus Y_1 can be calculated from:

$$Y_1^3 - Y_1[\delta Y_2^2(2Fr_2^2 + 1)] + 2\delta^2 Y_2^3 Fr_2^2 = 0 \tag{15.10}$$

where $\delta = \frac{\rho_2}{\rho_1}$.

In order to estimate density assumption influence on derivation of the residual energy and on the relative energy loss, calculation is performed for the both cases $\rho_1 \simeq \rho_2$ and $\rho_1 \neq \rho_2$. Results are illustrated in Figure 15.4 for conventional steps (m=0) and alternate blocks (m=4) overlay on the 30^o slope.

The similar values show that the error on relative energy loss when ρ_1 is assumed to be equal to ρ_2 is negligible. This assumption can therefore be mainatined.

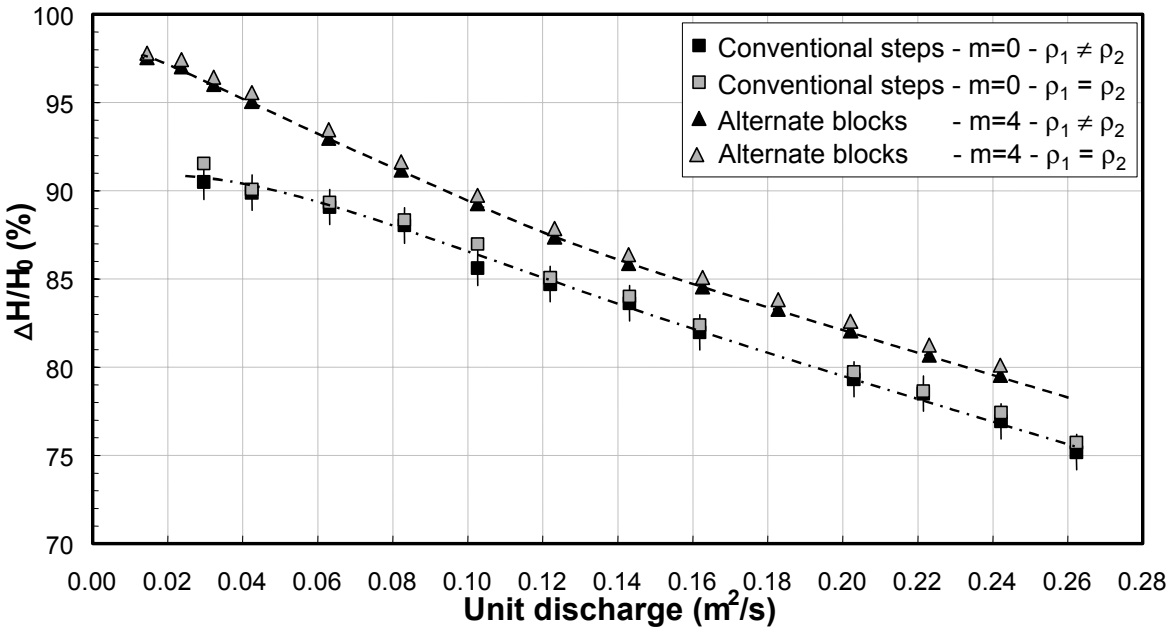

Figure 15.4: Effect of density assumption on relative energy dissipation $\Delta H/H_0$ for the 30^o conventional stepped chute (m=0) and stepped chute with spaced blocks (m=4)

15.3 Comparison of methods

The residual energy at the toe of the 30^o conventional stepped chute, obtained with the different mentioned methods are represented versus the roughness Froude $F_{*,\theta}$ in Figure 15.5. From this figure and from calculation of relative energy loss $\Delta H/H_0$, the following conclusions can be drawn.

- There is no significant difference when the mixture fluid is assumed to be incompressible. The difference between $H_{r,m}$ based on the mean density and the value determined from the integration over the flow depth $\overline{H_{r,m,i}}$ is about 1 %, in the order of uncertainty due to measurements.

- For developed skimming flow ($F_{*,\theta} > 4$), the residual energy $H_{r,w}$ for equivalent clear water flow has a different trend than the values computed with mixture flow characteristics or with the hydraulic jump method. In Paragraph 14.3, it was observed that the mean mixture velocity for $F_{*,\theta} > 4.5$ could be under-estimated because of fiber-optical probe perturbation for high discharges. However, from Figure 15.5 it can be noticed that the residual energy H_{r1} is quite similar to $H_{r,m}$ or H'_r but very different from $H_{r,w}$. Yet H_{r1} was computed independently from the velocity measurements therefore results are not influenced by the optical probe accuracy. Figure 15.5 shows that for large Froude numbers, $H_{r,w}$ is under-estimated since the two curves of $H_{r,m}$ and H_{r1} converge for low Froude numbers. This fact confirms that for $F_{*,\theta} > 4.5$, the mixture mean velocity is slightly under-estimated because of the influence of the optical probe tips. For $F_{*,\theta} \geq 7$, for example, the mean mixture velocity is about 5.5 % lower.

  However, based on experimental data, the clear water characteristics (Z_w and U_w) don't represent accurately the flow behaviour and can't be used to estimate energy dissipation.

- The mean residual energy estimated with the effective homogeneous mixture flow characteristics gives the best result. This is the closest to the data computed with the hydraulic jump method. The difference in the relative energy loss is within the range of 1 to 6 %, which is lower than the difference of 15 % mentioned by Tozzi (1994).

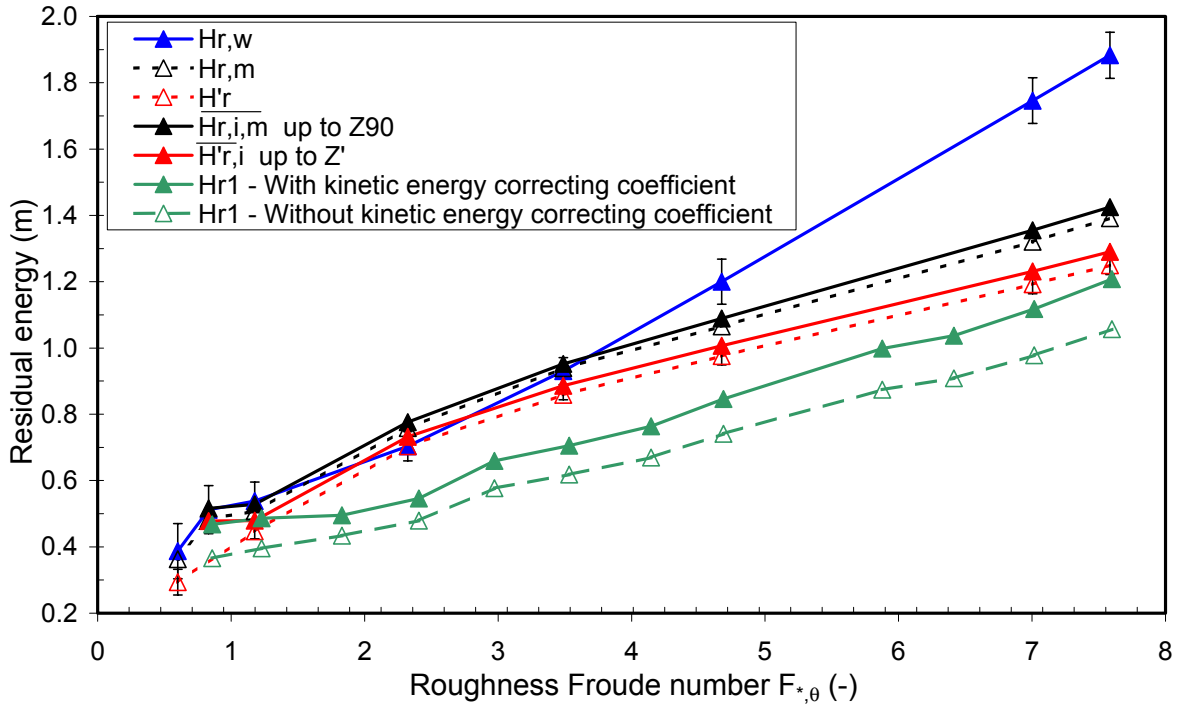

Figure 15.5: Comparison of the different computed residual energies at the toe of the 30^o conventional stepped chute

15.4 Conclusions

The equivalent clear water concept does not accurately determine the global energy dissipation. On the other hand, effective homogeneous mixture flow realistically represents the portion of flow involved in the energy loss process.

The hydraulic jump method is an easy and accurate tool to estimate the global relative energy loss at the toe of a structure. Nevertheless, to be accurate, the upstream front of the hydraulic jump must be located at the point where the plunging flow reaches the horizontal bottom of the stilling basin.
For flow with mean air concentration lower than 65 %, the assumption $\rho_1 = \rho_2$ can be applied without significant error on the residual energy. To avoid an under-estimation of the residual energy, the kinetic energy correction coefficient α_m must be implemented to take into account the non-uniform velocity distribution of the flow at the toe, then

$$H_{r1} = Y_1 + \frac{\alpha_m q_w^2}{2gY_1^2}$$

with α_m according to Table 14.2.

The residual energy derived from hydraulic jump method will be applied to all the tests to compare their efficiency. To remain conservative, the residual energy H_{r1} is corrected with a correction factor η_H such as:

$$H_r = \eta_H H_{r1} \tag{15.11}$$

Based on comparison of H_{r1} and $H'_{r,i}$ for conventional steps (m=0), every step equipped with endsill (m=1) and every second step equipped with endsill (m=1/2) and $\theta = 30^o$, a correction factor $\eta_H = 1.15$ is recommended.

This correction factor takes into account the singular loss caused by the change of direction and the turbulent dissipation of the flow when it plunges into the stilling basin.

Chapter 16

Energy dissipation of aerated flow over stepped macro-roughness overlays

16.1 Relative energy loss

The relative energy loss is calculated using the hydraulic jump method. The method is applied to conventional steps (m=0), steps equipped with endsills (m=1/3, 1/2, 1) and steps equipped with blocks (m=4, 5, 6). The upstream sequent depth is derived assuming $\rho_1 = \rho_2$ (see Section 15.2). Since the kinetic energy correction coefficient cannot be experimentally estimated for all the overlays, it is assumed that for block overlays the value of α_m is the same as for $m = 1/2$. The relative energy loss is given by:

$$\frac{\Delta H}{H_0} = \frac{H_0 - H_r}{H_0} \tag{16.1}$$

with $H_0 = H_f + h_0 \cos\theta + \frac{q_w^2}{2gh_0^2}$, h_0 the opening of the jetbox, H_r the residual energy according to Equation 15.11.

16.1.1 Efficiency of conventional steps

The relative energy loss for an equivalent smooth chute with a slope angle $\theta = 18.6^o$ and $\theta = 30^o$ is computed with the numerical code developed by Falvey (1990) (see Appendix B). The values are compared with relative energy loss caused by conventional steps in Figure 16.1.

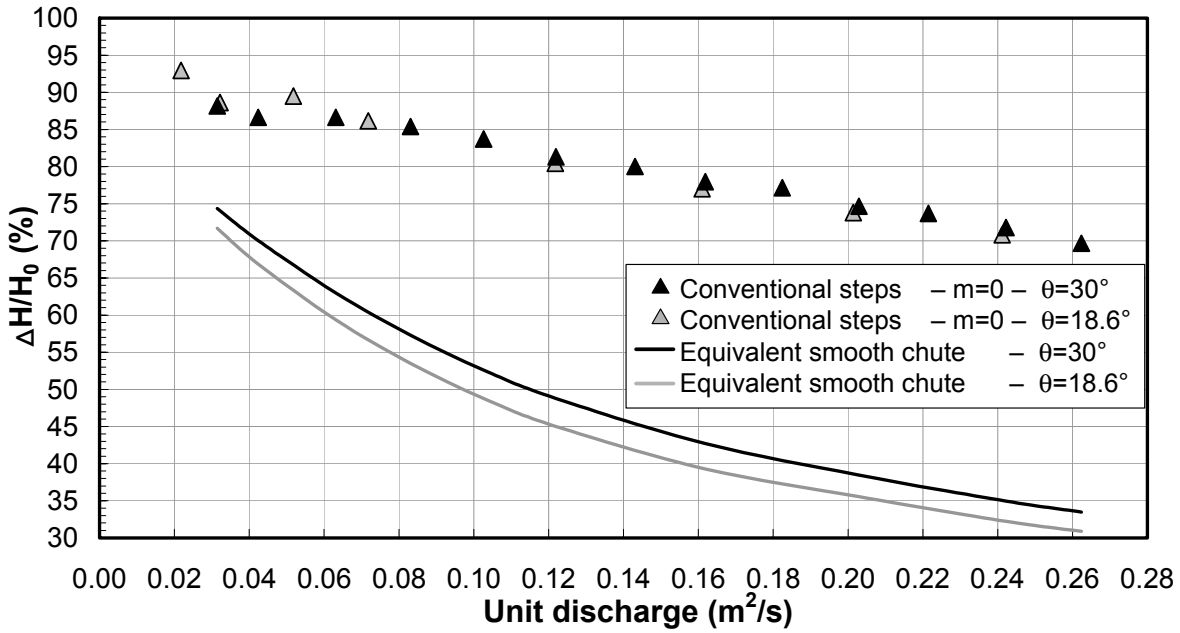

Figure 16.1: Comparison of the relative energy loss $\Delta H/H_0$ between conventional stepped and smooth chutes for $\theta = 18.6^o$ and $\theta = 30^o$

♢ *Comparison with smooth chute*

The results show that conventional steps produce a reduction of more than 35 % in the residual energy at the toe for higher discharges ($q_w > 0.08\ m^2/s$) compared to smooth chutes. For the highest discharge ($q_w = 0.27\ m^2/s$), about 70 % of the initial energy is dissipated for

both stepped slopes.

♢ *Flow regimes effect*

In agreement with Chamani & Rajaratnam (1994), the nappe flow is the most dissipative regime. As observed in Figure 16.1, for well developed skimming regime, when $Z_{90} \geq 1.5k_s$, the steps become less efficient as the discharge increases. Their influence is cushioned by the large skimming layer.

♢ *Slope effect*

Except for nappe flow regime, the slope effect on the relative energy loss is negligible between $\theta = 30^o$ and $\theta = 18.6^o$. The trend is in agreement with the observations of Peruginelli & Pagliara (2000). For nappe flow, conventional steps are more efficient for the flatter slope $\theta = 18.6^o$ whereas for skimming flow, energy dissipation is slightly higher for the 30^o slope.

For nappe flow over flatter slopes, partial hydraulic jumps can be developed on the horizontal face of the step. They contribute to head loss. For $\theta = 30^o$, no hydraulic jumps were observed.

Note that the number of steps is also different between the two slopes since the step height remains the same. Therefore results are the combination of both slope and number of steps.

16.1.2 Efficiency of 2D overlays: steps equipped with endsills

The relative energy loss caused by conventional steps and steps equipped with endsills are compared in Figure 16.2 for the 30^o inclined flume.

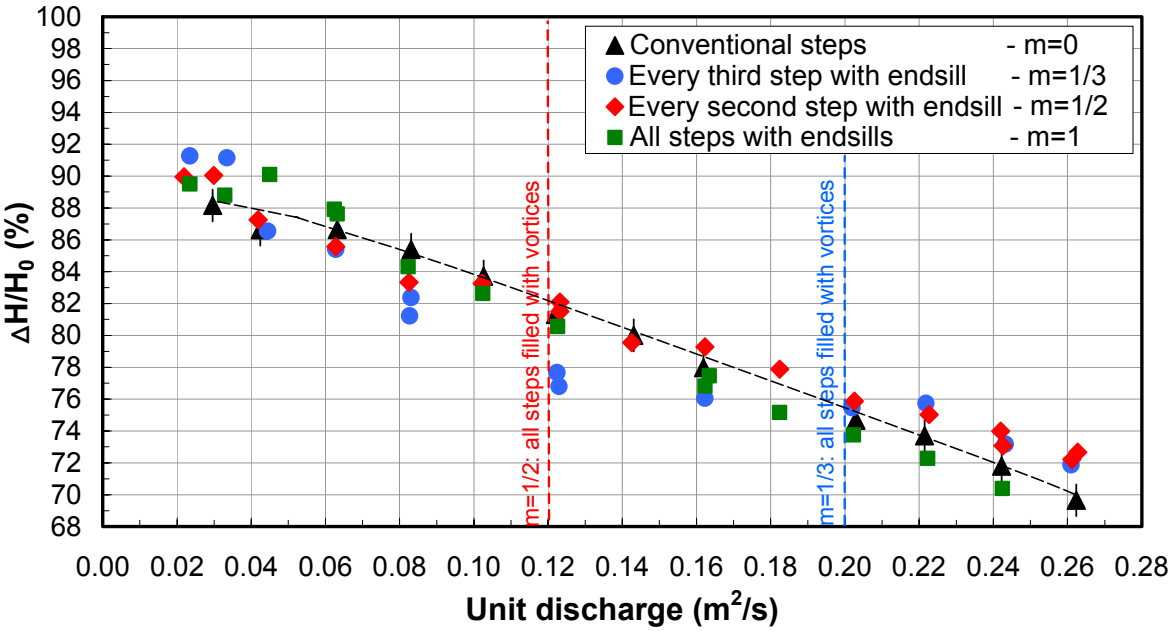

Figure 16.2: Comparison of the relative energy loss $\Delta H/H_0$ between conventional stepped chute and stepped chute equipped with endsills for $\theta = 30^o$

From this figure, the following conclusions can be made.

- Endsill on every steps (m=1) does not increase energy dissipation. Even though, as soon as skimming flow is established, this overlay tends to be less efficient than conventional steps. In fact, even if the length of the friction under the vortices is larger ($h_{v,1} = h_{v,0} + 3/2h_s$), the internal transverse jets on the endsill outer edges are shorter and the separation zone vortices/internal jet is broken by the endsill itself. As a consequence, head losses are lower than for conventional steps. The global result on energy dissipation agrees with the results on velocity.

- Endsill on every third step (m=1/3) causes less energy dissipation until $q_w = 0.20\ m^2/s$, when all the steps start to be filled with water and recirculating cells. For flows less than $q_w = 0.12\ m^2/s$, the fluid skips over the two steps immediately downstream of the endsill. Then for $0.12\ m^2/s < q_w < 0.20\ m^2/s$, the flow skips over one step. Therefore an important portion of steps is inefficient regarding head loss. This results in a relative energy loss 3 to 4 % lower than for conventional steps up to $q_w = 0.12\ m^2/s$.

  When skimming flow is established, the gain of energy dissipation at the highest discharge is about 2 % compared with conventional steps, but with the negative side effect that the flow depth is highly swelled and the free surface is unstable (see Section 14.2).

- For endsill on every second step (m=1/2), again, it is only when all the steps are filled with recirculating cells (for $q_w = 0.12\ m^2/s$) that this overlay becomes more efficient than conventional steps. In fact, when skimming flow is well established, this overlay produces an increase of energy dissipation of about 2 %.

  This configuration represents a mixture between the case of conventional steps and all steps equipped with endsills. Therefore, this small increase of head loss may be attributed to the successive widening and narrowing of the flow caused by the passage from one step with endsill to the other step without endsill.

- The behaviour of the overlays m=1/2 and m=1/3 stresses the important contribution of each step in the dissipation process since when 1 to 2 or 2 to 3 steps are not filled with recirculating cells and internal jets, the relative energy loss is significantly lower.

For the particular case of nappe flow regime, it can be seen in Figure 16.2 that all the configurations with endsills are more efficient than conventional steps. The drop from the top of the endsill to the horizontal face of the step is higher and the impacted jet is deflected more, which creates an additional energy loss.

This trend is also valid for $\theta = 18.6^o$ where for the range of tested discharges the most efficient endsills overlay correspond to $m = 1/2$ with a gain of about 2% of energy dissipation.

In conclusion, for discharges up to $q_w = 0.28\ m^2/s$ and $18.6^o \leq \theta \leq 30^o$, the optimal overlay with the skimming regime corresponds to $m = 1/2$.

16.1.3 Efficiency of 3D overlays: steps equipped with blocks

Behaviour description

The three overlays corresponding to steps equipped with blocks are different regarding the ratio e_r/b_r and the density $d_r = \frac{N_r \forall_r}{N_s \forall_s} = m\frac{h_r b_r l_r}{h_s B_f l_s}$ as described in Section 11.1.3. Their

resulting relative energy loss versus unit discharges are shown in Figure 16.3 along with values for conventional steps (m=0) and every second step equipped with endsill (m=1/2).

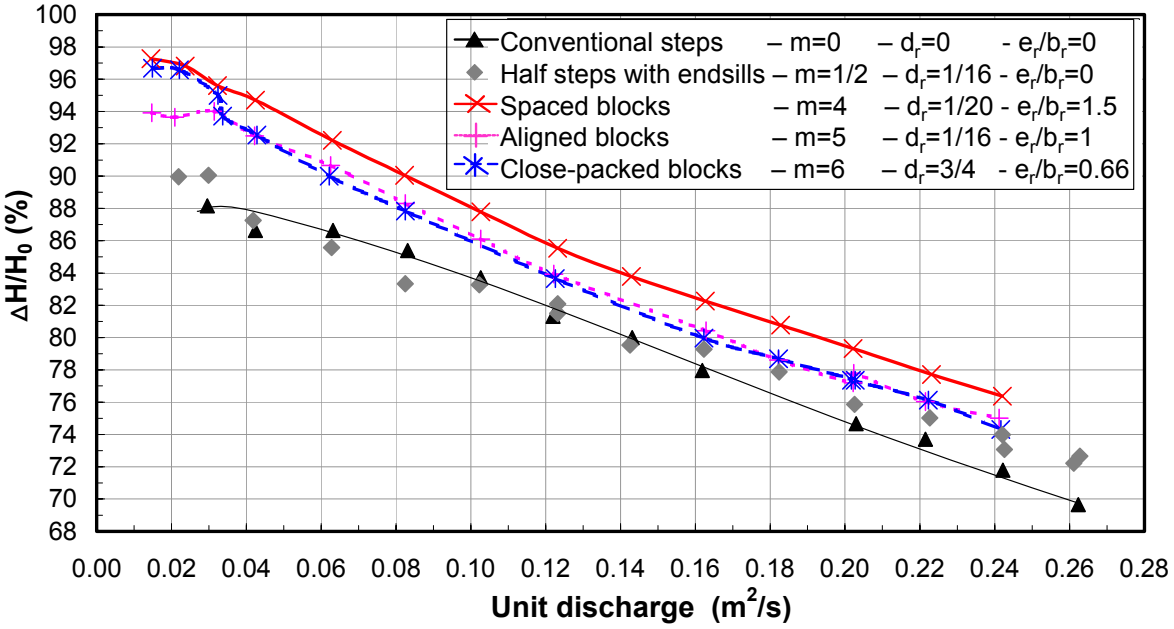

Figure 16.3: Comparison of the relative energy loss $\Delta H/H_0$ between conventional stepped chute and stepped chutes equipped with blocks for $\theta = 30^o$

These data permit to highlight the following behaviours.

- Alternate spaced blocks (m=4) lead to a significant increase of head loss. For all discharges, the dissipation rate is higher by about 5 to 8 % compared with conventional steps. This interesting result may be attributed to the drag form effects (wakes upstream and downstream of blocks, contractions between blocks) added by the blocks themselves.

  For the highest tested discharge ($q_w = 0.242\ m^2/s$) and slope of $\theta = 30^o$, the spaced blocks overlay (m=4) allows a dissipation of about 76.5 % of the initial energy of the flow instead of 71 % for conventional steps and 35 % for equivalent smooth chute.

- The efficiency of the other blocks overlays is not as efficient when the skimming layer above the blocks is about 2 times thicker than k_r ($k_r = h_r \cos\theta$ the blocks normal height). For the highest discharges, their efficiency becomes similar to the overlay $m = 1/2$.

- Since the only difference between the block overlays is their transverse distribution over the width of the flume, the contribution of the drag form effect must be the source of the increase in the head loss. Depending on the space between the blocks, both longitudinal and transverse trajectories of flow are modified. If the blocks are closed-packed, the main portion of the flow skims over the blocks as the flow depth increases. The flow becomes similar to the case of $m = 1/2$ for skimming regime. With a relative large space between the blocks ($e_r/b_r > 1$), the portion of the fluid which flows between the blocks and which is under the influence of the drag form perturbation is significant compared to the

portion which skims above the pseudo-bottom formed by the blocks edges. In addition, if the space is wide enough, the transverse jets caused by the contraction between two blocks interact, which contributes to energy loss.

Note that for this type of overlay, since transverse effect between two blocks contribute to the energy dissipation process, results may depend also on the flume width B_f.

Comparison with existing guidelines for baffles on smooth chute

Sayre & Albertson (1963) and Harleman & Rumer (1963) studied the flow resistance for several overlays consisting in different distribution of sheet rectangular baffles over very flat slope (< 1 %) and for non aerated flow. They concluded that the overlay is more dissipative if (notation given in Fig. 11.4):

- $b_r/h_r >> 1$,
- $e_r/h_r << 1$,
- $x_r/h_r << 1$

.

Peterka (1958) tested flow over baffles directly anchored on smooth spillway or drops. Prototype tests on a 1V:2H slope showed that the optimal baffles system which can resist flow up to 5.6 m^2/s has the following design:

- $h_r = 0.8h_c$ with h_c the critical depth of the design discharge,
- $b_r = e_r = \frac{3}{2}h_r$,
- $x_r = 2h_r$ and if $h_r < 0.9\ m$, x_r can be increased up to $6h_r$.

For flatter slopes, they found that the longitudinal space x_r between the baffles can be increased to provide the same vertical gradient between two rows of baffles.

The tested block overlays are quite different from these two previous sets of experiments since they are fixed on stepped bottom with $h_r = \frac{1}{2}h_s$. However, their geometrical characteristics are summarized in Table 16.1 in order to be compared with the Peterka (1958) and Sayre & Albertson (1963) results.

m	b_r/h_r	e_r/h_r	e_r/b_r	x_r/h_r	d_r
4	**1.67**	**2.5**	**1.5**	**8**	**1/20**
5	1.67	1.67	1	8	1/16
6	1.67	1.1	0.66	8	3/40

Table 16.1: Geometric characteristics of the tested block overlays on the 30^o stepped chute

The following conclusions can be drawn:

- For blocks width b_r:
  The optimal overlay is obtained with $b_r/h_r > 1$ and $b_r/h_r = \frac{5}{3}$, which is not far from the recommended value $b_r/h_r = \frac{3}{2}$.

- For blocks height h_r:
  The optimal baffle height was given for $0.8h_c$. In the tested cases, h_r is fixed to 0.03 m. Then the blocks must be optimal for hydraulic condition such as $h_c = h_r/0.8$ for low discharges around $q_w = 0.02$ m^2/s. This is actually the case.

- For blocks transverse space e_r:
  For nappe flow (low discharges), $m = 6$ dissipates more energy than $m = 5$. Then energy loss are higher for lower values of e_r/h_r which is in agreement with the results of Sayre & Albertson (1963).

  For higher discharges (transition and skimming regimes), the blocks are most efficient when $e_r/b_r > 1$ (or $e_r/h_r > 1.7$). Therefore, the optimum is obtained for $e_r \neq b_r$ and $e_r/h_r = 2.5$ which are different conditions than the guidelines values for baffles.

- For blocks longitudinal space x_r:
  For all the overlays $x_r = 8h_r$ which is larger than the threshold recommended by Peterka (1958).

Therefore, flow over blocks fixed on steps behave differently than flow over classical baffles on smooth bottom. The main difference lies in the development of recirculating cells inside the step cavity filled with water and the internal jet which comes transverse to the mean flow.

16.2 Sources of energy dissipation

Skimming flow is the most likely condition encountered in prototypes. For this reason, a synthesis of the energy efficiency of the tested overlays for $\theta = 30^o$ is given in Figure 16.4 for this regime. In order to highlight the relevant parameter which contributes to the increase of head loss compared to conventional steps, the following parameters are significant:

- The parameter L_{fr} which characterizes the length where friction occurred under the recirculating cells and at the interaction cells/skimming layer: $L_{fr} = l_v + h_v + x_v$ where l_v, h_v and x_v are respectively the dimensions of the recirculating cells on horizontal and vertical step faces and at the interface cells/skimming layer.

- A parameter L_{dr} which characterizes the drag form influence of transverse internal jets at the step or endsill or block outer edges, the transverse jets caused by contraction between two blocks and the wakes and separation zones.

- the density of covering $d_r = \frac{N_r \forall_r}{N_s \forall_s}$ (Eq. 11.2) and the roughness density ratio $\psi = \frac{h_r b_r}{x_r(e_r + b_r)}$ (Eq. 11.3)

It can be seen that the most relevant source of energy dissipation lies in the drag forms. In previous studies of skimming flow in stepped spillways, head losses are associated with friction caused only by recirculating cells. In contrast with this result, it is suggested that head losses can be divided into:

- **A friction term** mainly caused by the shear stress at the step faces under the recirculating cells but also under the internal jet on the horizontal face (see Fig. 12.2 and 12.4). Since the velocity of the skimming layer is considerably higher than the velocity

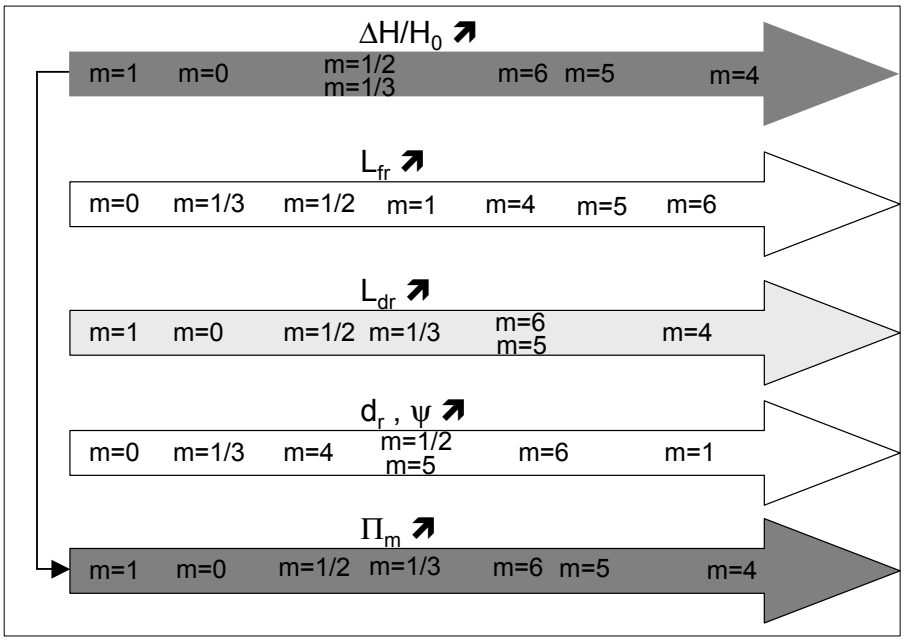

Figure 16.4: Schematic representation of energy dissipation efficiency caused by the stepped macro-roughness overlays along with variation of several parameters - For $\theta = 30^o$

of the rotating vortex [Sánchez-Juny et al. (2000)], the shear stress at the interface of the recirculating cells/skimming layer is negligible. In addition, by analyzing the vertical and horizontal distributions of the Reynolds shear stress, Nariai et al. (2001) also concluded that for skimming flow, the friction losses are widely attributable to the shear stress under the recirculating cells.

Finally, the decrease of energy dissipation rate when 1 to 2 steps or 2 to 3 steps are empty for $m = 1/2$ and $m = 1/3$, the contribution of this friction term caused by the step form effects is not negligible. This conclusion is in contradiction with the experiment of Yasuda & Chanson (2003) who considered that the destruction of the recirculating cells contributes nothing to the residual energy.

- **A drag term** caused by the internal transverse jet at the step or endsill or block outer edge, by the separation zone at the interface recirculating cells/internal jet (m=0), and between two recirculating cells (m=1/2, m=1/3, m=4,5,6) as well as by the transverse jet and wakes create by the blocks. The drag term seems to increase significantly the energy dissipation and it makes a large contribution to the total head loss.

16.3 Dissipation coefficient

16.3.1 Discussion about friction coefficient

Many studies of friction coefficient for stepped spillways design assume that for skimming flow, the friction coefficient is the result of shear stress at step faces under recirculating cells and between vortices and skimming layer.

Then, the relations to estimate friction coefficient are those of Darcy-Weisbach and Colebrook-White. Both were established for non aerated uniform flow over smooth or rough bottom.

However, since head losses are result of both friction and drag effects, this notion of friction factor appears to be too restrictive and inaccurate. The mean flow characteristics of mean longitudinal velocity, depth, kinetic energy correction coefficient cannot distinguish friction from drag influence.

Moreover, the classical friction formula are mostly applied either for mixture (Z_{90}, U_m) or equivalent clear water (Z_w, U_w) flow characteristics. As shown by Chanson et al. (2000) or Matos (2000a), the use of these different definitions results in widely scattered values. For this reason, application of classical friction laws for effective homogeneous flow characteristics (see Chapter 13) is also discussed herein.

Darcy-Weisbach friction coefficient

Flow is assumed to be similar to a uniform 1D fluid with a mean density $\rho = \rho_w$ or $\rho = \rho_m \simeq \rho_w(1-C)$ with C the mean air concentration, a uniform depth $Z = Z_{w,u}$ or $Z = Z_{90,u}$ and a mean velocity $U = U_w = q_w/Z_w$ or $U = U_m = \frac{1}{Z_{90}} \int_0^{Z_{90}} u_m(z)dz$.

Friction effect is represented by a Reynolds stress tensor $\tau_0 = \rho g Z \sin\theta$ at the pseudo-bottom [Rajaratnam (1990), Yasuda & Ohtsu (1999), ...]. In uniform region, Darcy-Weisbach friction coefficient f_u, at the pseudo-bottom, is then derived from:

$$f_u = \frac{8\tau_0}{\rho U^2} = \frac{8g\sin\theta Z}{U^2} \tag{16.2}$$

where $f_{w,u}$ and $f_{m,u}$ correspond to the friction coefficient for equivalent clear water and mixture flows respectively.

Colebrook-White

This widely used relation was originally established for turbulent uniform flow in circular or narrow rectangular flumes. Several studies tried to fit Colebrook-White law to laboratory data [Tozzi (1994), Christodoulou (1999), Chanson et al. (2000), Boes & Minor (2000),...].

For a conventional stepped chute of 30^o, Boes & Minor (2000) proposed a friction factor for equivalent clear water flow $f_{c\ w,u}$ in the uniform region defined by Equation 16.3:

$$\frac{1}{\sqrt{f_{c\ w,u}}} = 2.69 - 1.318 \log\left(\frac{k_s}{wD_h}\right) \tag{16.3}$$

where $D_h = 4B_f Z_{w,u}/(B_f + 2Z_{w,u})$ is the hydraulic diameter corrected by a form coefficient $w = 0.90 - 0.38\exp\left(\frac{-5Z_{w,u}}{B_f}\right)$ if $Z_{w,u}/B_f \geq 0.4$ and $w = 0.6$ for $Z_{w,u}/B_f < 0.4$, with B_f the flume width.

Note that this approach assumes an equivalent roughness at the pseudo-bottom equal to $k_s = h_s\cos\theta$. Velocity measurements have shown that this assumption is obviously not the case.

Darcy-Weisbach friction coefficient for effective homogeneous flow

Since accurate equivalent roughness at the pseudo-bottom is unknown, the friction factor is estimated with the Darcy-Weisbach law which is independent of the macro-roughness height. The friction factor f'_u, is defined with the effective homogeneous flow. For transition and skimming regimes, for conventional steps (m=0) and $\theta = 30^o$, f'_u is plotted versus the roughness Froude number $F_{*,\theta} = q_w/\sqrt{g\cos\theta k_s^3}$ in Figure 16.5.

$$f'_u = \frac{8g\sin\theta Z'_u}{U'^2} \tag{16.4}$$

where Z'_u and U' are respectively the uniform depth and mean velocity of the effective homogeneous flow as defined in section 13.1.2.

Comparison of the different friction definitions for conventional steps

A comparison of the resulting friction coefficients estimated with these three approaches is given in Figure 16.5.

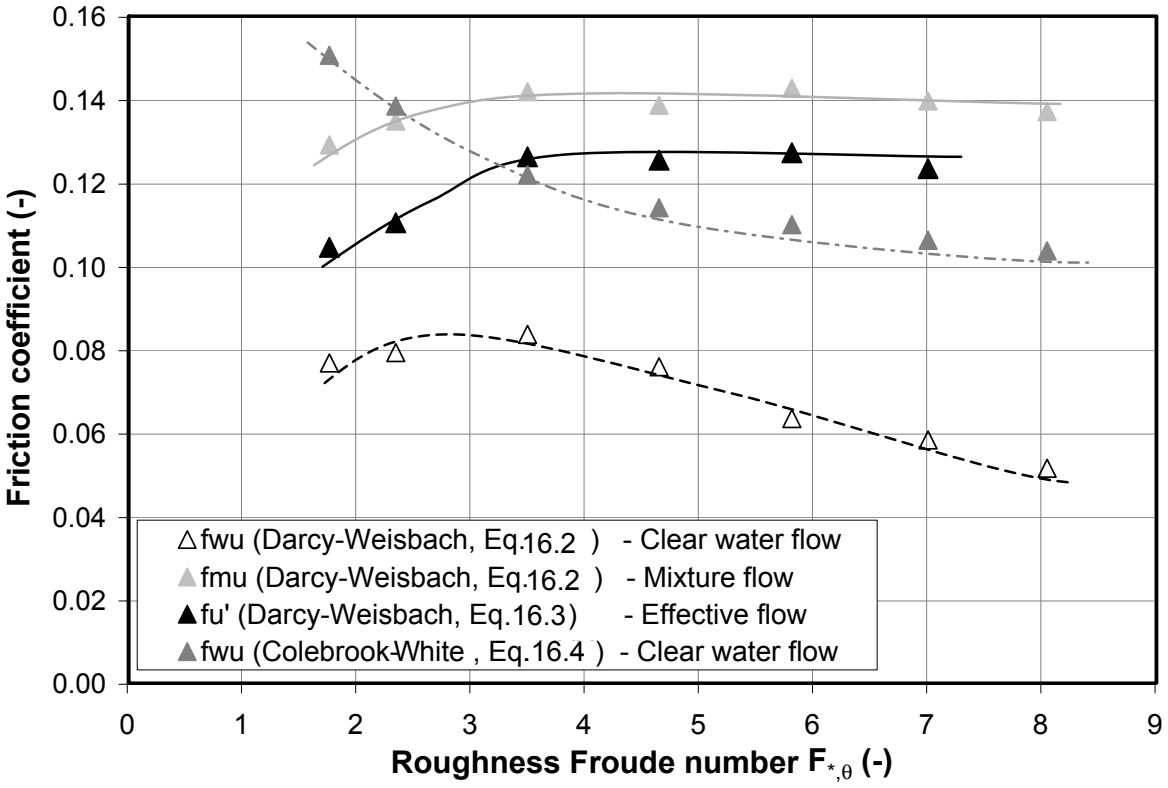

Figure 16.5: Comparison of friction factors estimated with Colebrook-White and Darcy-Weisbach laws for transition and skimming flows over a 30^o conventional stepped chute

The scatter of Darcy-Weisbach friction coefficients with $Z_{w,u}$, Z'_u and $Z_{90,u}$ approaches highlight the importance of an accurate definition of the portion of flow which contributes effectively to friction process: clear water concept overestimates air effect on energy dissipation

as already observed in Section 15.3 (under-estimation of $f_{w,u}$ for high discharges).

The friction factor may remain constant with discharge for skimming regime since both recirculating and internal jet are observed to be quite independent of discharge. That is well represented by the Darcy-Weisbach law applied to either mixture or homogeneous flows.

Furthermore, $f_{m,u}$ and f'_u are larger for skimming flow which can be explained by non developed vortices during transition regime.

Since the relative energy loss tests have shown that homogeneous flow is the most realistic portion of flow that contributes to the dissipation process, f'_u is recommended as the most realistic friction coefficient.

However, based on a friction law, f' really corresponds to a combination of shear stress and drag effects as already mentioned. The accuracy of this value is discussed just below.

Inaccuracy of friction coefficient to represent head losses

In Figure 16.6, f'_u is plotted versus $F_{*,\theta}$ for transition and skimming flows over a $\theta = 30^o$ inclined chute and for the overlays $m = 0$ and $m = 1$.

The friction factor results are in agreement with the residual energy values at the toe of the chute: $f'_u = 0.117$ for m=1 which is lower than $f'_u = 0.126$ for m=0. This demonstrates that f'_u is a type of global "dissipation" coefficient and not only a friction coefficient. Indeed, if the friction coefficient is assumed to result from recirculating cells only, for $m = 1$ which produces larger size of recirculating cells, the friction coefficient should lead to a higher value than for $m = 0$. This is actually not the case since $f'_{u,\ m=1} < f'_{u,\ m=0}$.

Moreover, if the value of f'_u for conventional steps is applied to Equation 15.5 [Chanson (1994b)], then this leads to an underestimation of residual energy at the toe of the 30^o conventional stepped chute at a value of about 8 to 15 % for skimming flow.

16.3.2 Discussion about dissipation coefficient

Since there is no way to distinguish drag from friction coefficients, a global dissipation coefficient ξ_u might be estimated based on Bernouilli equation applied between the crest and the toe of the chute. However, this assumes uniform conditions and a hydrostatic pressure distribution. With this first approach, dissipation coefficient could be estimated by:

$$H_0 - H_r = \xi_u \frac{U'^2}{2g} \tag{16.5}$$

with U' the mean velocity of the homogeneous flow in uniform region and H_0 and H_r the crest head and the residual energy at the toe of the flume respectively.

Then this dissipation coefficient could be defined as a function of head loss dimensionless parameter Π_m (Eq. 16.6), dimensionless critical depth, h_c/h_s, mean air concentration C and roughness Froude number, $F_{*,\theta}$:
$\xi_u = \phi(\Pi_m, \frac{h_c}{h_s}, C, F_{*,\theta})$.

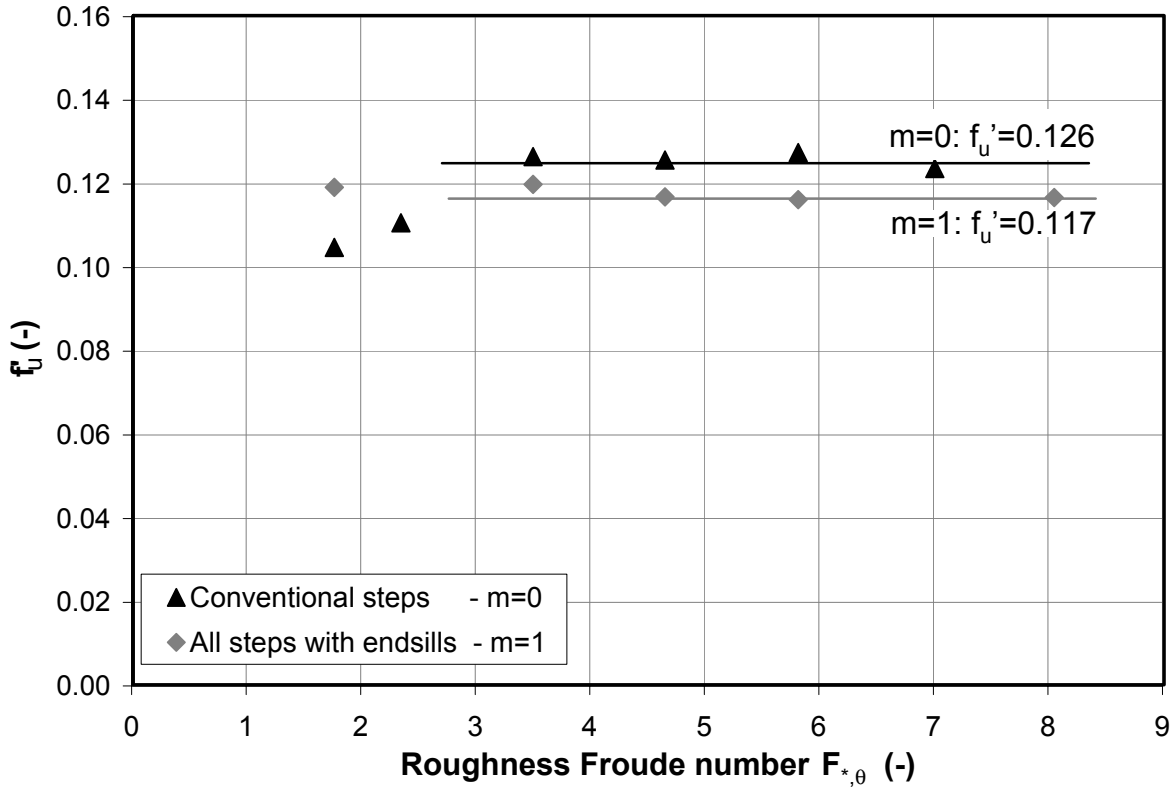

Figure 16.6: Friction factors estimated with equation 16.4 for transition and skimming effective homogeneous flows over a 30^o chute with conventional steps (m=0) or every step with endsill (m=1)

16.4 Conclusions and perspectives

Conclusions

Stepped macro-roughness overlays are a good method to dissipate flow energy along the downstream slope of an overtopped structure.

For conventional steps, with $18.6^o \leq \theta \leq 30^o$ and discharges up to $q_w = 0.28\ m^2/s$, the residual energy at the toe of a chute can be reduced by 35 % more than that for an equivalent smooth chute.

For nappe flow regime, head losses are mainly due to form effect such as hydraulic jump developed on the horizontal step face or break and deflection of the plunging nappe.

For skimming flow, energy loss is due to a mixture of friction and drag head losses resulting of the form effect caused by steps such as recirculating cells and internal transverse jets. However, the drag term caused by the internal jet transverse to the flow and the separation zone between cells and jets seems to be the most efficient in the dissipation process.

For this reason, a solution to improve energy loss is to increase the drag form effect through additional macro-roughness elements fixed on the steps.

Alternate endsills over the width of the flume or spaced rectangular blocks fixed with

an alternate pattern at the nose of the steps fulfilled this challenge. Indeed, every second step equipped with endsill (m=1/2) overlay increases the relative energy loss by 2 to 3 % . The most efficient stepped macro-roughness tested overlay is the spaced alternate rectangular blocks (m=4) characterized with $e_r/b_r = 1.5$ (where e_r is the transverse space between two blocks and b_r the block width). This configuration increases the relative energy loss for the highest tested discharge $q_w = 0.24\ m^2/s$ by 5 %.

The tests show that the relevant parameters to increase the head losses lie in:

- the longitudinal distribution parameter x_r/x_s for endsills overlays (with x_r and x_s respectively the longitudinal distance between two endsills and between two steps),
- the dimensionless transverse space e_r/b_r between blocks for blocks overlays,

The increase of the step height for conventional steps must have insignificant effect.

Based on the tested overlays, a dimensionless head loss parameter Π_m is defined by Equation 16.6:

$$\Pi_m = \frac{e_r}{b_r} + \frac{h_s}{x_s} + \frac{h_{r*}}{x_r} + \frac{1}{N*} + \frac{l_s - l_r}{l_s} \tag{16.6}$$

where h_r* is the effective additional depth caused by the macro-roughness elements ($h_{r*} = 0$ for m=0 and m=1 and $h_r* = h_r$ for the other overlays) and $N*$ the number of conventional steps following a step equipped with endsill or with block.
This parameter Π_m includes the influence of mean slope (h_s/x_s), the broken slope effect due to alternate endsills or blocks longitudinal distribution (h_r*/x_r), the internal transverse jet and separation zone influences ($1/N*$), the destruction of the separation zone on the horizontal face ($(l_s - l_r)/l_s$) and finally the contraction effect (e_r/b_r). Values for overlays are given in Table 16.2. The variation of Π_m is shown in Figure 16.4. It can be seen that Π_m follows the same trend as the relative energy loss. It represents the effective influence of the macro-roughness elements.

Overlays	Π_m
$m = 0$	1.5
$m = 1/3$	2.042
$m = 1/2$	1.875
$m = 1$	1.25
$m = 4$	3.375
$m = 5$	2.875
$m = 6$	2.541

Table 16.2: Dimensionless head loss coefficient for skimming flow on the tested overlays and for $\theta = 30^o$

These conclusions can be applied for the flatter slope ($\theta = 18.6^o$) regarding conventional steps and steps equipped with endsills.

Head losses cannot be represented only by Darcy-Weisbach friction coefficient since they are caused by both friction and drag effects. A global dissipation coefficient has to be defined,

similarly to that previously done for classical head loss coefficients for river flows.

♢ *Empirical relationships for endsills overlays*
Residual energy H_{r1} has been corrected with the safety factor $\eta_H = 1.15$ (see Chapter 15). Except for the overlay $m = 1/3$ where the values of $\Delta H/H_0$ are scattered, the variation of $\Delta H/H_0$ with the relative critical depth $\frac{h_c}{N_s h_s}$ (with N_s the number of steps along the chute) can be accurately approximated ($R^2 > 0.99$) with an exponential relationships. For transition and skimming aerated flows over the $m = 0,\ 1/2,\ 1$ overlays and $\theta = 30^o$:

$$\frac{H_r}{H_0} = \frac{\Pi_m \tan\theta}{10} \exp\left(A_m \frac{h_c}{N_s h_s}\right) \tag{16.7}$$

with:

$m = 1/2 \Rightarrow A_m = 18.45$
$m = 0 \Rightarrow \quad A_m = 25.26$
$m = 1 \Rightarrow \quad A_m = 31.03$

♢ *Empirical relationships for blocks overlays*
For blocks overlays (m=4, 5, 6), the variation of the relative energy loss $\Delta H/H_0$ versus the relative critical depth $\frac{h_c}{N_s h_s}$ follows a power law rather than an exponential one. After correction with the safety factor, for all flow discharges over a 30^o stepped chute, the residual energy at the toe of the chute is given by the following equations ($R^2 = 0.988$ to $R^2 = 0.998$):

$$\frac{H_r}{H_0} = 10 B_f \Pi_m \tan\theta \left(\frac{h_c}{N_s h_s}\right)^{b_m} \tag{16.8}$$

with B_f the flume width and:

$m = 4 \Rightarrow b_m = 1.212$
$m = 5 \Rightarrow b_m = 1.131$
$m = 6 \Rightarrow b_m = 1.094$

Perspectives

Since the efficiency of overlays is mainly the result of drag form effect, it is of interest to perform sensitive study on the dimensionless geometric parameters such as:

- h_r/x_r for endsills overlays, with an increase of the endsill height of $h_r = \frac{3}{4}h_s$,
- e_r/b_r, h_r/b_r, h_r/x_r for blocks overlays. Based on the present results, it appears relevant to investigate: $e_r/b_r = 2$ (with $h_r/h_s = 1/2$), $b_r/h_r = 1.11 < 3/2$ and $x_r/h_r = 5.3 \leq 6$ (with $h_r = \frac{3}{4}h_s$)

Finally, another way to increase the drag form could to add a reverse slope on each step (see Fig. 16.7). In fact, the slope imposed at the horizontal face may contribute to increase the zone of influence of the transverse internal jet and the perturbation of the mean skimming flow layer. In addition, it would lead to a large zone of friction under the internal jet on the horizontal face. Then both friction and singular (or drag) head losses would be increased. However, it could lead to a significant swelling of the flow depth, which has to be tested.

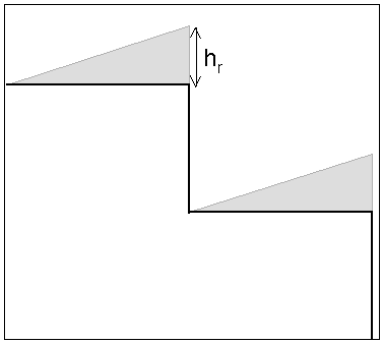

Figure 16.7: Sketch of a reverse inclined step overlay

Note that the addition of a reverse slope has been tested for gabions overlay [Peyras et al. (1991)]. This has lead to an enhance of the gabions stability and to an increase of the energy dissipation.

The conclusions on the 30^o slope have to be verified for the 18.6^o slope.

Part V

Numerical modeling of high velocity aerated flow over macro-roughness : a first approach

Chapter 17

Generalities

17.1 The challenge of numerical modeling of aerated flow over macro-roughness

Because of the high turbulence, the self aeration process, and the irregular wavy and rough free surface, most of the studies of the hydraulic behaviour of flow over stepped chutes are made on physical models. By measuring the principal flow parameters such as air concentration, velocity, depths, pressures, a panel of empirical hydraulic design relationships, generally closely related and limited to their tested domain can be assessed. Providing a more general description of the flow behaviour requires a mathematical definition of its hydrodynamic and self-aeration process. However, very few models exist and have been validated.

Recent courses on Modeling and Computation of Multiphase Flows (Zurich, 2000), clearly demonstrate that for two-phase flows, commercial 2D or 3D codes like CFX, Fluent or Flow3D have been applied to liquide-gas flows in conduits with well defined gas structures such as bubble, slug or annular flows. For the case of free surface flows, the mayor difficulties come in defining the flow surface and in modeling the two-phase exchanges at the instable interface, between the mixture wavy air-water flow and the atmospheric air crossed by water droplets. The picture in Figure 17.1 illustrates the random ejections of droplets and the presence of air gaps between two waves.
In addition, these codes require the knowledge of the 2D or 3D boundary conditions and there is still an incomplete understanding of the physics of flow very near the roughness. The current instrumentation does not allow a precise definition of the turbulence intensity in the boundary layer nor of the 3D velocity components of the flow in this region.

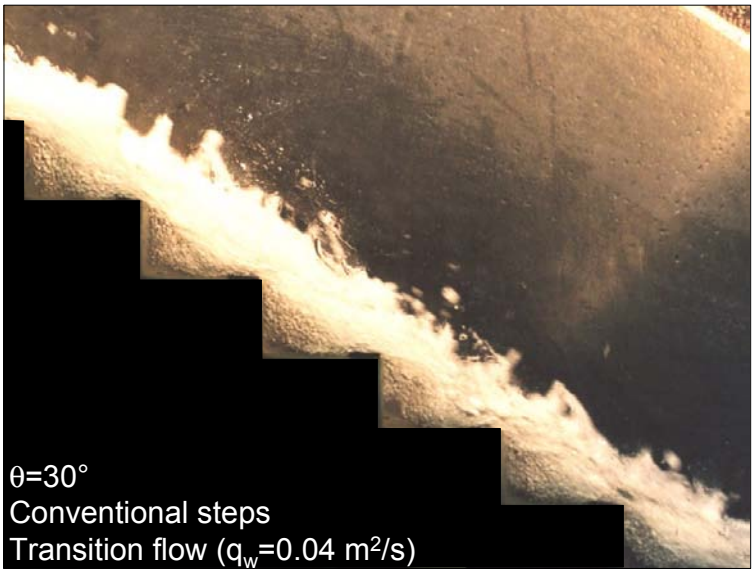

Figure 17.1: Side view of the wavy and rough aerated free surface for the transition flow regime over the 30^o stepped inclined chute

Appropriate 2D (2DV) and 3D models have recently been presented by a few authors, in particular Benmamar, Kettab & Thirriot (2003) who have attempted to model the two-dimensional turbulent boundary layer flow in a stepped channel. However, this 2DV model,

based on an implicit finite difference scheme, does not include air entrainment and it is strictly limited to the region upstream the inception point. Thus, this program can be of interest for designers to define the region of cavitation risk, but no more. In addition, this model purports to state the details of the momentum governing equation, *i.e* to define the turbulent and viscous terms in the longitudinal and vertical axis. However, due to the complexity of the flow, it imposes a set of unrealistic assumptions such as hydrostatic pressure distribution, laminar shear stress, free surface profile similar to a gradually varied flow in a uniform channel. An impressive turbulent 3D simulation of stepped spillway based on the volume of fluid (VOF) method had been proposed by Chen et al. (2002). The turbulence of the flow was implemented by the $k-\epsilon$ turbulence equations with a modified resulting pressure term for modeling the non-hydrostatic pressure distribution. The aeration is taken into account in the mixture density parameter as well as in the mixture molecular viscosity, with a tracking of the free surface based on a time-dependent simulation. Momentum, turbulence and continuity equations are solved for a single-phase mixture fluid. The comparison of the water surface and the velocity vector in the vertical plane and pressure measurements over the step faces for a steep slope (1V:0.75H) provided encouraging results. However, they still have to be validated with air entrainment consideration. In addition, clarification of the assumptions is lacking in their papers that are necessary to define the limits of this model.

Finally, 2DV and 3D models are still widely restrictive and expensive in terms of CPU. For instance, existing methods like VOF [Hirt & Nichols (1981), Zaleski (2000)] or Marker-and-Cell (MAC) [Tome, McKee & Gensmack (1994)] especially require CPU resources. In the other hand, a few numerical models of aerated flow over stepped chute are currently available, but they still have to be validated for aerated flow and for a variety of slopes.

These existing models, nevertheless, pointed out that the principal difficulties which still need to be modeled realistically lie in:

- the undefined rough free surface (development of an effective and accurate tracking of the free surface location),
- the non-uniform density and velocity profiles with a reliable turbulence model to represent the 3D turbulent structure (implantation of an appropriate boundary condition and a sufficient adapted mesh refinement),
- the non-hydrostatic pressure distribution (definition of an additional term),
- the self-aeration and air concentration development along the chute.

17.2 Approach and goals of the numerical study

To provide a more general and accurate description of the flow behaviour, one of the objectives of the research is to propose a simple and realistic "mathematical" description of the aerated flow over macro-roughness.

In order to have a control of the response of the implemented equations, the first approach consists in modeling the flume of LCH-EPFL, with identical entrance conditions at the jetbox and for the simplest macro-roughness system which is the conventional steps. The numerical phase defines, analyzes and compares the flow behaviour with some validation provided by

the experimental results of the tests conducted on both the 30^o and the 18.6^o gated stepped flume. The model provides the base for further generalization of the governing equations with aerated flows over macro-roughness.

For this purpose, a synergy between the experimental study conducted in the steep stepped flume and the numerical background in modeling shallow-water two-phase (water and sediment) flows over steep slopes of the Laboratory of Applied Hydrodynamic and Hydraulic Constructions (HACH) of the University of Liège, Belgium (ULg) was undertaken.

In order to avoid the difficulties encountering with a 2D or 3D vertical model as mentioned above, a **quasi-2D model** of aerated flow over conventional stepped chutes was developed by HACH-ULg on the basis of an existing finite volume 2D numerical model for free surface non-aerated flow. The base of the proposed numerical approach consists in a depth-averaging of the classical Navier-Stokes equations but with their extension to take into account the bottom topography and the principal flow characteristics such as:

- the self-aeration process with an air-transport equation,
- the uneven vertical velocity distribution due to turbulence with a correction factor,
- the drag form effect of the macro-roughness with an adapted friction coefficient.

Because these additional terms are calibrated and/or derived from the experimental results, the resulting model is then a "hybrid" simulation (analytical and empirical) of aerated flow over stepped chute. As it is shown below, this depth-average model is an attractive compromise between realism and cost-time efficiency.

If this approach does not develop to a "turnkey" code, nevertheless it provides the basis of general model of the flow behaviour of aerated flow over conventional steps that is not restricted in the experimental tested conditions and one that can be used with confidence for prototypes application.
It could also be an useful preliminary design tool for designers to define optimal protection systems for overtopped embankment dams.

Chapter 18

Numerical model description

The experimental study, Part IV, highlighted the two-dimensional structure of the flow in the vertical plane. However, this fact does not preclude assessing the relevant characteristics of the flow with a depth-averaged technique. In fact, as shown below, a simple quasi-2D model can provide accurate results economically.

The following numerical development is included in the software package **WOLF**, which has been developed at HACH-ULg. WOLF includes a complete set of numerical tools designed for simulating free surface flows with a wide range of applications, notably:

- for one phase hydrodynamic flow with:
  - simulation of hydrological runoff, catchments determination for hydrology application (WOLFHYDRO) [Archambeau, Erpicum, Mouzelard & Pirotton (2001)],
  - 1D modeling of river networks for routing of floods (WOLF 1D) [Erpicum, Archambeau, Dewals, Mouzelard & Pirotton (2003)].
- for hydrodynamic coupled with air or sediment transport (WOLF2D) [Dewals, Archambeau, Erpicum, Mouzelard & Pirotton (2002)], with quasi-3D simulations for dam breaks, inundation maps and river morphology applications [Archambeau, Dewals, Detrembleur, Erpicum & Pirotton (2003)].

The following modeling of the aerated flow is based on the WOLF2D module.

18.1 Basic principles of the quasi-2D model

The code, WOLF2D, concerns the numerical resolution of the Navier-Stokes two-dimensional equations integrated over the flow depth. The aim of this study is to establish the governing equations of the aerated flow over macro-roughness and not to examine the numerical development of the code. The details of the numerical method can be found in Pirotton (1997) and Mouzelard, Archambeau & Pirotton (2000). However, briefly, it has to be known the principal characteristics of this model are described.

The spatial scheme is based on the finite volume method. The equations are then integrated through a set of cells covering the whole modeled domain. This conserves the transported mass and momentum values through very small volumes. As a consequence the method also simulates the sharp changes of flow regimes and instabilities such as hydraulic jumps.

The time iteration is based on an explicit scheme which permits the differential equations to be solved with the 3-step Runge-Kutta algorithm. The efficiency of such a method had been proven and it is well known because of its low computation cost.

In parallel to the solution of the equations, a permanent analysis of the numerical stability optimizes the calculation time step to ensure the convergence of the results.

18.1.1 Hydrodynamic model

♢ *Spatial scheme*

A sketch of the modeled flume along with the axis notations is given in Figure 18.1. The depth integration is carried out along the z axis.

The finite volume scheme is applied for the space discretization in order to assure exact mass and momentum conservation and to simulate possible hydraulic jumps in the nappe flow regime.
The meshing along the modeled flume axis is comprised of volumes that are 1 cm long (in the x axis) and $h_m + z_b$ high, h_m being the calculated depth of the mixture flow and z_b the height of the topography.

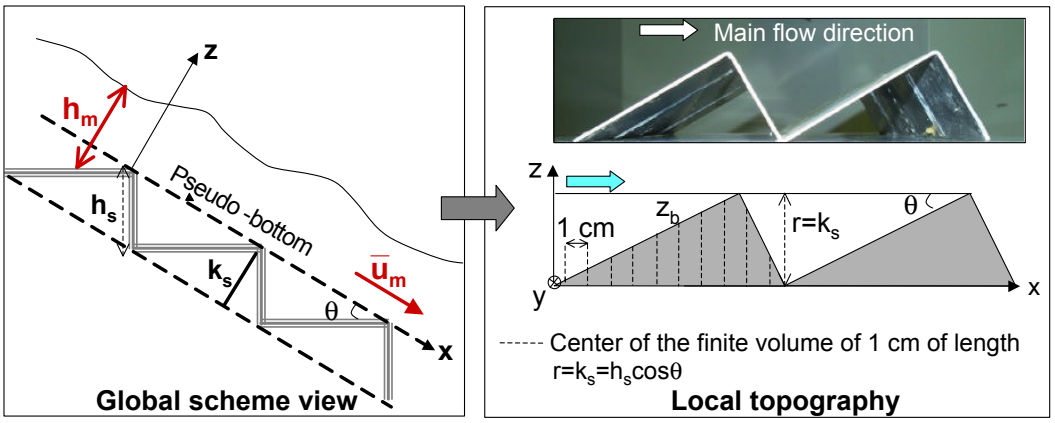

Figure 18.1: Sketch of the stepped flume and zoom on the local topography modeled in WOLF2D, with unknowns and axis notations

♢ *Two-phase flow consideration*
The model is based on the description of the air-water mixture flow as a single incompressible fluid of mean density given by Equation 9.1 (see Chapter 9.1, Part III):
$\rho_m(x,t) = \rho_w(1-\overline{C}) + \rho_a\overline{C} \simeq \rho_w(1-\overline{C})$
with ρ_w and ρ_a respectively the density of water and of air, $\overline{C}$ the local mean air concentration. Therefore, the model has the particularity that only a single set of equations in which air-water fluid mixture with the mixture height, h_m is transported with a mean longitudinal velocity $\overline{u_m}$.

♢ *General assumptions*
In this first stage, the following assumptions are considered to solve the set of equations:

- Uniform distribution of the flow over the flume width
  $\Rightarrow \frac{\partial}{\partial y} = 0$
- Viscosity negligible compared with the convection terms,
- Coriolis effect negligible,
- Small normal velocity component (w_m) compared to the longitudinal one (u_m), no transverse velocity (v_w). Then, w_m^2 can be neglected compared to u_m^2.

♢ *Governing equations*
Under these assumptions, the governing equations are simplified and given in the following.

◇ Depth-averaged continuity equation (mass balance)

$$\frac{\partial}{\partial t}(\rho_m h_m) + \frac{\partial}{\partial x}(\rho_m h_m \overline{u_m}) = 0 \tag{18.1}$$

◇ Depth-averaged momentum equation

Assuming that the significant velocity is the longitudinal one and is parallel to the main flow direction simplifies the corresponding momentum equation. As a consequence the pressure field p is found to be almost hydrostatic everywhere. A depth-averaging operation applied to the second local momentum equation results in the momentum balance given by Eq. 18.2:

$$\frac{\partial}{\partial t}(\rho_m h_m \overline{u_m}) + \frac{\partial}{\partial x}(\rho_m h_m \rho_{xx} \overline{u_m}^2) + \frac{\partial}{\partial x}(\frac{g}{2}\rho_m h_m^2 \cos\theta)$$

$$+\rho_m g h_m \cos\theta \frac{\partial z_b}{\partial x} = \rho_m g h_m \sin\theta + \tau_{bx} \tag{18.2}$$

with g, the gravity acceleration, θ, the mean slope of the pseudo-bottom, z_b, the local bed elevation, τ_{bx}, the losses term and ρ_{xx}, the Boussinesq coefficient which represents the uneven velocity profile in the water depth. The diffusive contributions, which are not explicitly included, can be combined with the losses term.

◇ Air transport

In addition to the basic hydrodynamic equations, the mean air concentration must be simultaneously defined at any location along the slope and at any time. Then, an equation for the aeration process has to be solved. On the basis of the laboratory observations and due to the high velocity of the flow, it is suggested that the aeration process along the chute can be represented principally by a transport equation:

$$\frac{\partial \overline{C}}{\partial t} + \overline{u_m}\frac{\partial \overline{C}}{\partial x} = S_a \tag{18.3}$$

with S_a , the air source term which has to be defined to represent realistically the process of air entrainment and detrainment described in Part III, Chapter 8.2.1 and to be fitted with the experimental data.

This set of equations forms the mathematical system to be solved for the **three primitive unknowns h_m, $\overline{u_m}$ and $\overline{C}$** that characterize the aerated flow.

◇ *Initial and boundary conditions*

As already mentioned, the validation in this first stage uses the model data from the stepped flume of LCH-EPFL. Therefore, the initial conditions corresponds to the jetbox data: initial specific water discharge q_w and opening of the jetbox h_0 for the initial flow depth. The initial air concentration is of course set at 0.

The principle of depth-averaging itself does not impose a bottom velocity condition.

The characteristic velocities analysis determines the number of upstream and downstream boundary conditions [André, Dewals, Pirotton & Schleiss (2003)]. These are as follows:

- At the upstream boundary of the scheme, the flow is first considered without approaching velocity ($u_{m,0} = 0$) with only the specification of the discharge to impose q_w.

- At the downstream boundary of the domain, the flow is supercritical. Then there are no imposed boundary conditions.

18.1.2 Numerical implementation

The numerical implementation conducted by the HACH-ULg and has no impact on the physics of modeling of the flow behaviour. All details concerning this part as to be find in André et al. (2003) and Dewals, André, Schleiss & Pirotton (2004). They are not developed herein.

18.2 Modeling of the flow characteristics: 1D-approach

The aim of this simulation is to assess the relevant characteristics defined experimentally by the two-dimensional flow structure in any cross section and to include them through the depth-averaging of the advective and pressure terms of the momentum equation (Eq. 18.2). At this stage, as already mentioned, the vertical component of the velocity is considered negligible compared to the longitudinal one.

18.2.1 Self-aeration

The source term S_a of Eq. 18.3, has:

- to take into account air entrainment and detrainment as a function of the flow conditions,
- to satisfy the observed conditions along the slope, *i.e* $\overline{C} = 0$ upstream of the inception point and downstream, $\overline{C}$ is increasing along the chute up to $\overline{C} = C_u$ in the uniform region.

The onset of air entrainment is implemented in the source term (see the following Equation 18.4) with a variable $m_I = 0$ upstream of the inception point and $m_I = 1$ downstream of it. The position of this inception point is given according to the experimental results in the 18.6^o and 30^o flumes (see Part IV, paragraph 14.1.1).

The air concentration at saturation, C_u is given as a function of the chute slope, of the roughness Froude number $F_r* = q_w/\sqrt{g \sin\theta k_s^3}$ according to the experimental relationship given in paragraph 14.1.2, Part IV with $k_s = h_s \cos\theta$.

On this basis, the air source term is globally expressed by Equation 18.4:

$$S_a = -\Gamma m_I \sqrt[\beta]{\left(\frac{\partial \overline{u_m}}{\partial x}\right)^2}(\overline{C} - C_u) - u_r \overline{C}\sqrt{1-\overline{C}} \tag{18.4}$$

with Γ and β, calibrated constants of the advective term, u_r, the air bubble rise velocity of the diffusive term. The size of the bubbles for conventional steps bottom is of same order of magnitude as that of smooth chute, $u_r \simeq 0.4\,m/s$, according to Wood (1991). The diffusive term $u_r\overline{C}\sqrt{1-\overline{C}}$ had been derived from the depth-averaged diffusivity model of air bubbles for open channel, developed in Chanson (1997).

18.2.2 Flow structure

The preliminary numerical calculations, when considering only the use of the transport Equation 18.3 but not the ρ_{xx} coefficient in the momentum equation, resulted in a non realistic shape of the mixture flow free surface (result illustrated below in Figure 19.1). In fact, the undulation of the free surface is the result of the turbulent structure of the flow due to the steps. Assuming a uniform velocity profile over the water depth is clearly too simplistic for stepped spillway application. For this reason, as already mentioned, a correction coefficient of the velocity, ρ_{xx}, is implemented in the momentum Equation 18.2 to take into account the non uniformity of the vertical velocity profile. This models indirectly the macro-turbulent structures.

By definition, the Boussinesq coefficient is given by:

$$\rho_{xx} = \frac{A}{q^2} \int \int_A \overline{u_m}^2 dA \tag{18.5}$$

For transition and skimming flows, the two main structures to be modeled are:

- the vortices developed inside the step, under the pseudo-bottom. These vortices appear for all discharges over the whole vertical step face and over the upstream 2/3 of the horizontal face for the 30^o and 18.6^o slopes.
- the internal jet at the step edge.

For the particular case of the nappe flow, except at the step edge, ρ_{xx} has no sense inside the step where either a pool of water and an air cavity develops. If a hydraulic jump develops, it is directly modeled with the equations.

Finally, for transition and skimming flows, the following assumptions had been made:

- Inside the step, for $z < r$ (see Fig. 18.2), the recirculating cells are assumed to be characterized with a triangular velocity distribution.
- At the pseudo-bottom, the interface velocity u_b is given according to the experimental results.
- Above the pseudo-bottom, for $z > r$, the velocity of the skimming layer is assumed to be non-uniform, characterized by ρ_{edge}. The uneven distribution coefficient is based on the velocity profile measurements at the step edge.

On this basis, the longitudinal variation of ρ_{xx} is given by Equation 18.6:

$$\rho_{xx} = \frac{1}{3} \frac{h_m \, r}{(h_m - r)^2} \left(\frac{u_b}{\overline{u_m}}\right)^2 + \frac{h_m}{h_m - r} \rho_{edge} \tag{18.6}$$

18.2.3 Friction

The macro-roughness elements (in this case, the steps) have a significant contribution on the head losses along the slope. The step topography is directly implemented in the governing equations and the flow structures are indirectly modeled through the coefficient ρ_{xx} in the

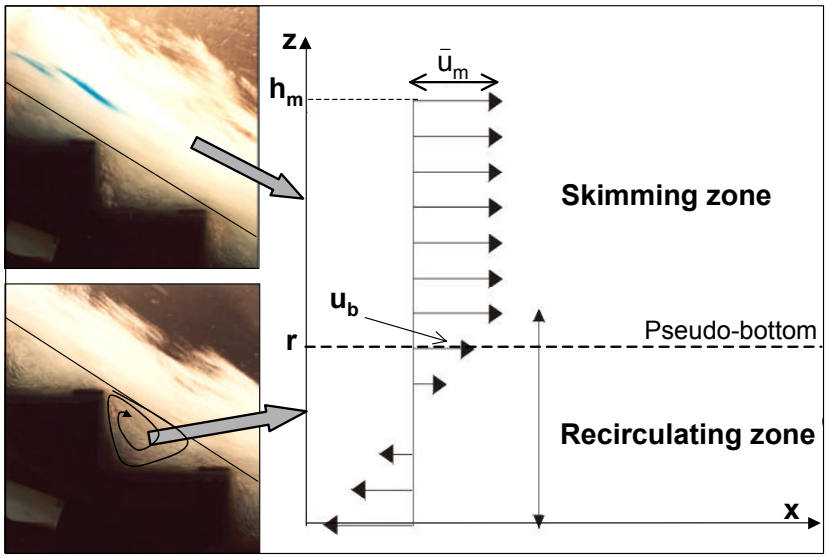

Figure 18.2: Sketch of the velocity profile assumed to represent the recirculating cells inside the steps in the numerical simulations

momentum balance. Therefore, it seems reasonable to suggest that the friction losses term along the chute may be represented by the shear stress effect on the step faces. In this first approximation, the resulting external friction term had been modeled by the Manning relation (Equation 18.7) with n, the Manning coefficient, fitted in order to obtain a velocity and flow depth comparable to the experimental results.

$$\tau_{bx} = g n^2 h_m (1 - \overline{C}) \overline{u_m} \frac{\sqrt{\rho_{xx} \overline{u_m}^2}}{R_h^{4/3}} \tag{18.7}$$

with R_h the hydraulic radius. With no wall effect, $R_h = h_m$, which is the case in the modeling of the flow in the axis of the LCH-flume. In order to handle properly wall friction in a narrower flume, this expression can be replaced by $R_h = b h_m/(b + 2h_m)$, with b the spillway width [Collard (2003)].

A good modeling of the dissipation process would be achieved when the numerical results reflect the experimental observations with a Manning coefficient in the uniform region as close as possible to the classical values. The coefficient corresponds to $n = [0.013 - 0.016]$ $s/m^{1/3}$ for studied cases.

18.2.4 Pressure

The assumptions which neglect the normal component of the velocity and of hydrostatic pressure distribution are not realistic. They simplify this first stage of developing.

Chapter 19

Results and validation of the 1D-approach

One of the more relevant validation of the governing equations of the aerated flow over stepped chutes lies in the ability to simulate the uniform depth as given by the experimental results. This would then show that the resulting energy dissipation due to the steps is realistically modeled by the semi-empirical governing equations.

19.1 30^o mild stepped flume

To verify the proposed general theoretical model of aerated flows over macro-roughness, the numerical simulations from HACH-ULg are applied to the 30^o stepped chute assembled at LCH, in the transition and skimming flow regimes.
In the following, the comparison between the model results and the experimental data is based on:

- the free surface form: waves amplitude and phase of the surface of the flow,
- the air concentration development along the chute,
- the longitudinal mean velocity in the uniform region,
- the normal mixture depth in the uniform region.

19.1.1 Air entrainment

A sensitivity study of the source term S_a, by varying the coefficients Γ and β in the advective term and by considering the diffusive term of Eq. 18.4, has been lead to obtain a realistic air concentration development.

Figure 19.1a presents a comparison between the computed free surface for $\rho_{xx} = 1$ (no turbulence effect), with and without the air transport equation, with the measured free surface for skimming flow ($q_w = 0.12\, m^2/s$) in the uniform region. It can been seen that if the air transport equation permits the swelling of the mixture flow depth, it is not enough to cushion the topography effect on the free surface which exactly follows the form of the steps.

Regarding all the tested cases, the optimal representation of the self-aeration process is given by the term source of Equation 19.1

$$S_a = -\Gamma m_I (\overline{C} - C_u) \tag{19.1}$$

In fact, the consideration of the diffusive term $U_r \overline{C} \sqrt{1 - \overline{C}}$ as well as the factor $\sqrt[\beta]{\left(\frac{\partial \overline{u}_m}{\partial x}\right)^2}$ (see example for $\beta = 1$ in Fig. 19.1b) showed incoherent variations of $\overline{C}$ (and hence of h_m) along the slope without reaching the uniform air concentration.

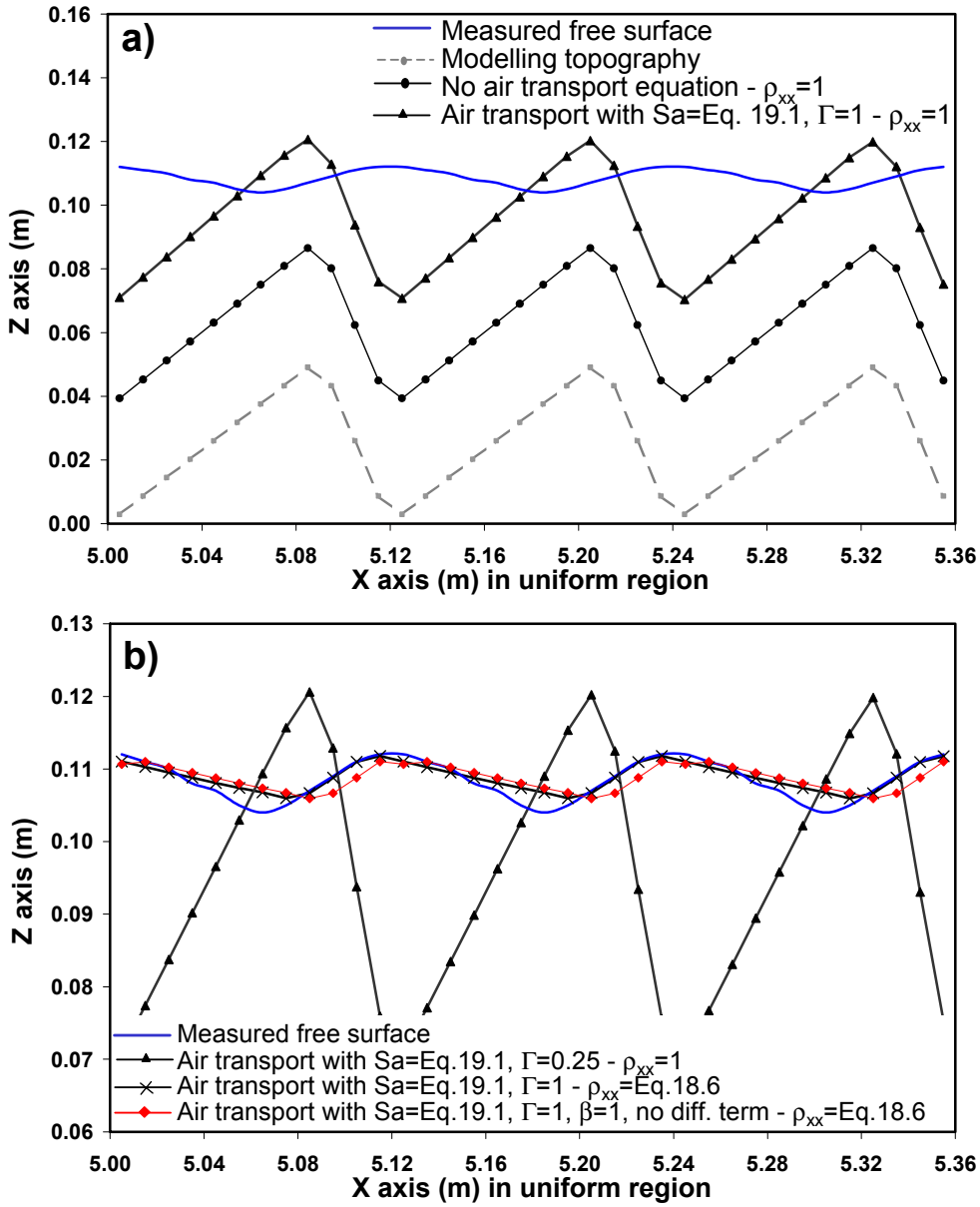

Figure 19.1: Air entrainment transport equation effect on the mixture flow depth in the uniform region, for $q_w = 0.12\, m^2/s$: (a) Comparison with or without the air transport equation; (b) Comparison with or without the $\sqrt[\beta]{\left(\frac{\partial \overline{u_m}}{\partial x}\right)^2}$ term in the air transport equation

Finally, as shown in Figure 19.2 for $q_w = 0.12\ m^2/s$, with $\Gamma = 0.25$, the longitudinal development of the air concentration realistically represents the longitudinal variation of $\overline{C}$, fitting with the measurements and also with the experimental relation proposed by Boes (2000a) (Eq. 9.7, Part III, Chapter 9.1.2) for a 30^o inclined stepped chute.

$$\overline{C}(X_i) = C_u \left[1 - \exp\left[-0.05(X_i + 25)\right]\right]$$

where $X_i = (x - L_i)/Z_{m,i}$ and L_i, $Z_{m,i}$, respectively the longitudinal position and mixture

depth at the inception point.

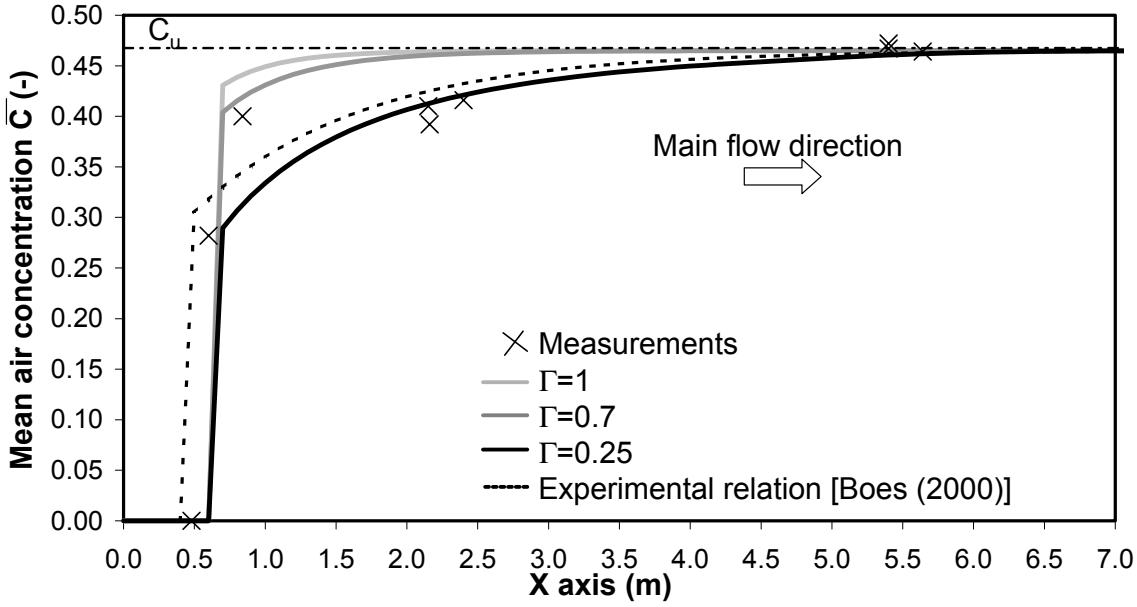

Figure 19.2: Air entrainment transport equation effect on the computed longitudinal variation of $\overline{C}$ with S_a according to equation 19.1, for $q_w = 0.12\,m^2/s$. Comparison with measured data and Eq. 9.7 [Boes (2000)]

19.1.2 Velocity distribution

Without any correction of the uniform velocity profile assumed in the momentum equation, the longitudinal variation of the flow depth is incorrect.
Sensitivity analysis of ρ_{xx} effects in the momentum balance has then been carried out,

- first only considering the contribution of the internal jet effect:
  $\rho_{xx} = \rho_{edge}$ with ρ_{edge} computed according to Eq. 18.5, applied to the measured velocity profiles in the uniform region,
- second with the only contribution of the recirculating cells inside the step:
  $\rho_{xx} = \frac{h_m}{(h_m - r)^2}(h_m - \frac{2}{3}r)$
- and finally with the global ρ_{xx} according to Eq. 18.6.

An example of the results on the mixture flow depth for the skimming flow regime ($q_w = 0.12\,m^2/s$) is given in Figure 19.3. It can be seen that the edge contribution (curves with diamond dots), representing the internal jet impact, has an effect on the widening of the flow depth (amplitude of the waves crest) while the recirculating cells (round dots curve) have an effect on the contraction of the flow depth (slope of the waves). This is in good agreement with the observed tendency. As a result, the tests have clearly shown that the semi-empirical expression of the Boussinesq coefficient ρ_{xx}:

- contributes to the swelling of the flow depth.

- acts on the waves amplitudes of the free surface, which is similar to the observations. For increasing discharge, the waves amplitudes decrease significantly since the turbulent structures effect on the free surface are cushioned by the large skimming layer.
- influences the longitudinal variation of the mean mixture velocity $\overline{u_m}$.
- has no influence on the variation of the wave lengths with the discharge. In fact, the observations have shown that the maximum waves are shifted downstream with an increasing discharge.

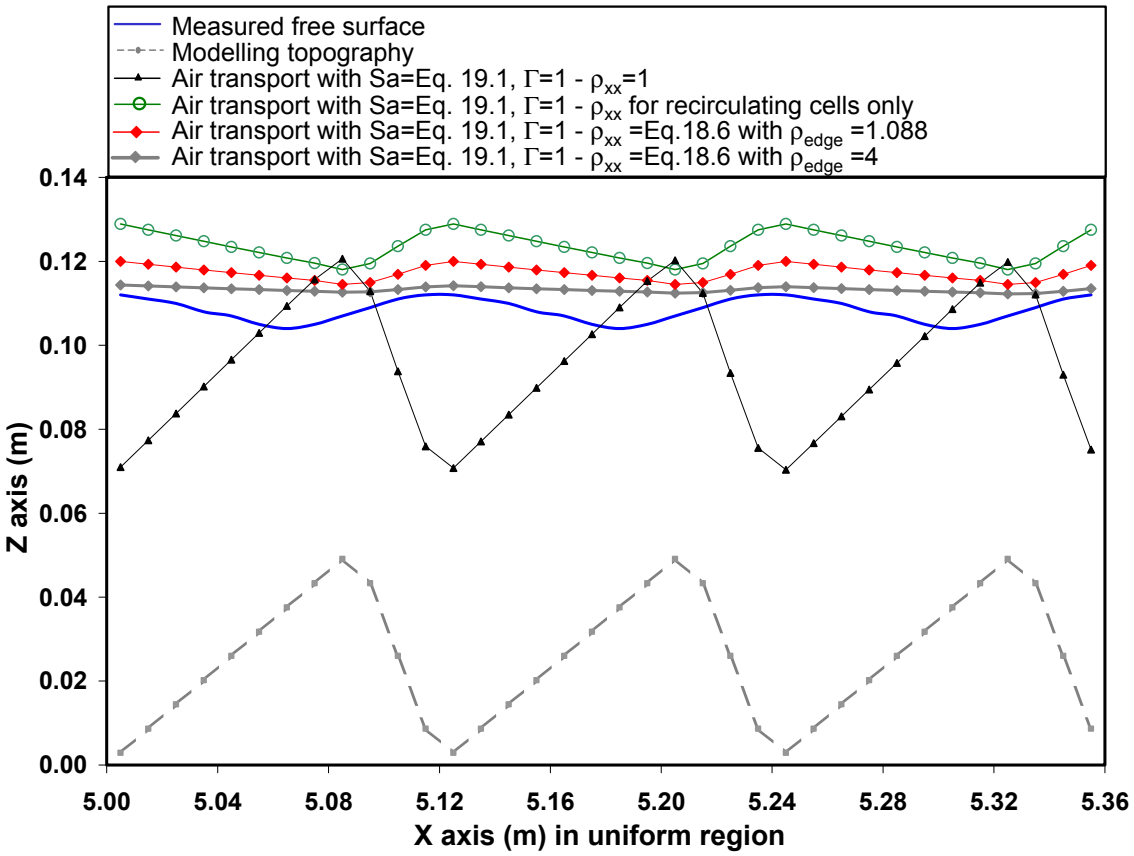

Figure 19.3: Effect of ρ_{xx} on the flow depth in the uniform region, for $q_w = 0.12\,m^2/s$, for a Manning coefficient $n = 0.03\,s/m^{1/3}$ (without the coefficient ρ_{xx})

19.1.3 Friction term

For identical air entrainment terms and Boussinesq coefficient, the sensitive tests on τ_{bx} show that without considering ρ_{xx} in the loss term, the calculated mean flow velocity is about 25 % higher than the measured one. Figure 19.4 shows the sensitivity of the friction and the ρ_{xx} terms on the solution. The results are in good agreement with the physics of the flow. The consideration of ρ_{xx} in the friction term is indirectly equivalent to the increase of the global friction factor due to the additional shear stress on the step faces involved by the recirculating

cells.

Finally, inclusion of ρ_{xx} in τ_{bx} according to Equation 18.7 results in a good fit of the flow characteristics for a Manning coefficient of $n = 0.024\ s/m^{1/3}$. This value is significantly reduced from the initial result of $n = 0.03\ s/m^{1/3}$ but it is still over-estimated. This means that the model still needs to be improved in order to represent more accurately the flow behaviour.

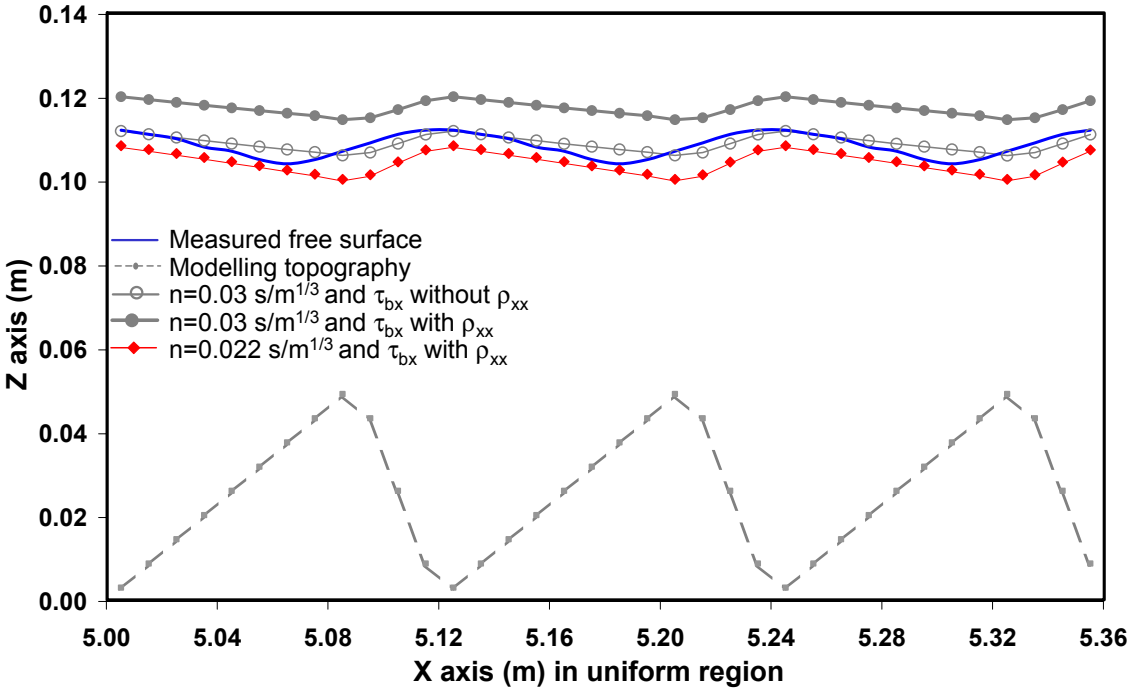

Figure 19.4: Effect of loss term on the flow depth in the uniform region, for $q_w = 0.12\,m^2/s$, for S_a according to Eq. 19.1 with $\Gamma = 1$ and for ρ_{xx} according to Eq. 18.6

19.1.4 Conclusions

The present model for describing the hydraulic behaviour of aerated flows over a 30^o stepped gated flume is based on the depth-averaged balance of mass and momentum for an air-water mixture flow and on a transport equation for the air concentration. The velocity is assumed to be 1D-component. The simulation has provided promising results, as shown in Figure 19.5 for $q_w = 0.12\ m^2/s$ and $q_w = 0.16\ m^2/s$ in the uniform region.

The validation compares the experimental data of the mean mixture velocity, mixture depth and air concentration in the uniform region, as well as the longitudinal variation of the mean air concentration and the free surface flow shape, for the transition and skimming flows over the 30^o gated stepped flume.

Since the simulated flow depth and velocity remain of same order of magnitude as the measurements, the computed residual energy at the toe of the modeled flume is thus validated.

In spite of these promising results, modeling of the 2D turbulent structures in the vertical plane still could be improved. In fact, the Boussinesq coefficient as defined herein overestimates the Manning coefficient. In addition, waves on the free surface are somewhat out of phase compared to observations.

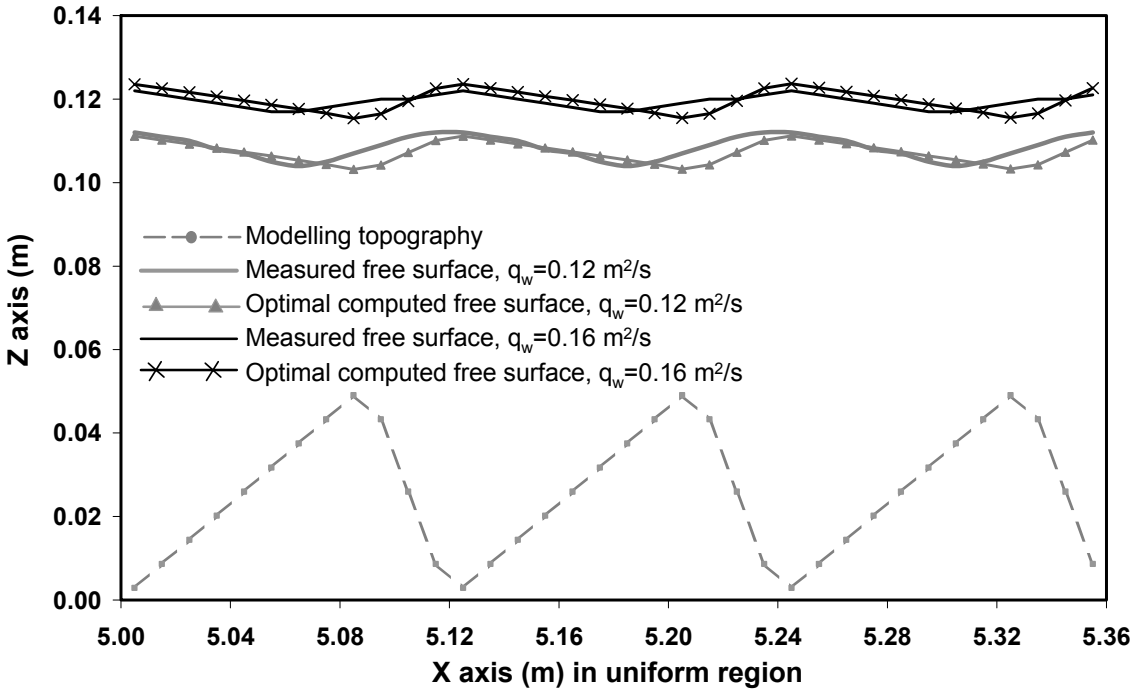

Figure 19.5: Computed normal mixture depth in the uniform region, for $q_w = 0.12\ m^2/s$ and $q_w = 0.16\ m^2/s$ with ρ_{xx} given by Eq. 18.6 and $n = 0.024\ s/m^{1/3}$ (without wall effect)

19.2 52^o steep stepped spillway model

♢ *Modeling*

The quasi-2D model was applied to simulate a laboratory model at HACH-Ulg of a 52^o crested stepped spillway. The description of the $2.034\ m$ high and $0.494\ m$ wide flume equipped with $0.03\ m$ high rectangular steps is given in Collard (2003). In addition to the slope, the major difference of this model compared to the 30^o flume of LCH-EPFL lies in the entrance configuration which is an ogee crest.

The hydrodynamic model and the numerical simulation were exactly the same as described above. However, in this case, the flume was modeled over its whole length and a hydraulic radius equal to $R_h = bh_m/(b + 2h_m)$ was used to account for the wall effect on the flow resistance. More details can be found in Dewals et al. (2004).

The air source term S_a was included according to Eq. 19.1 with $\Gamma = 0.25$. As in the previous 30^o slope simulation, position of the inception point and the uniform air concentration were imposed according to experimental results.

♢ *Results*

For the tested discharges for transition and skimming flow regimes (q_w varying from $0.0449\ m^2/s$ to $0.0607\ m^2/s$), the most realistic results were obtained for a Manning coefficient $n = 0.025\ s/m^{1/3}$.

In the uniform region, results on the air concentration and mixture flow depth were satisfactorily identical to experimental data.

The longitudinal variation of the flow depth gave accurate result with a good decreasing and increasing tendency in the non aerated or aerated regions respectively. However, locally, just further downstream the spillway crest, the computed depths were slightly underestimated. This may be the effect of the initial specification of the discharge with the infiltration method and of the bottom curvature in the vertical plane. Nevertheless, this discrepancy has no influence on the region downstream of the inception point and on the uniform depth which were in good agreement with experimental value.

Results on the longitudinal variation of the computed air concentration are very encouraging as in the previous modeling of the gated flume. In this case, the computed values of the air concentration were compared with the empirical relationship (Eq. 9.5 and Eq. 9.6, Part III, Chapter 9.1.2) proposed by Matos (2000b) for a 53^o crested stepped spillway. The computed values were in good agreement with both Matos formula and experimental data. More details are given in Dewals et al. (2004).

♢ *Conclusions*

Despite increasing the slope angle, of the change of the steps height, of the entrance condition as well as of the modeling of the whole spillway, simulating the flow with the quasi-2D model as defined in the above Chapter 18 remains applicable. Based on the flow depth and the air concentration variation along the slope and in the uniform region, the computed results are in the same order of magnitude as the experimental data. However, the Manning coefficient is too large. The modeling of the head loss process has to be improved.

Chapter 20

Conclusions and Perspectives

20.1 Conclusions

The presented numerical quasi-2D model for the description of the hydraulic behaviour of aerated flow over stepped mild and steep slopes is based on the depth-averaged mass and momentum balance equation for a single air-water mixture fluid and on a transport equation for the air concentration.

For transition and skimming flow regimes, the flow characteristics such as the cells of recirculation below the pseudo-bottom and the internal jet at the step outer edge are considered by the Boussinesq coefficient which represents the uneven vertical distribution of the longitudinal component of the flow velocity. It models indirectly these macro-turbulent structures effect on the dissipation process.

For nappe flow regime, the method of finite volume itself models the hydraulic jump which can be partially or totally developed depending on the chute slope and on the discharge.

The results from studies on a 30^o gated stepped flume and a 52^o laboratory model of a crested spillway lead to the following set of semi-empirical equations that realistically predict flow characteristics (mixture depth, mean velocity and air concentration). Therefore the residual energy at the base of the modeled structures has been validated for this case of conventional steps system.

1. Mass balance
$$\frac{\partial}{\partial t}(\rho_m h_m) + \frac{\partial}{\partial x}(\rho_m h_m \overline{u_m}) = 0$$

2. Momentum balance
$$\frac{\partial}{\partial t}(\rho_m h_m \overline{u_m}) + \frac{\partial}{\partial x}(\rho_m h_m \rho_{xx} \overline{u_m}^2) + \frac{\partial}{\partial x}(\frac{g}{2}\rho_m h_m^2 \cos\theta) + \rho_m g h_m \cos\theta \frac{\partial z_b}{\partial x} = \rho_m g h_m \sin\theta + \tau_{bx}$$

3. Losses term
$$\tau_{bx} = g n^2 h_m (1 - \overline{C}) \overline{u_m} \frac{\sqrt{\rho_{xx} \overline{u_m}^2}}{R_h^{4/3}}$$

4. Air concentration transport
$$\frac{\partial \overline{C}}{\partial t} + \overline{u_m} \frac{\partial \overline{C}}{\partial x} = 0.25 m_I (\overline{C} - C_u)$$

with:

Air concentration at saturation:

$C_u = 0.560 F_{*,\theta}^{-0.105}$ for $\frac{h_m}{k_s} \leq 1$,
$C_u = 0.75 \sin\theta^{0.75}$ for $\frac{h_m}{k_s} > 1$
with $F_{*,\theta} = q_w / \sqrt{g \cos\theta k_s^3}$

Onset of air entrainment:

$m_I = 0$ if $x < x_i$ with $x_i = k_s \left(\frac{8.0}{\tan\theta} k_s F_{*,\theta}^{0.730} \right)$
$m_I = 1$ if $x \geq x_i$

Correction of uneven velocity profile:

$$\rho_{xx} = \frac{1}{3} \frac{h_m r}{(h_m - r)^2} \left(\frac{u_b}{\overline{u_m}}\right)^2 + \frac{h_m}{h_m - r} \rho_{edge}$$

where ρ_{edge} and $\frac{u_b}{\overline{u_m}}$ are determined experimentally.

Despite of these promising results, the required Manning coefficient of the external friction factor over the step faces (in Eq. 18.7) is too large. Therefore, an improvement of the modeling of the head loss mechanism still need to be studied.

20.2 Perspectives

The good compromise between the promising results and time-efficiency of this simplified 1D-approach of the quasi-2D model of aerated flow over stepped chute opens to a list of perspectives to improve the modeling of the energy dissipation process and to generalize the model for any macro-roughness system.

Onset of a 2D-approach

The effect of the internal jet transverse to the mean flow seems significant in the energy dissipation process for transition and skimming flow regime (see Part IV, Chapter 16.3). In addition, the non-hydrostatic pressure distribution may be essential to explain the mixture flow behaviour to explain the narrowing and widening of the flow depth along the steps. However, these relevant parameters have not yet been investigated in the experimental studies. In order not to fall in the difficulties encountered by a 2DV or 3D numerical models, a suggested compromise is to implement in the present model a vertical component of the velocity w_m, in the mass and momentum balance. In the same way as for u_m, w_m distribution can be represented by a simple schematic profile different below and above the pseudo-bottom and based on the visual observations.

The goal will be thus to express the vertical component as a function of the local angle between the topography and the pseudo-bottom as well as of the longitudinal velocity. The implementation of this component in the momentum equation which is developed for both x and z axis results in an additional pressure to the hydrostatic term.

Additional elements of validation

In order to control the inner behaviour of the aerated flow, the distribution of the pressure on the vertical and horizontal step faces could be compared with the experimental results of the 30^o flume of LCH-EPFL and with the values provided by Sánchez-Juny et al. (2000) for a 51.3^o stepped flume.

The computed flow characteristics will also be compared with experimental results of the flatter slope ($\theta = 18.6^o$).

Finally the numerical model has to be tested for different bottom topography such as steps equipped with endsills and steps equipped with blocks. It would allow the effect of shape and spatial pattern of the macro-roughness elements on the energy dissipation inner mechanism to be investigated.

Extension to prototype

In order to provide useful tool for engineer, the model would have to be tested for prototype cases. One of the goal would be to replace the detailed topography with an equivalent smooth slope in the momentum equation. In this case, the loss terms would not be implemented by the Manning relation but by two terms:

- A friction loss term represented by the Chezy equation. The global friction factor would include the external friction on the bottom and the internal friction on the pseudo-bottom due to the recirculating cells, function on the slope and on the mean flow velocity,
- A drag force term with a drag coefficient function of the macro-roughness dimensionless parameter (see Part IV, Chapter 16.3) which takes into account the macro-roughness element relative height, shape as well as the transverse and longitudinal relative space between the elements.

Part VI

Final conclusions

Chapter 21

Synthesis

Uncontrolled overtopping during flood events can represent a real danger for embankment dam safety. Erosion of the downstream slope and scouring at its base caused by the high velocity and energy of the flow can lead to breach formation and complete failure for long duration events.

Within this context and faced with the large number of overtopped embankment dams left un-rehabilitated, researchers have investigated surface protection solutions for downstream slopes. Tests showed that protection systems against erosion, such as seeded Goetextile or cable-tied cellular concrete blocks, are insufficient since they can resist only short events with a unit discharge of up to 3 m^2/s or a velocity of up to 9 m/s. Solution to survive more severe events consists in overlays which dissipate flow energy along the downstream slope. Conventional steps resulting from RCC techniques fulfill efficiently this challenge.

Flows over steep stepped chutes are quite complex, characterized by great aeration, high turbulence and a confused irregular wavy free surface. Consequently, most hydraulic studies of such flows are performed in physical models. However, a better description of flow behaviour as well as a more accurate approach to estimate energy dissipation are still needed to provide general guidelines for hydraulics of aerated flows over stepped macro-roughness chutes and for the design of optimal protective overlays.

As a contribution to this challenge, experimental study of flow over stepped chutes equipped with macro-roughness elements in a 8 m long, 0.5 m wide gated flume has been performed for a mild 30^o ($\simeq 1.7H:1V$) and a weak 18.6^o ($\simeq 3H:1V$) slopes, representing the range of typical embankment dams and spillways slopes.

Three types of stepped macro-roughness overlays have been investigated, namely conventional steps, steps equipped with endsills over the whole width of the flume and steps equipped with spaced rectangular blocks. Endsill overlays were characterized by different longitudinal distribution ratios x_r/x_s (where x_s and x_r are respectively the longitudinal spacing between two steps or two endsills), whereas block overlays were tested for different transverse patterns e_r/b_r (where e_r is the transverse spacing between two blocks of width b_r). Both endsills and blocks present the same height $h_r = \frac{3}{2}h_s$ (with h_s the step height) since previous studies showed that the height is not the relevant parameter regarding energy dissipation efficiency.

Considering step heights commonly found on prototypes, the physical model represents a scaling ration of to 1/5 to 1/15 with Froude similarity, and thus involves negligible scale effects. Tests were conducted for unit discharges of up to 0.28 m^2/s, that encompassed the nappe, transition and skimming flow regimes.

Flow depth, local air concentration and longitudinal velocities were measured with a double fiber-optical probe. Pressures at the macro-roughness faces were recorded with piezo-resistive sensors. A stilling basin was constructed at the base of the flume to estimate global residual energy by measuring jump sequent depths with ultrasound sensors. Experiments were aimed at understanding and defining aerated flow behaviour over conventional steps and at assessing the influence of additional macro-roughness elements (endsills and blocks).

The work focused particularly on:

- self-aeration process (onset of air entrainment, vertical distribution of air concentration, concentration at saturation),
- flow regimes (onset of regimes and macro-turbulent structures),

- flow layers with the concept of homogeneous aerated flow,
- flow velocities (mean velocity, vertical distribution, kinetic energy and momentum correcting coefficients),
- validation of an indirect method for energy dissipation estimation,
- energy dissipation mechanism (sources of head loss, relevance of drag form effect caused by macro-roughness, residual energy estimation)
- energy dissipation efficiency of stepped macro-roughness overlays.

Based on the discharges and slopes, the results lead to guidelines for the design of dissipative systems consisting of conventional steps equipped with additional macro-roughness elements. However, experimental results remain limited to their tested domain.

To provide more general governing equations for aerated flows over macro-roughness stepped chutes, a numerical modeling of two phase flows over conventional steps was investigated in collaboration with the Laboratory of Applied Hydrodynamic and Hydraulic Constructions at the University of Liège. A quasi-2D numerical model based on the finite volume method was developed. It consists of applying the classical depth-averaged simplified Navier-Stokes equations (viscosity and Coriolis terms neglected) to a 1D incompressible air-water mixture flow over mild and steep slopes with a stepped topography.

The self-aeration process is modeled by a transport equation of depth-averaged air concentration whereas turbulent structures such as internal jets and recirculating cells for transition and skimming regimes are implemented using the Boussinesq correction coefficient. The latter represents the non uniform vertical velocity distribution.

This theoretical description of aerated flow over steps, tested for the 30^o gated stepped flume of LCH-EPFL and the 52^o crested spillway laboratory model of HACH-Ulg, yields realistic predictions of mixture depth, mean flow velocity, air concentration and wave amplitudes of the flow free surface. Despite these promising results, an improvement of the drag form influence caused by the steps could be achieved by implementing a vertical velocity component.

Finally, on the basis of existing protection systems of embankment dams and on results from previous studies of flows over conventional stepped flumes, the present experimental and numerical investigations result in hydraulic relationships for the main flow characteristics (depth, air concentration, velocity, relative energy loss) under uniform flow conditions. First hand guidelines for optimisation of the design of stepped macro-roughness overlays have to be developed.

Chapter 22

Empirical relationships and characteristics of aerated flows over steps with macro-roughness elements

Notations are given in the list of symbols at the beginning of the document. To be simplified, please note that in the following:

- m=0: conventional steps
- m=1/2: every second step equipped with an endsill
- m=1: every step equipped with an endsill
- m=4: spaced blocks
- m=5: aligned blocks
- m=6: close-packed blocks

Flow characteristics

Flow regimes

♢ *Structure*

The nappe, transition and skimming flow regimes that can be observed for conventional steps are also well-distinguished for steps with endsills or blocks. The main macro-structures characterizing both nappe (air cavity, jet impact and deflection) and skimming regimes (re-circulating cells, internal transverse jet) are similar for all overlays. However, block overlays lead to an increase of the 3-D pattern of recirculating cells and create a series of transverse jets between two blocks.

♢ *Onset*

Alternating endsills and blocks modify the onset of transition and skimming regimes.

- For $18.6^o \leq \theta \leq 30^o$ and m=0, m=1/2, m=1, onset of flow regimes is given by:
  - Transition flow:

$$\frac{h_c}{h_s} = \left(\frac{0.743}{\eta_m}\right)\left(\frac{h_s}{l_s}\right)^{-0.244} \tag{22.1}$$

  - Skimming flow:

$$\frac{h_c}{h_s} = 0.939\eta_m\left(\frac{h_s}{l_s}\right)^{-0.364} \tag{22.2}$$

  where $\eta_m = 1$ for m=0 and $\eta_m = -lnm + 1$ for $0 < m \leq 1$

- For m=4 and m=5 and $\theta = 30^o$:
  - Transition flow:

$$\frac{h_c}{h_s} = 0.525\frac{h_s}{l_s}^{-0.244} \tag{22.3}$$

– Skimming flow:

$$\frac{h_c}{h_s} = 0.776 \frac{h_s}{l_s}^{-0.364} \tag{22.4}$$

♢ *Remarks*

1. Onset of transition and skimming flow regimes do not only represent visual criteria but also they can be observed in the behaviour of air concentration and velocity profiles as well as in the frequency spectra of pressures at the step faces.

2. Depth, air concentration, velocity and pressure behaviours for the skimming regime can be divided into

   - an established skimming flow from the onset up to discharges where $\frac{h_c}{h*} < 2$
   - a well-developed skimming flow for $\frac{h_c}{h_s} \geq 2$ when drag form effect are mainly cushioned by the large skimming layer

   with $h* = h_s$ for m=0 and m=1 and $h* = h_s + h_r$ for m=1/2.

Self-aeration model

♢ *Self-aeration mechanism*
For nappe flow regime, air is mainly entrained at the plunging point where the nappe is broken or when a hydraulic jump is developed.

For transition and skimming regimes, self-aeration is initiated at the free surface: air bubbles are trapped at the flow surface when turbulent forces overcome surface tension and bubble rise velocity.

♢ *Onset of air entrainment*

For both the 18.6^o and the 30^o slopes, as compared to equivalent smooth chutes, the increased roughness is due to macro-roughness elements (steps and endsills). These displace the onset of air entrainment closer to the crest chute. This reduces the reach of the dam slope prone to cavitation.

For slopes equipped with conventional steps, a good approximation of the longitudinal location of the point of inception is given by :

$$\frac{L_i}{k_s} = \frac{8.0}{\tan\theta} F_{*,\theta}^{0.730} \tag{22.5}$$

For well developed skimming flow, the two overlays $m = 1/2$ and $m = 4$ lead to a displacement of the point of inception upstream.

♢ *Mean air concentration*

Mean air concentration depends on flow regimes:

- For $F_{*,\theta_*} \leq 4$, mean air at saturation C_u decreases exponentially from nappe flow to established skimming flow:

  $$C_u = A F_{*,\theta*}^{-b} \tag{22.6}$$

  with

$m = 0, m = 1 \Rightarrow A = 0.55, b = 0.12$
$m = 1/2 \quad \Rightarrow A = 0.62, b = 0.16$

- For $F_{*,\theta_*} > 4$ (well developed skimming flow) mean air concentration becomes independent of discharge and depends principally on the equivalent pseudo-bottom slope:

$$C_u = 0.81 \sin \theta_*^{0.81} \tag{22.7}$$

where $F_{*,\theta_*} = q_w / \sqrt{g \cos \theta_* k_*^3}$.
For $m = 0$ and $m = 1$, $h_* = h_s$, $k_* = k_s$ and $\theta_* = \theta = 30^o$ whereas for $m = 1/2$, $h_* = h_s + h_r$, $k_* = k_s + k_r$ and $\theta_* = 33.3^o$.

$\diamondsuit$ *Vertical air concentration distribution*

The shape of the profile follows the same behaviour regardless of endsill configurations and flow regions.

For nappe flow regime, profiles are predicted by the exponential relationship experimentally established by [Chanson & Toombes (2001b)]:

$$c(z) = K_3 \left[1 - \exp\left(- \lambda \frac{z}{Z_{90}} \right) \right] \tag{22.8}$$

where K_3 and λ depend on the mean air concentration C: $K_3 = \dfrac{0.9}{1 - \exp(-\lambda)}$ and $C = K_3 - \dfrac{0.9}{\lambda}$.

For transition and skimming flow regimes, the homogeneous portion of the aerated flow is accurately described by the ADM profile (advective air bubbles diffusion models) developed by Chanson (2000):

$$c(z) = 1 - tanh^2 \left(K' - \frac{\frac{z}{Z_{90}}}{2D'} \right) \tag{22.9}$$

with $K' = arctanh(\sqrt{0.1}) + [1/(2D')]$ and $C_u = 2D' \left[tanh\left(arctanh(\sqrt{0.1}) + \frac{1}{2D'} \right) - \sqrt{0.1} \right]$.

$\diamondsuit$ *Air concentration boundary layer*

- For $m = 0$, the vertical distribution of the air concentration indicates the presence of a boundary layer in the portion of the flow below $z/Z_{90} = H_{90} = 0.25$, for all discharges during transition and skimming regimes.
- For $m = 1$, results are similar and endsills have no effect on this inner layer of the flow.
- $m = 1/2$ provides a thicker air concentration boundary layer: $H_{90} \leq 0.3 - 0.35$.

Mixture flow layers

$\diamondsuit$ *Free surface*

The shape of the free surface reflects the drag form effects caused by macro-roughness:

- Narrowing at the separation zone between recirculating cells and internal jet or between two recirculating cells. It is located just upstream of the step outer corner.

- Widening at the place where the internal jet is entrained by the skimming layer, then at the inner step corner.

These effects are cushioned for well developed skimming flow. As a result, the free surface becomes smoother.

For nappe and transition flows, rollwaves are observed for all overlays. These instabilities have a frequency of about 1 Hz and a maximale amplitude 3 to 3.5 times the mean mixture flow depth.

$\diamondsuit$ *Mixture flow depth*

The addition of endsills and blocks results in an increase of mixture flow depth of about $\left(\frac{k_s + k_r}{ks}\right) Z_{90,m=0}$ for transition and skimming flows and of about 2 times for nappe flow.

A longitudinal space x_r larger than $2x_s$ between two endsills lead to a high instability of the free surface with local elevations 3 to 3.5 higher than the mean depth.

For $18.6^o \leq \theta \leq 30^o$, for the three flow regimes, mixture flow depth in uniform region can be estimated by:

- $m = 0$:

$$\frac{Z_{90,u}}{k_s} = 0.580 F_{*,\theta}^{0.6 \cos\theta} \tag{22.10}$$

- $m = 1/2$ and $m = 1$:

$$\frac{Z_{90,u}}{k_s} = A F_{*,\theta}^{\frac{2}{3} 0.6 \cos\theta} \tag{22.11}$$

with:

$m = 1/2 \Rightarrow A = 1.109$
$m = 1 \quad \Rightarrow A = 1.030$

- $m = 4,\ 5,\ 6$:

$$\frac{Z_{90,u}}{k_s} = 0.942 F_{*,\theta}^{0.51 \cos\theta} \tag{22.12}$$

$\diamondsuit$ *Recommendations on side wall design*

Irregular wavy free surface flow , spray and water drops ejections should be considered in the design of the side wall height h_d.

According to Boes & Minor (2000), for conventional steps:

$$h_d = \eta Z_{90,u} \tag{22.13}$$

with $\eta = 1.2$ for concrete dams and $\eta = 1.5$ for embankment dams.

To take into account rollwaves it may be suggested for embankment dams under nappe flow conditions to increase the safety factor to 3 for all tested stepped macro-roughness overlays:

$$h_d = 3 Z_{90,u} \tag{22.14}$$

with $Z_{90,u}$ estimated according to Equations 22.10, 22.11, 22.12.

◊ *Flow layers*

Above the pseudo-bottom defined by the steps outer edges (m=0), the endsills (m=1/2, m=1) or the blocks (m=4, 5, 6), the mixture flow depth can be divided into 2 layers:

1. A homogeneous aerated layer which corresponds to a mass of water which transports air bubbles.
   This layer is characterized by an air concentration lower than 0.7 and air bubble size lower than 20 mm. Homogeneous flow depth can be accurately derived based on the probability density function of the local air concentration signal $f(c)$ and on an intermittence parameter $T_{int} = \int_0^{0.7} f(c)dc$ according to Cain (1978) and Falvey (1980). This depth can be approximated by the depth at 70 % of air concentration.

   Particularly this part of the aerated flow is involved in the momentum transport, mass continuity and energy dissipation processes.

2. Free surface aerated layer, which mainly consists in a mass of air that is trapped between splashing waves, rollwaves and a mass of water droplets and spray ejections. Herein, air content is higher than 70 %.

Flow velocity

◊ *Vertical distribution*

Similar to flow over gravel, skimming flow over stepped macro-roughness overlays is characterized by two layers above the pseudo-bottom formed by the steps (m=0) or endsills (m=1, m=1/2) outer edges:

1. **The rough boundary layer** or lower layer in the portion $0 < z/Z_{90} = H_{90} < H_{limit}$ which is influenced by shear stress and overall form effects due to the steps.
   For m=0, $H_{limit} = 0.25$
   For m=1 and m=1/2, above the endsills outer edges, $H_{limit} = 0.20$
   For m=1/2, above the steps outer edges, $H_{limit} = 0.30$

   Herein, the flow experiments a logarithmic velocity profile.

2. **The upper layer** which depends on the surface velocity.
   For $H_{limit} \leq H_{90} \leq 0.95$ the flow, quasi-parallel to the pseudo-bottom, follows a power law. For $H_{90} > 0.95$, velocity remains constant and then $U_{90} = 1$.
   For skimming flow and $\theta = 30^o$, in the uniform region, velocity profiles in between $H_{limit} < H_{90} \leq 0.95$ are given by:

   - For $m = 0$, $m = 1$:
     $$U_{90} = 1.01 H_{90}^{1/N} \tag{22.15}$$
     with for $1.7 \leq F_{*,\theta} < 7.5$, $N = \frac{11.2}{F_{*,\theta}^{0.52}}$ and for $F_{*,\theta} \geq 7.5$ $N = 3.9$.
   - For $m = 1/2$:
     - above endsills outer edges
       $$U_{90} = 1.01 H_{90}^{1/6} \tag{22.16}$$

– above step outer edges

$$U_{90} = 1.02\sqrt{H_{90}} \tag{22.17}$$

♢ *Mean velocity*

For $m = 0$ and $m = 1$, mean velocities are quite identical, showing that there is no substantial influence of endsills.

However, for $m = 1/2$, the mean velocity at the step outer edge is smaller. This results from the important separation zone between 2 consecutive recirculating cells near the step outer edge, and from the change of slope between one step with endsill and the consecutive one without endsill.

♢ *Coriolis and Boussinesq coefficients*

To take into account the non-uniform velocity distribution, kinetic energy and momentum correction coefficients have been computed accounting for air influence. This leads to the following results:

	$\rho_{xx,m}$	α_m
Nappe flow		
m=0	1.15	1.30
m=1/2, m=1	1.05	1.15
Transition flow		
m=0, m=1	1.11	1.25
m=1/2	1.05	1.15
Skimming flow		
m=0	1.08	1.16
m=1/2	1.05	1.10
m=1	1.07	1.14

Table 22.1: Empirical values of Boussinesq ($\rho_{xx,m}$) and Coriolis (α, m) correction coefficients for aerated flow over the 30^o chute in the uniform region

For skimming flow, coefficients are similar to classical values for torrents [Kolupaila (1956)].

Energy dissipation efficiency

♢ *Source of dissipation*

For stepped macro-roughness overlays, the relevant sources of energy dissipation are the drag caused by the steps and the additional endsills or blocks. Head losses can be divided into:

- **A friction term** mainly caused by the shear stress at the step faces under the recirculating cells but also under the internal jet on the end of step/endsill/block horizontal face.
- **A drag term** caused by:
  - internal jet at the step or endsill or block outer edge transverse to the mean flow,

– separation zone at the interface recirculating cells/internal jet (m=0), and between two recirculating cells (m=1/2, m=4),
– broken slope from one step equipped with endsill to the following conventional steps (m=1/2, m=4) which creates narrowing and widening of the skimming layer,
– transverse contraction jets and wakes created by the blocks (m=4).

This drag term increases substantially the energy dissipation rate and has a large contribution to the total head loss. This is the dominant head loss.

♢ *Dimensionless head loss parameter*

A dimensionless parameter that characterizes the different head loss contributions is defined as:

$$\Pi_m = \frac{e_r}{b_r} + \frac{h_s}{x_s} + \frac{h_{r*}}{x_r} + \frac{1}{N*} + \frac{l_s - l_r}{l_s} \tag{22.18}$$

where h_{r*} is the effective additional depth caused by the macro-roughness elements: $h_r* = 0$ for m=0 and m=1, $h_r* = h_r$ for the other overlays. $N*$ is the number of conventional steps following a step equipped with endsill or with block.

Π_m includes the influence of the mean slope (h_s/x_s), a broken slope effect due to alternate endsills or blocks longitudinal distribution $(h_r * /x_r)$, internal transverse jet and separation zone influences $(1/N*)$, destruction of the separation zone on the horizontal face $((l_s - l_r)/l_s)$ and finally a contraction effect (e_r/b_r).

As a consequence, it appears inaccurate to represent head losses by Darcy-Weisbach or Colebrook-White laws. It might be more realistic to use a dissipation or head loss coefficient ξ_u such as: $H_0 - H_r = \xi_u \frac{U'^2}{2g}$ with U' the homogeneous flow longitudinal mean velocity and $\xi_u = \phi\left(\Pi_m, \frac{h_c}{h_s}, C, F_{*,\theta}\right)$.

♢ *Residual energy at base of chutes*

Based on results for $\theta = 30^o$ and under uniform flow conditions, residual energy is given by the following equations.

- For 2D stepped overlays: m=0, m=1 and m=1/2

$$\frac{H_r}{H_0} = \frac{\Pi_m \tan\theta}{10} exp\left(A_m \frac{h_c}{N_s h_s}\right) \tag{22.19}$$

with:

$m = 1/2 \Rightarrow A_m = 18.45$
$m = 0 \quad \Rightarrow A_m = 25.26$
$m = 1 \quad \Rightarrow A_m = 31.03$

- For 3D stepped overlays: m=4, m=5, m=6

$$\frac{H_r}{H_0} = 10 B_f \Pi_m \tan\theta \left(\frac{h_c}{N_s h_s}\right)^{b_m} \tag{22.20}$$

with:

$m = 4 \Rightarrow b_m = 1.212$
$m = 5 \Rightarrow b_m = 1.131$
$m = 6 \Rightarrow b_m = 1.094$

According to Boes & Hager (2003b), the minimum relative crested dam height $H_{D,u}$ required for uniform flow over conventional steps is given by:

$$\frac{H_{D,u}}{h_c} \simeq 24(\sin\theta)^{2/3}. \tag{22.21}$$

In the flow developing region, drag form effects caused by macro-roughness are the same as in uniform region. In addition, mean air concentration is lower than the air concentration in uniform region. Since air tends to reduce friction and drag coefficients, using Equations 22.19 or 22.20 for chutes that have not attained yet uniform flow might results in conservative design.

Simplified governing equations for aerated flow over conventional mild and steep stepped slopes

Experimental and numerical work results in the following set of 1D depth-averaged equations.

1. Mass balance
$$\frac{\partial}{\partial t}(\rho_m Z_m) + \frac{\partial}{\partial x}(\rho_m Z_m \overline{u_m}) = 0$$

2. Momentum balance
$$\frac{\partial}{\partial t}(\rho_m Z_m \overline{u_m}) + \frac{\partial}{\partial x}(\rho_m Z_m \rho_{xx,m} \overline{u_m}^2) + \frac{\partial}{\partial x}(\frac{g}{2}\rho_m Z_m^2 \cos\theta) + \rho_m g Z_m \cos\theta \frac{\partial z_b}{\partial x} = \rho_m g Z_m \sin\theta + \tau_{bx}$$

3. Friction term (only bottom and wall effects)
$$\tau_{bx} = g n^2 Z_m (1 - \overline{C}) \overline{u_m} \frac{\sqrt{\rho_{xx,m} \overline{u_m}^2}}{R_h^{4/3}}$$
with $R_h = Z_m$ for wide chute and $R_h = B_f Z_m/(B_f + 2Z_m)$ for narrower flume of width B_f.

4. Air concentration transport
$$\frac{\partial \overline{C}}{\partial t} + \overline{u_m}\frac{\partial \overline{C}}{\partial x} = 0.25 m_I (\overline{C} - C_u)$$

with:

- Air concentration at saturation:
  C_u given according to relationships, Eq.22.6 and 22.7.
- Onset of air entrainment:
  $m_I = 0$ if $x < L_i$
  $m_I = 1$ if $x \geq L_i$
  with L_i given by Eq. 22.5.

- Correction of uneven velocity profile:

$$\rho_{xx} = \frac{1}{3}\frac{Z_m r}{(Z_m - r)^2}\left(\frac{u_b}{\overline{u_m}}\right)^2 + \frac{Z_m}{Z_m - r}\rho_{edge}$$

  where ρ_{edge} is given by Table 22.1 and $\frac{u_b}{\overline{Z_m}}$ are determined experimentally.

Chapter 23

Methods for energy dissipation estimation

Based on a comparison of different methods for residual energy estimation for m=0, m=1/2 and m=1, it is suggested that:

1. Equivalent clear water flow characteristics lead to over-estimated residual energy for developed skimming flow ($F_{*,\theta} > 4$).

2. Residual energy computed based on friction coefficient according to Equation 15.5 (Part IV) [Chanson (1994b)] leads to an under-estimation which over-estimates the energy dissipation rate.

3. Homogeneously aerated flow is the portion of flow which is effectively involved in the dissipation mechanism.

4. Accuracy of energy dissipation estimated from hydraulic jump methods depends strongly upon the position of the jump. To be accurate, the upstream front of the jump has to be located at the cross section where the plunging flow reaches the horizontal bottom of the stilling bassin.

5. Residual energy derived from hydraulic jump method (H_{r1}) has to be corrected by a correction factor equal to 1.15 such as:

$$H_r = 1.15 H_{r1} \tag{23.1}$$

Chapter 24

Optimal tested overlays

Criteria for an optimal stepped macro-roughness overlay

Main criteria used to evaluate the efficiency of stepped macro-roughness overlays are as follows:

1. Minimum residual flow energy at the toe of the chute, thus, maximum energy dissipation efficiency.
   Regarding design, it diminishes the size of the stilling basin at the base of the chute.

2. Minimum swelling of mixture flow depth and minimisation of free surface instabilities.
   Regarding design, it would limit the size of the side walls.

3. Limitation of pressure fluctuations as well as of negative and positive extremes.
   Regarding design, stability of the macro-roughness elements must be assured by avoiding large hydrodynamic loads. Their fatigue, which depends on frequencies of peaks of pressure, must be limited. Cavitation caused by large negative pressures has to be avoided.

4. Location of inception point as close as possible to the dam or spillway crest to reduce the reach of the downstream slope prone to cavitation.

5. Reduction of duration of the transition regime.
   During this regime, recirculating cells which contribute to head losses are not developed and some steps can be inefficient regarding energy dissipation. In addition the free surface presents a significant wavy pattern during this regime for steps with alternating endsills.

6. Realism and simplicity of the macro-roughness elements.

7. Environmental integration.

Optimal stepped macro-roughness overlay

Based on these criteria, a summary of tested stepped macro-roughness overlays are given in Figure 24.1. Results indicate that among the tested overlays, the **optimal protection** against erosion of downstream slope and scouring of the structure base corresponds to **spaced alternate blocks (m=4) fixed at the end of horizontal steps face**.

As an example, for a 1:10 scaled prototype, the steps are 1.04 m length, 0.6 m high and 50 m width. Rectangular blocks of height equal to $1/2h_s = 0.3$ m, 0.5 m width and 0.26 m long are fixed at the horizontal step outer edge with a transversal spacing equal to 0.75 m ($e_r/b_r = 1.5$). Blocks have an alternate pattern along the slope. Against the side wall, half blocks can be fixed each two steps. For $q_w = 7.6$ m^2/s (maximum tested unit discharge) or $F_{*,\theta} = 6.95$, this overlay dissipates 76.5 % of the initial energy at the crest of dam.

	m=1/3	m=1/2	m=1	m=4	m=5, 6
1) Energy dissipation	2 to 4 % lower up to $F_{*\theta}$=5.8	2 % higher for $F_{*\theta}$>3.5	Less efficient (1 to 2% lower)	6 to 8% higher	3 to 4% higher
2) Flow depth	Instable free surface 2 to $3Z_{90m=0}$	1.4 to $2Z_{90m=0}$	1.2 to $2Z_{90m=0}$	1.4 to $2Z_{90m=0}$	1.4 to $2Z_{90m=0}$
3) Pressure	Negative peak High fluctuation High endsill load	Weak negative peaks Mild endsill load Low fluctuation	Negligible negative peaks Low endsill load Low fluctuation	Weak negative peaks Low blocks load Low fluctuation	Weak negative peaks Low blocks load Low fluctuation
4) Inception point		For $F_{*\theta}$>3.5, closer to crest	Idem than conventional steps	For $F_{*\theta}$>3.5, closer to crest	Idem than conventional steps
5) Regime	Long transition flow duration with inactive steps	Mild transition flow duration with inactive steps	Idem than conventional steps	Short nappe and transition duration	Short nappe and transition duration
6) Structural (volume per step V_r – Scale dim.)	V_r=2.610^{-4} (m^3/step)	V_r=3.910^{-4} (m^3/step)	V_r=7.810^{-4} (m^3/step)	V_r=3.110^{-4} (m^3/step)	m=5: V_r=3.910^{-4} m=6: V_r=4.710^{-4} (m^3/step)
7) Environment					

Figure 24.1: Summary of behaviour of tested stepped macro-roughness overlays regarding efficiency criteria - $F_{*,\theta} = q_w/\sqrt{g\cos\theta(h_s\cos\theta)^3}$, $Z_{90m=0}$: mixture flow depth for m=0

Part VII

Additional research

Based on the present results several further investigations and developments could be performed to improve and extend the general knowledge of aerated flows over stepped chutes with macro-roughness.

Experimental tests

With respect to flow regimes, flow depth, pressures and overall energy dissipation, the tested blocks systems appear as a promising solution for embankment dams protection. Experimental tests have concerned a sensitivity study on transverse space e_r between two blocks (of width b_r and height h_r and longitudinal space x_r) and thus on contraction effect.

In order to provide more general definition of hydraulics of flow over this type of overlays and to optimize the blocks pattern it would be of interest to assess other relevant parameters such as e_r/b_r, h_r/b_r, h_r/x_r, h_r/h_s with h_s the step height.

Another way to increase the drag form could be to add a reverse slope on each step. In fact, this slope at the horizontal face may contribute to increase the deflection and then the zone of influence of the transverse internal jet. It would be then interesting to estimate the effect of the reverse slope angle on residual energy. Note that the important transverse jet developed at the reverse slope outer edge might have a negative consequence regarding flow depth.

Velocity measurements

Visual observations, velocity measurements and numerical tests have highlighted the non negligible vertical component of the flow velocity in the rough boundary layer. This parameter can not be measured with Fiber-optical probe. For this reason, a Particule Image Velocimetry (PIV) instrumentation which measures the 3D component of flow velocity without intrusion could be interested to adapt for aerated flow.

Jetbox influence

During preliminary tests concerning jetbox, it was shown that in the uniform regions, air concentration and energy dissipation are independent of the jetbox opening. However, this is not the case upstream of inception point and in developing flow region.

Hager & Boes (2000) established relevant backwater and drawdown curves for conventional stepped spillways in order to extrapolate results from gated flumes to crested spillways. However, this development assumes that the jetbox has no effect on the turbulent boundary layer and consequently on self aeration process. It would be interesting to verify this assumption by comparing the longitudinal variation of the velocity and air concentration profiles around the inception point and down to the uniform region for jetbox and crested equivalent flumes with same slope and steps.

Cavitation and fatigue of macro-roughness elements

Cavitation is a local mechanism caused by a drastic local change of pressure. However, previous results on cavitation risk are based on air concentration measurements. In addition, because of the fragile instrumentation such as optical or resistive probes, measurements are taken at least at 1 mm above the bottom which seems quite approximative to draw conclusions

about cavitation prediction. Therefore it would be more accurate to estimate risk of onset of cavitation using pressure measurements.

In fact, in the uniform region where the pressure measurements have been done, the lowest cavitation index was estimated at about 10 which is pretty large compared to the classical threshold for incipient cavitation [Falvey (1990)]. It would then be more relevant to measure pressures in the reach upstream of the inception point to determine the drop of pressures in the sensitive zone such as downstream of steps, endsill or block and also at the zone where wakes and separation zones can occurred.

For design interest, in addition to cavitation, fatigue of macro-roughness element is a relevant information to estimate their resistance for long duration flood events. Statics analysis of frequency and time distribution of pressure peaks could indicate the repetitive load on the steps, endsills or blocks faces and then highlight the fragile zones.

Assessment on dissipation coefficient

It was seen that global dissipation coefficient ξ_u which includes friction and drag terms can be derived from residual energy when uniform conditions are attained at the toe of the chute.

In order to derive this coefficient in any flow regions, pressure measurements can be extended to estimate the surface forces (F_h on the horizontal face and F_v on the vertical face) applied on a control volume (see Fig. 24.2). Since air concentration and velocity profiles can be measured at upstream and downstream cross sections of this volume, dissipation term and thus dissipation coefficient can be computed from the momentum equation in the longitudinal axis.

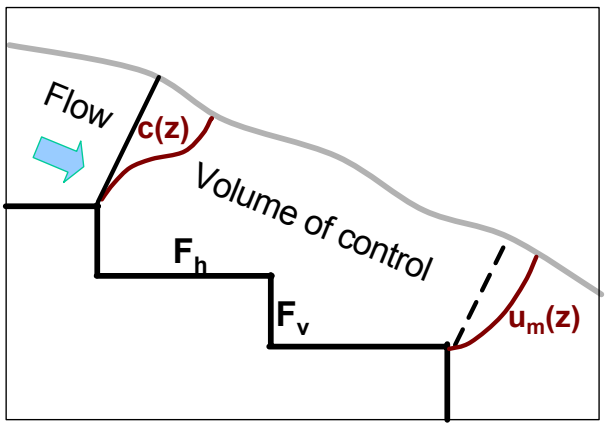

Figure 24.2: Definition of a control volume along the slope

Environmental integration

Blocks and endsills overlays have been tested for clean flows. Their behaviour for flows with sediments or floating debris has to be tested. This will verify if there is a risk of overload on the macro-roughness elements or of obstruction of step cavity, which might reduce significantly the energy dissipation efficiency and endanger the stability of the overlay.

Vertical distribution of pressure

All the existing results on flows over stepped chutes assume a hydrostatic pressure distribution. It was seen that is not the case. Since measurements of pressures in the water depth seem difficultly feasible, vertical non-hydrostatic profile can be assessed with the improvement of the quasi-2D numerical model of flows over conventional steps.

In order not to fall in the difficulties encountered by a 2D vertical or 3D numerical model, a suggested compromise is to implement in the present model a vertical component of the velocity w_m, in the mass and momentum balance. This implementation of w_m in the momentum equation applied for both x and z axis might result to an additional pressure term to the hydrostatic distribution.

Acknowledgment/Remerciements

Ce travail de thèse s'est déroulé au Laboratoire de Constructions Hydrauliques (LCH) de l'École Polytechnique Fédérale de Lausanne sous la direction du professeur A. Schleiss à qui j'adresse mes vifs remerciements pour la sympathie, la confiance, les encouragements, l'aide scientifique qu'il m'a accordé au cours de ces années. Je le remercie également pour ses minutieuses corrections d'anglais dans ce mémoire.
C'est avec grand plaisir que j'ai intégré l'équipe du LCH et travaillé quotidiennement dans une ambiance dynamique et chaleureuse grâce à la sympathie de tout le personnel. En particulier, je tiens à exprimer le plaisir que j'ai eu à travailler avec:

- Dr Jean-Louis Boillat qui a toujours été là pour un encadrement scientifique et technique de qualité et pour nos longues discussions amicales,
- Louis Schneiter, René Fontanella et Pampam Pantillon qui ont fait vivre l'installation expérimentale à travers blagues et surprises,
- et bien sur tous les anciens et actuels petits "cocots" et "cocottes" du laboratoire qui se reconnaîtront, pour leur amitié, complicité et encouragement durant ces années si agréables.

Je fais aussi un petit clin d'oeil à S. Lemesle qui a connu les joies des joints en silicone pendant un été!

Je tiens aussi à remercier Prof. M. Pirotton pour sa riche et pertinente collaboration dans ce projet de recherche mais aussi pour son amitié. Je n'oublie pas toute l'équipe de ses doctorants qui m'ont si bien accueillie à Liège malgré leur expériences de sédimentation dans les tasses! J'ai une reconnaissance particulière pour Benjamin qui s'est plongé sans retenu dans les écoulements sur escaliers.

Je tiens également à remercier l'Office Fédéral des Eaux et de la Géologie (OFEG) qui a financièrement soutenu ce projet de thèse, et en particulier Monsieur H. Pougatsch. Les interventions des ingénieurs Messieurs Bremen, Gencer, Gerodetti et Müller à certaines étapes de ma thèse ont contribué à s'assurer du réalisme pratique du projet.

I gratefully thank Prof. J. Matos for his relevant assistance and all the time he has devoted to discussions and advises on my work as well as for his confidence and encouraging.

I want also to thank Prof. H. Falvey for the interesting scientific discussions, his help for the "English writing", his relevant ideas and his confident feelings that we have shared during these years.

Prof. A. Ervine belongs also to these persons that I appreciate a lot to meet and discuss with during visits in Lausanne or during conferences.

I do not forget the sympathy and opening of Dr. R. Boes and Dr Ch. Kramer from the VAW (Versuchsanstalt für Wasserbau, Hydrologie und Glaziologie) of the Swiss Federal Institute of Technology in Zurich.

Ces années de thèse ont été accompagnées de moments précieux d'amitié, de rire et d'aventures. Je tiens donc à remercier chaleureusement tous mes ami(e)s qu'ils soient à Lausanne, Tolochonaz, Lully, Pully, Marseille, Nantes, Paris, Belgique ou Oxford. Sans les nommer, ils savent comme leur amitié et leur soutien ont sincèrement compté. Parmi eux, merci à tous les courageux qui ont relu ma thèse!

Faire une thèse avec un enfant, oui, cela est possible, surtout lorsqu'on a la chance d'avoir confié Soline aux super éducatrices de la Croque et de Valency que je remercie sincèrement.

Je ne finirai pas ces remerciements, certes longs mais sincères, sans penser énormément à mes parents et ma soeur et sa petite famille. Depuis le tout début, ils ont toujours été là pour m'encourager et me soutenir à 100 % dans mes challenges. Des tas de merci de suffiraient pas. Les encouragements de tatie, tonton et Eliane ont aussi contribué à rendre les efforts plus faciles.

Enfin, et comme le meilleur est toujours pour la fin, je ne saurai à quel point remercier Soline et Philippe qui sont mes deux soleils, la mer et le vent indispensables à l'accomplissement de cette thèse et surtout à tout le bonheur, les plaisirs et les rires quotidiens.

Bibliography

Abt, S., R. & Johnson, T., L. (1991). Riprap design for overtopping flow, *J. of Hydraulic Engineering* **117**(8): 959–972.

Ahmann, M. & Zapel, E. (2000). Stepped spillways, a dissolved gas abatement alternative, *in* H.-E. Minor & W. Hager (eds), *Proceedings of the International Workshop on Hydraulics of Stepped Spillways*, IAHR, A.A. Balkema/Rottersam/Brookfield, Zürich, Switzerland, pp. 45–52.

Albert, R. & Gautier, J. (1992). Evacuateurs fondés sur remblai, *La Houille Blanche* (2/3): 147–157. In french.

Albertson, M. e. a. (1960). *Fluid Mechanic for Engineers*, Englewood Cliffs, NJ, USA.

Amador, A., Tembleque, F., Sánchez-Juny, M., Puertas, J. & Dolz, J. (2002). Aplicación de la técnica particle image velocimetry al estudio de aliviaderos escalonados, *Proc. of XX Hydraulic Congress, Latinamerican*, Ciudad La Habana, Cuba.

André, S., Boillat, J.-L. & Schleiss, A. (2001). High velocity two-phase turbulent flow over macro-roughness stepped chutes: Focus on dynamic pressures, *in* ISEH (ed.), *Int. Symposium on Environmental Hydraulics*, ISEH, Tempe, Arizona, USA. In CD.

André, S., Boillat, J.-L. & Schleiss, A. (2004). Two-phase flow characteristics of stepped spillways - discussion, *Accepted in J. of Hydraulic Engineering, ASCE* . Paper by Boes, R.M. Hager, W.H. in J. of Hyd. Eng. 129(9), 2003.

André, S., Dewals, B., Pirotton, M. & Schleiss, A. (2003). Quasi 2d-numerical model of aerated flow over stepped chutes, *XXX IAHR Congress on water Engineering and research in a learning society: Modern Developments and Traditional Concepts*, Vol. Theme D: CFD Models and Applications, IAHR, Thessaloniki, Greece, pp. 671–678.

André, S., Matos, J., Boillat, J.-L. & Schleiss, A. (2004). Energy dissipation and hydrodynamic forces of aerated flow over macro-roughness linings for overtopped embankment dams, *in* F. Yazdandoost & J. Attari (eds), *International Conference on Hydraulics of Dams and River Structures*, Balkema, Tehran, Iran, pp. 189–196.

Archambeau, P., Dewals, B., Detrembleur, S., Erpicum, S. & Pirotton, M. (2003). A set of efficient numerical tools for floodplain modelling, *in* G. Jirka & W. Uijttewaal (eds), *Shallow Flows*, A:A: Balkema/Rottersam/Brookfield.

Archambeau, P., Erpicum, S., Mouzelard, T. & Pirotton, M. (2001). Impact studies and water management with wolfhydro: a new physically based hydrological solver, *in* ISEH (ed.), *Proc. of the Int. Symposium on Environmental Hydraulics*, Vol. CD, Tempe, Arizona, USA.

ASCE (1994). *Alternatives for overtopping protection of dams*, Vol. Publication Data, American Society of Civil Engineers, 345 East 47th Street, New York 101017-2398. Committee on Overtopping Protection.

Baker, R. (1997). Design of stepped-block spillways, *Special publication 142*, CIRIA.

Bathurst, J. (1988). Velocity profile in high-gradient, boulder-bed channels, *Proc. Int. Conference On Fluvial Hydraulic*, Budapest, Hungary.

Benmamar, S., Kettab, A. & Thirriot, C. (2003). Numerical simulation of turbulent flow upstream of the inception point in a stepped channel, *XXX IAHR Congress on water Engineering and research in a learning society: Modern Developments and Traditional Concepts*, Vol. Theme D: CFD Models and Applications, IAHR, Thessaloniki, Greece, pp. 679–686.

Boes, R. (2000a). *Zweiphasenströmung und Energieumsetzung an Grosskaskaden*, PhD thesis, Swiss Federal Institue of Thecnology Zürich (ETHZ) - VAW, Switzerland. In German.

Boes, R. (2000b). Characteristics of skimming flow over stepped spillways - discussion, *J. of Hydraulic Engineering, ASCE* **126**(11): 860–862. by Chamani, M.R. and Rajaratnam, N.

Boes, R. & Hager, W. (1998). Fiber-optical experimentation in two-phase cascade flow, *in* K. Hansen (ed.), *Proc. Int. RCC DAms seminar*, Denver, USA.

Boes, R. & Hager, W. (2003a). Two-phase flow characteristics of stepped spillways, *J. of Hydraulic Engineering* **129**(9): 661–670.

Boes, R. M. & Hager, W. H. (2003b). Hydraulic design of stepped spillways, *J. of Hydraulic Engineering* **129**(9): 671–679.

Boes, R., Matos, J., Ohtsu, I. & Tatewar, S. P. (2000). Hydraulics of skimming flow on modeled stepped spillways - discussion, *J. of Hydraulic Engineering* **126**(12): 947–954.

Boes, R. & Minor, H.-E. (2000). Guidelines for the hydraulic design of stepped spillways, *in* H.-E. Minor & W. Hager (eds), *Proceedings of the International Workshop on Hydraulics of Stepped Spillways*, IAHR, A.A. Balkema/Rottersam/Brookfield, Zürich, Switzerland, pp. 163–170.

Bollaert, E. (2002). *Transient water pressures in joints and formation of rock scour due to high-velocity jet impact*, Communication 13, Laboratory of Hydraulic Constructions, Swiss Federal Institute of Technology in Lausanne, Switzerland.

Bos, M. (1976). Discharge measurement structures, *Rapport 4*, Laboratorium voor Hydraulica an Afvoerhydrologie, Landouwhogeschool, Wageningen, The Netherlands.

Bosshard, M. (1991). Überflutbarkeit kleiner dämme, *Versuchsanstalt für wasserbau*, Hydrologie und Glaziologie (VAW) - Swiss Federal Institute of Technology, Zurich, Switzerland. In German.

Cain, P. (1978). *Measurements Within Self-Aerated Flow on a Large Spillway*, PhD thesis, Department of Civil Engineering, University of Canterbury, Christchurch, New Zeland.

Cain, P. & Wood, I. (1981). Measurements of self-aerated flow on a large spillway, *J. of Hydraulics Division* **197**(HY11). ASCE.

Canovaro, F., Paris, E. & Solari, L. (2003). Analysis of resistance of flow over macro-scale roughness: first results, *XXX IAHR Congress on water Engineering and research in a learning society: Modern Developments and Traditional Concepts*, Vol. Theme C: Hydraulic Resistance, IAHR, Thessaloniki, Greece, pp. 1–8.

Chamani, M. R. (2000). Air inception in skimming flow regime over stepped spillways, *in* H.-E. Minor & W. Hager (eds), *Proceedings of the International Workshop on Hydraulics of Stepped Spillways*, IAHR, A.A. Balkema/Rottersam/Brookfield, Zürich, Switzerland, pp. 61–67.

Chamani, M. & Rajaratnam, N. (1994). Jet flow on stepped spillways, *J. of Hydraulic Engineering* **120**(2): 254–259.

Chamani, M. & Rajaratnam, N. (1999). Characteristics of skimming flow over stepped spillways, *J. of Hydraulic Engineering* **125**(4): 361–368. ASCE.

Chanson, H. (1993). Réduction des pertes de frottement pour des écoulements à surface libre avec entraînement d'air. augmentation de la débitance d'un coursier d'évacuateur de crues, *La Houille Blanche* **48**(5): 303–313. In French.

Chanson, H. (1994a). Hydraulics of skimming flows over stepped channels, *J. of Hydraulic Research* **32**(3): 445–460.

Chanson, H. (1994b). Comparison of energy dissipation between nappe and skimming flow regimes on stepped chutes, *J. of Hydraulic Research* **32**(2): 213–218.

Chanson, H. (1994c). *Hydraulic design of stepped cascades, channels, weirs and spillways*, Pergamon, Oxford, UK.

Chanson, H. (1995). Air bubble entrainment in free-surface flows - experimental investigations, *Technical Report Report CH46/95*, University of Queensland, Australia.

Chanson, H. (1997). Air bubble entrainment in open channels : Flow structure and bubble size distributions, *Int. J. Multiphase Flow* **23**(1): 193–203.

Chanson, H. (2000). Characteristics of skimming flow over stepped spillways - discussion, *J. of Hydraulic Engineering, ASCE* **126**(11): 862–865. by Chamani, M.R. and Rajaratnam, N.

Chanson, H. (2001). Caractéristiques diphasiques des ecoulements sur les coursiers en marches d'escalier, *La Houille Blanche* **8**: 16–28.

Chanson, H. (2002a). Air-water flow measurements with intrusive, phase-detection probes : Can we improve their interpretation, *J. of Hydraulic Engineering* **128**(3): 252–255.

Chanson, H. (2002b). Discussion : Enhanced energy dissipation in stepped chutes, *Water and Maritime Engineering* **154**(4): 343–345.

Chanson, H. & Toombes, L. (2001a). Strong interactions between free-surface aeration and turbulence down a staircase channel, *14th Australasian Fluid Mechanics Conference*, Adelaide University, Australia.

Chanson, H. & Toombes, L. (2001b). Experimental investigations of air entrainment in transition and skimming flows down a stepped chute - application to embankment overflow stepped spillways, *Technical Report CE158*, University of Queensland, Australia.

Chanson, H. & Toombes, L. (2002a). Energy dissipation and air entrainment in stepped storm waterway: Experimental study, *J. of Irrigation and Drainage Engineering* **128**(5): 305–315.

Chanson, H. & Toombes, L. (2002b). Experimental investigations of air entrainment in transition and skimming flows down a stepped chute, *Canadian J. of Civil Engineering* **29**(1): 145–156.

Chanson, H., Yasuda, Y. & Ohtsu, I. (2000). Flow resistance in skimming flow: A critical review, *in* H.-E. Minor & W. Hager (eds), *Proceedings of the International Workshop on Hydraulics of Stepped Spillways*, IAHR, A.A. Balkema/Rottersam/Brookfield, pp. 95–102.

Chen, Q., Dai, G. & Liu, H. (2002). Volume of fluide model for turbulence numerical simulation of stepped spillway overflow, *J. of Hydraulic Engineering* **128**(7): 683–688.

Chen, Y., Anderson, B. & Simons, L. (1986). Development of a methodology for estimating embankment damage due to flood overtopping, *Final report*, US Federal Highway Administration and US Forest Service.

Chow, V. (1959). *Open channel hydraulics*, McGraw Hill.

Christodoulou, G. (1999). Design of stepped spillways for optimal energy dissipation, *Hydropower & Dams* **Issue 5**: 90–93.

Collard, M. (2003). Etude expérimentale et théorique des écoulements biphasiques sur les évacuateurs en marches d'escalier. Engineering diploma report, University of Liège, Belgium.

Compagny, M. (2004). *http://www.maccaferri-usa.com/soil.html*, Sitweb.

Dewals, B., André, S., Schleiss, A. & Pirotton, M. (2004). Validation of a quasi-2d model for aerated flows over mild and steep stepped spillways, *6th International Conference on Hydroinformatics*, Liong, Singapore. Submitted.

Dewals, B., Archambeau, P., Erpicum, P., Mouzelard, T. & Pirotton, M. (2002). Coupled computations of highly erosive flows with wolf software, *Proc. of the 5th Internatioal Conference on Hydro-Science & Engineering*, Warsaw.

Diez-Cascon, J., Blanco, J., Revilla, J. & Garcia, R. (1991). Studies on the hydraulic behaviour of stepped spillways, *Water Power & Dam Construction* pp. 22–26.

Ditchey, E. & Campbell, D. (2000). Roller compacted concrete and stepped spillway, *in* H.-E. Minor & W. Hager (eds), *Proceedings of the International Workshop on Hydraulics of Stepped Spillways*, IAHR, A.A. Balkema/Rottersam/Brookfield, Zürich, Switzerland, pp. 171–178.

Erpicum, S., Archambeau, P., Dewals, B., Mouzelard, T. & Pirotton, M. (2003). Optimising a cascade of hydroelectric power stations with the wolf package, *Water Ressources Management* pp. 65–74. C.A. Brebbia Editor.

Essery, I. & Horner (1978). The hydraulic design of stepped spillways, *Technical report 33*, CIRIA. 2d edition.

Falvey, H. T. (1980). Air-water flow in hydraulic structures, *Engineering Monograph 41*, Bureau of Reclamation, United States Department of the Interior, Denver, Colorado, USA.

Falvey, H. T. (1990). Cavitation in chutes and spillways, *Engineering Monograph 42*, Bureau of Reclamation, United States Department of the Interior, Denver, Colorado, USA.

Ferrando, Moñino, A. & Rico, Riera, J. (2002). On the incipient aerated flow in chutes and spillways, *J. of Hydraulic Research* **40**(1): 95–97.

Fratino, U., Amador, A., Valenzano, B., Renna, F., Sánchez-Juny, M. & Dolz, J. (2003). Air inception and pressure fields over a stepped spillway in transition flow regime, *XXX IAHR Congress on water Engineering and research in a learning society: Modern Developments and Traditional Concepts*, Vol. Theme D: Experiments on Stepped Spillways, IAHR, Thessaloniki, Greece, pp. 711–718.

Fratino, U. & Piccinni, A. (2000). Dissipation efficiency of stepped spillways, *in* H.-E. Minor & W. Hager (eds), *Proceedings of the International Workshop on Hydraulics of Stepped Spillways*, IAHR, A.A. Balkema/Rottersam/Brookfield, Zürich, Switzerland.

Frizell, K. (2000). Effects of aeration on the performance of an adv, *Conf. on Water Resources Engineering and Water Resources Planning & Management*, ASCE, minneapolis, USA. CD-ROM.

Frizell, K., Ehler, D. & Mefford, B. (1994). Developing air concentration and velocity probes for measuring in hughly-aerated flow, *Proc. of Hydraulic Engineering Conference*, ASCE, Buffalo, N.Y., USA, pp. 268–277.

Frizell, K., Mefford, B., Vermeyen, T. & Morris, D. (1996). Us5544973: Concrete step embankment protection, *Patenet plaques*, Delphion Intellectual Property Network, http://www.delphions.com.

Gray, E. W. (1991). Cellular concrete blocks for overtopping protection of earth dams, *in* ICOLD (ed.), *Proc. of the 17th Congress on Large Dams of the International Committee on Large Dams*, Q.67 - R.25, ICOLD, Vienne, Austria, pp. 415–434.

Guo, J., Liu, Z. & Lu, Y. (2003). Field observation on the rcc stepped spillways with the flaring pier gate on the dachaoshan project, *XXX IAHR Congress on water Engineering and research in a learning society: Modern Developments and Traditional Concepts*,

Vol. Theme D: Experiences from Models and Prototypes, IAHR, Thessaloniki, Greece, pp. 473–478.

Hagen, V. (1982). Re-evaluation of design floods and dam safety, *in* ICOLD (ed.), *Proc. of the 14th Congress on large Dams of the International Committee on Large Dams*, Q.52 - R.29, Rio de Janeiro, pp. 475–491.

Hager, W. (1991). Uniform aerated chute flow, *Journal of Hydraulic Engineering* **117**(4): 528–533.

Hager, W. & Boes, R. (2000). Backwater and drawdown curves in stepped spillway flow, *in* H.-E. Minor & W. Hager (eds), *Proceedings of the International Workshop on Hydraulics of Stepped Spillways*, IAHR, A.A. Balkema/Rottersam/Brookfield, Zürich, Switzerland, pp. 129–136.

Hager, W. H. (1992). *Energy dissipators and hydraulic jump*, Vol. 8, Kluwer Academic Publishers.

Hansen, K. (1989). Performance of roller compacted concrete dam rehabilitations, *6th Annual ASDO Conference*, Albuquerque, New Mexico, pp. 21–26.

Hansen, K. (2000). History & development of rcc dams, *in* K. Hansen (ed.), *Proc. International of RCC Dams Seminar*, Denver, USA.

Harleman, D. & Rumer, R. (1963). Roughness spacing in rigid open channels - discussion, *American Society of Civil Engineers - Transactions* **128**(3417): 388–393.

Hewlett, H., Boorman, L. & Bramley, M. (1987). Design of reinforced grass waterways, *Technical report*, CIRIA.

Hirt, C. & Nichols, B. (1981). Volume of fluid (vof) method for dynamics of free boundaries, *J. of Computational Physics* **39**: 201–225.

ICOLD (1984). River control during dam construction, *Bulletin 48*, ICOLD.

ICOLD (1997). Dams less than thirty meters high - cost savings and safety improvements, *Bulletin 109*, ICOLD.

James, C. S., Matos, J., Ohtsu, I. & Tatewar, S. P. (2001). Onset of skimming flow on stepped spillways, *J. of Hydraulic Engineering* **127**(6): 519–525.

Killen, J. M. (1968). *The Surface Characteristics of Self-Aerated Flow in Steep Channels*, PhD thesis, University of Minnesota, St. Anthony Fally Hydraulic Laboratory.

Kobus, H. (1984). Local air entrainment and detrainment, *in* H. Kobus (ed.), *Proc. of Symposium on scale effects in modelling hydraulic structures*, Vol. 4.10, Esslingen, Germany, pp. 1–10.

Kolupaila, S. (1956). Methods of determination of the kinetic energy factor, *The port engineer* **5**(1): 12–18.

Lane, E. (1939). Entrainment of air in swiftly flowing water, *J. of Civil Engineering* **9**(2): 89–91.

Lempérière, F. (1993). Dams that have failed byflooding : an analysis of 70 failures, *Water Power & Dam Construction* pp. 19–24.

Manso de Almeida, P. & Schleiss, A. J. (2002). Stability of concrete macro-roughness linings for overflow protection of earth embankment dams, *Canadian J. of Civil Engineering* **29**: 762–776.

Mateos-Iguácel, C. & Elviro-García, V. (2000). Stepped spillway studies at cedex, *in* H.-E. Minor & W. Hager (eds), *Proceedings of the International Workshop on Hydraulics of Stepped Spillways*, A.A. Balkema/Rottersam/Brookfield, Zürich, Switzerland, pp. 87–94.

Matos, J. (1999). Emulsionamento de ar e dissipação de energia do escoamento em descarregadores em degraus, *Research report*, IST Lisbon. (in Portuguese).

Matos, J. (2000a). Characteristics of skimming flow over stepped spillways - discussion, *J. of Hydraulic Engineering, ASCE* **126**(11): 865–868. by Chamani, M.R. and Rajaratnam, N.

Matos, J. (2000b). Hydraulic design of stepped spillways over rcc dams, *in* H.-E. Minor & W. Hager (eds), *Proceedings of the International Workshop on Hydraulics of Stepped Spillways*, A.A. Balkema/Rottersam/Brookfield, Zürich, Switzerland, pp. 187–194.

Matos, J. (2001). Onset of skimmin flow on stepped spillways - discussion, *J. of Hydraulic Engineering, ASCE* **127**(7): 519–521. by Chamani, M.R. and Rajaratnam, N.

Matos, J. (2002). Roller compacted concrete and stepped spillways: From new dams to dam rehabilitation, *in* e. a. Llanos (ed.), *Dam maintenance and Rehabilitation*, Swetz & Zeitlinger, Lisse, Madrid, Spain, pp. 553–560.

Matos, J. & Frizell, K. (2000). Air concentration and velocity measurements on self-aerated flow down stepped chutes, *Proc. of ASCE conference*, ASCE, Minneapolis, USA. CD-ROM.

Matos, J., Frizell, K., André, S. & Frizell, K. (2002). On the performance of velocity measurement techniques in air-water flows, *in* e. a. Wahl (ed.), *Proc. of the specialty conference on Hydraulic Measurements and Experimental Methods*, ASCE, Estes Park, Colorado, USA. CD.

Matos, J., Pinheiro, A., Quintela, A. & Frizell, K. H. (2001). On the role of stepped overlays to increase spillway capacity of embankment dams, *Proc. ICOLD EUropean Symposium*, ICOLD, A.A. Balkema/Rottersam/Brookfield.

Matos, J., Quintela, A., Sánchez-Juny, M. & Dolz, J. (2000). Air entrainment and safety against cavitation damage in stepped spillways over rcc dams, *in* H.-E. Minor & W. Hager (eds), *Proceedings of the International Workshop on Hydraulics of Stepped Spillways*, A.A. Balkema/Rottersam/Brookfield, Zürich, Switzerland, pp. 69–76.

McLean, F. & Hansen, K. (2000). Roller compacted concrete for embankment overtopping protection, *Geotechnial practice for dam rehabilitation*, ASCE, New York, USA, pp. 1–22.

Minor, H.-E. (1998). Report of the european r & d working group "floods", *in* L. Berga (ed.), *Proc. of the International Symposium on new trends and guidelines on Dam Safety*, A.A. BALKEMA/ROTTERDAM/BROOKFIELD, pp. 1541–1550.

Minor, H.-E. (2000). Spillways for high velocities, *in* H.-E. Minor & W. Hager (eds), *Proceedings of the International Workshop on Hydraulics of Stepped Spillways*, IAHR, A.A. Balkema/Rottersam/Brookfield, Zürich, Switzerland, pp. 3–10.

Mouzelard, T., Archambeau, P. & Pirotton, M. (2000). An effective resolution of quais-3d surface flows for spillways design and impact studies, *Proc. of Hydroinformatics 2000*, Vol. CD.

Nariai, N., Ohmoto, T. & Yakita, K. (2001). Turbulent flow structure in stepped steep open-channel, *in* ISEH (ed.), *Proc. of the 2001 International Symposium on Environmental Hydraulics*, IAHR, Tempe, Arizona, USA. CD.

OFEG (2002). *Directives relatives à la sécurité des ouvrages d'accumulation*, OFEG, Bienne.

Ohtsu, I. & Yasuda, Y. (1997). Characteristics of flow conditions on stepped channels, *Proc. of XXVII IAHR Biennal Congress*, Vol. Theme D, San Francisco, USA, pp. 583–588.

Ohtsu, I., Yasuda, Y. & Takahasi, M. (2000). Characteristics of skimming flow over stepped spillways - discussion, *J. of Hydraulic Engineering, ASCE* **126**(11): 869–871. by Chamani, M.R. and Rajaratnam, N.

Olivier, H. (1967). Through and overflow rockfill dams - new design techniques, number 7012, Inst civil engeeners, pp. 433–471. For discussion.

Pagliara, S. & Peruginelli, A. (2000). Limiting and sill-controlled adverse-slope hydraulic jump, *J. of Hydraulic Engineering* **126**(11): 847–851.

Pegram, G. G. S., Officer, A., K. & Mottram, S. R. (1999). Hydraulics of skimming flow on modeled stepped spillways, *J. of Hydraulic Engineering* **125**(5): 500–510.

Peruginelli, A. & Pagliara, S. (2000). Energy dissipation comparison among stepped channel, drop and ramp structures, *in* H.-E. Minor & W. Hager (eds), *Proceedings of the International Workshop on Hydraulics of Stepped Spillways*, IAHR, A.A. Balkema/Rottersam/Brookfield, Zürich, Switzerland.

Peterka, A. (1953). The effect of entrained air on cavitation pitting, *Proc. of 5th IAHR/ASCE Congress*, Vol. Joint meeting paper, Minneapolis, USA, pp. 507–518.

Peterka, A. (1958). Air-water flow in hydraulic structures, *Engineering Monograph 25*, Bureau of Reclamation, United States Department of the Interior, Denver, Colorado, USA.

Peyras, L., Royet, P. & Degoutte, G. (1991). Ecoulement et dissipation sur les déversoirs en gradins de gabions, *La Houille Blanche* (1): 37–47. In French.

Pinheiro, A. & Fael, C. (2000). Nappe-flow in stepped channels - occurence and energy dissipation, *in* H.-E. Minor & W. Hager (eds), *Proceedings of the International Workshop on Hydraulics of Stepped Spillways*, IAHR, A.A. Balkema/Rottersam/Brookfield, Zürich, Switzerland, pp. 119–126.

Pinto, N. d. S. (1984). Model evaluation of aerators in shooting flow, *in* H. Kobus (ed.), *Proc. of Symposium on scale effects in modelling hydraulic structures*, Vol. 4.2, Esslingen, Germany, pp. 1–6.

Pirotton, M. (1997). *Une approche globale pour modéliser la genèse et la propagation des crues naturelles ou accidentelles*, Classe des Sciences, Académie Royale de Belgique.

Powledge, G. R. & Sveum, D. L. (1988). Overtopping embankment dams - an aternative in accomodating rare floods, *in* ICOLD (ed.), *Seizième Congrès Des Grands Barrages*, Q. 63 - R. 35, ICOLD, San Francisco, USA.

Powledge, G., Ralston, D. C., Miller, P., Chen, Y. H., Clopper, P. E. & Temple, D. M. (1989). Mechanics of overflow erosion on embankments. part 2: Hydraulic and design considerations, *Journal of Hydraulic Engineering* **115**(8): 1056–1075.

Pravdivets, Y. P. & Slissky, S. M. (1981). Passing floodwaters over embankment dams, *Water Power and Dam Construction* pp. 30–32.

Rajaratnam, N. (1990). Skimmimg flow in stepped spillways, *J. of Hydraulic Engineering* **116**(4): 587–591.

Rajaratnam, N. & Chamani, M. (1995). Energy loss at drops, *J. of Hydraulic Research* **33**(3): 373–384.

Rehbock, T. (1929). *Wassermessung mit scharfkantigen Ueberfallwehren*, Vol. 73. Zeitschrift VdI.

Rutschmann, P. (1988). *Belüftunseinbauten in Schussrinnen*, PhD thesis, Swiss Federal Institue of Thecnology Zürich (ETHZ) - VAW, Switzerland. In German.

Sayre, W. W. & Albertson, M. L. (1963). Roughness spacing in rigid open channels, *American Society of Civil Engineers - Transactions* **128**(3417): 343–427.

Schwalt, M. & Hager, W. (1992). Die strahlbox, *Schweiz. Ing. Archit.* **110**(27-28): 547–549. In German.

Serafim, J. (1981). Safety of dams judged from failures, *Water Power and Dam Construction* pp. 32–35.

Shvidchenko, A. B. & Pender, G. (2001). Large flow structures in a turbulent open channel flow - discussion, *J. of Hydraulic Research* **39**(1): 109–111.

Sánchez-Juny, M. (2001). *Comportamiento hydráulico de los aliviaderos escalonados en presas de hormigón compactado. Análisis del campo de presiones*, PhD thesis, Universitat Politècnica de Catalunya, Spain. In spanish.

Sánchez-Juny, M., Pomares, J. & Dolz, J. (2000). Pressure field in skimming flow over a stepped spillway, *in* H.-E. Minor & W. Hager (eds), *Proceedings of the International Workshop on Hydraulics of Stepped Spillways*, IAHR, A.A. Balkema/Rottersam/Brookfield, Zürich, Switzerland, pp. 137–145.

Straub, L. & Anderson, A. (1958). Experiments on self-aerated flow in open channels, *J. of Hydraulics Division* **84**(HY7). ASCE.

Stutz, B. (1996). *Analyse de la structure diphasique et instationnaire de poches de cavitation*, PhD thesis, Institut National Polytechnique de Grenoble, France. In French.

Temple, D. e. a. (1987). Stability design of grass-lined open channels, *Handbook 667*, USDA.

Timblin, J., Grey, P. & Morrison, W. (1988). Emergency spillways using geomembranes, *in* ICOLD (ed.), *XVI ICOLD Congress on LArge Dams*, Q. 61 - R. 28, San Francisco, USA.

Tome, M., McKee, S. & Gensmack, A. (1994). Computational marker and cell method for free surface flows in general domains, *J. of Computational Physics* **110**: 171–186.

Toombes, L. & Chanson, H. (2000). Air-water flow and gas transfer at aeration cascades: a comparative study of smooth and stepped chutes, *in* H.-E. Minor & W. Hager (eds), *Proceedings of the International Workshop on Hydraulics of Stepped Spillways*, IAHR, A.A. Balkema/Rottersam/Brookfield, Zürich, Switzerland, pp. 77–84.

Tozzi, M. J. (1994). Residual energy in stepped spillways, *International Water Power and Dam Construction* pp. 32–34.

USBR (2004). Data base of dam failures.

Viparelli, M. (1953). Flow in a flume with 1:1 slope, *Proc. of Minnesota Int. Hydraulics Convention*, IAHR/ASCE, Minneapolis, Minnesota, EUA, USA, pp. 415–423.

Vischer, D., Volkart, P. & Siegenthaler, A. (1982). Hydraulic modelling of air slots in open chute spillways, *Proc. of Hydraulic Modelling of Civil engineering structures*, Coventry, U.K., pp. 239–252.

Wilhelms, S. & Gulliver, J. (1989). Self-aerating spillway flow, *In Proc. of the 1989 National Conference on Hydraulic Engineering*, ASCE, LA, USA, pp. 881–886.

Wittler, R. J. & Abt, S. R. (1990). The influence of uniformity on riprap stability, *Hydraulics 1990 - National Conference on Hydraulic Engineering*, R-90-12, United State Bureau of Reclamation.

Wood, I. (1983). Uniform flow region of self-aerated flow, *J. of Hydraulic Division, ASCE* **109**(3): 447–461.

Wood, I. R. (1991). Free surface air entrainment on spillways, *in* I. R. Wood (ed.), *Air Entrainment in free-surface Flows*, iahr edn, Vol. 4 of *Hydraulic Structures Design Manual*, A.A. Balkema/Rottersam/Brookfield, chapter 3, pp. 55–84.

Yasuda, Y. & Chanson, H. (2003). Micro-and macro-scopic study of two-phase flow on a stepped chute, *XXX IAHR Congress on water Engineering and research in a learning society: Modern Developments and Traditional Concepts*, Vol. Theme D: Experiments on Stepped Spillways, IAHR, Thessaloniki, Greece, pp. 695–702.

Yasuda, Y. & Ohtsu, I. (1999). Flow resistance of skimming flow in stepped channels, *Proc. 28th IAHR Congress*, Vol. B14, IAHR, Graz, Austria. In CD.

Yasuda, Y. & Ohtsu, I. (2000). Characteristics of plunging flows in stepped channel chutes, *in* H.-E. Minor & W. Hager (eds), *Proceedings of the International Workshop on Hydraulics of Stepped Spillways*, IAHR, A.A. Balkema/Rottersam/Brookfield, Zürich, Switzerland, pp. 147–152.

Yasuda, Y. & Ohtsu, I. (2003). Effect of step cavity area on flow characteristics of skimming flows on stepped chutes, *XXX IAHR Congress on water Engineering and research in a learning society: Modern Developments and Traditional Concepts*, Vol. Theme D: Experiments on Stepped Spillways, IAHR, Thessaloniki, Greece, pp. 703–710.

Zaleski, S. (2000). Multiphase-flow cfd with volume of fluid (vof) methods, *in* ETH (ed.), *Proc. of the Modelling and Computation of Multiphase Flows*, Vol. Part IIB, Zurich, Switzerland.

Part VIII

Appendix

Appendix A

Homogeneous flow data

A.1 Conventional steps (m=0) - 30^o slopping chute

The characteristics of the effective homogeneous flow, according to the intermittence approach (section 13.2, Part IV) are represented in the table A.1.

Regime	q_w (m^2/s)	F_0 (-)	Z' (m)	C' (-)	U' (m/s)	q'_w (m^2/s)	$\frac{\Delta q'_w}{qw'}$ (%)
T	0.0606	5.5	0.0308	0.383	3.40	0.0629	- 4
SF	0.0807	4.3	0.0363	0.363	3.59	0.0809	0
SF	0.1205	4.3	0.0502	0.369	3.95	0.1219	- 1
SF	0.1603	4.1	0.0559	0.354	4.25	0.1491	7
SF	0.2004	4.1	0.0608	0.357	4.33	0.1633	18
SF	0.2416	4.1	0.0657	0.352	4.57	0.1873	22

Table A.1: Characteristics of the effective homogeneous bubbly flow in the fully developed region, for skimming flow over conventional stepped chute

A.2 All steps with endsills (m=1) - 30^o slopping chute

The characteristics of the effective homogeneous flow, according to the intermittence approach (section 13.2, Part IV) are represented in the table A.2.

Regime	q_w (m^2/s)	F_0 (-)	Z' (m)	C' (-)	U' (m/s)	q'_w (m^2/s)	$\frac{\Delta q'_w}{qw'}$ (%)
T	0.0402	5.3	0.0257	0.379	2.912	0.0447	- 11
SF	0.0806	4.6	0.0360	0.334	3.44	0.0797	1
SF	0.1205	4.2	0.0458	0.346	3.93	0.113	6
SF	0.1607	4.4	0.0509	0.322	4.21	0.1404	12
SF	0.2338	4.2	0.0640	0.320	4.64	0.1952	16

Table A.2: Characteristics of the effective homogeneous bubbly flow in the fully developed region, for skimming flow over conventional stepped chute

Appendix B

Hydraulic behaviour over smooth chutes

In order to be able to compare the efficiency of the macro-roughness lining tested, the characteristics of the flow over an equivalent smooth chute of 18.6^o and 30^o slopes had been assessed. The calculations are lead on a computational program developed by Falvey (1990) for engineers to calculate the hydraulic and cavitation properties of free water surface flows.

This appendix does not intend to give a detail of the calculation which is described in the Monograph 42, but to give the basic equations used in program.

B.1 Basic equations

Flume geometry

The flume geometry computed consists in a rectangular section, 8 m long, 0.5 m width flume with a 18.6^o and 30^o slopes. The incoming flow is controlled by both the water discharge and the flow depth imposed by the jetbox. The roughness of the bottom is fixed at $k = 0.05\,mm$ to represent the aluminium smooth bottom. The slope had been modeling down to the toe of the flume and 10 cross sections permit to control the evolution of the flow properties.

Modeling

The water surface profile is based on the standard step method [Chow (1959)], including air entrainment. It assumes gradually varied flow in a uniform channel with friction factor lower than 0.115 and correction terms to take into account steep slope. The used algorithms are compiled in Microsoft-Fortran.

Friction factor :

The friction losses are based on the Darcy-Weisbach friction factor relation defined as:

$$S_f = \frac{f}{4R_h}\frac{U_w^2}{2g} \tag{B.1}$$

where $S_f = E_f/L$ is the friction slope with E_f the head loss due to friction over the length L, R_h the hydraulic radius and U_w the equivalent clear-water flow mean velocity. The friction factor (f) is determined from the Colebrook-White equation for open channel flow, Eq. B.2:

$$\frac{1}{\sqrt{f}} = -2log\Big(\frac{k}{12R_h} + \frac{2.5}{R_e\sqrt{f}}\Big) \tag{B.2}$$

where $R_e = 4R_hU_w/\nu$ is the Reynolds number with ν =the kinematics viscosity .

Pressure distribution :

Because the flow is over steep slope, the assumption of a hydrostatic pressure distribution is no longer accurate. In order to correct the hydrostatic term, the wall pressure head (E_{wall}) at a flow of depth Z_m is given by Equation B.3:

$$E_{wall} = Z_m cos\Theta \tag{B.3}$$

where Θ=chute slope.

Froude number for steep slope :

To take into account of the steep slopping chute, the Froude number (F_Θ) is given by:

$$F_\Theta = \frac{\sqrt{\alpha} U_w}{g Z_w cos\Theta} \tag{B.4}$$

where $\alpha = \frac{1}{U_w^3 A} \int_0^A (u_w^3 dA_i)$ is the kinetic energy correction factor due to the non uniform velocity distribution and $1.0 \leq \alpha \leq 1.1$, Z_w=the clear-water depth, A=the cross section area , u_w=the local longitudinal equivalent clear-water flow velocity at any depth z .

Air entrainment :

In order to estimate the characteristics of the mixture air-water flow, an air concentration empirical model is included in the program as soon as air entrainment is initiated (when the boundary layer thickness equals the flow depth). It is given by Equation B.5 from Falvey (1980):

$$C = 0.05Fr - \frac{\sqrt{Esin\Theta}}{63} \tag{B.5}$$

where $E = (g\rho_w Z_w^2)/\epsilon$=the Eötvös number with ρ_w the density of the water and ϵ the interfacial surface tension.

The mean air concentration in the uniform region (C_u) had also been compared with the empirical formula of Hager (1991), Equation B.6:

$$C_u = 0.75 sin\Theta^{0.75} \tag{B.6}$$

which highlights that the saturated air concentration (*i.e* the mean air concentration in the uniform region) is only affected by the slopping chute.

B.2 Flow characteristics

Under its assumptions, the program provides good approximation of the mixture flow and clear water hydraulic parameters as well as cavitation properties which are not exploited in the thesis context. In the following Figure B.1, the mean air concentration, mixture depth, mixture velocity and relative energy dissipation are represented for the aerated flow over smooth 18.6^o and 30^o slopping chutes, in the uniform region. These curves would be the basis to compare the effect of macro-roughness linings on the hydraulic of the aerated flow.

For all the tested discharges, at the toe of the chute, the results on the mixture and clear water depths which kept constant at the downstream cross-sections show that the quasi-uniform region (or namely the fully developed region) is attained. However, it appears that with this computational program, the main air concentration decreases continuously with the increasing of the discharge though the Hager formula Eq. B.6 or the Straub & Anderson (1958) experimental results concluded that for steep smooth slopes, air concentration is only depending on Θ in the uniform region.

It is also to notice that the air entrainment is less important for smaller slope which was expected since the velocity and turbulence forces are lower. Finally whatever the discharges,

the energy dissipation is less efficient with smaller slope: this tendency is different for slope equipped with macro-roughness overlays which comforts the fact that the energy dissipation process for flow over macro-roughness is not only the fact of friction head loss.

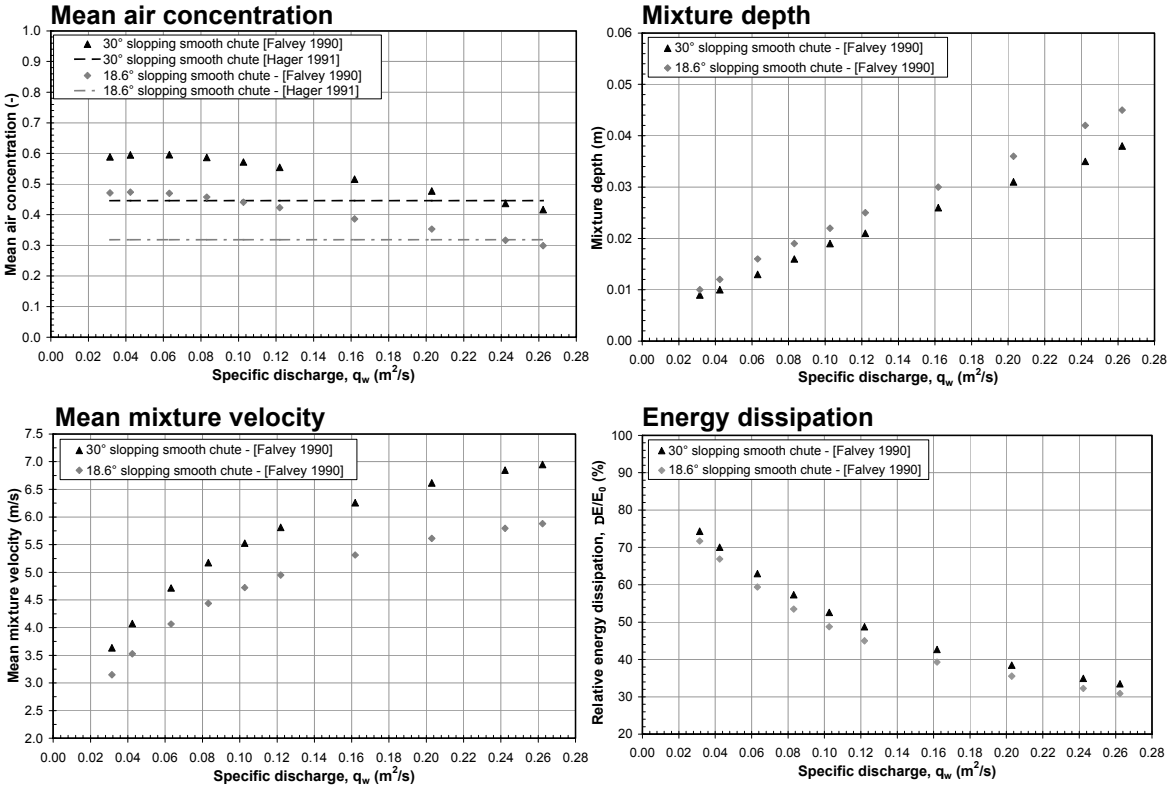

Figure B.1: Evolution of the flow characteristics (mean air concentration, mixture depth, mixture velocity, energy dissipation rate) at the toe of the 18.6^o and a 30^o smooth chutes

Communications du Laboratoire de constructions hydrauliques ISSN 1661-1179
Ecole Polytechnique Fédérale de Lausanne
Editeur: Prof. R. Sinniger

N°	1	1986	W. H. Hager Discharge measurement structures
N°	2	1988	N. V. Bretz Ressaut hydraulique forcé par seuil
N°	3	1990	R. Bremen Expanding stilling basin
N°	4	1996	Dr R. Bremen Ressaut hydraulique et bassins amortisseurs, aspects hydrauliques particuliers
N°	5	1997	Compte-rendu du séminaire à l'EPFL Recherche dans le domaine des barrages, crues extrêmes

Communications du Laboratoire de constructions hydrauliques
Ecole Polytechnique Fédérale de Lausanne
Editeur: Prof. Dr A. Schleiss

N°	6	1998	N. Beyer Portner Erosion des bassins versants alpins suisse par ruissellement de surface
N°	7	1998	G. De Cesare Alluvionnement des retenues par courants de turbidité
N°	8	1998	J. Dubois Comportement hydraulique et modélisation des écoulements de surface
N°	9	2000	J. Dubois, J.-L. Boillat Routing System - Modélisation du routage de crues dans des systèmes hydrauliques à surface libre
N°	10	2002	et suivants, voir verso page titre

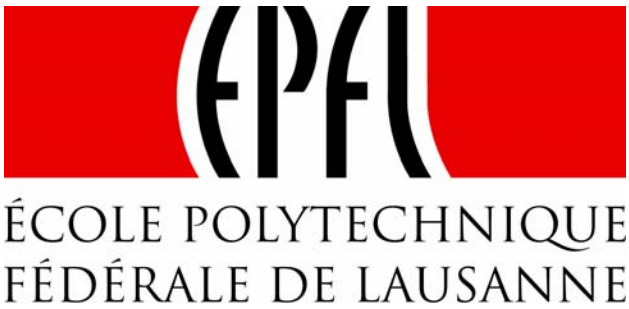

ISSN 1661-1179

Prof. Dr A. Schleiss
Laboratoire de constructions hydrauliques - LCH
EPFL, Bât. GC, Station 18, CH-1015 Lausanne
http://lchwww.epfl.ch
e-mail: secretariat.lch@epfl.ch